Impedance eduction of acoustic liners with complex sound fields and shear flows

Jinyue Yang

THESE DE DOCTORAT

DE
LE MANS UNIVERSITE
SOUS LE SCEAU DE
LA COMUE ANGERS – LE MANS

ECOLE DOCTORALE N° 602
Sciences de l'Ingénierie et des Systèmes
Spécialité : « *Acoustique* »

Par

Jinyue YANG

Impedance eduction of acoustic liners with complex sound fields and shear flows

Thèse présentée et soutenue au Mans, le 26 novembre 2024
Unité de recherche : UMR CNRS 6613 Laboratoire d'Acoustique de l'Université du Mans
Thèse N° : 2024LEMA1023

Rapporteurs avant soutenance :

Francesco Avallone	Professeur des Universités à Politecnico di Torino
Julio Cordioli	Professeur des Universités à Federal University of Santa Catarina (UFSC)

Composition du Jury :

Président :	Régis Marchiano	Professeur des Universités à l'Université Pierre et Marie Curie
Examinateurs :	Elke Deckers	Professeure associée à KU LEUVEN
	Rémi Roncen	Chargé de recherche à l'ONERA
	David Marx	Chargé de recherche à l'Institut Pprime
Dir. de thèse :	Gwénaël Gabard	Professeur des Universités à l'Université du Mans
Co-dir. de thèse :	Thomas Humbert	Ingénieur de recherche à l'Université du Mans

Acknowledgements

Je tiens à exprimer ma profonde gratitude à mes deux directeurs de thèse. Faire de la recherche est un processus où l'on découvre constamment l'étendue de sa propre ignorance. Sans leur soutien, il m'aurait été difficile de surmonter cet abîme d'incertitude. Merci à Gwénaël, dont le sérieux et la rigueur scientifique ont souvent éclairé mes réflexions par des remarques précises et pertinentes, et dont le professionnalisme m'a beaucoup inspiré. Merci à Thomas, ton enthousiasme et ta vivacité ont rendu cette aventure encore plus enrichissante, et c'est un honneur d'avoir été ta première doctorante. Au cours de ces trois années, tu m'as accompagnée dans chaque étape de mon travail, me montrant une attention constante et un soutien précieux. Je tiens également à remercier chaleureusement Joachim pour sa participation active à nos réunions hebdomadaires et pour nos discussions qui ont considérablement clarifié mes travaux expérimentaux. Un grand merci aussi à Eric Portier, pour son soutien technique et la mise à disposition des logiciels nécessaires au bon déroulement de mes expériences.

Je remercie également les membres du jury d'avoir accepté d'évaluer mon travail de thèse et pour les échanges constructifs que nous avons pu avoir après ma présentation. Merci à toutes les personnes qui ont assisté à ma soutenance et pour vos messages d'encouragement, qui ont été pour moi une source précieuse de motivation.

Au cours de mes trois années de doctorat, j'ai vécu des moments tantôt monotones, tantôt passionnants. Une grande partie de cette joie provient de ma rencontre avec un groupe de merveilleuses amies (Yuyang, Yuyao, Xiaoyu, Zichun, Yuhan, etc..). Merci pour nos moments de partage et de bonheur, qui m'ont empêché de me sentir isolée avec notre convivialité. Une autre source de bonheur est venue du groupe de 11h45, avec Charlotte, Anis, Juliette, Martin, Alexis... Ensemble, nous avons travaillé en synchronisation pour nos propres recherches, nous encourageant et nous soutenant mutuellement, particulièrement célébrant les joies de J&M et de leur Pavel. Merci à vous tous pour votre présence, qui a enrichi ma vie sociale. Merci aussi à Dr. Meng et Dr. Dong, nos discussions et vos suggestions m'aident à découvrir mon chemin dans plusieurs aspects.

Merci à mes amis de ma ville natale pour leurs encouragements et leur confiance. Notre amitié est un trésor que je chérirai toujours. Enfin, merci à ma famille pour leur compréhension et leur support. Grâce à vous, comme mon précieux pilier, j'ai pu explorer de nouveaux horizons en toute sérénité.

Merci à XiaoYaoWan de m'avoir aidé à maintenir mon équilibre émotionnel, et merci à moi-même d'avoir eu le courage d'avancer sans relâche. Ces trois années de travail de recherche représentent actuellement 12% de ma vie. Ce chiffre diminuera avec le temps, mais la signification et l'impact de cette expérience ne feront que croître.

Contents

Introduction

Acoustic lining is one of the key technologies for controlling aero-engine noise [1–3]. Due to its effectiveness in low cost, low weight, it has been widely applied in aircraft engines, particularly in the surface treatment of the intake, bypass, and exhaust sections of nacelles, as shown in Figure 1. The measurement of the liner performance and the study of its behaviour are important topics in its development and design. This thesis focuses on the measurement of acoustic liners under conditions representative of aircraft nacelles, namely complex acoustic fields within large ducts and sheared high-speed flows.

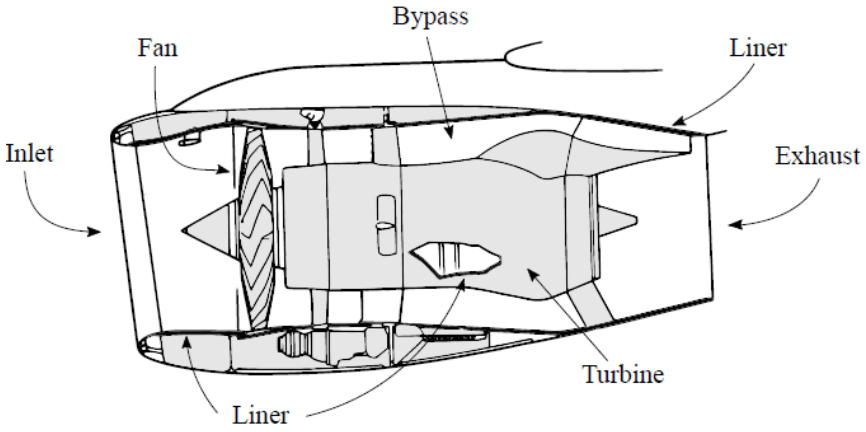

Figure 1: Schematic view of liner positions in a turbofan engine nacelle [4].

Liner characterisation

In duct acoustics, the process of liner optimisation is typically achieved through numerical simulations of the given problem and geometry. This results in the computation of the optimal impedance (or the geometry) of the liner to be installed for effective noise reduction [5, 6]. The acoustic impedance is defined as the ratio between the acoustic pressure and the normal particle velocity at the surface of the liner. Following the optimisation, measurements are required to verify the liner's performance in different environments. In this context, impedance measurements are crucial, as impedance is a parameter that remains independent of the duct geometry, unlike other acoustic quantities such as absorption or transmission loss. However, it has been shown [7] that the flow velocity and the incident Sound Pressure Level (SPL) have an impact on the impedance, so that the measurements have to be performed under conditions close to the targeted application. To this end, several studies [8, 9] have investigated factors such as the incident amplitude of the incident acoustic field, flow velocity, and flow profile. However, these investigations have predominantly been conducted in small-scale test ducts, which do not adequately represent the complex conditions found in engine nacelles. In the latter situation,

the acoustic field is more complex due to a larger number of propagating modes, and the effects of flow shear require further investigation in large-scale ducts. To address these investigations, the MAINE Flow facility [10–12], which includes a large cross-sectional duct, has been established at LAUM for liner measurements under a controlled large amplitude incident acoustic field and a high-speed airflow.

Common experimental methods to assess the liner impedance in presence of flows include the in-situ method [13] and impedance eduction techniques [14–18]. The former focuses on local effects, but requires damaging the liner sample, whereas the latter is based on an acoustic propagation model within the duct, and therefore generally leads to the effective average impedance along the entire lined section. Also, impedance eduction methods can be categorised as inverse or direct, depending on whether the impedance is obtained by iterative calculations or not. This thesis focuses on the direct method for impedance eduction and its development in the context of large ducts. Therefore, an accurate propagation model is needed to consider the framework of multimodal sound fields and large Mach number subsonic flows.

Acoustic propagation models incorporate physical effects to varying extents, depending on the hypotheses made. With regard to flow effects, the assumption of uniform flow has been shown to lead to errors in the process of educing the impedance, highlighting the importance of accounting for flow shear in realistic situations [9, 19]. For example, a comparative study in the NASA GFIT facility [9] reveals discrepancies between the impedance obtained using uniform or shear flow, especially at high flow velocities. However, Jing et al. [20] demonstrates that impedance eduction considering shear flow is minimally influenced by the boundary layer's exact shape, consistent with earlier findings [21]. Nevertheless, Spillere et al. [18] observes that more realistic flow profiles can impact impedance eduction in their larger cross-section test duct, differing from previous observations. Bonomo et al. [22] further highlights how varying flow profiles can cause discrepancies in impedance results across different test rigs, suggesting that accurate impedance calculations should account for the flow profile. With these studies occurring in different contexts, key questions remain: To what extent does mean flow shear impact impedance eduction, and how are these effects influenced by factors such as duct size, frequency and flow velocity?

Concerning existing test facilities, published experimental results are mainly obtained with small cross-section ducts in which the flow and the incident sound field can be more easily generated and controlled. However, in these test ducts, only plane wave propagates at most frequencies of interest, with limited studies addressing shear flow effects with multimodal fields in larger ducts. NASA's studies [23, 24] report similar impedance eduction results between a small cross-section duct (GFIT) and a large-scale duct (CDTR) under the uniform flow assumption. Discrepancies were observed only at very low or very high frequencies, attributed to low attenuation and the emergence of higher-order modes, respectively [24]. While these data provide valuable insights into differences between small and large ducts, the precise impact of mean flow shear in large ducts remains to be thoroughly investigated. Additionally, at typical measurement frequencies, multimodal propagation is more prevalent in large ducts. Roncen et al. [25] assesses uncertainties in flow profiles using Bayesian inference, and concludes that uniform flow assumptions do not significantly affect single-mode propagation results, but that multimodal cases require further investigations. Given the lack of studies in multimodal acoustic field, it is crucial to develop impedance eduction techniques, enabling more experimental investigations in large ducts that account for higher-order modes.

Objectives and outline of the thesis

This thesis aims to develop direct impedance eduction techniques for large ducts with sheared flows. It begins with a review on acoustic liners in presence of flow, outlining the current state of research. This is followed by a detailed description of the propagation models that simulate acoustic fields in large ducts, serving as key tools for both experimental and numerical studies. Using these tools, new direct impedance eduction methods are developed and compared with the traditional algorithm [15]. The primary objective is to analyse, through parametric studies, the influence of shear flow on acoustic propagation and attenuation in ducts equipped with liners, as well as to assess the validity of the uniform flow assumption inherent in the traditional algorithm. A secondary purpose is to implement these direct impedance techniques and to evaluate the performance of both existing and newly developed methods through numerical simulations and experimental validations in the large duct of MAINE Flow facility. To these ends, the thesis is organised into five chapters.

Chapter 1 provides an overview of the background and evolving demands for the application of acoustic liners. It details the physical mechanisms associated with acoustic liners and outlines the existing empirical design methods. The chapter also reviews experimental methods and facilities commonly used for the characterisation of acoustic liners. Based on existing modelling and experimental research, it concludes with some considerations on the influence of various physical conditions on the liner performance, including high sound pressure levels and flow effects.

In Chapter 2, the numerical and experimental methods employed in this thesis are described. It begins with a description of the MAINE Flow facility. Following this, a multimodal approach is used to simulate the acoustic field within large ducts: the convected Helmholtz equation is used to account for a uniform flow, and the linearized Euler equations for a sheared flow. Furthermore, the chapter provides a detailed explanation of both the traditional direct impedance eduction algorithm and the newly developed methods that account for lined-lined (so-called double-liner) configuration and/or sheared flow. These models and methods are employed in Chapter 3 to assess several aspects of the impact of shear flow in a lined duct. The impedance eduction techniques are also used for numerical simulations (in Chapter 4) based on pressure data computed through the multimodal models, and for experimental analysis (in Chapter 5) using data measured in the MAINE Flow facility.

The direct impedance eduction method can be broadly divided into two steps: extracting wavenumbers from the sound field signals and calculating the acoustic impedance using these wavenumbers. Consequently, the impact of shear flow on impedance eduction is considered in relation to these two stages. Additionally, the overall performance of impedance eduction is influenced by liner attenuation [17, 24, 26]. In view of these, Chapter 3 provides a detailed analysis of the effects of shear flow by focusing on three key aspects: acoustic propagation within the duct, the accuracy of impedance eduction results, and the sound attenuation performance of acoustic liners within the duct. The study examines various parameters, including boundary layer thickness, flow velocity, propagation direction, and different liner configurations. The chapter first investigates the impact of shear flow on acoustic propagation by analysing the differences in wavenumbers under uniform and shear flow conditions. Next, it evaluates the accuracy of calculating impedance through comparing result errors obtained using the traditional method (which assumes uniform flow and applies the Ingard-Myers boundary condition) with those from the

proposed method (which accounts for flow shear). The influence of shear is also assessed in terms of transmission coefficients.

Chapter 4 simulates the eduction process by numerically conducting impedance eduction using pressure signals from the lined section, within the acoustic field simulated by the multimodal models described in Chapter 2. In other words, the direct impedance eduction experiments conducted in the MAINE Flow duct are replicated through numerical simulations. The analysis covers several key aspects, including wavenumber estimation methods, liner configurations, flow assumptions used in impedance calculations, the presence of noise in pressure signals, mode disturbances in the incident sound field, and the positioning and deployment of the microphone array. These simulations assess the performance of impedance calculations under both single-liner and double-liner configurations, considering uniform and shear flow assumptions. The underlying mechanisms driving the performance differences between the two configurations are then discussed in detail. Finally, to improve the effectiveness of the double-liner configuration in practical experiments, the use of a 2-line microphone array is proposed.

The last chapter of this thesis presents the experimental part, conducted with the large duct (MAINE Flow) and incorporating newly developed ideas such as the double-liner configuration and the two microphone arrays (1-line and 2-line). For data post-processing, two methods are developed and compared to accurately select the correct wavenumbers from the experimental data, which are essential for calculating precise impedance values. During testing, liner samples are measured under various conditions to analyse the effects of different liner configurations, incident modes, sound pressure levels, flow velocities, and propagation directions. The chapter also compares the results obtained using uniform flow and shear flow models during the impedance calculation. Additionally, the impact of microphone spacing is discussed, and the performances of different microphone arrays in impedance eduction are compared. Finally, the chapter introduces tests conducted on two sets of optimised liners, specifically designed for their high-frequency attenuation in the presence of flow.

Finally, the key findings in this thesis are summarised in the conclusions and a number of perspectives are provided for future work.

Résumé

Les traitements acoustiques ("acoustic liners" en Anglais) sont une technologie clé pour contrôler le bruit émis par les moteurs d'avion, en particulier dans le traitement de surface des sections d'admission, de dérivation et d'échappement des nacelles. L'étude expérimentale de leur comportement et la mesure de leurs performances sont des sujets importants pour la conception et le développement de ces traitements. Cette thèse se concentre sur la mesure des revêtements acoustiques dans des conditions représentatives des nacelles d'avion, à savoir des champs acoustiques complexes à l'intérieur de grands conduits où existent des écoulements cisaillés de grande vitesse.

Le processus d'optimisation des revêtements acoustiques est généralement réalisé au moyen de simulations numériques d'une situation. Cela permet de calculer l'impédance optimale (ou la géométrie) du traitement à installer pour une réduction efficace du bruit [5, 6]. L'impédance acoustique est définie comme le rapport entre la pression acoustique et la vitesse particulaire normale à la surface du revêtement. Après l'optimisation, des mesures sont nécessaires pour vérifier les performances du revêtement dans différents environnements. Dans ce contexte, les mesures d'impédance sont essentielles, car l'impédance est un paramètre indépendant de la géométrie du conduit, contrairement à d'autres grandeurs acoustiques telles que l'absorption ou la perte par transmission. Cependant, il a été démontré [7] que la vitesse d'écoulement et le niveau de pression sonore incidente (SPL) influencent l'impédance, de sorte que les mesures doivent être effectuées dans des conditions proches de l'application visée. À cette fin, plusieurs études [8, 9] ont examiné des facteurs tels que l'amplitude du champ acoustique incident, la vitesse de l'écoulement et le profil d'écoulement. Cependant, ces recherches ont été principalement menées dans des conduits d'essai de petite section, qui ne représentent pas adéquatement les conditions complexes rencontrées dans les nacelles de moteurs. Dans ce dernier cas, le champ acoustique est plus complexe en raison d'un plus grand nombre de modes propagatifs, et les effets du cisaillement de l'écoulement doivent être étudiés plus en détails dans de grands conduits. Pour mener à bien ces études, le banc d'essai MAINE Flow [10–12], qui comprend un conduit de grande section, a été mis en place au LAUM pour caractériser des traitements acoustiques dans des conditions contrôlées, avec un champ acoustique incident à grande amplitude et un écoulement d'air à grande vitesse.

Les méthodes expérimentales courantes pour évaluer l'impédance du revêtement en présence d'écoulement sont les techniques dites d'«impedance eduction» (la mesure d'impédance) [14–18]. La plupart de ces techniques repose sur un modèle de propagation acoustique dans un conduit, et conduisent généralement à l'impédance moyenne effective sur l'ensemble de la section de traitement. En outre, les méthodes d'«impedance eduction» peuvent être inverses ou directes, selon que l'impédance est obtenue par des calculs itératifs ou non. Cette thèse vise à developper la méthode directe d'«impedance eduction» dans le contexte des grands conduits en prenant en compte des champs acoustiques complexes et des écoulements cisaillés.

Cette thèse commence par une étude bibliographique sur les revêtements acoustiques en présence d'écoulement, qui décrit l'état actuel de la recherche sur le sujet. Elle est suivie d'une description détaillée des modèles mis en place au cours de cette thèse pour simuler la propagation de champs acoustiques en conduits avec écoulement. Grâce à ces outils, de nouvelles méthodes directes de mesure d'impédance sont développées et validées. Le premier objectif est d'analyser, au moyen d'études paramétriques, l'influence de l'écoulement cisaillé sur la propagation et l'atténuation acoustiques dans les conduits traités, ainsi que d'évaluer la validité de l'hypothèse d'écoulement uniforme inhérente à l'algorithme traditionnel. Un objectif secondaire est de mettre en œuvre ces techniques de mesure d'impédance et d'évaluer la performance des méthodes existantes et nouvellement développées par le biais de simulations numériques et de validations expérimentales dans le grand conduit de MAINE Flow. Dans l'évaluation de la performance des méthodes, les effets de champ acoustique incident sont aussi étudiés, accompagnés de recommandations sur l'antenne de microphone à utiliser. De ce fait, la thèse est organisée en cinq chapitres.

Le premier chapitre présente l'application des traitements acoustiques pour l'aéronautique et les mécanismes physiques en jeu. Il présente ensuite les méthodes d'«impedance eduction» pour mesurer et évaluer les revêtements, ainsi qu'une liste détaillée des bancs d'essai existants dans la littérature. Le chapitre rappelle également les études [8, 19] qui prennent en compte les effets du niveau de pression acoustique (SPL) et des conditions d'écoulement sur les performances des revêtements et sur la précision des mesures. Cependant, il est identifié que peu d'études [18, 20] considèrent des vitesses d'écoulement élevées et les effets de la couche limite, et les conduits de grande taille présentant des champs acoustiques multimodaux. En outre, bien que certaines recherches aient mis en évidence l'influence du cisaillement de l'écoulement sur les résultats de la mesure d'impédance, on ne comprend toujours pas clairement comment et dans quelle mesure l'écoulement cisaillé a un impact sur l'impédance et/ou sa mesure. Cela souligne la nécessité d'une analyse systématique pour mieux comprendre ces effets.

Le chapitre 2 pose les bases méthodologiques de cette thèse. Une description détaillée de l'installation MAINE Flow est fournie, caractérisée par sa grande section transversale qui supporte un champ acoustique multimodal contrôlé et des vitesses d'écoulement élevées. Grâce à la synthèse et à la détection modales, cette installation permet de mesurer les traitements pour chaque mode acoustique individuel, ce qui sert à une évaluation plus complète du traitement acoustique. Pour simuler la propagation acoustique dans un conduit à trois segments, des modèles multimodaux avec un écoulement uniforme (en utilisant l'équation de Helmholtz convectée) ou cisaillé (en utilisant les équations d'Euler linéarisées) sont introduits. Une méthode pseudo-spectrale est employée pour le calcul de mode à l'intérieur de chaque segment, tandis qu'une approche de raccordement modal traite les discontinuités dans la direction axiale. Les champs acoustiques simulés par ces modèles seront essentiels dans l'étude numérique suivante.

La méthode directe de mesure d'impédance peut être divisée en deux étapes : i) l'estimation des nombres d'ondes constituant le champ acoustique et ii) le calcul de l'impédance acoustique à partir de ces nombres d'ondes. En ce qui concerne la première étape, deux méthodes de type Prony, KT (Kumaresan–Tufts) et HTLS (Hankel Total Least Square), sont décrites. Sur cette base, la méthode directe est développée et étendue pour prendre en compte une configuration à deux traitements face à face (dites «double-liner») avec un écoulement moyen uniforme ou cisaillé. Pour les cas d'écoulement cisaillé, la méthode utilise le déplacement vertical acoustique

comme variable, plutôt que la vitesse verticale acoustique, afin de contourner les problèmes numériques liés aux profils d'écoulement avec des dérivées infinies aux bords. L'approche proposée ici réduit considérablement le temps de calcul par rapport à [19].

En utilisant les modèles de propagation et les méthodes directes de mesure d'impédance, et par le biais d'une analyse paramétrique dans le cas 2D, le chapitre 3 examine les effets du cisaillement sur la propagation acoustique, la précision des calculs d'impédance et l'atténuation provoquée par traitement. En comparant les hypothèses d'écoulement uniforme et cisaillé, l'étude met en évidence l'influence significative du cisaillement de l'écoulement moyen, en particulier dans les grands conduits et à haute fréquence. Les effets sont plus prononcés pour la propagation contre l'écoulement et pour des vitesses d'écoulement plus élevées, ce qui est en accord avec les études récentes [18, 24, 117]. L'analyse démontre également que l'impact du cisaillement est similaire pour les configurations à un seul ou à deux traitements, et que le modèle d'écoulement uniforme est peu précis en cas de vitesses d'écoulement élevées et de couches limites épaisses. Ces résultats soulignent aussi la nécessité d'intégrer les considérations relatives à l'écoulement cisaillé dans l'optimisation des revêtements acoustiques afin d'obtenir des prédictions précises et des performances optimales.

En simulant la mesure d'impédance, le chapitre 4 révèle d'abord la meilleure robustesse de la méthode HTLS pour l'estimation des nombres d'ondes sur la base des données de pression obtenues par une antenne linéaire de microphones, par rapport à la méthode KT. Ensuite, il est démontré que dans un grand conduit, des améliorations significatives des résultats obtenus se produisent lors de l'utilisation du modèle d'écoulement cisaillé combiné à une configuration à deux traitements, par rapport à l'écoulement uniforme traditionnel et à la configuration à un seul traitement. Les raisons du meilleur fonctionnement de la configuration à deux traitements sont le maintien de la symétrie du champ acoustique incident et l'augmentation de l'atténuation, ce qui réduit l'incertitude sur les mesures d'impédance. En outre, cette configuration s'avère plus fiable face aux perturbations liées au bruit d'écoulement, ce qui en fait un choix prometteur pour les expériences.

En ce qui concerne l'influence du champ acoustique incident, la présence de modes de différent types de symétrie, rencontré dans les expériences réelles, peut modifier la mesure d'impédance. Une antenne de microphones à deux lignes est proposée pour atténuer ces perturbations. En séparant les modes symétriques et antisymétriques, cette antenne améliore considérablement la précision de la mesure d'impédance avec la configuration à deux traitements.

Dans l'ensemble, ces simulations soulignent les avantages de la méthode prenant en compte l'écoulement cisaillé, de la configuration à deux traitements et de l'antenne de microphones à deux lignes, ouvrant la voie à une mesure d'impédance plus précise et plus fiable dans les travaux expérimentaux.

Le dernier chapitre présente la mise en œuvre expérimentale des méthodes directes de mesure d'impédance dans MAINE Flow, validant ainsi les méthodologies développées dans les chapitres précédents. Lors du post-traitement des signaux expérimentaux, une approche est proposée pour la sélection des nombres d'ondes qui met l'accent sur les contributions physiques de chaque nombre d'ondes. Il est confirmé expérimentalement que la configuration à deux traitements est supérieure à la configuration à un seul traitement, en raison des meilleures performances en matière d'estimation des nombres d'ondes et d'atténuation acoustique. En outre, la prise en compte de l'écoulement cisaillé améliore la fiabilité et la qualité des résultats d'impédance, en particulier pour les hautes fréquences, la propagation vers l'amont

et les vitesses d'écoulement élevées, ce qui est conforme aux conclusions de l'étude numérique.

D'après les résultats, les modes antisymétriques présentent de meilleures performances en matière de mesure d'impédance que les modes symétriques, probablement en raison de leur plus grande atténuation, bien que des recherches supplémentaires soient nécessaires pour comprendre pleinement ce comportement. L'évaluation de différentes antennes de microphones (à une ligne ou à deux lignes) montre que l'antenne à deux lignes améliore la régularité des résultats, sans modifier les tendances générales. Cependant, des problèmes de résolution sont observés avec un espacement des microphones de 4 cm, dans les cas de propagation vers l'amont avec des écoulements à grande vitesse. Des essais avec des traitements spécialement conçus et optimisés pour l'atténuation des hautes fréquences sont également menés, soulignant à nouveau l'importance de l'atténuation pour la précision de la méthode de mesure d'impédance.

Perspectives: Cette thèse a proposé une méthode de mesure d'impédance basée sur un modèle de propagation 2D en tenant compte d'écoulement cisaillé. Il serait pertinent de considérer en plus le profil d'écoulement de la troisième dimension afin de rendre la méthode plus précise. Vu que la performance des modes antisymétriques est meilleure que celle des modes symétriques, l'étude pourrait viser à l'interaction des modes d'ordres hauts avec l'écoulement cisaillé pour mieux comprendre ce phénomène. À l'échelle expérimentale, l'antenne de microphone à deux lignes pourrait s'améliorer en prenant un plus petit espacement des microphones adjacents, afin de retourner les problèmes de résolution. La précision de la vitesse d'écoulement s'est montrée aussi important pour le calcul précis d'impédance. Par conséquent, il serait bon d'étudier la sensibilité de la méthode avec différents profils d'écoulement. Enfin, au vu des effets importants du cisaillement dans de grands conduits, la méthode inverse [126] pourrait être développée en incluant le cisaillement.

Chapter 1

Review on acoustic liners with flow

1.1 Acoustic liner

Noise emissions from commercial air transport have long been a crucial issue in relation to public health, economic competitiveness and technological developments. Aircraft noise mainly contains two categories: the noise generated by the airframe and the noise radiated from the propulsion system [27]. The relative level of these noise sources varies depending on the aircraft type and flight conditions. Typically, the propulsion noise (related to the turbofan engine) dominates during take-off and is comparable to the airframe noise during the landing phase.

Turbofan noise originates from multiple components within the engine itself (refer to Figure 1.1). Primarily, this includes noise from turbo-machinery and the exhaust jet. Developments in engine design, particularly the increase in engine bypass ratios, have significantly abated jet noise by decreasing the speed of the jet [28]. The engine bypass ratio (BPR) defines the relationship between the mass of cooler air directed around the core engine to the mass of air passing through the core. Indeed, since the 1960s, the use of high bypass ratio engines has reduced combined engine noise levels by more than 20 Effective Perceived Noise Decibels (EPNdB) [29]. Thus, turbofan noise has become the main noise source in the aircraft engine (see Figure 1.2).

A major component of turbofan noise is the interaction between the fan rotor and stator, which propagates through the duct and then radiates to the far field. This specific noise source arises from the impingement of the rotor wakes on the stator

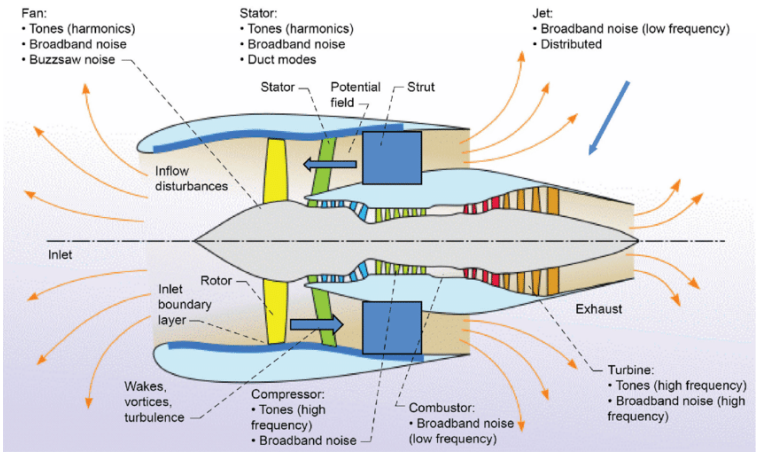

Figure 1.1: Sources of turbofan engine noise [30]: turbo-machinery and the exhaust jet.

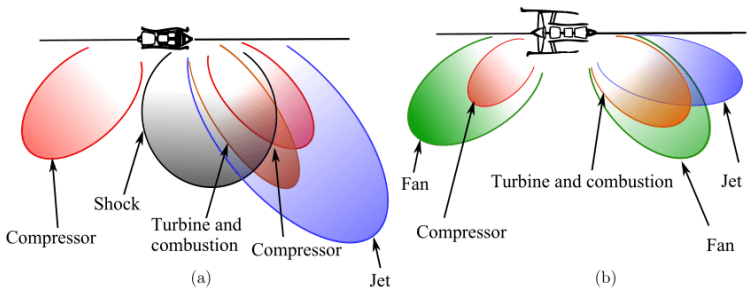

Figure 1.2: Evolution of the directivity and the relative levels of the different engine noise sources as a function of the engine architecture (or BPR): (a) low BPR (single flow turbojet). (b) High BPR (turbofan engine) [3].

vanes, causing pressure fluctuations on the stator vanes which then excites acoustic duct modes [31]. Since fan noise sources may behave differently depending on operating conditions, turbofan noise encompasses a broad spectrum of frequencies [27].

The reduction of fan noise radiation to the far field can be achieved through two principal strategies [32]. The first strategy focuses on the reduction of the noise sources, including mitigating interaction mechanisms, tuning the stator cascade parameters, and adjusting the number of rotor blades and stator vanes [29]. The second strategy involves attenuating noise after its generation, which includes implementing duct wall treatments and manipulating sound diffraction mechanisms to manage how noise travels and dissipates. Given the complexity of engine design, a significant research effort has been dedicated to the implementation of duct wall treatments.

This is primarily achieved through the installation of acoustic liners within the nacelle ducts and along the inner walls of aircraft engines, aiming to enhance noise absorption by tuning the boundary conditions during its propagation. Indeed, as an acoustic wave moves away from a source of noise within an enclosed duct, the acoustic energy at a boundary may be attenuated through absorption of acoustic waves [1]. Given the severe operating conditions, it is essential for liners to possess robust material properties and structural rigidity. Figure 1.3 illustrates liners commonly used in modern aircraft engines. The construction of these liners typically involves three key components: perforated sheets, cavity structures (typically honeycomb) and a rigid backplate. Tandem assembly of these components can form liner structures with different degrees of freedom. Common acoustic liners consist of either one layer of honeycomb structure or two layers separated by a porous sheet, which are referred to as single-degree-of-freedom (SDOF) and double-degrees-of-freedom (DDOF), respectively.

The liners with (honeycomb) cavities prevents propagation in the transverse direction within the cavity, and the propagation occurs only normal to the plate, irrespective of whether the incident wave approaches the perforated plate at a non-normal angle. This type of liners is denoted as locally-reacting, because the response of the liner depends solely on the local acoustic pressure, and not on the structure of the sound field above the liner [33]. Additionally, there exist non-locally-reacting liners that permit the transverse propagation of sound inside the liner. This can be achieved by substituting the cellular honeycomb structure between the face-sheet and the rigid backplate with structures which allow propagation of the sound laterally insides [2]. However, the discussion of non-locally-reacting liners falls outside

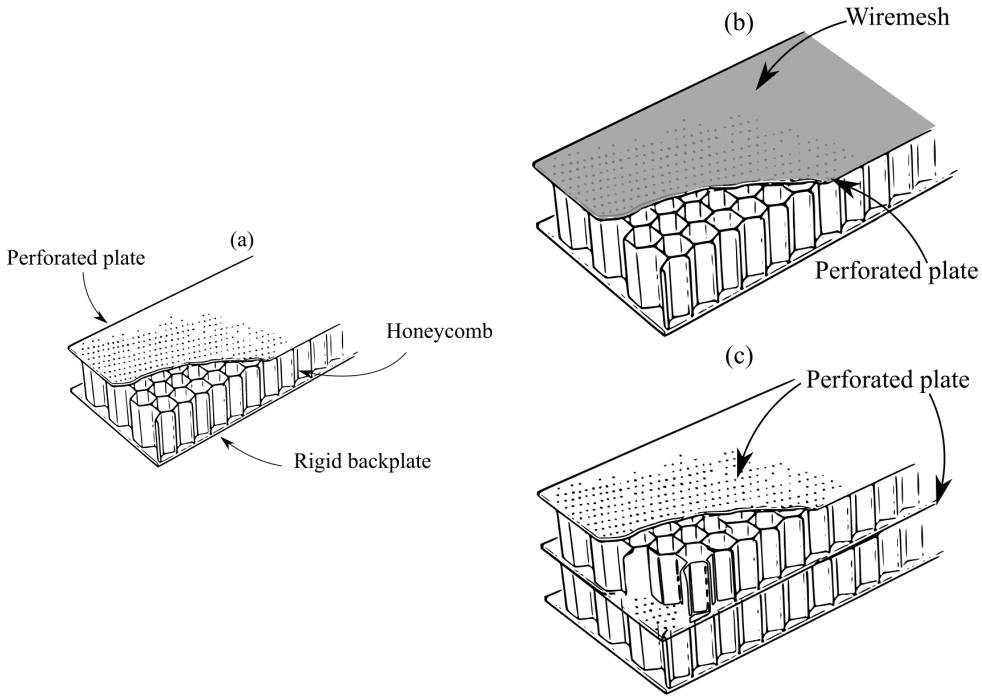

Figure 1.3: Representations of typical locally-reacting liners applied in the aeronautical industry [3]: (a) SDOF liner; (b) wire-mesh SDOF liner; (c) DDOF liner.

the scope of this thesis and will not be further addressed.

Locally-reacting liners achieve noise reduction through two primary mechanisms [28]. The first mechanism involves the physical damping of pressure fluctuations within the porous "resistive" structure of the face sheet, where viscous resistance dissipates acoustic energy and converts it into heat. The second is the cancellation of the direct incident sound wave by the wave reflected from the solid backplate inside the honeycomb cavity. The latter supports designing as a function of the incident acoustic wave the cavity depth, following the 1/4 wavelength theory, which primarily influences the noise reduction frequency band of the acoustic liner around its resonance frequencies [34]. The combination of the orifices and cavities makes the liner as an array of Helmholtz resonators. Consequently, both SDOF and DDOF liners are effective within narrow frequency ranges and require tuning to specific one or two frequencies, respectively.

The performance of an acoustic liner can be assessed by measuring the sound absorption it induces. However, the acoustic absorption does not only depend on the liner itself, but also on the dimensions of the duct in which it is placed. In contrast, the acoustic impedance is a less affected parameter, which depends on frequency, the liner geometry and material, sound pressure level (SPL) and flow conditions. It is thus more suited to characterise acoustic liners in a determined-physical case. The acoustic impedance $\hat{Z}$ of a boundary can be defined as the complex ratio of the acoustic pressure p and the normal component of the acoustic particle velocity u_n, as a function of the angular frequency ω:

$$\hat{Z}(\omega) = \frac{p(\omega)}{u_n(\omega)} = \hat{R}(\omega) + \mathrm{i}\hat{X}(\omega). \tag{1.1}$$

The real part $\hat{R}$ represents the acoustic resistance, which reflects the dissipation of

acoustic energy, and the imaginary part $\hat{X}$ represents the acoustic reactance, which reflects the liner effect on the phase of acoustic propagation. In addition, some studies[35] use the admittance $\hat{Y} = 1/\hat{Z}$ in computational analyses. Also, the specific impedance $Z = \hat{Z}/\rho_0 c_0$ is also used, where $\hat{Z}$ is normalised by the medium impedance.

1.2 Physical mechanisms and liner impedance models

A common way of acoustic liner design is to reach an impedance value in order to reduce noise as much as possible within the target frequency range. After determining the desired impedance for the liner, the next step is to design the liner material and geometry to achieve this specified impedance. For instance, with a typical SDOF liner, the relevant parameters are percentage open area (POA, or porosity), hole diameter (with circular holes), plate thickness, cavity depth, and even cavity cross dimensions and cavity wall thickness. The design process typically relies on semi-empirical acoustic impedance models. With given geometric parameters, flow condition and sound amplitude, semi-empirical models are able to compute an impedance value by integrating specific acoustic theories with regression of extensive experimental data.

For instance, Guess model [36] is a commonly used one. Considering one simple perforated liner consisting of a plate with cylindrical perforations, a cavity and a back plate, the model takes into consideration the following physical mechanisms:

(1) visco-thermal losses [37, 38] on the rigid boundaries of such liner, including i) the dissipation in the viscous boundary layer, ii) the sound dissipation in the thermal boundary layer, as the unsteady heat transfer at the wall acts as a sink of sound [39]. The visco-thermal effects relate to the thickness of the perforated plate, the diameter of the perforation and the porosity.

(2) radiation effects [7] at the entrance and the exit of the orifices. The resistive part of the radiation impedance relates to the sound field generated by the velocity within the orifice, while the radiation reactance stands for the impact of the inertial mass of the local air movement near the orifice. The latter is typically considered as a mass "end correction" in the semi-empirical model. The radiation effects relate to the diameter of the perforation.

(3) interaction effect [40, 41] between the apertures of the plate. This effect is also included in the model as an end correction. Ingard [40] found that the end correction depends significantly on the separation distance. Later, Melling [41] considered this effect in the case with enough small separation, and revealed that i) the shear region between the adjacent apertures is disturbed, affecting the resistance, and ii) in terms of the reactance, the attached mass of two apertures interacts. The interaction effect relates to the diameter of the porosity and only influences the reactance.

(4) viscous edge effects [40] occurring at both ends of the aperture, as well as at the sharp corners. The resulting dissipation affects the resistance of the liner and is typically taken into account by adding a correction to the length of the neck, i.e. the thickness of the perforated plate. The viscous edge effects relate to the thickness of the perforated plate, the diameter of the perforation and the

porosity, as well as the incident amplitude and flow velocity when the non-linear effects (with a jet extending from the neck) or the presence of a grazing flow is considered.

(5) back-plate reflection [40]. With (honeycomb) cavities, locally-reacting liners limits the propagation normal to the perforated plate. The tangential velocity to the viscous boundary layer along the cavity walls is low, thus the viscous losses are negligible. Additionally, the thermal effects are generally neglected [40]. Therefore, the cavity is assumed to be purely reactive and the reactance is expressed by a cotangent function in terms of the depth of the cavity.

Furthermore, corrections have been derived based on Guess model to consider non-linear effects at high amplitudes and flow effects. The physical mechanisms concerning these effects are described in the following.

Non-linear effects

In the linear regime, liners exhibit acoustic properties which are unaffected by a change in the amplitude of incident waves, with a linear relationship between the acoustic pressure and velocity at its surface at a given frequency. However, depending on the plate geometry, liners can display a non-linear behaviour where the impedance shows a dependency on the wave amplitude. Melling [41] first realized that the linear or non-linear behaviour depends mostly on the incident sound amplitude.

For low incident amplitudes, a numerical simulation by Tam and Kurbatskii [42] demonstrated that the flow through the orifice is laminar and unsteady and the losses are mainly due to viscous dissipation in the shear layer. For high incident amplitudes, pulsatory effects dominate, leading to the formation of jet flow and vortex rings. These structures quickly convert acoustic energy into hydrodynamic energy through viscosity [43].

More precisely, focusing on one orifice, the experimental study of Ingard and Ising [7] found that the relationship between the acoustic pressure and velocity at the orifice, is linear at sufficiently low pressure levels, and approaches a square-law relation described by Bernoulli's law at high amplitudes. There, the resistive component of the orifice impedance dominates and proportionally increases with the incident amplitude, while the reactance decreases and the reduction depends on the orifice geometric size. The study also indicates that in the non-linear regime, flow separation and jet formation occur at the orifice. Then, Melling [41] suggested that with the formation of jet, the primary dissipation mechanism is turbulence, but this mechanism was not confirmed by subsequent studies. The numerical analysis [42] observed a vortex-shedding mechanism taking place at the opening of the resonator, which is responsible for the conversion of acoustic energy into hydrodynamic energy and further viscous dissipation into heat. Jing et al. [44] demonstrated that the non-linear acoustic behaviour of an orifice depends mainly on the vortex shedding rate at the orifice edge and the convection speed of the shed vortex in the vicinity of the orifice.

In Guess model [36], the non-linear effects at high incident amplitude are concerned by corrections associated to the acoustic particle velocity in the orifice. The corrections account for both resistance and reactance.

Flow effects

In presence of a grazing flow at the surface of the perforated plate, the liner impedance is affected, usually with a trend which is that the resistance increases and the reactance decreases [4]. Ingard and Ising [7] investigated the flow effects by considering the superimposed flow in the orifice, at a small amplitude of the incident sound pressure, so that the case is in the linear regime in the absence of the grazing flow. This investigation explained that the presence of the grazing flow over the liner yields an additional fluctuating flow in the orifice to the acoustic oscillation, resulting in the formation of jets. Hence, the influence of the grazing flow on the orifice impedance is somehow similar to that of high incident amplitudes on the non-linear impedance in the absence of flow. Therefore, the flow effect is concerned in Guess model [36] also as additional corrections associated to the flow velocity, which are in similar form to the corrections of non-linear effects.

1.3 Experimental characterisation of acoustic liners

Prior to installation in a nacelle, it is crucial to characterize the liner using a test bench and, if feasible, under realistic conditions. This step is essential to verify whether the liner meets the acoustic impedance anticipated by the semi-empirical models, such as the Guess model described in the last section. However, conducting acoustic impedance measurements directly on full-scale engines is expensive and not convenient. Since the impedance of locally-reacting acoustic liners is not influenced by the curvature of the liner itself, measurements are generally performed on small and flat samples in a controlled environment recreating actual conditions. In the following, the main methods for measuring acoustic liner impedance are described.

(1) Normal-incident impedance tube (NIT)

Impedance tubes are used to measure surface acoustic impedance and the absorption coefficient of porous materials or perforated liners under no-flow and normal incidence conditions [2, 45]. The tube is equipped with an acoustic source on one side and a test sample on the other side. For measurements, there are two types shown in Figure 1.4.

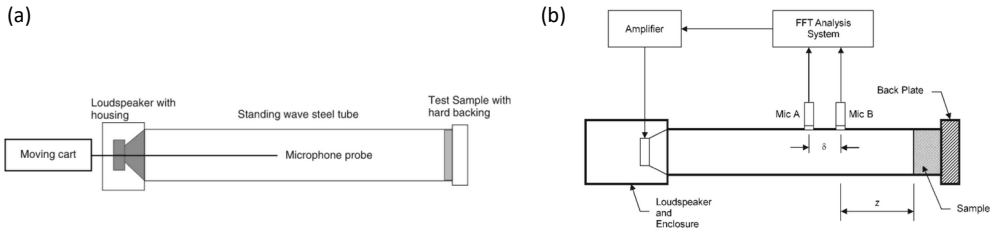

Figure 1.4: Schematic representation of two measurement techniques in an impedance tube [46]: (a) movable probe microphone; (b) two fixed microphones.

The first (shown in Figure 1.4(a)) uses a movable probe microphone face to the tested sample, to measure the sound pressure of the standing-wave pattern in the tube. With $r = (\mathrm{SWR} - 1)/(\mathrm{SWR} + 1)$ where SWR is the standing

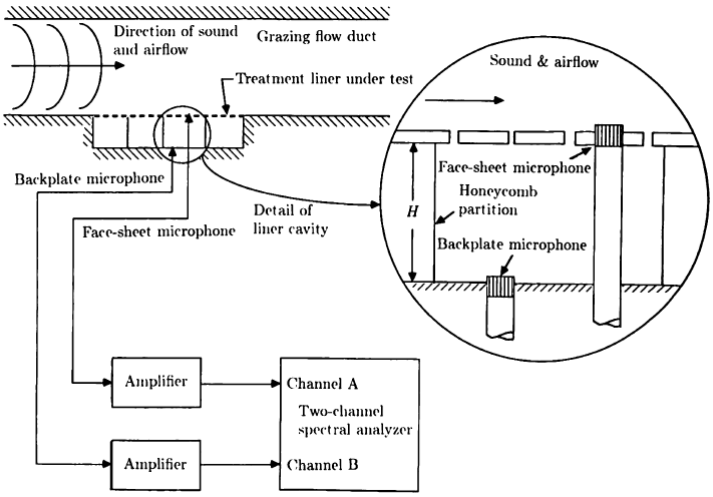

Figure 1.5: The implementation of the In-situ method [2].

wave ratio, defined by the ratio between measured maximum and minimum amplitude of the standing wave pattern, the impedance is calculated:

$$Z = \frac{1 + re^{-i(\pi+2kD)}}{1 - re^{-i(\pi+2kD)}}. \tag{1.2}$$

Here, $k = \omega/c_0$ is the free-field wavenumber and D is the distance between the first measured minimum of wave amplitude and the sample.

The second, in Figure 1.4(b), is based on the transfer function of two fixed microphones which are located at two different axial positions in the tube wall. The complex pressure reflection coefficient is obtained as

$$RC = \frac{H_{AB} - e^{-ik\delta}}{e^{i(k\delta)} - H_{AB}} e^{i2kz}, \tag{1.3}$$

where H_{AB} is the transfer function between microphone position A and B, δ is the microphone spacing, z is the distance between the sample and the closest microphone (i.e. microphone B in Figure 1.4(b)). Then the acoustic impedance of the sample is calculated from the relation $Z = (1 + RC)/(1 - RC)$.

(2) In-situ method (Dean Method)

Considering the characteristics of the response of a locally-reacting acoustic liner to acoustic waves, Dean [13] proposed an in-situ two-microphone method to measure the acoustic impedance of the acoustic liner under tangential flow conditions. Based on the original definition in Eq. (1.1), this method obtains the impedance directly from locally measured pressures and velocities. Therefore, unlike other methods described in this section, this method does not rely on any acoustic propagation model in lined ducts with flow. The apparatus shown in Figure 1.5 is representative of the in-situ method used for the determination of liner impedance, also called two-microphone method in literature [2, 47, 48]. One microphone is inserted through the face sheet (microphone A) and the other is mounted flush on the backplate of a chosen cavity (microphone B). They must be small enough to have negligible effects on the propagation within the cavity. Typically, measurements are done at frequencies below the

first cut-off frequency of the high order modes, so only the plane wave exists in the cavity. Thus, if the viscous effects are ignored and hence the acoustic particle velocity inside the small holes is assumed to be uniform, the normalised impedance Z of a SDOF liner is obtained from the measured quantities by the expression:

$$\frac{Z}{\rho_0 c_0} = -\mathrm{i}\frac{p_A p_B \mathrm{e}^{\mathrm{i}\varphi_{AB}}}{p_A^2 \sin(kh)}, \tag{1.4}$$

where the numerator part is the cross spectral density between microphones A and B, the denominator contains p_A^2 the auto spectral density of microphone A, and h the cavity depth.

The in-situ method is often used when local information is required about the effects of grazing flow on the liner impedance, and can be used in a laboratory duct or on the actual engine installation [2]. This method has been widely used for the measurements of locally-reacting acoustic liners [18, 49], as it allows directly obtaining the local impedance. However, when using this method, it is inevitable to destroy the structure of the acoustic liner. While attempts have been made to avoid the destruction using techniques like Particle Image Velocimetry (PIV) [50], success has been limited. And for multi-degree-of-freedom acoustic liners, the implementation of this method will be more difficult. Zandbergen [51] introduces the extension of the method to DDOF liners and shows difficulty of implementation for accurate results. Meanwhile, since only a single microphone measures the acoustic pressure information on the surface of the acoustic liner, the measurement results are greatly affected by the surface pressure fluctuations in the turbulent boundary layer, and the measurement error is large if the microphone is not exactly flush with the surface, or if the flow velocity is high, or if there is leakage.

(3) Single Mode method

This method is based on the infinite waveguide model in a duct with a lined boundary, where the imaginary part of the propagating wavenumbers appears to determine the acoustic energy attenuation rate. Based on this, Armstrong [52] proposed the infinite waveguide method, also called Single Mode Method (SMM) by NASA [9, 14]. This method requires that the lined duct has an infinite length and constant cross-section. Also, an acoustic liner with a uniform impedance is installed on the duct wall. The method proceeds by assuming that the flow present in the duct is uniform, and that only a single dominant acoustic mode exists in the duct and remains formally unchanged during propagation, as shown in the schematic in Figure 1.6.

Under these conditions, the measured sound pressure level $\mathrm{SPL}(x)$ and the phase $\varphi(x)$ at the centreline of the rigid wall varies linearly along the axial direction of the duct [14, 52] (see Figure 1.6). Thus, the axial propagation constant (i.e. the acoustic wavenumber k_x) of the dominant mode can be determined from the slope of the line:

$$k_x = \frac{\mathrm{d}\varphi(x)}{\mathrm{d}x} + \frac{\mathrm{i}}{20\log_{10}(\mathrm{e})}\frac{\mathrm{dSPL}(x)}{\mathrm{d}x}. \tag{1.5}$$

To calculate the impedance of the liner, this axial propagation constant is used in conjunction with the normal mode solution based on a propagation model, such as the convected wave equation and the local-reacting wall impedance

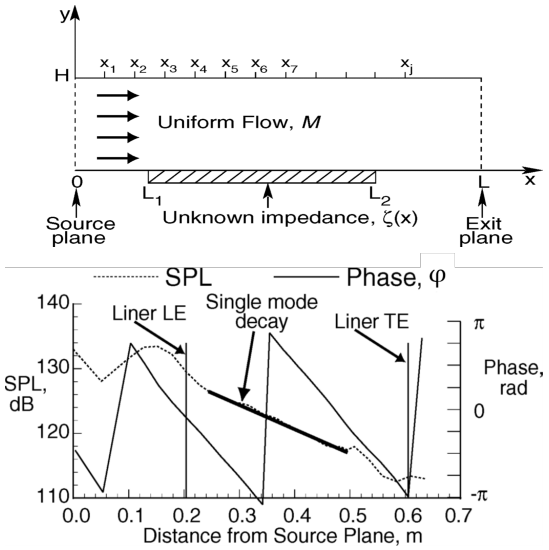

Figure 1.6: Schematic (top) of the single mode method and example (bottom) of sample SPL and phase profiles [14].

boundary condition. Therefore, if the assumptions are valid, this method involves only simple algebraic calculations with high efficiency. Unfortunately, the assumption of single mode can hardly hold in practical conditions. The finite length of acoustic liner will inevitably excite multiple propagating acoustic modes, in which case the measurement results of this method will contain large errors. Nonetheless, this approach provides the basic process for the direct impedance eduction method, which will be later introduced and applied.

(4) Inverse method

Since non-negligible impedance discontinuities cause errors in the Single Mode method, liner impedance measurements must consider a duct consisting of multiple sections, typically arranged in a rigid-lined-rigid succession. The inverse method, also known as the objective function method, is an optimisation process that involves minimising the difference between acoustic quantities in experimental and simulated sound fields within the test duct. It begins with an estimate of the liner impedance to compute the simulated acoustic field and iterates to provide a new estimate of impedance until the computed parameters agree with the measured value. The agreement is judged by the minimisation of the cost function:

$$Z = \arg\min_{Z} |AF_{Computed}(Z) - AF_{Measured}(Z)|, \tag{1.6}$$

where AF represents physical quantities of the acoustic field.

The idea first originated with Syed [53], using the attenuation SPL induced by the tested liner to establish the objective function. Since then, the inverse method has been developed and refined by NASA LaSR [54–57]. These studies use a finite element model to simulate the sound field inside the duct and consider the complex acoustic pressures at the wall as parameters in the objective function. With the development of numerical computational methods, the inverse method has obvious advantages over the in-situ method in terms of applicability and accuracy, becoming the mainstream acoustic impedance

measurement method since 2000. This method has evolved in two main aspects: the modelling and the methodology used to compute the simulated field, and the acoustic parameters considered in the construction of the objective function. Various models can be used to simulate the acoustic field accounting for different flow effects, such as the Convected Helmholtz Equation (CHE) [9] for uniform mean flow, the Linearized Euler Equations (LEE) [56, 58] for inviscid sheared flow and the Linearized Navier–Stokes Equations (LNSE) [59] for viscous flow. To compute the acoustic field, [16, 49, 60] use a semi-analytical multimodal method instead of the finite-element method. Moreover, other acoustic parameters can also be considered in the objective function, such as the scattering matrix [16, 61], insertion loss [62, 63], acoustic pressure [64], acoustic wavenumber [19], exit impedance [21, 65–67], etc. Furthermore, the accuracy of the cost function can be improved by considering supplementary parameters or effects, such as boundary conditions [60], flow direction [60], impedance model (geometry parameters) [68] and SNR (Signal-to-Noise Ratio) [69]. In addition, the Laser Doppler Anemometry (LDA) technique has also been applied to obtain the measured acoustic velocity field [70–72] near the liner.

The inverse method presents inherent limitations. First, the simulated sound field is obtained using a propagation model which is based on several assumptions to simplify the computation. Hence, the lack of consideration of physical effects in the model's assumptions may raise issues on the accuracy of the impedance results. Secondly, accurate measurement of reflection conditions at source and exit sections within the flow duct is essential when using complex sound pressure as a comparison target. However, obtaining precise measurements under flow conditions is also challenging, leading to potential sources of error [55]. Furthermore, as with other iterative approaches, issues arise with determining initial guess and achieving convergence. The method may exhibit slow or non-convergent behaviour [56].

(5) Direct method

According to the principle of the Single Mode method, the problem of measuring the acoustic impedance of liners mainly lies in how to decompose the measured acoustic field and accurately obtain the wavenumber of each mode when multiple modes and reflections coexist in the duct. To that end, Jing et al. [15] have applied Prony's method [73], commonly used in signal processing and system identification domains for extracting sinusoids parameters from noisy or sampled data, to the acoustic mode identification in ducts. This approach marked the formation of the so-called direct method. The inverse and direct methods are the two main categories, collectively known as impedance eduction technique [17].

Given N equally spaced spatial measurement points on the wall of a lined duct, Prony's method is able to quickly identify the amplitudes and axial wavenumbers of up to the first $N/2$ principal modes. With an obtained axial wavenumber k_x, the unknown acoustic impedance can be calculated from the eigenvalue and dispersion relations based on the classical mode-decomposition analysis. This method is also called SFM (straightforward eduction method [15]) since it involves only one-off algebraic computation. However, it considers uniform mean flows, and is only applicable to ducts with constant cross-sectional area and uniform test liner structures.

Based on the initial basic principle, the direct method is being developed in different aspects. In terms of flow assumptions, the direct method has been extended to account for the presence of shear in flow by numerically solving the Pridmore Brown equation [20]. Further, Zhang et al. [74] considered the sheared boundary layer separately from the core uniform flow region, and proposed an alternative boundary condition using effective admittances at the interfaces between boundary layers and core flow regions. This work aims also at mitigating the discrepancy in acoustic impedance determined in a test-rig subjected to both upstream and downstream acoustic excitation.

Regarding the measurement of the acoustic wavenumber, the strategic design of the microphone array is crucial. The array is usually 1D-equally-spaced microphones mounted on the wall opposite to the liner [75, 76], while some researchers consider their installation on the lateral wall [26]. More recently, various innovative microphone arrays and associated algorithms have also been developed. A diagonally mounted microphone array [77, 78] has been positioned on the wall opposite to the test liner within a flow duct to simultaneously capture information from both axial and transverse directions, which enables the realization of the full modal decomposition using Prony's method. However, a significant challenge arises due to the too small spanwise microphone spacing. To address this issue, Chen et al. [79] extended the direct method to three-dimensional, employing an evenly spaced rectangular array in the lined section of the flow duct. Subsequently, Qiu et al. [80] introduced a zigzag microphone array design to overcome the problem of limited spanwise microphone spacing, building upon the idea of the diagonal microphone array [77].

Additionally, the Laser Doppler Velocimetry (LDV) technique has also been employed [81] to measure the periodic fluctuating velocity of the acoustic field, with the objective of retrieving wavenumbers from the equally spatially-spaced acoustic velocity information.

Concerning the wavenumber identification, efforts have been made to enhance extraction accuracy and stability. Renou et al. [76] and then Watson et al. [26] advocated for the use of the Kumaresan–Tufts (KT) method [82] over Prony's method for identifying wavenumbers, aiming to improve the precision of the extraction process. Subsequently, other identification techniques have been applied in the domain of impedance eduction. For instance, Bayesian inference methods have been employed [25], as well as the Matrix-Pencil approach [81, 83], to further advance the wavenumber extraction procedures.

Following on these developments, the direct method is being used more widely, and it will be the experimental method used in this work.

Each impedance eduction technique possesses distinct advantages and drawbacks, prompting numerous studies to compare and contrast these methods. Jones et al. [57] compared the NIT and inverse method using the convected Helmholtz equation. Then, a comparative study by Watson et al. [9] provided detailed evaluations of both the inverse and direct methods. In a subsequent study [24], these methods were tested in both small and large cross-sectional ducts, yielding consistent impedance results. Weng et al. [84] compared the inverse and direct impedance eduction techniques using propagation models with different flow assumptions. Bonomo et al. [17] conducted a parametric study to investigate the primary sources of uncertainties associated with the direct impedance eduction technique, aiding to understand how

to carry out an accurate direct impedance eduction. Additionally, they compared the In-situ method with the two impedance eduction techniques under conditions of grazing flow and high SPLs, demonstrating the robustness of In-situ results [8].

1.4 Flow ducts for impedance eduction

In practice, acoustic impedance are primarily experimentally measured through a flow duct test bench. The test rig is usually designed to facilitate impedance eduction of liners under controlled acoustic and flow conditions. For locally-reacting acoustic liners, its impedance is independent of the sample size, unless the non-linear effects is considered due to the evolution of SPL along the liner. Except for the In-situ method, other methods introduced above are averaged measurements and provide an effective value of liner impedance in the whole lined section. Most flow duct are small-sized rectangular cross-sectional. Many research organisations such as NASA, DLR, etc., as well as major aircraft and engine manufacturers have such flow ducts for acoustic liner measurements. Figure 1.7 shows a schematic for the general facility.

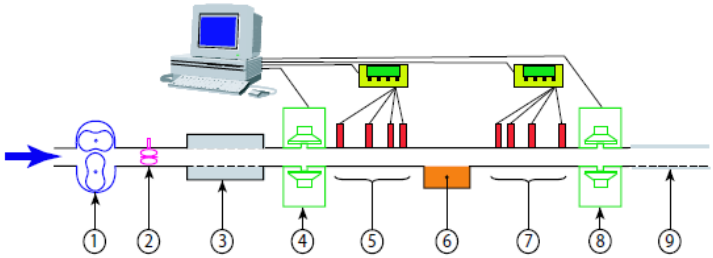

Figure 1.7: General schematic of the test rig for impedance eduction [16]: 1: Compressor, 2: Flowmeter, 3: Upstream anechoic termination, 4: Upstream source , 5: Upstream microphones, 6: Lined wall, 7: Downstream microphones, 8: Downstream source, 9: Downstream anechoic termination.

The experimental facility typically consists of multiple segments and comprises

- sound sources on both sides of the sample for generating incident waves,
- a compressor and fan to generate the flow,
- Pitot tube for measuring flow velocity,
- a test section for mounted liners, the other walls being rigid,
- acoustic terminations (usually anechoic),
- microphones on both sides of the sample for the decomposition of acoustic field into modal space,
- microphones mounted in the wall of the lined section (usually for direct impedance eduction).

The following is a brief list of the main published flow duct test benches. Due to the common structural features, the primary focus will be on the dimensions and the ability to control the acoustic field and the flow velocity. The flow velocity is

usually normalised as Mach number M by the sound velocity c_0. In Table 1.1, M_{max} stands for the maximum Mach number M_{max} on the flow velocity profile, also called centreline Mach number in literatures, and M_{bulk} is the bulk Mach number. More detailed description are unfolded in Appendix A.

Table 1.1: Published test rigs for impedance eduction.

Facility name	Cross-section [mm^2]	Liner length [mm]	max Mach number
NASA Grazing Flow Impedance Tube (GFIT) [57]	50.8×63.52	50.8 to 609.6	$M_{\text{max}} = 0.6$
NASA Curved Duct Test Rig (CDTR) [23]	152.4×381	762	$M_{\text{max}} = 0.5$
DLR DUct aCoustic Test Rig (DUCT-R) [85]	60×80	800	$M_{\text{max}} = 0.28$
NLR Flow Duct Facility (FDF) [86]	150×300	1050 [1]	$M_{\text{max}} = 0.7$
KTH flow acoustic test rig 1 [49]	32×32	50	$M_{\text{max}} = 0.3$
KTH flow acoustic test rig 2 [87]	70×25	25	$M_{\text{max}} = 0.2$
UFSC grazing Flow Liner Impedance eduction test Rig (FLIR) [22]	40×100	210	$M_{\text{max}} = 0.7$
Beijing University of Aeronautics and Astronautics (BUAA) test rig [78, 88]	51×51	800	$M_{\text{max}} = 0.25$
ONERA B2A [72]	50×50	150	$M_{\text{bulk}} = 0.5$

[1] The sample sizes for in-situ measurements are 170 mm $\times$ 32 mm, and for insertion loss measurements are 170 mm $\times$ 850 mm.

Table 1.2: Sound source of the published test rigs for impedance eduction.

Facility name	Source type	max SPL [dB]	Frequency range
NASA Grazing Flow Impedance Tube (GFIT)	stepped-sine	150	400 to 3000 Hz ($\Delta = 100$ Hz)
NASA Curved Duct Test Rig (CDTR)	stepped-sine, broadband	140	400 to 3000 Hz ($\Delta = 100$ Hz)
DLR DUct aCoustic Test Rig (DUCT-R)	multi-tone	130	up to 2200 Hz ($\Delta = 100$ Hz)
NLR Flow Duct Facility (FDF)	broadband and tonal	(150)[2]	1000 to 6000 Hz ($\Delta = 500$ Hz)
KTH flow acoustic test rig 1	stepped-sine	(150)	550 to 4100 Hz
KTH flow acoustic test rig 2	stepped-sine	(145)	200 to 2600 Hz ($\Delta = 40$ Hz)
UFSC grazing Flow Liner Impedance eduction test Rig(FLIR)	swept-sine	150	400 to 2500 Hz
Beijing University of Aeronautics and Astronautics(BUAA) test rig	single-tone	(135)	500 to 6000 Hz
ONERA B2A	multi-sine	(135)	300 to 3500 Hz

One of the motivations of flow duct facilities is to simulate engine operating conditions, such as high-speed flow and high incident wave amplitudes. These conditions pose significant challenges to achieve in experiments. Even though some ducts outlined in Table 1.1 and 1.2 manage to approach high SPL and flow velocity, investigations in these ducts is limited to small cross-section. It is questionable whether the conclusions about the physical effects of these pipe liners are applicable to the scale of the engine. Therefore, there remains a pressing need to carry out studies within larger ducts to further explore impedance eduction.

Some studies have been conducted to compare certain of these rigs. In [89], such a study compared results obtained with four flow rigs, as well as the corresponding normal incidence tubes. Then, with the establishment of different test rigs, numerous comparative studies have been involved more flow ducts. For instance,

- Busse et al. [90] compared results on the DLR DUCT-S and the NLR FDF;
- Busse et al. [85] compared results on the DLR DUCT-R and the NASA GFIT,
- Zhou et al. [87] made a comparison of the KTH duct to the results in [85];
- [91] : ONERA B2A and NASA ducts
- [23] : NASA GFIT and CDTR;
- [22] : UFSC test rig and NASA GFIT.

Most of them give basically the conclusion that results on different rigs more or less agree with each other in the absence of flow. The main discrepancies are found in the presence of grazing flow and also found for the high incident amplitude.

[2]Note that the values in parentheses in this table are overall SPLs.

1.5 Non-linear and flow effects in impedance eduction

As presented in the previous sections, the liner impedance is influenced in the presence of a high SPL or grazing flow. And studies have shown the impedance varies when the direction of propagation relative to the flow changes. In this section, we provide a review regarding these effects in the work of the impedance eduction.

High SPL: non-linear effects

Since changing SPL affects liner behaviours, it is vital to account for different incident amplitudes in the impedance eduction. Many studies made attempts to control the incident SPL [8, 12]. Moreover, Lafont et al. [72] considers the evolution of SPL in the acoustic field, such that the impedance is space-dependent along the duct axis. For liners with a non-linear behaviour with respect to SPL, a threshold value is shown, above which the effects of the incident SPL on the resistance of the liner can be described with a space-dependent resistance. Under this threshold, the resistance remains constant. Besides, the discrepancies between upstream and downstream educed impedances, which is an issue needed to be understood [76], are shown to increase for higher SPLs [8].

Flow effects

Impedance eduction methods (both inverse and direct methods) rely on the acoustic propagation model in ducts and involve a boundary condition accounting for physical effects at the liner surface to describe the liner impedance. Regarding the effects of flow, most studies employ the assumption of a uniform and inviscid mean flow with the Ingard–Myers impedance condition [92, 93].

The Ingard–Myers boundary condition (IM–BC) assumes an infinitely thin boundary layer adjacent to the impedance wall and acoustic particle displacement continuity across a vortex sheet over the liner face (slipping flow). Eversman et al. [94] as well as Tester [95] have validated that the acoustic effect of a non-slipping inviscid sheared flow approaches that of an inviscid plug flow[3] as the boundary layer thickness tends to zero. The IM–BC at a lined wall with a normalised impedance Z, where the acoustic pressure and normal velocity at the liner surface are denoted p and v respectively, writes

$$v = \frac{D_0}{Dt}\frac{p}{\mathrm{i}\omega\rho_0 c_0 Z}, \tag{1.7}$$

where $D_0/Dt = d/dt + u_0 \cdot \nabla$ is the material derivative along the mean flow velocity u_0. u_0 is assumed tangential to the boundary.

The IM–BC plays a role in both inverse and direct impedance eduction. In the former, it serves as an impedance condition for the modelling of lined walls during the iterative computation of the acoustic field. In the latter, it provides a straightforward relationship between the liner impedance and the acoustic wavenumbers. However, several studies [76, 96] have questioned its application in impedance eduction, since discrepancies have been measured between the educed impedances of a locally reacting liner using upstream and downstream propagating waves in presence of flow.

[3] Plug flow is a simple model of the velocity profile of a fluid flowing in a duct. In plug flow, the velocity of the fluid is assumed to be constant across the cross-section perpendicular to the axis of the duct. And the plug flow model assumes there is no boundary layer adjacent to the inner wall of the duct.

From a mathematical point of view, the IM–BC has problems relative to instabilities in simulation, and Brambley [97] found that the wave propagation problems consisting of impedance models with vanishing flow boundary layer are mathematically ill-posed. To avoid the ill-posedness of IM–BC, Rienstra and Darau [98] derived a regularised boundary condition by considering a thin finite boundary layer, unlike the infinite thin one in IM–BC, with a linear velocity profile and a uniform mean density. However, its use of incompressibility assumption that serves for computing hydrodynamic modes induces errors in the acoustic modes [99]. To the same end, Brambley [100] derived a closed-form effective boundary condition for a compressible, inviscid, and finite thin boundary layer of thickness δ by means of the method of composite expansions, with the flow remaining uniform above the boundary layer.

Schulz et al. [101] commented that this set of derived models are limited to thin boundary layers and operate under the assumption that raises concerns regarding real situations, particularly when dealing with turbulent flows and/or low frequencies. Furthermore, there is a lot of work aimed at improving the description of the boundary layer effects [102].

In the context of impedance eduction, the work of Spillere et al. [18] shows that using Brambley's impedance boundary condition instead of the IM–BC reduces but does not eliminate the discrepancies between upstream- and downstream-educed impedances. This may mean that the reasons for discrepancies involve more complicated effects, and are not only the failure of the infinite thin boundary layer model.

Furthermore, due to the inviscid assumption, the Ingard–Myers boundary condition fails to account for viscous effects like shear stress in acoustic boundary layers, which could significantly impact sound propagation within a lined duct and further the accuracy of impedance eduction results, especially with grazing flow.

Nayfeh [103] first included the molecular transport of momentum and heat within a sheared flow into an effective wall admittance to account for the viscosity. For the same purpose, Starobinski and Auregan [35, 104] account additionally for the mean flow velocity in the acoustic boundary layer and introduce an added normal displacement defined in terms of the heat flux and the shear stress at the wall. This considers both the transfer of axial momentum and heat flux of the stationary flow into the lined wall as the main effect of viscosity. Moreover, Aurégan et al. [35] derive a modified impedance condition with two additional coefficients β_v and β_t (see Eq. (23) in Ref. [35]) standing for the viscous and thermal diffusion. More recently, Schultz et al. [101] use a momentum transfer impedance ξ_T (see Eq. (9) in Ref. [101]), defined by the ratio between the acoustic wall shear stress and the wall normal particle velocity, as a free parameter besides the wall impedance. The authors explain for the wave-direction dependence of educed impedance that even if the impedance and momentum transfer impedance do not depend on the structure of the acoustic field, the effective impedance observed outside the acoustical boundary layer becomes a non-locally reacting boundary condition. Similarly, Aurégan [105] uses a stress-impedance by introducing a friction factor $f_w = \tau_w / p_w$ that links the pressure p_w to the shear stress τ_w at the wall:

$$Y_w^* = \frac{\omega - U_0 k_x}{\omega} \left(Y_w + \frac{k_x}{\omega} f_w \right). \tag{1.8}$$

To summarise, these models indicate that, with flow, impedance is not sufficient any more. Then the difference between the results in the two directions can be eliminated by setting up a system of equations associating the impedance of the wall and

the proposed parameter. To do so, Renou and Aurégan [76] employed the modified IM–BC [35] including only the parameter β_v relative to the transfer of momentum (see Eq. (24) in Ref. [76]). Further attempts have been done by Spillere et al. [60] to identify physically the correctness of the available boundary condition models, using one and two identical lined walls, denoted in this manuscript as **single-** and **double-liner** configurations, respectively. This investigation used the single-liner configuration to educe the liner impedance and any additional parameter in different boundary condition models, whereas the double-liner case served for the comparison between measured data and simulated data using parameters inferred from the former case. However, in this investigation, first, unphysical values are obtained for the additional parameters; secondly, with the double-liner configuration, weak agreement is shown between measurements and simulations using the obtained parameters. Besides the boundary condition, the uniform flow assumption is also pointed out as issues in the model of duct acoustic propagation, and further in the impedance eduction.

Published results indicate that the assumption of uniform flow may introduce errors in the impedance eduction results. A comparative study in the NASA GFIT [9] shows that differences occur between the eduction results using the assumptions of uniform and shear flow, and could be greater at higher Mach numbers. More recently, Jing et al. [20] exploit a straightforward method for impedance eduction in the presence of shear flow and boundary layer effects, and show that the eduction was not susceptible to the exact shape of the boundary layer, similar to the conclusions in Ref. [21]. Roncen et al. [25] evaluate the uncertainties on the flow profile in the modal decomposition based on Bayesian inference. They conclude that the uniform flow assumption does not introduce significant errors when considering only one mode propagation, and suggested more exploration on the impact of the use of the uniform flow assumption when considering multiple mode propagation. Subsequently, [19] note that an apparent mismatch between wavenumber definitions appeared when considering a uniform mean flow, which can be reduced but not removed by considering an inviscid sheared flow. However, when considering a larger duct, Spillere et al. [18] note that the educed impedance is affected when considering a more realistic flow profile, which differs from the previous observations. Moreover, Bonomo et al. [22] discuss that different flow profiles (boundary layer displacement thickness) lead to disparities in educed impedance, when comparing results on two test rigs, i.e. the NASA GFIT and UFSC duct, with a same centreline or same average Mach number. The comparison uses a constant value as Mach number in the calculation of impedance, which is based on a wavenumber-impedance relationship [15] deduced from the uniform flow assumption and the Ingard–Myers boundary condition. This suggests that the flow profile need be taken into consideration when calculating the impedance. Consequently, some questions remain: to what extent does the mean flow shear alters the impedance eduction? Is this effect influenced by other parameters such as duct size, frequency, flow velocity?

Most of experimental research focused on small cross-section ducts, while studies on the effect of shear flow in large ducts are limited. An existing study at NASA [23, 24] shows similar impedance eduction results in a duct with small cross-section (the GFIT) and in a large-scale duct (the CDTR) when using the uniform flow assumption. The only discrepancies observed between the two ducts were at the very low, or very high, frequencies, This was explained by the low attenuation and the appearance of a higher-order mode, respectively [24]. While these experimental data provides useful information on the differences observed between small and large ducts, the impact of the mean flow shear on the eduction method remains to be

more precisely assessed.

1.6 Conclusions

This chapter describes the application of acoustic liners, introduces impedance eduction methodologies for measuring and evaluating acoustic liners, and summarises existing test benches for impedance eduction, along with the physical effects and impacts under varying conditions.

Previous research have not fully accounted for realistic operating conditions of acoustic liners, such as large-sized ducts, multimodal sound field, high flow velocities, and boundary layer effects. Particularly regarding different incident modes, most existing studies are limited to the propagation of plane waves due to the small size of the test benches. The mean flow shear has been shown to have influences on the impedance eduction results, but there is no explicit conclusion on these effects. Moreover, it is not clear how the sheared flow affects the process of impedance eduction, and what these effects are under different conditions, following inconsistent observations in published work [18, 20]. Thus, the present work aims to investigate the effects of sheared flow and multimodal incident field on the impedance eduction, numerically and experimentally. This study relies on the MAINE Flow facility [12], a large-duct test bench described in Chapter 2.

Chapter 2

Numerical methodologies and experimental techniques

This chapter presents the numerical and experimental methodologies employed in this thesis. It includes descriptions of the MAINE Flow facility, models for multimodal acoustic propagation and algorithms for direct impedance eduction. MAINE Flow is both the framework for the analytical numerical studies and the experimental facility in this study. Section 2.1 outlines its general description and capabilities for controlling acoustic and flow conditions. Then, Section 2.2 introduces a multimodal method for simulating the acoustic field in a duct composed of three sections, as encountered in the test duct, accounting for either uniform or sheared mean flow. Finally, Section 2.3 details both direct impedance eduction traditional algorithms and the approaches newly developed in this study. These models and methods will be employed in Chapter 3 to assess the impact of shear flow. And the impedance eduction techniques will be used and assessed through the numerical simulation using pressure data computed by the multimodal models (Chapter 4) and through the experiments using pressure data measured in the MAINE Flow facility (Chapter 5).

2.1 MAINE Flow facility

MAINE Flow (Multimodal Acoustic ImpedaNce Eduction with Flow) [11, 12] is a large duct facility designed to provide high-speed flow conditions and a controlled multimodal acoustic field, allowing for an assessment of the behaviour of the acoustic treatment in realistic flow and acoustic conditions. Figure 2.1 (Top) shows two views of the MAINE Flow facility, which consists of a 10 m-long duct with a rectangular cross-section of dimensions 150×280 mm^2 [12]. The section dedicated to direct impedance eduction, used in the present study, spans a length of 800 mm. On the narrow sides of this section, one or two face-to-face liner samples can be installed. These configurations are referred as single-liner and double-liner, with the latter specifically involving two identical liners. The former is a common configuration for the direct impedance eduction [9, 15, 17], whereas the latter is a newly developed approach in this study, aimed at improving impedance eduction results in such large ducts, which will be discussed later through simulations and experiments.

At the upstream end of the duct (upstream the acoustic sources), an anechoic termination is installed to limit the end reflections. And a diverging section is quasi-anechoic on the other side. The flow is driven by a fan working in suction mode. Figure 2.1 (Bottom) displays the flow profile measured just upstream of the liner using a Pitot tube. Only the profile in the direction perpendicular to the liner is

shown. In this example, the corresponding mean Mach number is the average value over the 2D cross-section $M_{ave} = 0.63$, the largest available flow velocity.

In the regions (denoted 1 and 3 in Figure 2.1) upstream and downstream of the lined section, 60 flush-mounted microphones are used for the modal decomposition of the acoustic field [11], and placed at optimised positions. Then, on each side, 24 loudspeakers and 66 compression chambers are employed to generate and control a desired acoustic field with a maximum available incident amplitude of 150 dB. This combination of microphones and acoustic sources allows the independent generation and detection of the 24 modes that are cut-on at 4000 Hz. We describe briefly the procedure for the generation of a desired acoustic field. More details can be found in [11].

(1) Generation of a stepped-sine signal by each source located upstream or downstream of the test section and simultaneous acquisition by all the microphones located in the upstream and downstream lined sections, i.e. zones 1 and 3 in Figure 2.1.

(2) Modal decomposition of the acoustic field in the ducts upstream and downstream for stepped sine sweep case, using the wavenumbers under the assumption of dissipative propagation in a uniform flow [106].

(3) Identification of the transfer matrix between the acoustic sources and the incident acoustic modes in the duct, according to the propagation matrix which is obtained in (2) and relates the commands on each source and the amplitudes of each mode. Here each source is excited one-by-one on each side.

(4) Excitation of particular acoustic modes or mode combinations. This operation is achieved by a pseudo-inversion of the transfer matrix between the sources and the modes, including a penalization to ensure that no source is excited above a certain limit so that the physical integrity of all the sources is preserved.

This procedure is performed for each considered flow velocity and for waves propagating in the same direction as the flow, and against it. When a target mode is generated, there are inevitably other cut-on modes. A mode can be considered correctly generated at a particular frequency on basis of a criterion of emergence (typically of 20 dB) of this mode above the other modes cut-on at this frequency.

Figure 2.2 displays 3D schematics of the test section, with both single- and double-liner configurations. H denotes the duct dimension perpendicular to the liner and the dimension associated with the width of liner is denoted W.

2.2 Multimodal model for acoustic propagation in duct with flow

The multimodal model simulates the acoustic propagation in a duct such as the MAINE Flow, which serves as tools for the parametric study in Chapter 3 and provides the pressure data for the numerical impedance eduction in Chapter 4. This section starts with the governing equations used to model the uniformly convected acoustic waves. The model for the numerical calculation of 2D multimodal acoustic propagation in a flow duct consisting of several segments is introduced. Two assumptions for the mean flow profile will be separately applied: uniform flow and inviscid sheared flow.

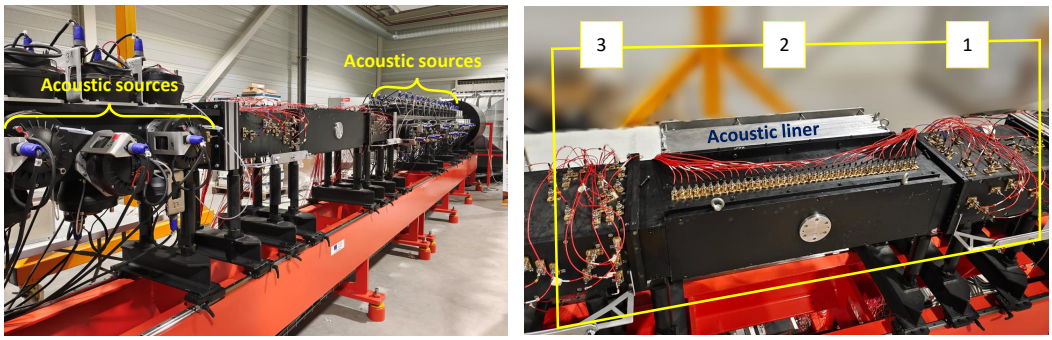

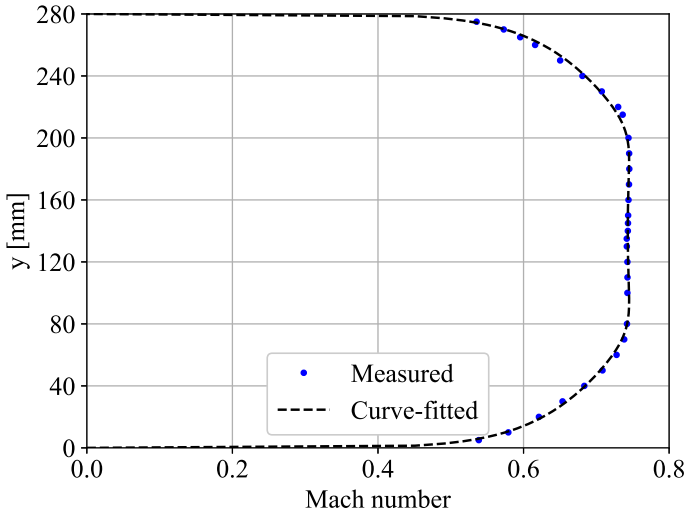

Figure 2.1: Top, left: general view of the MAINE Flow duct with acoustic sources marked by yellow brackets upstream and downstream of the test section. Top, right: view of the test section, 2 indicates the lined section with the microphone array for direct impedance eduction, while 1 and 3 are rigid sections used for modal decomposition. Bottom: Mach number profile measured upstream of the liner in the direction perpendicular to it when the average Mach value over the cross-section is $M_{\text{ave}} = 0.63$.

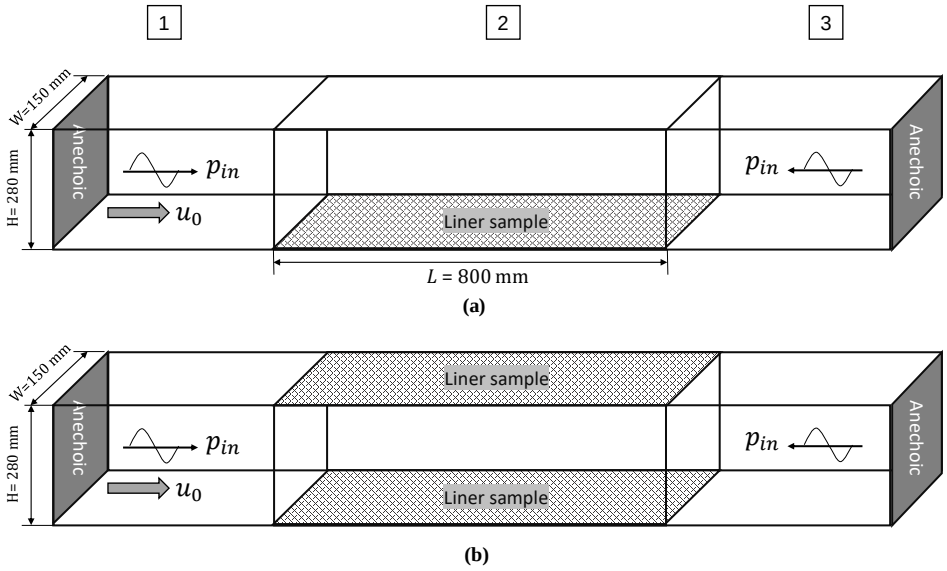

Figure 2.2: Schematics of MAINE Flow facility with a lined middle section (2) and rigid sections (1 and 3) on each side. (a): single-liner configuration, (b): double-liner configuration. The length of the lined section is $L = 800$ mm and the width of the liner is $W = 150$ mm. The distance between the two lined walls is $H = 280$ mm. The incident waves p_{in} can be generated at both sides. The both ends are set anechoic. The flow of velocity u_0 can be sent from left 1 to right 3, being uniform or sheared in the numerical study.

2.2.1 Governing equations

We consider the case in the absence of external sources and heat transfer, with assumptions of inviscid, ideal and isentropic fluid. In such case, a fluid motion can be described by the Euler equations [107]. The later consist of the continuity equation (2.1), the momentum conservation equation (2.2) and the energy equation (2.3):

$$\frac{D\rho^w}{Dt} + \rho^w \nabla \cdot \mathbf{u}^w = 0. \tag{2.1}$$

$$\rho^w \frac{D\mathbf{u}^w}{Dt} + \nabla p^w = \mathbf{0}. \tag{2.2}$$

$$\frac{Dp^w}{Dt} + \rho^w c^2 \nabla \cdot \mathbf{u}^w = 0. \tag{2.3}$$

The notations with superscript ^{w} stand for the whole flow field quantities. ρ^w is the flow density, $\mathbf{u}^w$ is the flow velocity vector field, p^w is the pressure, c^w is the speed of sound in the flow, and $D/Dt = \partial/\partial t + \mathbf{u}^w \cdot \nabla$ is the material derivative.

In acoustics, we are often concerned with small unsteady perturbations over a mean flow, such that the flow variable can be written

$$\rho^w = \rho_0 + \rho; \quad \mathbf{u}^w = \mathbf{u}_0 + \mathbf{u}; \quad p^w = p_0 + p.$$

In this approach, the whole flow field quantity (denoted with superscript ^{w}) is decomposed into steady base flow quantities (denoted with subscript $_0$) and unsteady perturbed variables (unscripted). This decomposition is introduced into the

Euler equations, while neglecting the feedback between the base flow and the perturbation field. Subsequently, by disregarding non-linear terms (deemed negligible for the acoustic field), the Euler equations are linearized to describe the propagation of small-amplitude perturbations:

$$\frac{\partial \rho}{\partial t} + \nabla \cdot (\rho_0 \mathbf{u} + \rho \mathbf{u}_0) = 0, \tag{2.4}$$

$$\rho_0 \frac{D_0 \mathbf{u}}{Dt} + \rho \frac{D_0 \mathbf{u}_0}{Dt} + \rho_0 (\mathbf{u} \cdot \nabla) \mathbf{u}_0 + \nabla p = \mathbf{0}, \tag{2.5}$$

$$\frac{D_0 p}{Dt} + \mathbf{u} \cdot \nabla p_0 + \rho_0 c_0^2 \nabla \cdot \mathbf{u} + \rho_0 c^2 \nabla \cdot \mathbf{u}_0 = 0. \tag{2.6}$$

Here, $D_0/Dt = \partial/\partial t + \mathbf{u}_0 \cdot \nabla$ is the material derivative associated to the base flow.

In this thesis, the acoustic problem in the duct is simplified to a two-dimensional case, where the width of the duct is neglected. Despite this simplification, the study remains valid for analysing the acoustic field and the impedance eduction within both uniform and sheared flows [20, 22, 26]. The flow structure in two-dimensional cases focuses on a single plane vertical to the width dimension of three-dimensional ducts, and allows effectively representing the effects.

A 2D duct as depicted by Figure 2.3 is considered, in which either a uniform or a shear mean flow is aligned with the axis. The first and third sections have hard boundaries, while the walls of the middle section can be treated with a locally reacting liner (either both the upper and lower walls, or only the lower wall). The height of the 2D duct is denoted H and the length of each section is L_n. The axial coordinate is denoted x, and y is the vertical coordinate. The duct exits are considered anechoic. The following propagation models are for linear acoustic waves with an implicit time dependence given by $e^{+i\omega t}$, where ω is the angular frequency.

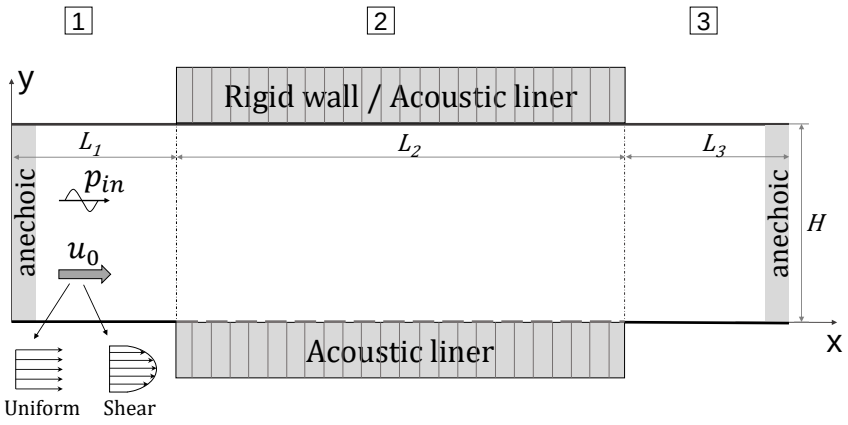

Figure 2.3: Schematic of the 2D duct with three sections. L_n is the length of n-th section. The boundaries of the middle section are either lined-rigid or lined-lined. The incident wave p_{in} is sent from the left. The flow inside the duct is assumed to be uniform or sheared. The upstream or downstream propagation are controlled by the direction of the imposed flow.

2.2.2 Model with uniform flow

With a uniform mean flow along the axial direction, the acoustic pressure field inside the duct is governed by the convected Helmholtz equation:

$$\frac{1}{c_0^2}\frac{D_0^2 p}{Dt^2} - \nabla^2 p = 0, \tag{2.7}$$

where ∇^2 is the Laplacian operator.

For a hard wall, the boundary condition gives

$$\frac{\partial p}{\partial n} = 0, \tag{2.8}$$

indicating that the normal particle velocity vanishes at the duct wall, where n is the unit normal to the wall, towards the outside of the duct. In the case of a lined wall, the liner is assumed to have a constant impedance value along the axis, and Eq. (1.7), the Ingard–Myers boundary condition [92, 93], is used to describe the relation between the acoustic velocity and pressure at the wall:

$$v = \frac{D_0}{Dt}\frac{p}{\mathrm{i}\omega\rho_0 c_0 Z},$$

where Z is the specific surface impedance (i.e. normalised by $\rho_0 c_0$). Thus, the boundary condition at the lined wall writes

$$\frac{\partial p}{\partial n} = -\frac{\mathrm{D}_0^2}{\mathrm{D}t^2}\frac{p}{\mathrm{i}\omega c_0 Z}, \tag{2.9}$$

2.2.2.1 Mode calculation

In each section of the duct, the acoustic pressure can be sought in the following modal form:

$$p(x,y) = \sum_n A_n^+ \Psi_n^+(y)\mathrm{e}^{-\mathrm{i}k_{xn}^+ x} + \sum_n A_n^- \Psi_n^-(y)\mathrm{e}^{-\mathrm{i}k_{xn}^- x}, \tag{2.10}$$

where each mode is defined by an amplitude $A_n^\pm$, a shape function $\Psi_n^\pm$ and an axial wavenumber $k_{xn}^\pm$. The symbol $\pm$ selects the direction of propagation. Then, the transverse wavenumber k_y is defined using the dispersion relation of the acoustic waves in a uniform flow

$$k_{yn}^2 = \frac{1}{c_0^2}(\omega - u_0 k_{xn})^2 - k_{xn}^2, \tag{2.11}$$

which allows to write the axial wavenumber as:

$$k_{xn}^\pm = \frac{\pm c_0\sqrt{\omega^2 - (c_0^2 - u_0^2)k_{yn}^2} - u_0\omega}{c_0^2 - u_0^2}. \tag{2.12}$$

This expression indicates that each transverse wavenumber k_{yn} matches two possible axial wavenumbers corresponding to waves propagating in the positive and negative directions.

The wavenumbers and shape functions are solutions of an eigenvalue problem given by Eq. (2.7)–(2.9) while assuming solutions of the form $p = \Psi(y)\mathrm{e}^{-\mathrm{i}k_x x}$. For a

hard-wall section, this eigenvalue problem can be solved analytically:

$$\Psi_n(y) = \cos\left(k_{yn} y\right), \quad \text{with} \quad k_{yn} = n\pi/H. \tag{2.13}$$

For a lined section, the problem is addressed using a pseudo-spectral method based on Chebyshev polynomials, following the approach outlined by Boyd [108]. In this method, each mode shape Ψ is represented as a series expansion in Chebyshev polynomials: $\Psi(y) = \sum_{n=0}^{N-1} \alpha_n T_n(y)$, where $T_n(y)$ are the Chebyshev polynomials and α_n are their associated coefficients. The convected Helmholtz equation is discretized and solved at Chebyshev points along the duct height. The linear system is further constrained by applying boundary conditions Eq. (2.9) and/or Eq. (2.8). The eigenvalue problem is then solved to determine the axial wavenumbers k_x and the corresponding mode shape functions. A detailed description of this computational process is provided in Appendix B.1.

Among the obtained modes, it is then necessary to distinguish the acoustic modes from the hydrodynamic modes and to reorder the wavenumbers in both directions of propagation. Hydrodynamic modes in ducts typically appear along the real axis in the complex plane, ranging from $\mathrm{Re}(k_x) = \omega/u_0$ to $\mathrm{Re}(k_x) \to \infty$ in the complex plane [109]. Therefore, to isolate the acoustic modes, we limit $\mathrm{Re}(k_x)$ such that it does not exceed ω/u_0. Then, for acoustic modes propagating in the positive (or negative) axial direction in a hard-walled duct with uniform flow, their axial wavenumbers are located in a quadrant of the complex plane defined by

$$\begin{aligned} &\mathrm{Im}(k_x^+) \leq 0\,, \quad \mathrm{Re}(k_x^+) \geq \frac{\omega u_0}{u_0^2 - c_0^2}\,; \\ \text{or} \quad &\mathrm{Im}(k_x^-) \geq 0\,, \quad \mathrm{Re}(k_x^-) \leq \frac{\omega u_0}{u_0^2 - c_0^2}\,. \end{aligned} \tag{2.14}$$

For a lined duct, the propagation direction of the acoustic modes can be identified using a heuristic rule with a diagonal defined by $\mathrm{Im}(k_x) = \mathrm{Re}(k_x) - u_0\omega/(c_0^2 - u_0^2)$:

$$\mathrm{Im}(k_x^+) \leq \mathrm{Re}(k_x^+) - \frac{\omega u_0}{u_0^2 - c_0^2} \quad \text{and } \mathrm{Im}(k_x^+) < 0\,, \tag{2.15a}$$

$$\mathrm{Im}(k_x^-) \geq \mathrm{Re}(k_x^-) - \frac{\omega u_0}{u_0^2 - c_0^2} \quad \text{and } \mathrm{Im}(k_x^-) > 0\,. \tag{2.15b}$$

The intersection with the real axis at $-u_0\omega/(c_0^2 - u_0^2)$ represents the real part of the just cut-on modes in a hard-walled duct. Modes that propagate in the positive direction appear in the lower half of the complex plane, while those propagating in the negative direction are found in the upper half. Subsequently, the acoustic modes are ordered based on the attenuation rates, which are anticipated by the absolute value of their associated transverse wavenumbers. As a final remark, the normalisation of the mode shape function is crucial for interpreting and comparing the amplitudes of the modes in a uniform way in the subsequent mode-matching step.

2.2.2.2 Mode matching

Once the modal basis is known in each section, a mode-matching method developed by Gabard and Astley [110] is used to compute the whole duct field by connecting the modal solutions in each sections considering the discontinuity of boundary at interfaces. Mode-matching is applied at the leading and trailing edges of the liners, and allows computing the modal amplitudes $A_n^{\pm}$ in each section, based on the

conservation of mass and momentum. The continuity condition is obtained from a variational statement of the field equations and impedance boundary conditions over a vanishingly small transition region between rigid and lined segments. We first present the theory of this approach and then apply it to this study.

In the original mode-matching method [110], a 3D duct is considered with the assumption that the axial change in liner impedance occurs over a finite region $\pm\epsilon$ on either side of the matching plane at $x = 0$, as shown in Figure 2.4. In this small transition region, the acoustic pressure $p(x, y, z)$ and velocity amplitudes $\mathbf{u}(x, y, z) = [u, v, w]$ satisfy the linearised momentum and continuity equations. The matching conditions are established for this finite transition region and the limit $\epsilon \to 0$ is taken to simulate an abrupt discontinuity at $x = 0$. The cross-section of the duct at $x = 0$ defines an area S bounded by a contour Γ. In regions (1) and (2) on either side of the transition region, the complex amplitudes of the acoustic pressure and the velocity are taken equal to p_1, u_1, v_1 and w_1 for $x < -\epsilon$, and p_2, u_2, v_2 and w_2 for $x > \epsilon$.

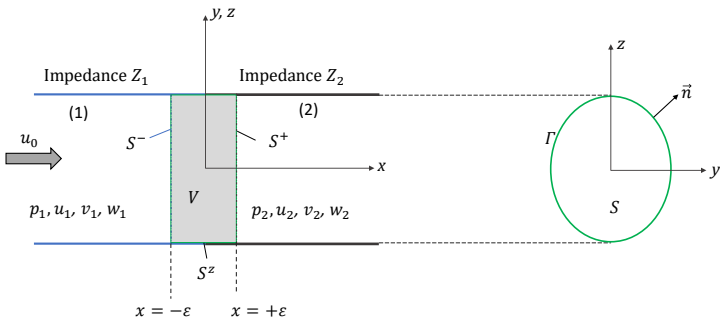

Figure 2.4: Schematic for the mode matching at liner discontinuity (modified from [110]). x is the axial axis, y and z axis lie in the cross-section. Z_1 and Z_2 are impedances of boundary in region (1) and (2), respectively. u_0 is the velocity of the flow in duct and only has the axial component. Grey region: thin transition volume for the matching conditions with the length $2\epsilon \to 0$.

To formulate the matching conditions in the duct, particularly in the matching region, only the axial momentum equation and the continuity equation are considered. They are written in conservative form:

$$\mathrm{i}\omega u + \nabla \cdot (u_0 u + \frac{1}{\rho_0} p, 0, 0) = 0, \tag{2.16}$$

$$\mathrm{i}\omega p + \nabla \cdot (u_0 p + \rho_0 c_0^2 u, \rho_0 c_0^2 v, \rho_0 c_0^2 w) = 0. \tag{2.17}$$

These equations are solved within a region bounded by the left and right planes (S^- and S^+) near the interface, and bounded by the thin section of the duct wall (S^z).

The impedance boundary condition on the duct lined wall is Eq. (2.9). The impedance varies continuously and the values at the edge of the region on the pipe wall are $Z = Z_1$ and $Z = Z_2$. Then, Eq. (2.16) and (2.17) are multiplied by a continuous weighting function $W(y)$ and integrated over the region volume V. The region is assumed infinitely thin. By applying Green's theorem, substituting the boundary

conditions, the equations become

$$\int_S u_0 \overline{W}(u_2 - u_1)\mathrm{d}S + \int_S \frac{1}{\rho_0}\overline{W}(p_2 - p_1)\mathrm{d}S = 0, \tag{2.18}$$

$$\int_S \rho_0 c_0^2 \overline{W}(u_2 - u_1)\mathrm{d}S + \int_S u_0 \overline{W}(p_2 - p_1)\mathrm{d}S = \int_\Gamma \frac{\mathrm{i}u_0\rho_0 c_0^2}{\omega}\overline{W}\left(\frac{p_2}{Z_2} - \frac{p_1}{Z_1}\right)\mathrm{d}\Gamma. \tag{2.19}$$

When the flow in the duct is uniform, the two previous equations can reduce to

$$\int_S u_0 \overline{W}(p_2 - p_1)\mathrm{d}S = -\frac{\mathrm{i}u_0^2}{c_0^2 - u_0^2}\frac{\rho_0 c_0^2}{\omega}\int_\Gamma \overline{W}\left(\frac{p_2}{Z_2} - \frac{p_1}{Z_1}\right)\mathrm{d}\Gamma, \tag{2.20}$$

$$\int_S u_0 \overline{W}(u_2 - u_1)\mathrm{d}S = \frac{\mathrm{i}u_0^2}{c_0^2 - u_0^2}\frac{c_0}{\omega}\int_\Gamma \overline{W}\left(\frac{p_2}{Z_2} - \frac{p_1}{Z_1}\right)\mathrm{d}\Gamma. \tag{2.21}$$

To match the modal solutions across a liner discontinuity, the acoustic pressure field expression (2.10) is substituted into Eq. (2.20) and Eq. (2.21). Thus the mode amplitudes in two sections are linked by

$$\begin{bmatrix} \mathbf{P}_2^+ & -\mathbf{P}_1^- \\ \mathbf{M}_2^+ & -\mathbf{M}_1^- \end{bmatrix}\begin{pmatrix} \mathbf{A}_2^+ \\ \mathbf{A}_1^- \end{pmatrix} = \begin{bmatrix} \mathbf{P}_1^+ & -\mathbf{P}_2^- \\ \mathbf{M}_1^+ & -\mathbf{M}_2^- \end{bmatrix}\begin{pmatrix} \mathbf{A}_1^+ \\ \mathbf{A}_2^- \end{pmatrix}, \tag{2.22}$$

where $\mathbf{A}_n^\pm$ is the amplitude of the acoustic pressure in the n-th zone. The sign $\pm$ indicates the propagation direction and the sub-matrices $\mathbf{M}_{1,2}^\pm$ and $\mathbf{P}_{1,2}^\pm$ are formed as follows:

$$(\mathbf{M}_n^\pm)_{a,b} = \int_s \left(u_0 + c_0^2\frac{k_{xb,n}^\pm}{\omega - u_0 k_{xb,n}^\pm}\right)\overline{W_a}\Psi_{n,b}^\pm \mathrm{d}S - \int_\Gamma \frac{iu_0\rho_0 c_0^2}{\omega Z_n}\overline{W_a}\Psi_{n,b}^\pm \mathrm{d}\Gamma \quad \text{for } n = 1, 2, \tag{2.23}$$

$$(\mathbf{P}_n^\pm)_{a,b} = \int_s \frac{\omega\overline{W_a}\Psi_{n,b}^\pm}{\rho_0(\omega - u_0 k_{xb,n}^\pm)}\mathrm{d}S \quad \text{for } n = 1, 2, \tag{2.24}$$

where a and b are the mode index and $\Psi_{n,b}$ is the mode shape function of mode b in n-th zone . The trial function W_a is chosen as $\Psi_{2,b}^+$ for $\mathbf{P}_n^+$ and $\Psi_{1,b}^-$ for $\mathbf{M}_n^+$.

For a 2D duct with 3 sections (hard-lined-hard) as considered in this study, the mode-matching conditions are established at the interfaces on each side of the lined section, as indicated in Figure 2.5. According to Eq. (2.22), two linear systems of equations are written: Eq. (2.25) for the upstream interface 1-2 and Eq. (2.26) for the downstream interface 2-3. Here, the index n of the wavenumbers k_x represents the n-th segment.

$$\begin{bmatrix} \mathbf{P}_2^+ & -\mathbf{P}_1^- \\ \mathbf{M}_2^+ & -\mathbf{M}_1^- \end{bmatrix}\begin{pmatrix} \mathbf{A}_2^+ \\ \mathbf{A}_1^- \end{pmatrix} = \begin{bmatrix} \mathbf{P}_1^+ & -\mathbf{P}_2^- \\ \mathbf{M}_1^+ & -\mathbf{M}_2^- \end{bmatrix}\begin{bmatrix} \mathrm{e}^{-\mathrm{i}\mathbf{k}_{x,1}^+ L_1} & \mathbf{0} \\ \mathbf{0} & \mathrm{e}^{\mathrm{i}\mathbf{k}_{x,2}^- L_2} \end{bmatrix}\begin{pmatrix} \mathbf{A}_1^+ \\ \mathbf{A}_2^- \end{pmatrix}, \tag{2.25}$$

$$\begin{bmatrix} \mathbf{P}_4^+ & -\mathbf{P}_3^- \\ \mathbf{M}_4^+ & -\mathbf{M}_3^- \end{bmatrix}\begin{pmatrix} \mathbf{A}_3^+ \\ \mathbf{A}_2^- \end{pmatrix} = \begin{bmatrix} \mathbf{P}_3^+ & -\mathbf{P}_4^- \\ \mathbf{M}_3^+ & -\mathbf{M}_4^- \end{bmatrix}\begin{bmatrix} \mathrm{e}^{-\mathrm{i}\mathbf{k}_{x,2}^+ L_2} & \mathbf{0} \\ \mathbf{0} & \mathrm{e}^{\mathrm{i}\mathbf{k}_{x,3}^- L_3} \end{bmatrix}\begin{pmatrix} \mathbf{A}_2^+ \\ \mathbf{A}_3^- \end{pmatrix}. \tag{2.26}$$

The expressions for $\mathbf{M}_n^\pm$ and $\mathbf{P}_n^+$ given by Eq. (2.23) and Eq. (2.24) become

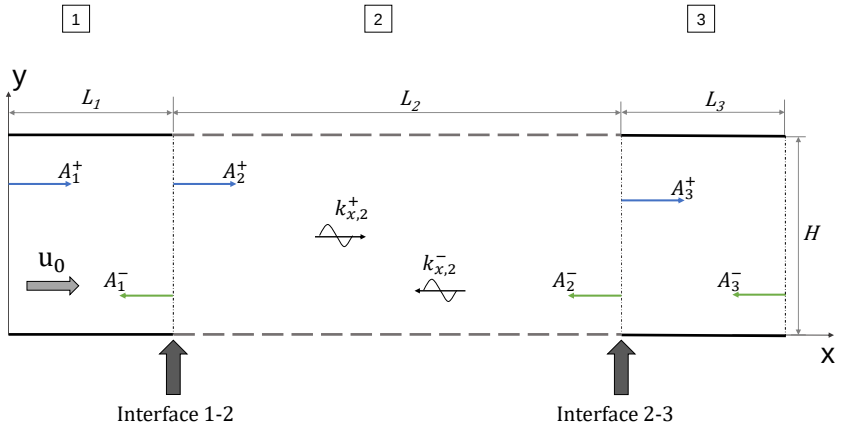

Figure 2.5: 2D duct schematic and wave amplitudes $A_n^{\pm}$ in the n-th segment, with wavenumbers $k_{x,n}^{\pm}$, respectively. x is along the duct axis and y is along the duct height. L_n is the length of each segment. H is the duct height. u_0 is the velocity of the grazing flow.

$$(\mathbf{M}_n^{\pm})_{a,b} = \int_0^h (u_0 + c_0^2 \frac{k_{xb,n}^{\pm}}{\omega - u_0 k_{xb,n}^{\pm}}) \overline{W_a} \Psi_{n,b}^{\pm} dy - \left[\frac{i u_0 \rho_0 c_0^2}{\omega} A_n \overline{W_a} \Psi_{n,b}^{\pm} \right]_{(y=0)}^{(y=h)}, \quad (2.27)$$

$$(\mathbf{P}_n^{\pm})_{a,b} = \int_0^h \frac{\omega}{\rho_0(\omega - u_0 k_{xb,n}^{\pm})} \overline{W_a} \Psi_{n,b}^{\pm} dy. \quad (2.28)$$

Here, $\mathbf{M}_n^{\pm}$ and $\mathbf{P}_n^{+}$ with $n = 1, 2$ are for the interface 1-2, and $n = 3, 4$ for the interface 2-3. The trial functions in Eq. (2.27) for the first interface are $\Psi_{2,b}^{+}$ for $\mathbf{P}_n^{+}$ and $\Psi_{1,b}^{-}$ for $\mathbf{M}_n^{+}$. The trial functions in Eq. (2.28) for the second interface are $\Psi_{3,b}^{+}$ for $\mathbf{P}_n^{+}$ and $\Psi_{2,b}^{-}$ for $\mathbf{M}_n^{+}$. More details in the implementation are described in Appendix B.1.2.

2.2.3 Model with shear flow

We now develop a propagation model with a sheared mean flow in ducts. For parallel shear flows, the mean flow velocity is in the same direction everywhere and the flow properties are constant in the streamwise direction. However, the velocity magnitude depends on the vertical coordinate. In this flow case, we still consider a 2D model, where the mean flow velocity $[u_{0x}(y), u_{0y} = 0]$ is only in the axial direction and the value $u_{0x}(y)$ varies along the y axis. Two common models used to describe the sound propagation in parallel shear flows are the Linearised Euler Equations (LEEs) and the Pridmore Brown equation [111]. A problem with both models is that the gradient $u_0'(y)$ of the mean flow profile appears in these equations. For some common flow profiles, such as the inverse law profile [18], this velocity gradient tends to infinity at the duct wall, which can create difficulties for the numerical solutions. To avoid this issue, we introduce the vertical acoustic displacement ξ which is related to the vertical acoustic velocity v by $D_0\xi/Dt = v$, such that we can use the LEEs in this study. The LEEs can thus be written as follows in

terms of p and ξ:

$$\frac{\partial p}{\partial y} + \rho_0 \frac{D_0^2 \xi}{Dt^2} = 0 \quad , \tag{2.29a}$$

$$\rho_0 c_0^2 \frac{D_0^2}{Dt^2} \frac{\partial \xi}{\partial y} - c_0^2 \frac{\partial^2 p}{\partial x^2} + \frac{D_0^2 p}{Dt^2} = 0 \quad . \tag{2.29b}$$

It can be seen that the gradient of the mean flow does not appear explicitly. Also, from the definition of impedance $\rho_0 c_0 Z = p/v$, the impedance boundary condition can be directly written as $\xi = -p/(\mathrm{i}\omega\rho_0 c_0 Z)$ or $\xi = p/(\mathrm{i}\omega\rho_0 c_0 Z)$ for the lower or upper lined walls, respectively.

In each section, the pressure p and displacement ξ are written in modal form, as in Eq. (2.10). Assuming that p and ξ have an axial dependence given by $\mathrm{e}^{-\mathrm{i}k_x x}$ yields

$$\frac{\partial p}{\partial y} - \rho_0 (\omega - u_0 k_x)^2 \xi = 0 \quad , \tag{2.30a}$$

$$-\rho_0 c_0^2 (\omega - u_0 k_x)^2 \frac{\partial \xi}{\partial y} + c_0^2 k_x^2 p - (\omega - u_0 k_x)^2 p = 0 \quad . \tag{2.30b}$$

This eigenvalue problem for the axial wavenumbers k_x and mode shape functions p and ξ is also solved using the pseudo-spectral method, with N Chebyshev polynomials to represent p and ξ.

Once the axial wavenumbers are computed, the classification of the modes is performed. However, in the case of a sheared flow, the dispersion relation in Eq. (2.11) is not valid, so the transverse wavenumbers cannot be defined nor serve as the reordering indicator. Another way to achieve the reordering of wavenumbers is to use a smoothness indicator for each mode. This indicator is defined by the L2 norm of the associated mode shape, with smaller values for smoother mode. Based on this indicator, all modes can be reordered from the most to the least smooth. Additionally, when the average flow velocity $u_{0,\mathrm{ave}} > 0$ (resp. $u_{0,\mathrm{ave}} < 0$), the aforementioned condition for the model with uniform flow is not capable enough of separating right-running (resp. left-running) acoustic modes from hydrodynamic modes, and a second criterion is needed. For the acoustic modes, the largest expected value for $\mathrm{Re}(k_x^+)$ is close to $\omega/(c_0 + u_{0,\mathrm{ave}})$. For the hydrodynamic modes when $u_{0,\mathrm{ave}} > 0$, the smallest value of $\mathrm{Re}(k_x)$ is expected to be close to $\omega/u_{0,\mathrm{max}}$ with $u_{0,\mathrm{max}}$ being the largest value of the velocity profile. We therefore use the average of these two values as a threshold to discriminate between acoustic and hydrodynamic modes. More specifically, a wavenumber is retained as an acoustic mode if

$$\mathrm{Re}(k_x) < \frac{\omega}{2}\left(\frac{1}{u_{0,\mathrm{ave}} + c_0} + \frac{1}{u_{0,\mathrm{max}}}\right), \qquad \text{when } u_0 > 0; \tag{2.31a}$$

$$\mathrm{Re}(k_x) > \frac{\omega}{2}\left(\frac{1}{u_{0,\mathrm{ave}} - c_0} + \frac{1}{u_{0,\mathrm{max}}}\right), \qquad \text{when } u_0 < 0. \tag{2.31b}$$

The conditions Eq. (2.31) are only qualitative, but their robustness has been tested in practice.

Then, the whole acoustic field is calculated by the mode-matching method [110] using the matching conditions in equations (2.18) and (2.19). In this method, the axial acoustic velocity u is needed for the matching conditions, and the axial components in the conservation of momentum Eq. (2.5) provide a relationship for deriving u:

$$\rho_0 \frac{D_0 u}{Dt} + \rho_0 v \frac{\partial u_0}{\partial y} + \frac{\partial p}{\partial x} = 0. \tag{2.32}$$

Thus, using the vertical displacement ξ and the pressure p, the axial acoustic velocity u for a single mode writes:

$$u = \frac{k_x}{\rho_0(\omega - u_0 k_x)} p - \frac{du_0}{dy} \xi. \tag{2.33}$$

Now the propagation model with the assumption of a shear flow is obtained, enabling the numerical study on the wave propagation and providing the acoustic pressure field for the impedance eduction. Apart from these, the two propagation models with uniform or shear flow can be used for comparisons of the acoustic propagation and the impedance eduction between two flow cases and for the investigation of the effects of shear flow.

2.3 Direct impedance eduction technique

This section describes the algorithms for the direct impedance eduction method. In the 3-segment duct described before, once the acoustic field in the duct is known, either experimentally measured in the MAINE Flow duct described in Section 2.1 or numerically simulated using the multimodal models described in Section 2.2, the direct impedance eduction is used to provide the liner impedance. This technique can be split into two steps: estimating axial wavenumbers, and calculating the liner impedance from the wavenumbers. The first step relies on a linear array of equidistant microphones in the lined section (see Figure 2.6). From the pressure signals, the wavenumbers can be identified using an exponential parameter estimation method. Then, with one identified axial wavenumber k_x, the liner impedance can be obtained by means of a direct relationship considering the property of mean flow.

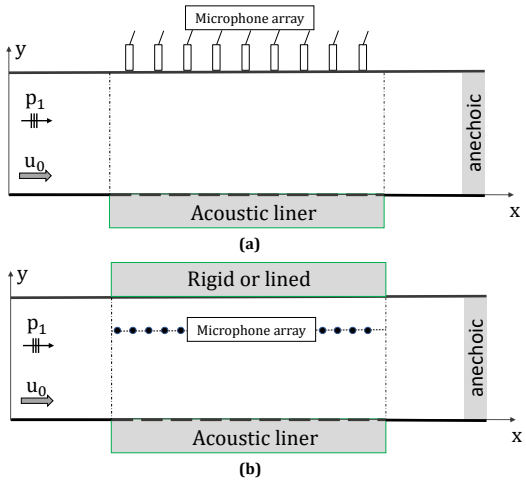

Figure 2.6: Schematics depicting the installation of microphones. (a): on the wall opposite to the liner in the traditional single-liner configuration [18], (b): on the lateral wall, which is compatible with the double-liner configuration [23].

2.3.1 Wavenumber estimation

Exponential parameter estimation [82, 112–115] is widely employed to retrieve the components of signals composed of a sum of exponentials. In the present study, the estimation is performed on the acoustic pressure p in the frequency domain. The latter can be indeed decomposed into a sum of modes with amplitudes A_n, i.e. $p = \sum_n A_n \mathrm{e}^{-\mathrm{i}k_{xn}x}$, enabling the estimation of wavenumbers from the acoustic pressure data. Two methods are introduced for this purpose: the Kumaresan–Tufts (KT) method and the Hankel Total Least Squares (HTLS) method.

2.3.1.1 KT method

The KT method proposed by Kumaresan and Tufts [82] is based on a linear prediction equation system. We consider N samples of the acoustic pressure, obtained in the lined section by an array of N equidistant microphones separated by a distance Δx. Since the propagation of a mode with a wavenumber k_x along the x axis is characterised by $\mathrm{e}^{-\mathrm{i}k_x x}$, the acoustic pressures measured by adjacent microphones differ by a factor $\mathrm{e}^{-\mathrm{i}k_x \Delta x}$. Thus, each of the first $N - L_{\mathrm{kt}}$ samples can be expressed as a linear combination of the following L_{kt} points. Here, L_{kt} is named the order of the linear prediction filter.

In this method, the linear prediction equations concern the samples in the backward direction. The system of $(N - L_{\mathrm{kt}})$ equations can then be expressed:

$$\underbrace{\begin{bmatrix} p(2) & \cdots & p(L_{\mathrm{kt}}+1) \\ p(3) & \cdots & p(L_{\mathrm{kt}}+2) \\ \vdots & \ddots & \vdots \\ p(N-L_{\mathrm{kt}}+1) & \cdots & p(N) \end{bmatrix}}_{\mathbf{H}_{\mathrm{kt}}} \underbrace{\begin{bmatrix} b(1) \\ b(2) \\ \vdots \\ b(L_{\mathrm{kt}}) \end{bmatrix}}_{\mathbf{B}} = - \underbrace{\begin{bmatrix} p(1) \\ p(2) \\ \vdots \\ p(N-L_{\mathrm{kt}}) \end{bmatrix}}_{\mathbf{D}}. \tag{2.34}$$

$\mathbf{H}_{\mathrm{kt}}$ is an $(N - L_{\mathrm{kt}}) \times L_{\mathrm{kt}}$ Hankel matrix composed of the samples, $\mathbf{B}$ is a column vector presenting the linear prediction coefficients, and $\mathbf{D}$ is the conjugates of the first $N - L_{\mathrm{kt}}$ samples. Referring to [76], the vector of the prediction coefficients $\mathbf{B}$ is obtained by

$$\mathbf{B} = -\mathbf{H}_{\mathrm{kt}}^{\dagger}\mathbf{D}, \tag{2.35}$$

where ${\mathbf{H}_{\mathrm{kt}}}^{\dagger}$ is the pseudo-inverse of $\mathbf{H}_{\mathrm{kt}}$. This can be given by the singular value decomposition of $\mathbf{H}_{\mathrm{kt}}$:

$$\mathbf{H}_{\mathrm{kt}} = \mathbf{U}\mathbf{\Sigma}\mathbf{V}^{\mathbf{H}}, \tag{2.36}$$

and

$${\mathbf{H}_{\mathrm{kt}}}^{\dagger} = \mathbf{V}\mathbf{\Sigma}^{-1}\mathbf{U}^{\mathbf{H}}. \tag{2.37}$$

Here, $\mathbf{\Sigma}$ is a rectangular diagonal matrix and contains the singular values of $\mathbf{H}_{\mathrm{kt}}$. The columns of $\mathbf{U}$ (resp. $\mathbf{V}$) are called left-singular vectors (resp. right-singular vectors). The superscript $^{\mathbf{H}}$ denotes the Hermitian transpose.

The essential idea in the KT method is to reduce the influence of the measurement noise by considering a reduced rank approximation of $\mathbf{H}_{\mathrm{kt}}$. This is done by using a truncated Singular Value Decomposition (SVD) of $\mathbf{H}_{\mathrm{kt}}$ with a truncation number M_t, meaning to keep only the first M_t most important components. Then, $\mathbf{H}_{\mathrm{kt}}$ can be express as

$$(\mathbf{H}_{\mathrm{kt}})_{M_t} = \mathbf{U}_{M_t}\mathbf{\Sigma}_{M_t}{\mathbf{V}^{\mathbf{H}}}_{M_t}, \tag{2.38}$$

where the size of $\mathbf{U}_{M_t}$ is $(N - L_{\text{kt}}) \times M_t$, the size of $\mathbf{\Sigma}_{M_t}$ is $M_t \times M_t$ and the size of $\mathbf{V}$ is $L_{\text{kt}} \times M_t$.

Therefore, the vector of prediction coefficients $\mathbf{B}$ can be estimated as

$$\mathbf{B} = -(\mathbf{H}_{\text{kt}})^{\dagger}_{M_t}\mathbf{D} = -\mathbf{V}_{M_t}\mathbf{\Sigma}^{-1}_{M_t}(\mathbf{U}^{\mathbf{H}})_{M_t}\mathbf{D}. \tag{2.39}$$

From the linear prediction coefficients, we can write the prediction-error filter polynomial

$$B(z) = 1 + \sum_{n=1}^{L_{\text{kt}}} b_n z^{-n}. \tag{2.40}$$

According to the roots z_n of this polynomial, the axial wavenumbers are obtained by the relationship $z_n = e^{-\mathrm{i}k^{\pm}_{xn}\Delta x}$, thus:

$$k_{xn} = \frac{\ln z_n + 2m\pi\mathrm{i}}{-\mathrm{i}\Delta x}. \tag{2.41}$$

Here, the natural logarithm results in periodic solutions $\ln z_n + 2m\pi\mathrm{i}$, where m is an integer. Consequently, each axial wavenumber are among multiple solutions, and the correct value depends on the choice of m. Jing et al. [20] addressed this issue by constraining the proper range of the real part of the axial wavenumber using the uniform-flow dispersion relation. Nevertheless, in this study, the logarithm function is computed using NumPy in Python 3, returning the solution of the natural logarithm whose imaginary part lies in $]-\pi, \pi]$. This solution is considered as the correct one to calculate the acoustic axial wavenumber, because the additional term $-2m\pi/\Delta x$ introduces an excessively large real part into the resulting wavenumber. For instance, with a microphone spacing $\Delta x = 0.02$ m, a typical choice in experiments [81], the additional term for $m = 1$ is approximately -314, which is not a physical solution for an acoustic mode. Therefore, this thesis only takes the value obtained by the NumPy function for the retrieved axial wavenumber.

2.3.1.2 Hankel Total Least Square method

In contrast to the previous method, the Hankel Total Least Square method [112] retrieves the wavenumbers by taking advantage of the subspace representation and of the shift-invariance property of the Vandermonde decomposition (VDMD). Again, a microphone array containing N complex samples is considered. All the pressure samples are included in an $L \times R$ Hankel Matrix:

$$\mathbf{H} = \begin{bmatrix} p(1) & \cdots & p(R) \\ p(2) & \cdots & p(R+1) \\ \vdots & \ddots & \vdots \\ p(L) & \cdots & p(N) \end{bmatrix}, \tag{2.42}$$

with L and R chosen so that $N = L + R - 1$ and $L > K$. Here, the numbers of row and column L and R do not have the same meaning as in the KT method, and K is

the truncation number used later. Then the VDMD decomposition of $\mathbf{H}$ is realised:

$$\mathbf{H} = \mathbf{SCT}^T = \begin{bmatrix} 1 & \cdots & 1 \\ z_1^1 & \cdots & z_K^1 \\ z_1^2 & \cdots & z_K^2 \\ \vdots & \ddots & \vdots \\ z_1^{L-1} & \cdots & z_K^{L-1} \end{bmatrix} \begin{bmatrix} c_1 & & \\ & \ddots & 0 \\ 0 & & c_K \end{bmatrix} \begin{bmatrix} 1 & z_1^1 & z_1^2 & \cdots & z_1^{R-1} \\ \vdots & \vdots & \vdots & \cdots & \vdots \\ 1 & z_K^1 & z_K^2 & \cdots & z_K^{R-1} \end{bmatrix}, \tag{2.43}$$

where the z_k are also called the generators and the superscript ^{T} denotes the transpose of the matrix. These poles form a diagonal matrix $\mathbf{Z} = \mathrm{diag}\{z_1, z_2, \ldots, z_K\}$. The goal is to obtain the poles z_k that link to axial wavenumbers. It can be noted that the matrix $\mathbf{S}$ (resp. $\mathbf{T}$) possesses the shift-invariance property:

$$\widehat{\mathbf{S}}_{\uparrow} = \widehat{\mathbf{S}}_{\downarrow}\mathbf{Z}, \tag{2.44}$$

where the up (down) arrow placed behind a matrix represents the deletion of the top (bottom) row of the considered matrix.

In the absence of noise, $\mathbf{H}$ can be decomposed as

$$\mathbf{H} = \begin{bmatrix} \widehat{\mathbf{U}} & \mathbf{U_0} \end{bmatrix} \begin{bmatrix} \widehat{\mathbf{\Sigma}} & 0 \\ 0 & \mathbf{\Sigma}_0 \end{bmatrix} \begin{bmatrix} \widehat{\mathbf{V}}^H \\ \mathbf{V}_0^H \end{bmatrix}, \tag{2.45}$$

where the bottom right corner of the singular values matrix $\mathbf{\Sigma}_0$ is null and the SVD of $\mathbf{H}$ reduces to the product $\widehat{\mathbf{U}}\widehat{\mathbf{\Sigma}}\widehat{\mathbf{V}}^{\mathbf{H}}$ consisting of the non-null part and the associated left and right singular vectors. The columns of $\mathbf{S}$ (resp. $\mathbf{T}$) span the same subspace as the columns of $\widehat{\mathbf{U}}$ (resp. $\widehat{\mathbf{V}^*}$). Therefore, $\widehat{\mathbf{U}}$ has also the shift-invariance property $\widehat{\mathbf{U}}_{\uparrow} = \widehat{\mathbf{U}}_{\downarrow}\mathbf{Z}$, so that the poles are obtained by the total least square (TLS) solution.

If noise is present, the truncated SVD is the best rank-K approximation of $\mathbf{H}$: $\widehat{\mathbf{H}}_{L\times R} = \widehat{\mathbf{U}}_{L\times K}\widehat{\mathbf{\Sigma}}_{K\times K}\widehat{\mathbf{V}}^{\mathbf{H}}_{K\times R}$. Here, K can be interpreted as the assumed number of present modes. Then, the equality in $\widehat{\mathbf{U}}_{\uparrow} = \widehat{\mathbf{U}}_{\downarrow}\mathbf{Z}$ does not hold any more. The total least square solution of the overdetermined set of linear equations $\widehat{\mathbf{U}}_{\uparrow} \approx \widehat{\mathbf{U}}_{\downarrow}\widetilde{\mathbf{Z}}$ is given by:

$$\widehat{\widetilde{\mathbf{Z}}} = -\mathbf{W}_{12}\mathbf{W}_{22}^{-1}, \tag{2.46}$$

where

$$\mathbf{W} = \begin{bmatrix} \mathbf{W}_{11} & \mathbf{W}_{12} \\ \mathbf{W}_{21} & \mathbf{W}_{22} \end{bmatrix} \tag{2.47}$$

is obtained from the SVD of the matrix $[\widehat{\mathbf{U}}_{\downarrow}\ \widehat{\mathbf{U}}_{\uparrow}]$:

$$[\widehat{\mathbf{U}}_{\downarrow}\ \widehat{\mathbf{U}}_{\uparrow}] \overset{SVD}{=} \mathbf{\Upsilon\Gamma W}^H. \tag{2.48}$$

Once $\widetilde{\mathbf{Z}}$ is estimated, its eigenvalues λ_k give an estimation of the signal poles z_k that links to axial wavenumbers. Finally the wavenumbers are computed:

$$k_{xk} = \frac{\ln \lambda_k}{\mathrm{i}\Delta x}, \tag{2.49}$$

where the natural logarithm result does not include other periodic solutions for the same reason as explained in the KT method.

Both methods effectively address the challenge of noisy signals. The KT method focuses on separating noise from the signal subspace by applying the Singular Value Decomposition (SVD) to a Hankel signal matrix. Its primary goal is to identify the

signal subspace that most accurately represents the observed data, and it has shown robustness to noise perturbation in applications such as impedance eduction in small ducts [17, 26]. In contrast, the HTLS method is specifically designed to manage noise more comprehensively by considering errors in both the signal and the matrix structure. The HTLS enhances the basic approach by using a Hankel matrix in conjunction with Total Least Squares to minimize errors across the signal and data matrix, thereby offering increased robustness in noisy environments. Both methods will be assessed in the simulated impedance eduction in Chapter 4.

2.3.2 Calculation of impedance

The second key step in the direct eduction of impedance is to calculate the liner impedance using a measured axial wavenumber k_x. This section first reviews the traditional method proposed by Jing et al. [15] for the '**single-liner** configuration,' where only the lower duct wall is lined. This method assumes a uniform mean flow and uses the Ingard–Myers boundary condition. Building on this foundation, we extend the method to a '**double-liner** configuration', where both the lower and upper walls are lined by the same material. In addition, we also deduce the solution for the unknown impedance when using different materials on two walls, one of which is known. Furthermore, to account for the effects of a parallel sheared mean flow, we introduce new solutions for determining the unknown impedance of the liner based on the Linearised Euler Equations for both configurations. These methods can be applied for either a single incident mode case or an incident multimodal field.

2.3.2.1 Uniform flow

For a uniform flow, the mode shape functions that satisfy Eq. (2.7) can be directly written as

$$\Psi_n(y) = a_n \cos(k_{yn} y) + b_n \sin(k_{yn} y), \tag{2.50}$$

where the transverse wavenumbers k_{yn} are given by the dispersion relation (see Eq. (2.11)):

$$k_{yn} = \sqrt{(k_0 - M k_{xn})^2 - k_{xn}^2}. \tag{2.51}$$

We first consider the traditional method that uses the single liner configuration where only the lower duct wall is treated. Substituting the above expression for Ψ_n into the Ingard–Myers condition (2.9) at $y = 0$, and into the hard-wall condition (2.8) at $y = H$, we obtain a closed-form expression for the specific impedance Z in terms of the mode wavenumbers [15]:

$$Z = \frac{\mathrm{i}(k_0 - M k_{xn})^2}{k_0 k_{yn} \tan(k_{yn} H)}. \tag{2.52}$$

Using the same assumption of flow, the method can be extended for the double liner configuration. The Ingard–Myers condition Eq. (2.9) is applied at both the upper and lower walls, with the assumption that they have the same impedance. This yields the following quadratic equation:

$$Q^2 - 2Q k_{yn} \cot(k_{yn} H) - k_{yn}^2 = 0\,, \quad \text{with } Q = \frac{(k_0 - M k_x)^2}{\mathrm{i} k_0 Z}\,. \tag{2.53}$$

The solutions for the impedance are

$$Z = \frac{(k_0 - Mk_{xn})^2 \sin(k_{yn}H)}{\mathrm{i}k_0 k_{yn}[\cos(k_{yn}H) \pm 1]}. \tag{2.54}$$

This expression contains two types of solutions distinguished by "$\pm$" in the denominator, in which "$-$" corresponds to symmetric modes and "$+$" to antisymmetric modes. The choice is completely controlled by the symmetry of the incident mode. Indeed, when the upper and lower walls are lined with the same material, the total sound field will retain the symmetry of the incident mode. As a consequence, if the incident mode is antisymmetric, then one should use the sign "$+$" in the expression above.

Note that Spillere et al. also provide an expression to calculate the impedance for both configurations (see Eq. (6) in [64]). However, their expression for the double-liner configuration is only applicable to symmetric acoustic fields. The present result in Eq. (2.54) is equally applicable to both types of incident modes.

Furthermore, for a configuration with two different liners, when the specific impedance of one liner is known as Z_1 at $y = 0$, the other liner impedance Z_2 at $y = H$ can be written as

$$Z_2 = \frac{(k_0 - Mk_{xn})^2[(k_0 - Mk_{xn})^2 \sin(k_{yn}H) - \mathrm{i}k_0 k_{yn} Z_1]}{\mathrm{i}k_0 k_{yn}^2 Z_1 \sin(k_{yn}H) + k_{yn}\cos(k_{yn})(k_0 - Mk_{xn})^2}. \tag{2.55}$$

When $Z_1 = Z_2$, Eq. (2.55) reduces to Eq. (2.54).

2.3.2.2 Shear flow

With shear flow, it is not possible to write a closed-form expression for the wall impedance like Eq. (2.52) or Eq. (2.54). Instead, the relation between Z and the axial wavenumber k_x remains implicitly defined by the governing equations Eq. (2.30). To compute the impedance Z associated to a given k_x, one approach is to use a non-linear optimisation method to iteratively adjust Z until one of the duct modes in the lined section has the expected wavenumber k_x. This approach requires solving the model presented in Section 2.2.3 many times, which can be computationally expensive [19]. Here, we reuse and extend the method from [20] to compute the wall impedance in a single calculation. In contrast with the shear flow model for the whole duct, Eq. (2.30) are now solved only in the lined section, for a known k_x and with modified boundary conditions.

For the case of a single liner on the lower wall $y = 0$, two boundary conditions are imposed on the hard wall (at $y = H$), while no condition is imposed on the lined wall. More specifically, the normal displacement is set to zero on the upper wall, $\xi(y = H) = 0$, which is consistent with a rigid surface, and pressure is also prescribed on that wall: $p(y = H) = 1$. These boundary conditions are sufficient to obtain a well-posed differential equation. This model is solved numerically with the same pseudo-spectral method as in Section 2.2.3. It is then straightforward to compute the impedance of the lined wall at $y = 0$:

$$Z = \frac{-p(0)}{\mathrm{i}\omega\rho_0 c_0 \xi(0)}. \tag{2.56}$$

This expression shows that the value of Z is independent of the amplitude of the sound field. This justifies the fact that $p(H)$ can be set to any non-zero value.

The procedure has to be modified for the case where the two walls are lined with the same impedance. Two separate solutions are computed. The solutions $p_1(y)$ and $\xi_1(y)$ satisfy $p_1(H) = 1$ and $\xi_1(H) = 0$, while the solutions $p_2(y)$ and $\xi_2(y)$ satisfy $p_2(H) = 0$ and $\xi_2(H) = 1$. We then construct a linear combination of these solutions:

$$p(y) = c_1 p_1(y) + c_2 p_2(y), \tag{2.57a}$$
$$\xi(y) = c_1 \xi_1(y) + c_2 \xi_2(y), \tag{2.57b}$$

so that this new solution has the same impedance at the two walls. In other words, we seek the constants c_1 and c_2 such that

$$\rho_0 c_0 Z = \frac{p(H)}{\mathrm{i}\omega\xi(H)} = \frac{p(0)}{-\mathrm{i}\omega\xi(0)}. \tag{2.58}$$

This expression reduces to a quadratic equation for Z:

$$\omega^2 \xi_1(0)\rho_0^2 c_0^2 Z^2 - i\omega[\xi_2(0) + p_1(0)]\rho_0 c_0 Z - p_2(0) = 0\,. \tag{2.59}$$

One of the two roots corresponds to a symmetric solution, while the other corresponds to an antisymmetric solution. Using the same argument as for the uniform flow method, it is easy to identify the correct value of Z based on the symmetry of the incident mode.

2.4 Conclusions

This chapter provides the methodological foundations of this thesis. First, the MAINE Flow facility is described featuring a large cross-section, which involves a multimodal acoustic field at high flow velocities. By utilizing mode synthesis and mode detection, the facility can measure acoustic liner properties separately for each cut-on acoustic mode, enabling a more detailed assessment of the acoustic treatment behaviour.

Next, multimodal models for acoustic propagation in a multi-segment duct with uniform or shear flow have been described. These models serve as a simulation tool to mimicking the acoustic propagation in the presence of airflow within a duct like the MAINE Flow facility. The models use a pseudo-spectral method for the mode calculation in each segments and a mode-matching approach to account for boundary discontinuities in the axial direction. They provide simulated acoustic fields in the flow duct, which will be used for a numerical study of shear flow effects and for simulated impedance eduction in the next chapters.

Regarding the direct impedance eduction, the traditional algorithm [15] is reviewed, which considers the single-liner configuration using a uniform flow assumption and the Ingard–Myers boundary condition. Based on that, the direct method is developed and extended for the double-liner configuration with either uniform or shear mean flow. The double-liner configuration is proposed to improve the impedance eduction results, which will be discussed in Chapter 4. In case of shear flow, acoustic vertical displacement ξ is considered as the variable instead of acoustic vertical velocity v in [20], in order to avoid the numerical issues associated with a flow profile that has infinite derivative at the boundary. In addition, extending the direct method to shear flow cases significantly reduces computation

costs compared to the inverse method that accounts for the flow shear. In the following, these methods are used to study the effects of shear flow on the calculation of impedance in Chapter 3 and to conduct numerical and experimental impedance eduction in the subsequent chapters.

Chapter 3

Parametric study of the shear flow effects

This chapter presents a parametric study of the effects of mean flow shear, using the multimodal propagation models and methodologies described in the previous chapter. This study considers flow profile parameters including the boundary layer thickness, the flow velocity and the propagation direction. In addition, both single- and double-liner configurations are included. The physical parameters is described in Section 3.1 before considering three aspects of the shear effects. First, Section 3.2 investigates the influence of the mean flow shear on the acoustic propagation in terms of the acoustic mode wavenumbers. Then, Section 3.3 focuses on the validity of the uniform flow assumption used when calculating the wall impedance from the knowledge of an acoustic axial wavenumber in the presence of flow shear. Finally, Section 3.4 explores how the presence of the mean flow shear affects the liner performance, i.e. the acoustic transmission.

3.1 Framework of the parametric study

3.1.1 Physical parameters

The following parametric studies are presented using non-dimensional parameters, based on the reference values ρ_0, c_0 and H. For instance, the angular frequency ω is converted into the Helmholtz number $He = \omega H/c_0$. This Helmholtz number will vary between 0.1 and 16, which covers a wide range of experimental facilities. For instance, for a small duct facility ($H = 4\,\text{cm}$ as in [116]) operating between 300 and 3000 Hz, the Helmholtz number varies roughly between 0.22 and 2.2. In contrast, for a large duct facility ($H = 28\,\text{cm}$ in the MAINE Flow [12]) operating in the same frequency range, He varies between 1.6 and 15.5 approximately.

A constant value $Z = 1 - \mathrm{i}$ is used for the liner impedance in this chapter. It has been checked that conclusions remain the same for other choices, including frequency dependent impedance functions $Z = 1 - \mathrm{i}\cot(k_0 h_{\text{cav}})$, with h_{cav} being the depth of the liner cavity, and rigid wall case. For the sake of brevity, these results are not shown here.

3.1.2 Velocity profiles

The velocity profile $u_0(y)$ of the studied shear flow follows an inverse power law:

$$\frac{u_0(y)}{u_{0\max}} = \begin{cases} (y/\delta)^{1/n}, & \text{for } 0 \le y \le \delta, \\ 1, & \text{for } \delta \le y \le 1-\delta, \\ [(1-y)/\delta]^{1/n}, & \text{for } 1-\delta \le y \le 1, \end{cases} \tag{3.1}$$

where have been introduced the boundary layer thickness δ, the power n and the maximum velocity $u_{0\max}$. For this profile, the relationship between the average and maximum velocity can be deduced:

$$u_{0\text{ave}} = \left(1 - \frac{2}{n+1}\frac{\delta}{H}\right) u_{0\max} \tag{3.2}$$

To study the effect of the boundary layer on sound propagation, it is recommended to use the displacement boundary layer thickness δ_1 defined in Eq. (3.3) to characterize the boundary layer [117]:

$$\delta_1 = \int_0^{H/2} \left[1 - \frac{u_0(y)}{u_{0\max}}\right] \mathrm{d}y. \tag{3.3}$$

For the profile defined by Eq. (3.1), it reads $\delta_1 = \delta/(n+1)$. The present parametric study will therefore focus on varying δ_1 instead of δ. Also, instead of defining directly the order n of the power law, the shape factor θ, which is the ratio of the displacement thickness to the momentum thickness of the boundary layer, is used. The momentum thickness of the boundary layer is defined by [118]:

$$\delta_2 = \int_0^{H/2} \frac{u_0(y)}{u_{0\max}} \left[1 - \frac{u_0(y)}{u_{0\max}}\right] \mathrm{d}y. \tag{3.4}$$

Thus, for the profile Eq. (3.1) we have $\theta = 1 + 2/n$. For the rest of the study, the shape factor is fixed to $\theta = 1.55$, which is typical of turbulent boundary layers [118]. Note finally that when comparing results obtained with a uniform flow and a shear flow, the same average Mach number M_{ave} will be used for the two cases.

The velocity profile given in Eq. (3.1) implies discontinuities of the velocity gradient at $y = \delta$ and $y = 1 - \delta$. This can be detrimental to the accuracy of the spectral method used in this thesis. A simple way to mitigate this is to smooth the profile by introducing blending functions that permit quick but smooth transitions from one part of the profile to the next. The following gives the detailed definitions of these blending functions, but note that this smoothing has a negligible effect on the flow properties δ_1, θ and M_{ave}.

The velocity profile is composed of three parts, each using one of the following functions:

$$f_1(y) = u_{0\max}(y/\delta)^{1/n}, \tag{3.5a}$$
$$f_2(y) = u_{0\max}, \tag{3.5b}$$
$$f_3(y) = u_{0\max}[(H-y)/\delta]^{1/n}, \tag{3.5c}$$

where f_1 and f_3 represent the boundary layers and f_2 represents the central region. To construct a smoothly varying profile $u_0(y)$ the three functions defined above are combined with blending functions $\tilde{b}_i(y)$:

$$u_0(y) = \sum_{i=1}^{3} f_i(y)\tilde{b}_i(y)\ . \tag{3.6}$$

The blending functions are defined as follows:

$$\tilde{b}_i(y) = \left\{b_i(y) - \min_{0\le y\le H}[b_i(y)]\right\} \Big/ \left\{\max_{0\le y\le H}[b_i(y)] - \min_{0\le y\le H}[b_i(y)]\right\}\ , \tag{3.7}$$

with

$$b_1(y) = g(\delta - y)\,, \quad b_2(y) = g(y - \delta)g(H - y - \delta)\,, \quad b_3(y) = g(y + \delta - H)\,, \tag{3.8}$$

and

$$g(y) = \frac{1}{2}\left[1 + \tanh\left(\frac{y}{d}\right)\right]\,. \tag{3.9}$$

The parameter d controls how quickly the functions b_i transition from 0 to 1. The scaling introduced in Eq. (3.7) ensures that the blending functions $\tilde{b}_i(y)$ vary exactly between 0 and 1. With the definition (3.6), the velocity profile $u_0(y)$ and all its derivatives are continuous. An example of blending functions is shown in Figure 3.1 where each blending function can be seen to vary smoothly, and quickly, between 0 and 1 at $y = \delta$ and $y = H - \delta$.

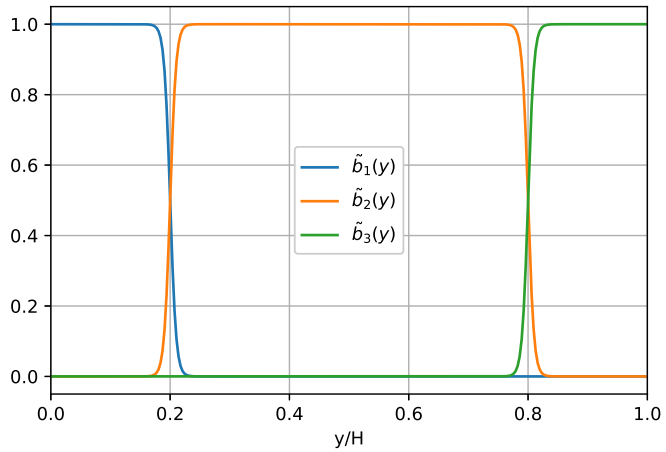

Figure 3.1: Blending functions $\tilde{b}_i(y)$ as defined by Eq. (3.7) for $\delta/H = 0.2$ and $d/H = 0.01$.

3.2 Acoustic propagation

First, the influence of the mean flow shear on the acoustic propagation is studied, by looking at the duct mode wavenumbers. These wavenumbers are calculated here for uniform flows and for shear flows using the methods introduced in Section 2.2.2 and 2.2.3 of Chapter 2.

3.2.1 Effects of the displacement thickness

Here, the displacement thickness δ_1 is varied between 0.01 and 0.1, which corresponds to 1% and 10% of the duct height, respectively. This range of values are based on data obtained in several facilities with different duct heights and Mach numbers [22]. The mean flow velocity is kept constant as $M_{\text{ave}} = \pm 0.3$, with the sign $+$ (resp. $-$) corresponding to the acoustic wave propagating downstream with the flow (resp. upstream against the flow). The velocity profiles are shown in Figure 3.2.

Figure 3.3 shows the axial wavenumbers $k_{x,\text{u}}$ and $k_{x,\text{s}}$ calculated respectively for a uniform flow or a shear flow with various boundary layer thicknesses in the single-liner case. For the first mode k_{x1} corresponding to the plane wave in the hard-wall

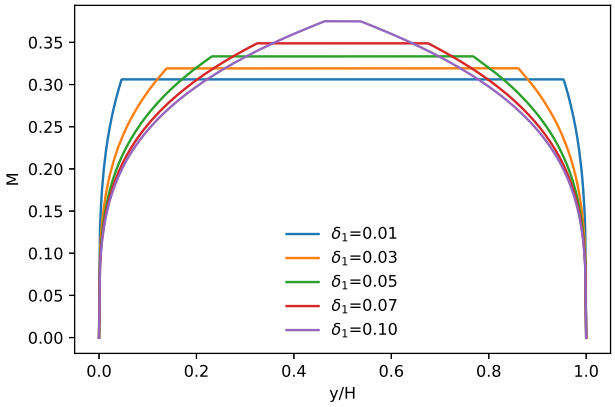

Figure 3.2: Examples of the velocity profiles given by Eq. (3.1) for various displacement thicknesses δ_1, with $M_{\text{ave}} = 0.3$ and $\theta = 1.55$.

duct, shown in Figure 3.3(a), the linear scaling of the axial wavenumber with the frequency is clearly visible. The variation of the wavenumber with δ_1 is visible for the imaginary part but difficult to assess for the real part. For the second mode k_{x2} displayed in Figure 3.3(b), the wavenumbers otained for the uniform flow and for the shear flow align closely, except for the imaginary part at $He < 2$. The insets shows variation of the wavenumber with δ_1, with a trend similar to k_{x1}. Nevertheless, it is not convenient to evaluate in this way the discrepancies over the total frequency range.

It is therefore preferable to plot the differences $k_{x,\text{s}} - k_{x,\text{u}}$ between the wavenumbers in order to investigate the shear flow effects, as shown in Figure 3.4. In the following, only the first mode k_{x1} is shown, but the same conclusions can be drawn for the other modes. First, it can be seen that the differences between the wavenumbers computed for uniform and sheared flows increase systematically with the boundary layer thickness δ_1. For downstream propagation and in the single-liner framework, see Figure 3.4(a), the difference between the uniform and shear flow cases is negligible when $He \lesssim 5$. For higher frequencies, one can observe that $k_{x,\text{s}}$ diverge more significantly from $k_{x,\text{u}}$. For the upstream propagation, shown in Figure 3.4(b), the differences on the real part of the wavenumber are larger than for the downstream case, but the differences on the imaginary part are much smaller and even tend to decrease at higher frequencies.

For the double-liner configuration, the trend in Figure 3.4(c) is similar to the single-liner case, with an increased difference at higher frequencies ($He \gtrsim 6$). Figure 3.4(d) shows that the differences for upstream propagation and a double-liner are also similar to the single-liner cases, but with larger effects at low frequencies.

The main trends to note in these results is that the effect of the boundary layer is more significant for larger δ_1 and for upstream sound propagation at high frequencies. In practice, it means that for experimental facilities with small duct ($He \lesssim 5$), the mean flow shear can be largely ignored, except for upstream propagation with two liners face to face. On the contrary, for larger ducts ($He \gtrsim 5$), the sheared mean flow should be taken into account for an accurate computation of the acoustic propagation with flow.

3.2.2 Effects of the mean flow velocity

To assess the influence of the flow velocity, we vary M_{ave} from 0.1 to 0.7 in both

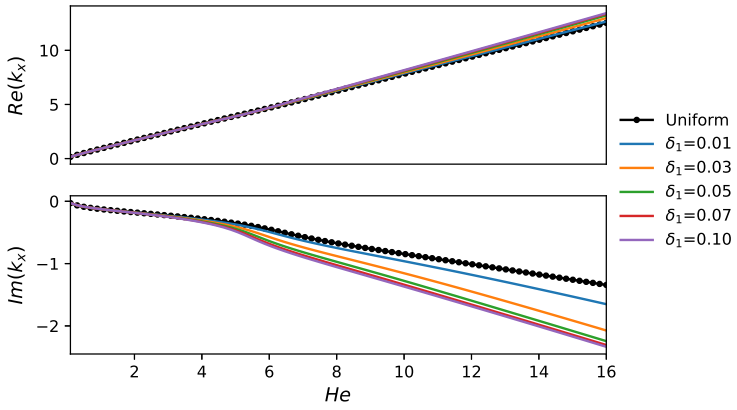

(a) k_{x1}

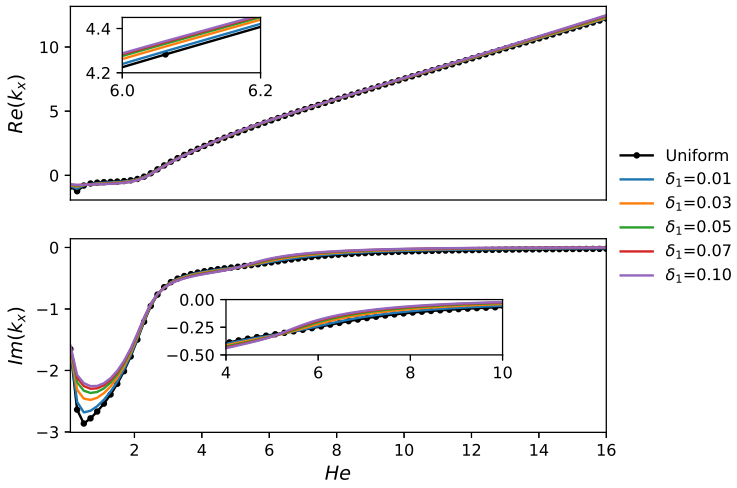

(b) k_{x2}

Figure 3.3: Axial wavenumbers calculated with a uniform flow or with a shear flow for various displacement thicknesses (mean flow velocity $M_{\text{ave}} = +0.3$) for the single-liner configuration.

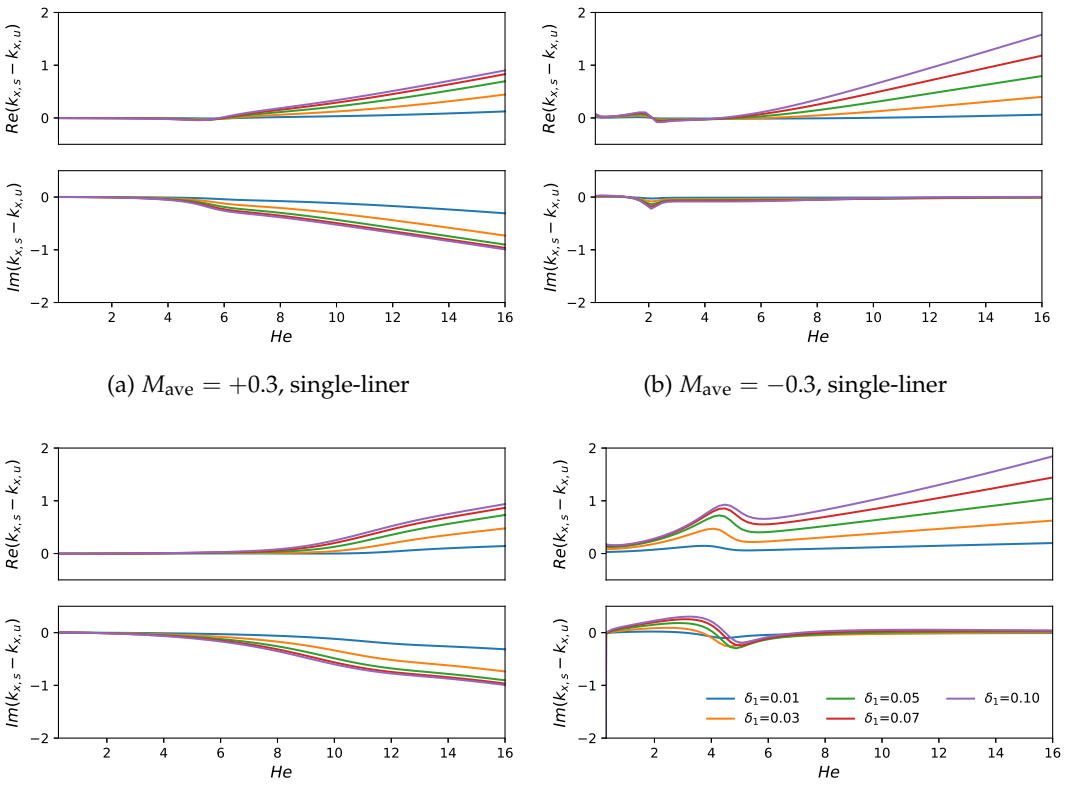

(a) $M_{\text{ave}} = +0.3$, single-liner

(b) $M_{\text{ave}} = -0.3$, single-liner

(c) $M_{\text{ave}} = +0.3$, double-liner

(d) $M_{\text{ave}} = -0.3$, double-liner

Figure 3.4: Differences between the axial wavenumbers $k_{x,\text{s}} - k_{x,\text{u}}$ obtained with a uniform or sheared flows as a function of the Helmholtz number He. (a,b): single-liner configuration. (c,d): double-liner configuration.

directions. The boundary layer thickness δ_1 is set to 0.05, which is a typical value in experiments [118].

In Figure 3.5, the differences in wavenumbers $k_{x,\mathrm{s}} - k_{x,\mathrm{u}}$ follow a similar trend for both the single- and double-liners. For downstream propagation ($M_{\mathrm{ave}} > 0$), shown in Figure 3.5(a) and 3.5(c), the differences remain small when $He \lesssim 5$, similar to the previous section. However, the differences become significant for higher frequencies, and the increase in the mean flow velocity only impacts slightly the magnitude of the wavenumber differences. For upstream propagation ($M_{\mathrm{ave}} < 0$), as shown in Figure 3.5(b) and 3.5(d), the differences are much larger, even at low frequencies. In this case, there is a clear trend whereby increasing the mean flow speed increases the differences in wavenumber.

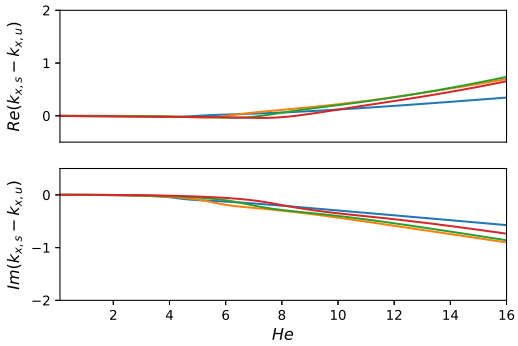

(a) Downstream propagation ($M > 0$), single-liner

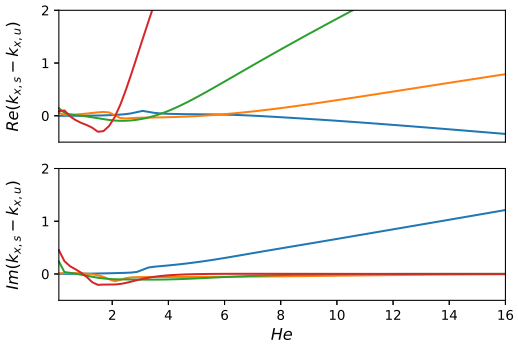

(b) Upstream propagation ($M < 0$), single-liner

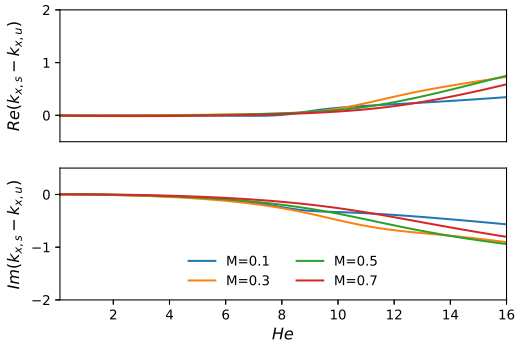

(c) Downstream propagation, double-liner

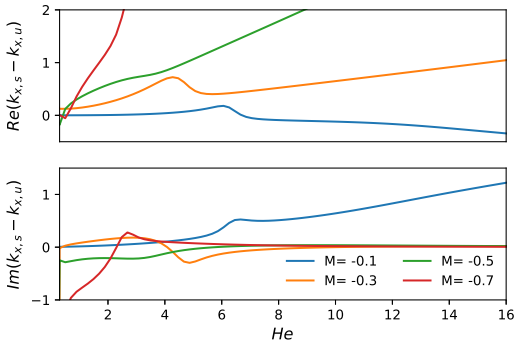

(d) Upstream propagation, double-liner

Figure 3.5: Differences between axial wavenumbers $k_{x,\mathrm{s}} - k_{x,\mathrm{u}}$ obtained with a uniform and sheared flow as a function of the Helmholtz number He. The mean Mach number M_{ave} is varied between 0.1 and 0.7 for both directions. (a,b): single-liner configuration. (c,d): double-liner configuration.

To summarise, this section shows that for downstream propagation, the mean flow shear has little influence on the acoustic propagation in small ducts and a more visible influence in large ducts. However, the effect of mean flow shear is much more important for upstream propagation (including in small duct) and even more so for the double-liner configuration. Also, the effects appear larger at higher frequencies.

3.3 Accuracy of the impedance calculation

We now discuss the validity of the uniform flow assumption traditionally used

when calculating the liner impedance given a set of wavenumbers. The parametric study still focuses on the influence of the boundary layer thickness and of the flow velocity, which vary in the same range as previously. The duct mode wavenumbers $k_{x,s}$ are first calculated in the lined section using the shear flow model from Section 2.2.3, for each case with various δ_1 and M_{ave}. These wavenumbers are then used as inputs for the two methods presented in Section 2.3.2 to calculate the impedance, either for a single-liner or a double-liner. Thus, this analysis excludes the influence of errors in the step of the wavenumbers estimation based on the pressure signals from the microphone array. The analysis compares the imposed value of the liner impedance and the calculated results Z_u or Z_s, where Z_u is the impedance obtained under the assumption of a uniform flow (Section 2.3.2.1), while Z_s is computed with the shear flow method (Section 2.3.2.2).

3.3.1 Effects of the displacement thickness

Figure 3.6 displays the difference between the calculated impedance and the imposed value, either for the uniform flow model or the shear flow model. The Mach number is $M_{ave} = \pm 0.3$, and the displacement thickness δ_1 varies between 0.01 and 0.1.

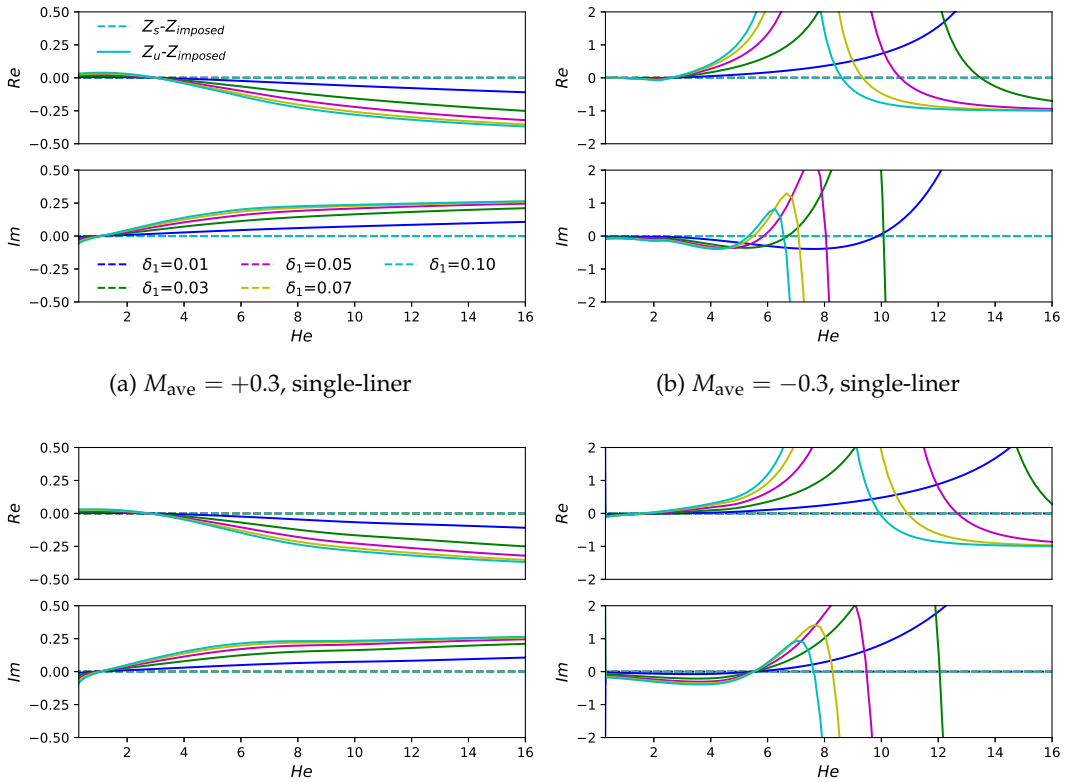

(a) $M_{ave} = +0.3$, single-liner

(b) $M_{ave} = -0.3$, single-liner

(c) $M_{ave} = +0.3$, double-liner

(d) $M_{ave} = -0.3$, double-liner

Figure 3.6: Differences between the calculated impedance and the imposed impedance $Z_u - Z_{imposed}$ (solid lines) and $Z_s - Z_{imposed}$ (dashed lines). δ_1 is varying from 0.01 to 0.1 and $M_{ave} = \pm 0.3$. (The vertical axis range is adjusted to improve the readability.)

The dashed lines in Figure 3.6 show that, in all the cases, there is no error on the calculated impedance when using the shear flow model with the correct δ_1 from Section 2.3.2.2. This is not surprising since the same propagation model with shear

flow Eq. (2.30) is used to calculate the axial wavenumber in the first place, and then to recover the impedance.

What is more interesting in Figure 3.6 is the quantitative assessment of the error introduced by assuming a uniform mean flow when calculating the impedance. The error on the impedance is steadily growing as we increase the boundary layer thickness. For Helmholtz numbers smaller than 3 or 4, the error on Z can be considered negligible. For downstream propagation and frequencies $He \gtrsim 5$ the error is larger, but the calculated impedance remains within 0.4 from the imposed value. However, for frequencies $He \gtrsim 5$, the discrepancies are much more important for upstream propagation (at least an order of magnitude larger). This indicates that the uniform flow assumption is only valid for small ducts and low frequencies. For large ducts, it is important to include the effect of the mean flow shear, especially when waves are propagating upstream.

3.3.2 Effects of the mean flow velocity

To assess the effect of the mean flow velocity on the impedance calculation, Figure 3.7 shows the error in the computed impedance as a function of the average Mach number M_{ave}.

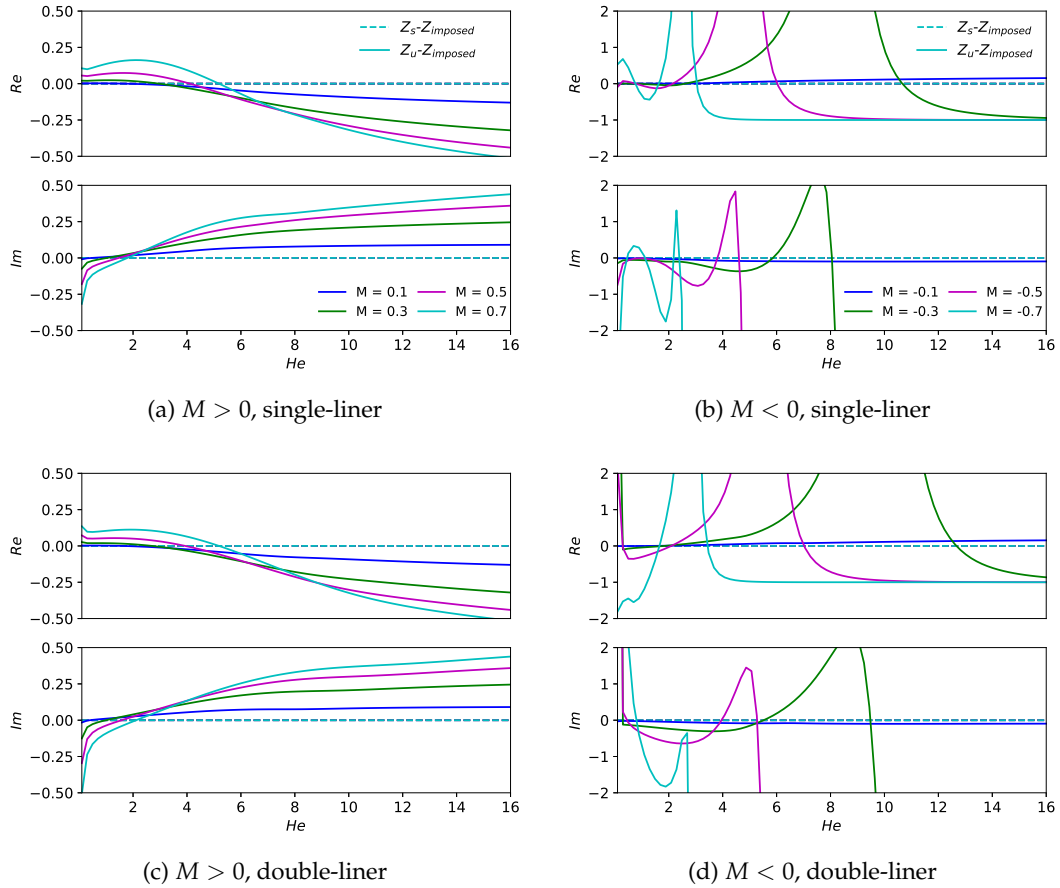

(a) $M > 0$, single-liner

(b) $M < 0$, single-liner

(c) $M > 0$, double-liner

(d) $M < 0$, double-liner

Figure 3.7: Differences between the calculated impedance and the imposed impedance $Z_{\text{u}} - Z_{\text{imposed}}$ (solid lines) and $Z_{\text{s}} - Z_{\text{imposed}}$ (dashed lines). M_{ave} is varying from 0.1 to 0.7 in both directions, $\delta_1 = 0.05$.

It is noted that the results are very similar in both liner configurations. Again, the results calculated using the shear flow method are in perfect agreement with the

imposed value, as expected. For the results calculated using the uniform flow assumption, the discrepancies with the imposed value tend to increase with the mean flow Mach number. For downstream propagation at low frequencies, these discrepancies can still be considered negligible, except for high flow velocities as $M_{\text{ave}} = 0.5$ and 0.7. However, the error increases steadily for higher frequencies to reach approximately 0.5. The situation is much worse for upstream propagation, where the error on the impedance is significantly larger at all frequencies (with the exception of the smallest flow velocity $M_{\text{ave}} = -0.1$ for which the error remains small at all frequencies).

Here, the same conclusions as in the previous section can be drawn. For small ducts and low frequencies, the effect of the mean flow shear can be safely neglected. For large ducts or high frequencies, the uniform flow assumption is inaccurate, especially for upstream propagation. This study reveals the importance of the mean flow shear for the impedance eduction in large ducts, which is never addressed in the previous studies. It is therefore recommended to use the shear flow method from Section 2.3.2.2 for accurate calculation of the wall impedance based on the axial wavenumber.

3.4 Acoustic transmission

We now consider the shear flow effects on the acoustic transmission through a lined section in a duct. The study is conducted for the 2D duct consisting of three sections depicted in Figure 2.3. The ratio of height and length of the lined section correspond to those of the MAINE Flow duct. The liner impedance remains the constant value $Z = 1 - \mathrm{i}$, at either one or two face-to-face walls. Then, the acoustic field in the whole duct is computed by using the propagation models in Section 2.2 for either a uniform or a sheared flow. The displacement boundary layer thickness δ_1 is varied from 0.01 to 0.10 and the average Mach number M_{ave} is varied from 0.1 to 0.7 in both directions, as in the previous sections.

This analysis focuses on the transmission coefficient of amplitude for each mode that propagates through the lined section of the duct. The transmission coefficient T is the ratio of the amplitudes of modes at the leading and trailing edges of the liner. The magnitude $|T|$ is presented and compared between the uniform and shear flow models. Additionally, acoustic transmission can also be expressed from an energy perspective, known as transmission loss. The analysis of transmission loss, which exhibits similar trends and conclusions, is detailed in Appendix C..

3.4.1 Validation in the no-flow case

First, it is expected that the two propagation models yields the same results in the absence of flow. Figure 3.8 shows the transmission coefficient in the case without flow for the single-liner configuration, using both uniform and shear flow models. For the sake of brevity, the results present the transmission coefficients only for the first 4 modes, which are representative and sufficient to demonstrate the conclusions. Each sub-figure displays the transmission coefficients $T_{m,i}$ between individual modes as a function of the Helmholtz number He, and $T_{m,i}$ remains 0 until the cut-off frequency of the mode of index $\min(m, i)$. It can be seen that the two sets of transmission coefficients are in agreement when there is no flow.

Figure 3.9 shows the transmission coefficient in the case without flow for the double-liner configuration. The agreement between the transmission coefficients

obtained by both models is great. In addition, it is shown that the transmission coefficient between odd and even indexed modes is 0, which is expected. Indeed, since the duct configuration is symmetric, the power of a mode is transmitted only to the modes with the same symmetry.

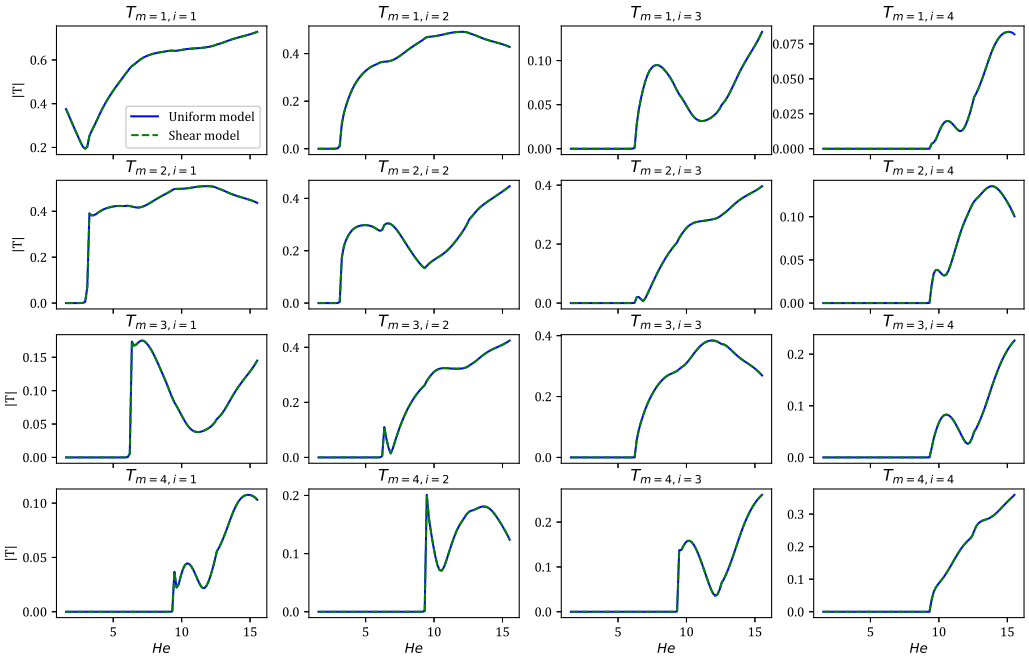

Figure 3.8: Transmission coefficient between each modes for the single-liner configuration with no flow using the uniform flow model (blue solid lines) and the shear flow model (green dashed lines). With i for incident modes and m for transmitted modes.

3.4.2 Effects of the displacement thickness

Figure 3.10 displays the transmission coefficients in the downstream propagation case with the single-liner configuration, for the uniform flow model and the shear flow model. The Mach number is $M_{\text{ave}} = \pm 0.3$, and the displacement thickness δ_1 varies between 0.01 and 0.1. In each sub-figure, the transmission coefficients for both the uniform and the shear flow models follow a similar trend as a function of He. The discrepancies between the two models appear modest for small He, and become more significant for larger He and for thicker boundary layers.

Figure 3.11 shows the transmission coefficients in the upstream propagation case with the single-liner configuration for both models. First, by comparing the sub-figures one by one for the two propagation directions displayed in Figure 3.10 and 3.11, the upstream propagation case generally shows larger difference between the two models. In most sub-figures, the results follow the same conclusion as in the downstream propagation case. Nevertheless, for some higher-order modes, such as $T_{3,1}$ $T_{4,1}$ $T_{3,3}$ and their inverses $T_{1,3}$ $T_{1,4}$, the trends for $T_{m,i}$ are different in the two models. Indeed, the trend for the shear flow model is following that of the uniform flow model at low frequencies, while the trend for thicker boundaries $\delta_1 \geq 0.03$ becomes different from the uniform flow model when $He > 10$. This implies that the effects of the mean flow shear is so important that the evolution of the T is completely changed, especially at high frequencies or in a large duct. Therefore, an

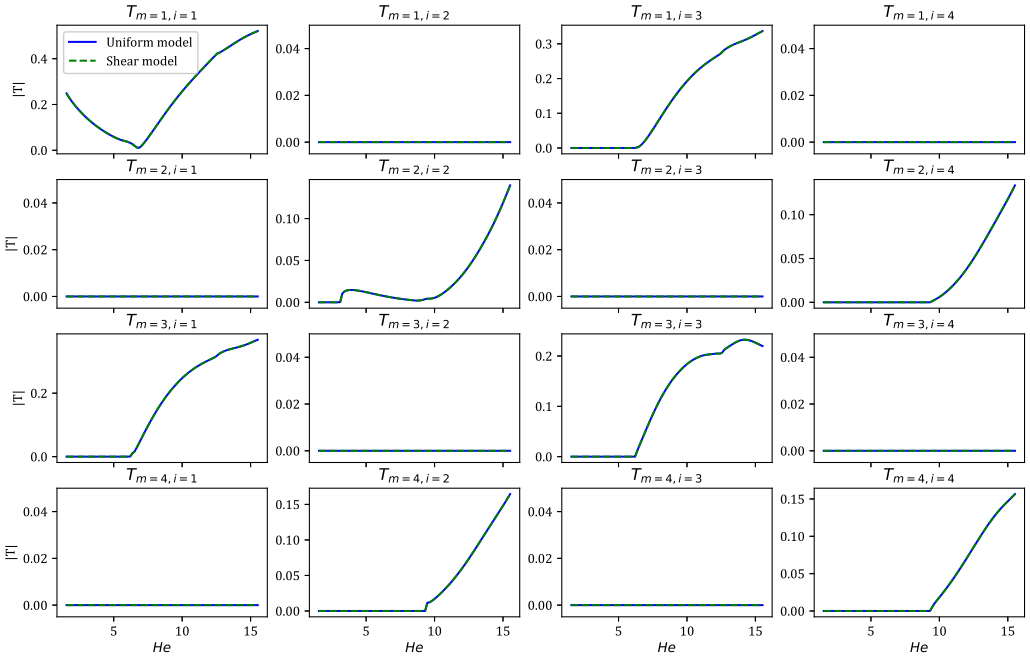

Figure 3.9: Transmission coefficient between each modes for the double-liner configuration with no flow using the uniform flow model (blue solid lines) and the shear flow model (green dashed lines). With i for incident modes and m for transmitted modes.

accurate model of the acoustic propagation with liner need to include considerations of shear flow, particularly when thick boundary layers are present.

Then, the transmission coefficients for the double-liner configuration in the downstream propagation case are shown in Figure 3.12. Since the transmission coefficient between modes with different symmetry, only sub-figures with non-zero $T_{m,i}$ are shown here. The discrepancies between $T_{m,i}$ for the two models increase with the boundary thickness δ_1, following a trend similar to that of the single-liner configuration. Furthermore, the values of T for antisymmetric modes (with even indexed) are smaller than those for symmetric modes (with odd indices), which implies that the attenuation of the former modes is greater.

In addition, Figure 3.13 presents the transmission coefficients for the double-liner configuration in the upstream propagation case. It clearly shows again that the effects of the mean flow shear increase with the boundary layer thickness. When comparing with the downstream propagation case in Figure 3.12, the shear flow results deviate from the uniform flow results by a much larger amount in the upstream propagation case. For example, in $T_{1,1}$, the deviation of the results with $\delta_1 = 0.1$ from the results of the uniform flow model is about 0.4 in the upstream propagation case, while it is 0.2 in the downstream case. In another example $T_{4,4}$, the results of the two models in the downstream propagation case are quite close, even with the maximum boundary layer thickness. However, in the upstream propagation case, including of a boundary layer with $\delta_1 = 0.05$ causes a significant decrease in T, from 0.20 to 0.05, or even lower at the largest He.

For the assessment of the performance of a liner, assuming a uniform flow leads to inadequate considerations of the flow effects and thus to the inaccurate predictions of the acoustic transmission. Thus, it is vital to account for the mean flow shear

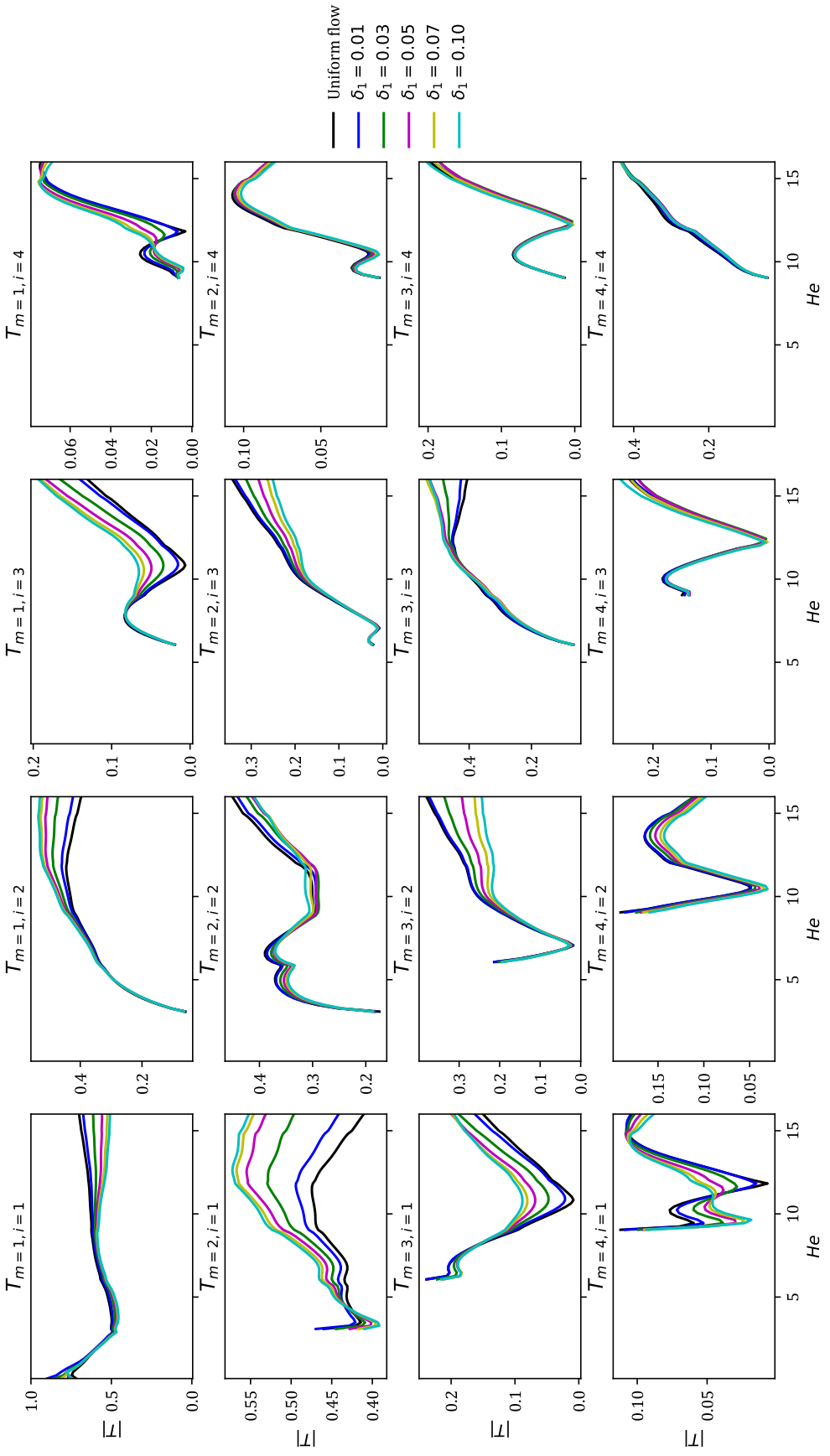

Figure 3.10: Transmission coefficients for the single-liner configuration in the downstream propagation case, with the uniform flow model (black lines) and the shear flow model (coloured lines). With δ_1 varying from 0.01 to 0.1, $M_{\text{ave}} = +0.3$.

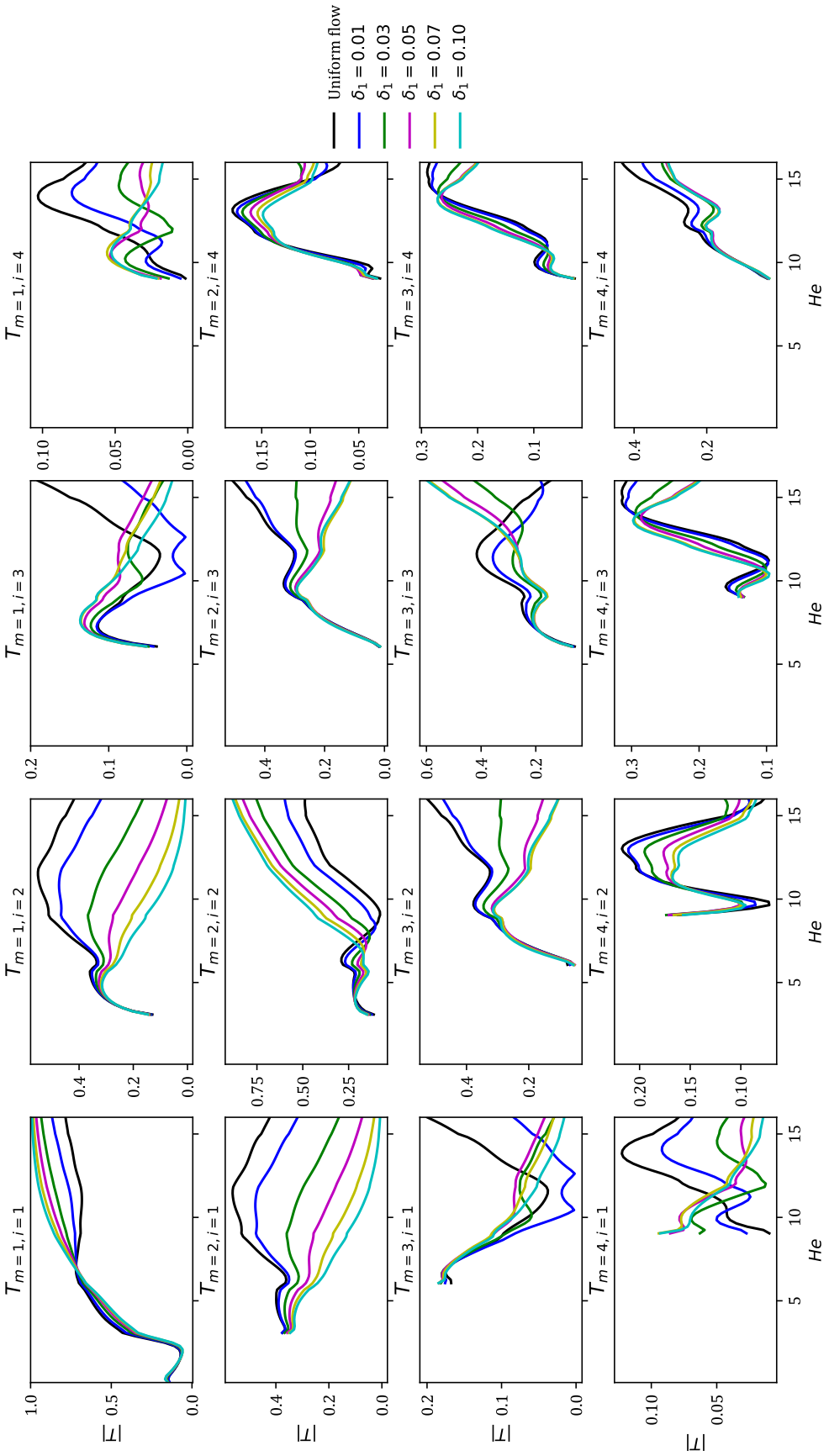

Figure 3.11: Transmission coefficients for the single-liner configuration in the upstream propagation case, with the uniform flow model (black lines) and the shear flow model (coloured lines). With δ_1 varying from 0.01 to 0.1, $M_{\text{ave}} = -0.3$.

in the propagation model for a duct like the MAINE Flow where many modes propagate. In particular, if the goal is to perform an optimization to determine the optimal impedance at a given frequency and a flow velocity, including shear is mandatory in order to achieve experimentally the expected performances.

3.4.3 Effects of mean flow velocity

This part studies the influence of the flow velocity on the discrepancies between the propagation models in terms of transmission coefficients. Since the results are very similar in both liner configurations, only the single-liner results are presented for brevity.

Figure 3.14 displays $T_{m,i}$ for the single-liner configuration in the downstream propagation case with $\delta_1 = 0.05$ and various M_{ave}. Note that the cut-off frequency of the higher-order modes varies with the Mach number. Hence, the curves for different flow velocities begin at different Helmholtz numbers. At the low velocity $M_{\text{ave}} = 0.1$, the transmission coefficients in blue near $He \simeq 9$ begin to show notable difference between uniform and shear flow models. When increasing the flow velocity, this effect becomes more pronounced and the discrepancies appear earlier (i.e. at lower He). When comparing the two models with a large Mach number, the transmission coefficients usually show a very different behaviour as a function of He.

Figure 3.15 exhibits $T_{m,i}$ in the upstream propagation case with single-liner configuration. The transmission coefficients, represented by the blue curves with $M_{\text{ave}} = -0.1$, exhibit similar trends between uniform and shear flow models, with discrepancies becoming more pronounced at higher He. For the other Mach numbers, the trends and values of results for two models are significantly different, particularly at high velocities $M_{\text{ave}} = -0.5$ and -0.7.

In summary, for small ducts, low frequencies, and low flow velocities, computing the transmission while neglecting the flow shear is acceptable. In contrast, for large ducts and high frequencies, the uniform flow assumption leads to acoustic transmission results that significantly deviate from those obtained by considering shear flow, particularly for upstream propagation or high flow velocities. In the latter cases, the effects of shear flow are critically important to account for in the calculation of the acoustic transmission.

3.5 Conclusions

To conclude, this chapter systematically assesses the effects of mean flow shear on the sound propagation in a 2D duct, on the direct eduction of impedance and on the acoustic transmission, by means of the models and methodologies described in the previous chapter. For the acoustic propagation, the modes are computed with both flow assumptions, and the acoustic wavenumbers are compared. In the context of direct impedance eduction, the impedance is computed starting from the same wavenumbers but using either the Ingard–Myers boundary condition or either the LEE where the mean flow shear is accounted for. Then, based on the propagation models for a 3-section (rigid-lined-rigid) duct, the transmission of the modal amplitudes and acoustic power in two flow cases are compared to provide more insights into the shear flow effects.

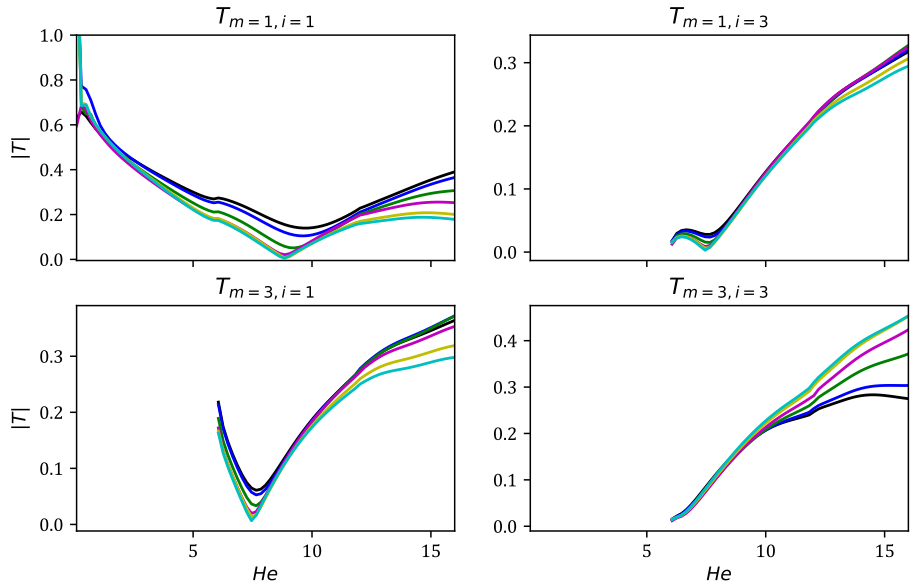

(a) Modes with odd indices.

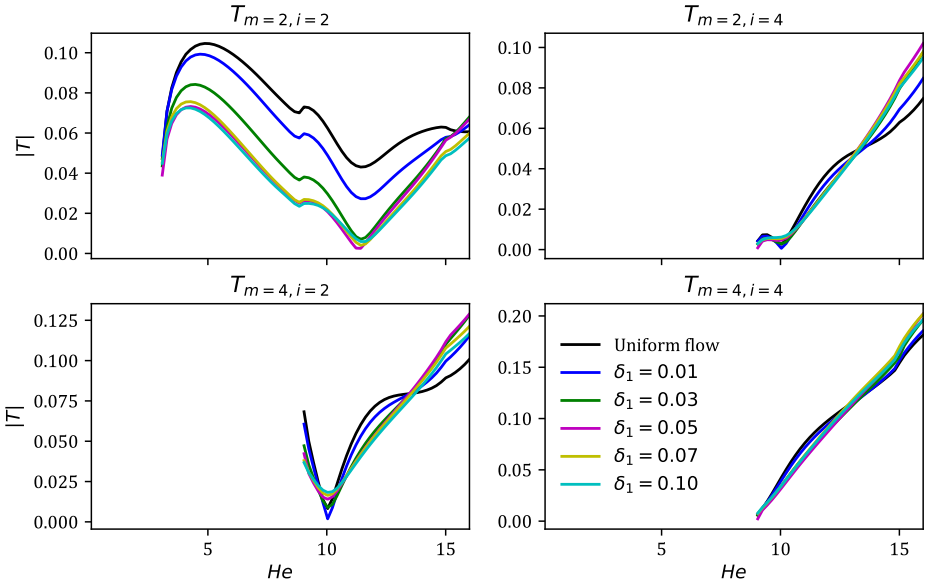

(b) Modes with even indices.

Figure 3.12: Transmission coefficients for the double-liner configuration in the downstream propagation case, with the uniform flow model (black lines) and the shear flow model (coloured lines). With δ_1 varying from 0.01 to 0.1, $M_{\text{ave}} = +0.3$.

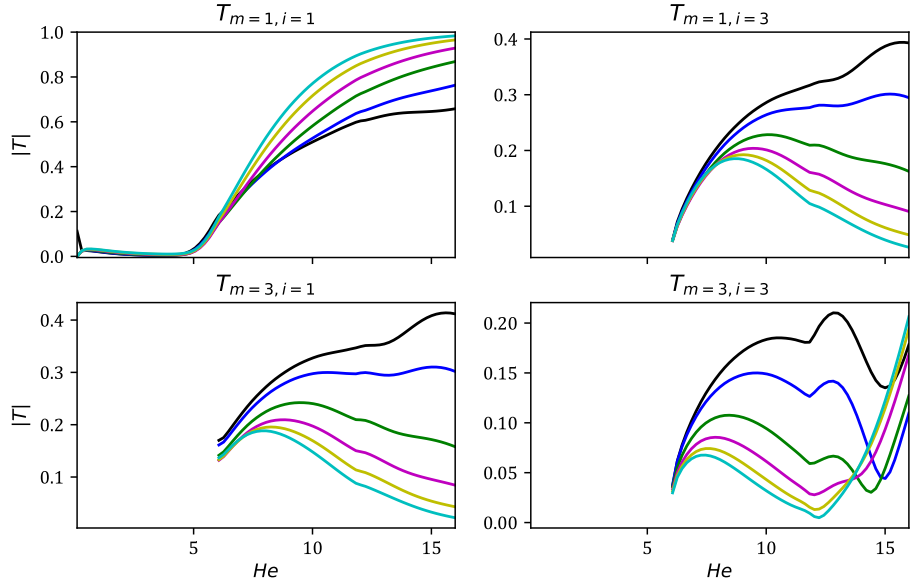

(a) Modes with odd indices.

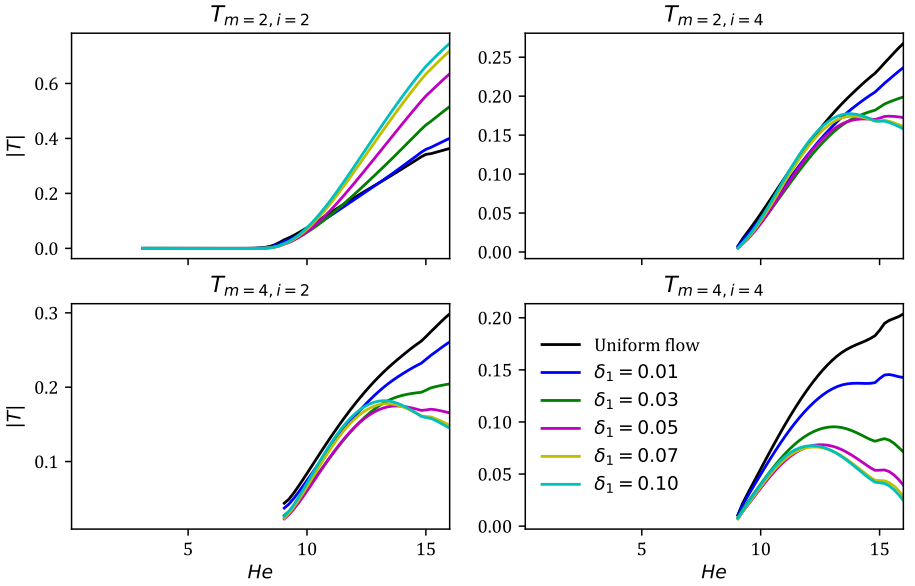

(b) Modes with even indices.

Figure 3.13: Transmission coefficients for the double-liner configuration in the upstream propagation case, with the uniform flow model (black lines) and the shear flow model (coloured lines). With δ_1 varying from 0.01 to 0.1, $M_{\text{ave}} = -0.3$.

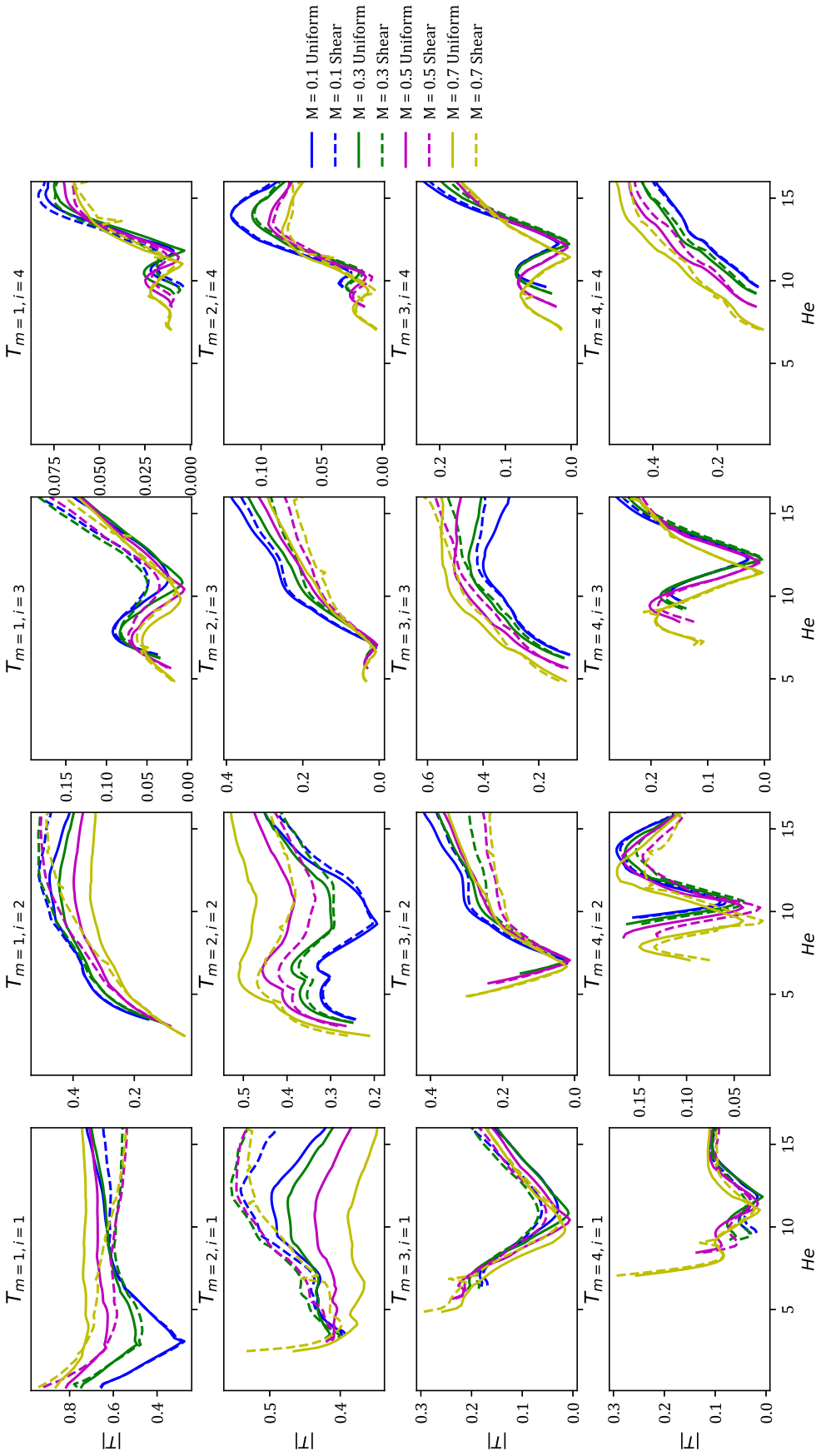

Figure 3.14: Transmission coefficients for the single-liner configuration in the downstream propagation case, with the uniform flow model (solid lines) and the shear flow model (dashed lines). With $\delta_1 = 0.05$ and $M_{\text{ave}} = +0.1$ (blue), $+0.3$ (green), $+0.5$ (magenta) and $+0.7$ (yellow).

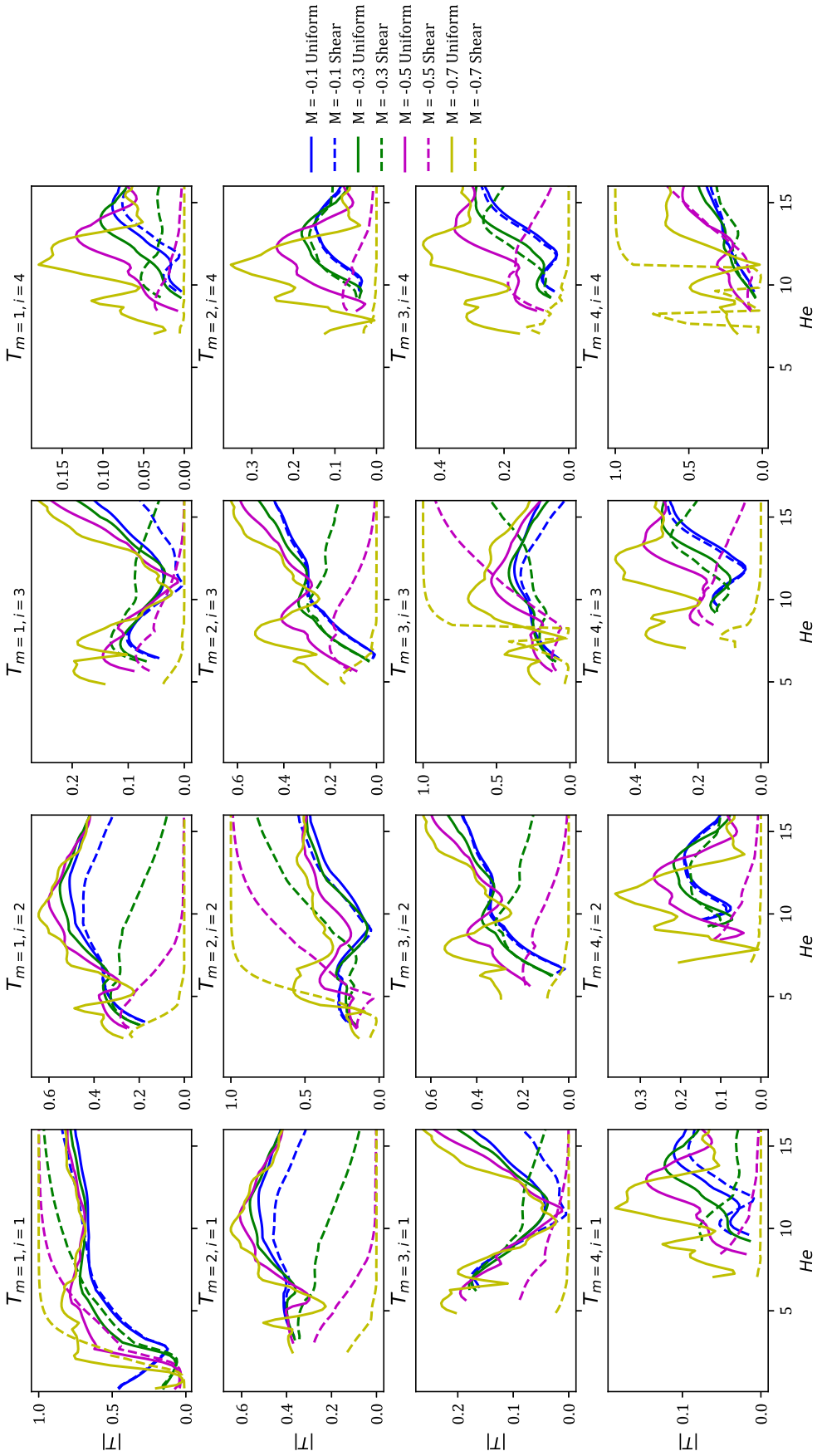

Figure 3.15: Transmission coefficients for the single-liner configuration in the upstream propagation case, with the uniform flow model (solid lines) and the shear flow model (dashed lines). With $\delta_1 = 0.05$ and $M_{\text{ave}} = -0.1$ (blue), -0.3 (green), -0.5 (magenta) and -0.7 (yellow).

Several existing studies have highlighted the significance of shear flow effects in similar aspects. Watson et al. [26] emphasised the necessity of incorporating boundary layer effects in impedance eduction at high flow velocities. Spillere et al. [18] demonstrated that considering the boundary layer in the boundary condition leads to improvements in the impedance eduction. Gabard [117] provided a detailed discussion on the impact of the boundary layer on liner attenuation, concluding that its effect is limited for downstream propagation but significant for upstream propagation. Gabard's analysis also revealed the unseparated link between the effects of boundary layer and the liner resistance, a factor not considered in this study.

This study examines the effects of shear flow in a relatively systematic manner, complementing and quantifying the extent of the effects under different parametric conditions. Moreover, previous studies have not considered the double-liner configurations, and the present study offers a supplement to this gap. The parametric study considers the influence of the Helmholtz number, the displacement boundary layer thickness, the Mach number, the direction of propagation and the liner configuration. The main conclusions are:

- The effects of the mean flow shear shows similar trends for both single- and double-liner configurations.
- The influence of the mean flow shear is more important for large Helmholtz numbers. While the uniform mean flow approximation is clearly valid for small ducts at low frequencies, the results presented here demonstrate that it is crucial to include the mean flow shear when considering large ducts and/or high frequencies.
- The shear flow effects are more important for upstream sound propagation, compared to downstream propagation.
- The validity of the uniform flow approximation decreases for high flow velocities and thick boundary layers. This is in line with the conclusion in [26].
- The presence of mean flow shear has shown non-negligible impact when considering the acoustic attenuation induced by a liner, in particular for high flow velocities and upstream propagation case. Indeed the acoustic transmission varies greatly depending on whether or not shear is taken into account, indicating that the uniform flow model may not be accurate enough to predict the acoustic field. Similar conclusions can be found in [117].
- For an optimization based on the acoustic transmission to determine the optimal impedance at a given frequency and a flow velocity, the consideration of shear is mandatory in order to achieve experimentally the expected performances.

As noted above, the shear flow effects have been shown important in the context of a large duct, for both single- and double-liner configurations. Part of these conclusions have been published in Journal of Sound and Vibration [119]. In the following chapter, we numerically simulate the impedance eduction process based on the pressure data in the lined section of the duct. The presence of noise is taken into account in order to evaluate the robustness of the eduction method for both liner configurations.

Chapter 4

Numerical simulation of impedance eduction

This chapter carries out numerically the impedance eduction using pressure signals from the acoustic field simulated by the multimodal models described in Chapter 2. The analysis considers several important aspects, including the wavenumber estimation methods, liner configurations, flow assumptions used in the impedance computations, noise in pressure signals, mode perturbations in the incident field, and the positioning of the microphone array.

The first step in direct impedance eduction involves the estimation of the wavenumbers. In this context, Section 4.1 compares the KT and HTLS methods described in Chapter 2 with respect to their accuracy and robustness within a traditional single-liner configuration. Subsequently, Section 4.2 presents numerical simulations to replicate the experimental process of direct impedance eduction in the MAINE Flow duct. These simulations assess the performance of impedance calculations using either the uniform or shear flow assumption for both single- and double-liner configurations. A detailed discussion follows, elucidating the mechanisms underlying the differences in the performance of both configurations. Furthermore, the influence of noise in the pressure signals is evaluated, and various configuration attempts are made to mitigate their impact on the eduction results. Lastly, Section 4.3 explores the effects of perturbations from modes other than the main incident mode on the eduction performance. The use of a 2-line microphone array is proposed in order to enhance the efficiency of the double-liner configuration in practical experiments.

4.1 Comparison between KT and HTLS method

This section compares both wavenumber estimation methods, KT and HTLS, for direct impedance eduction with the traditional single-liner configuration. Both methods can handle noisy signals by separating the noise subspace using Singular Value Decomposition (SVD), with the HTLS method further improving estimation robustness through the application of Total Least Squares. Both methods are used to retrieve the axial wavenumbers through the post-processing of the pressure signals from the microphones, which are simulated by the multimodal model described in Chapter 2. From the wavenumbers, the effective impedance of the liner can be calculated with the methods described in Section 2.3.2.

4.1.1 Simulations

4.1.1.1 Set-up

The comparison is conducted in relatively simple acoustic fields. A 2D small duct is considered with a height of 0.04 m, where shear flow effects can be neglected as per the analysis in Chapter 3. The configuration for the impedance eduction is comparable to that depicted in Figure 2.6(a), with microphones facing the liner, consistent with existing studies [15, 76]. The uniform flow model described in Section 2.2.2 is employed to simulate the acoustic pressure field, and subsequently, the uniform flow method outlined in Section 2.3.2.1 is used to calculate the liner impedance from the estimated wavenumbers. The axial wavenumber used here is the least attenuated, following the choice of previous studies, such as [15, 76].

A constant liner impedance $Z = 1 - \mathrm{i}$ is used as in the previous analysis. The frequency range is $[300, 3000]$ Hz with 30 Hz increments. Several lengths of the lined section are tested: $L_2 = 0.8, 0.6, 0.4$ and 0.2 m. A linear array with equally spaced microphones is located along the upper wall exactly opposing to the liner. The axial distance between two adjacent microphones is $\Delta x = 0.02$ m. To avoid the influence of discontinuities and scattering at the interfaces between the rigid and lined sections, the first measuring microphone is placed $\Delta x/2 = 0.01$ m into the lined section.

For the KT method, Renou et al. [76] recommend setting the column number L_{kt} of the Hankel matrix to 3/4 of the number N of signals. However, the implementation indicates that the truncation number M_t plays a more important role in achieving accurate results. When M_t is appropriately selected, variations in L_{kt} have minimal impact on the results. For the HTLS method, it is suggested in [120] that the column number L should be between 40% and 60% of N to ensure reliable results. This recommendation is tested and demonstrates good performance in this study. Therefore, the parameters for both methods are chosen to optimize the accuracy of the results, and their selected values are displayed in Table 4.1.

	KT			HTLS		
	N	L_{kt}	M_t	N	L	K
$L_2 = 0.8$ m	40	22	8	40	22	4
$L_2 = 0.6$ m	30	16	8	30	16	4
$L_2 = 0.4$ m	20	10	8	20	10	4
$L_2 = 0.2$ m	10	7	3	10	6	4

Table 4.1: Parameters used by the two wavenumber estimation methods for different liner lengths L_2.

4.1.1.2 Background noise

The presence of noise in the experiments, produced mainly by the turbulent boundary layer above the microphones, can significantly impact the impedance eduction results. In this study, the background noise is simulated by adding random signals to the simulated pressure signals calculated at the microphone positions. The noise signals are assumed to be uncorrelated between microphones and are generated with an amplitude following a normal distribution with mean value 0 and standard deviation σ. The random phase follows a uniform distribution in the range $[0, 2\pi]$. The Signal-to-Noise Ratio (SNR) is defined as $10\log_{10}(P_{\mathrm{in}}^2/\sigma^2)$, where P_{in} is

the pressure amplitude of the incident mode. In the results presented below, $P_{\text{in}} = 1$ and the SNR is readily adjusted by setting σ.

4.1.2 Comparison between KT and HTLS method

4.1.2.1 Results without noise

Firstly, the eduction process is conducted without noise. Figure 4.1 shows the educed impedance using the simulated acoustic pressure in the cases without flow and with flow at $M_{\text{ave}} = 0.3$ in both directions. The HTLS method provides a satisfactory agreement between the educed and the imposed impedances, except that the educed impedance for $L_2 = 0.2$ m in the presence of flow below 500 Hz deviates slightly from the imposed values. In contrast, the results for $L_2 = 0.2$ m using the KT method are completely different from the imposed value in all cases (see the insets in Figure 4.1). For longer liners, the educed impedance using the KT method shows a good agreement with the imposed values in the absence of flow, while discrepancies are observed in presence of flow at low frequencies ($<$500 Hz at $M_{\text{ave}} = -0.3$ and $<$1000 Hz at $M_{\text{ave}} = +0.3$) and they are larger when the liner length is increased.

According to the comparison above, the HTLS method generally demonstrates superior accuracy and robustness, even in cases involving very short liners where the sound attenuation is potentially weaker.

4.1.2.2 Results with noise

We now simulate the eduction process in the presence of noise using a SNR of 30 dB, which is close to the case in experiments. To obtain the mean and standard deviation of the educed impedance, 1000 realisations of the random noise are generated and the eduction process is applied to each one.

Figure 4.2 illustrates the educed impedance in the presence of noise and the flow with $M_{\text{ave}} = +0.3$ using the 0.8 m-long liner. The results show that the educed impedance obtained using the KT method deviates from the imposed value, whereas the HTLS method demonstrates a good agreement with the imposed impedance.

In summary, the HTLS method is more accurate and robust than the KT method, both in the case of poor acoustic attenuation and in the case with noise. Therefore, only the HTLS method will be used in the remainder of this thesis.

4.2 Simulation for MAINE Flow duct

In this section, we use numerical calculations to simulate the experimental process of direct impedance eduction in the context of the MAINE Flow duct, which features a larger cross-section. The pressure signals from the microphones are post-processed to estimate the axial wavenumbers, from which the liner impedance can be calculated with the methods proposed in Section 2.3.2.

4.2.1 Simulation settings

4.2.1.1 Set-up

To simulate a representative experimental setup, we use the parameters of the MAINE Flow facility introduced in Chapter 2 and modelled here as a 2D duct. The configuration is shown in Figure 4.3, where the duct height is 0.28 m and the lined

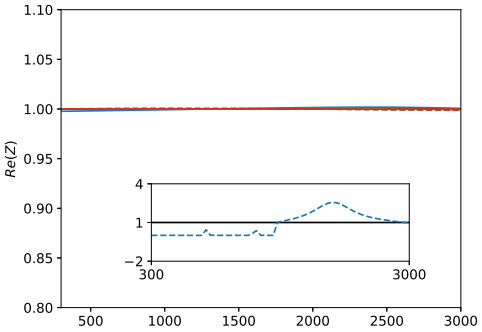

(a) Resistance, without flow.

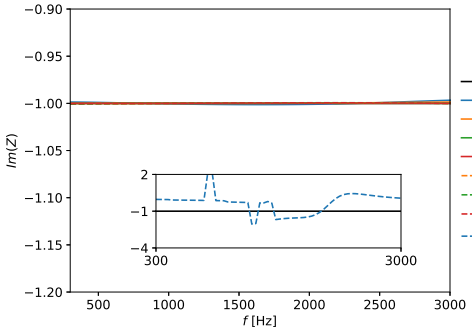

(b) Reactance, without flow.

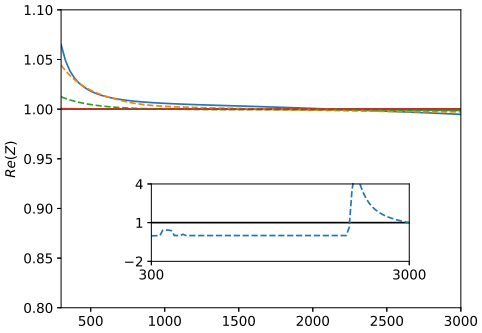

(c) Resistance, $M_{\text{ave}} = +0.3$.

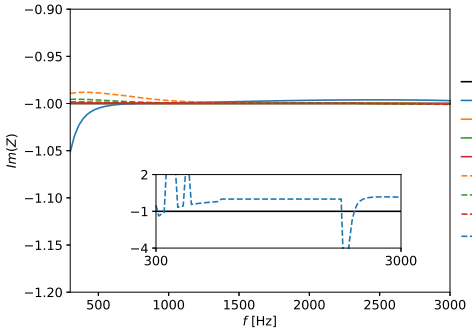

(d) Reactance, $M_{\text{ave}} = +0.3$.

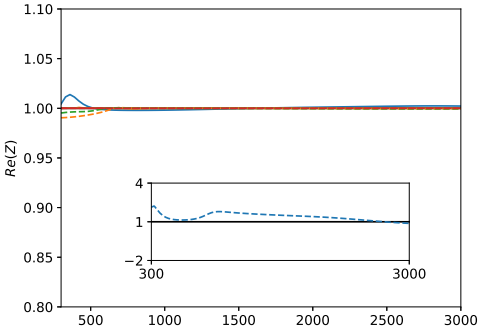

(e) Resistance, $M_{\text{ave}} = -0.3$.

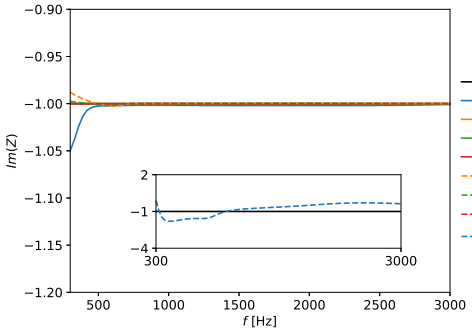

(f) Reactance, $M_{\text{ave}} = -0.3$.

Figure 4.1: Imposed impedance $Z = 1 - \mathrm{i}$ (black solid line) and educed impedance using wavenumbers estimated by the KT (dashed lines) or HTLS method (coloured solid lines) for a single-liner configuration within a duct of $H = 0.04$ m. The liner length is 0.2 (blue), 0.6 (orange), 0.4 (green) and 0.8 m (red). The pressure field is obtained with the uniform flow model using incident plane wave in the cases without flow ($M = 0$) and with flow ($M_{\text{ave}} = \pm 0.3$). Insets: enlarged y-axis range for the KT method with length of 0.2 m.

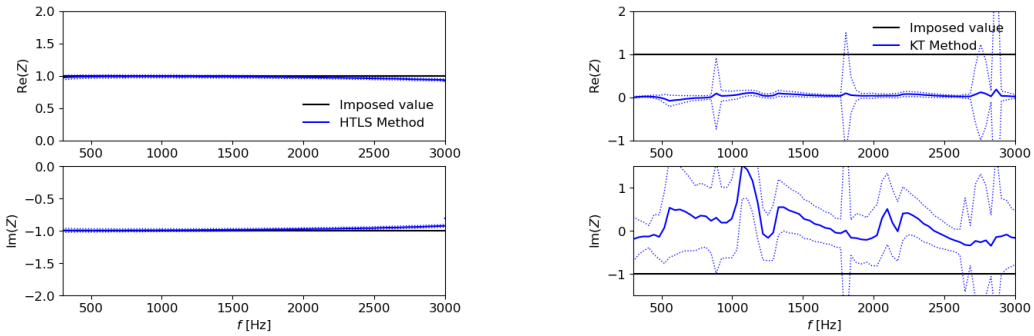

(a) HTLS method.

(b) KT method.

Figure 4.2: Imposed impedance $Z = 1 - \mathrm{i}$ (black solid line) and educed impedance using wavenumbers estimated by the KT (right) or HTLS method (left) for the single-liner configuration in presence of noise. The length of liner is 0.8 m. Blue solid line: mean value. Dashed lines: standard deviation. The pressure field is obtained by the uniform flow model using incident plane wave in the cases with flow ($M_{\mathrm{ave}} = +0.3$).

section has a length of 0.8 m. To acquire pressure signals for direct impedance eduction, a one-dimensional array of 40 evenly spaced flush-mounted microphones is positioned along the axis of the lined section, situated at $2/3H$ or $1/2H$ from the lower lined wall, following the configuration proposed in [23]. This position can avoid the pressure nodes of modes, especially for a configuration with symmetric boundaries, where the k-th zeros of the shape function of the n-th mode is located at $y = (2k-1)H/(2n)$. The distance between adjacent microphones is $\Delta x = 0.02$ m, with the first and last microphones placed 0.01 m into the lined section.

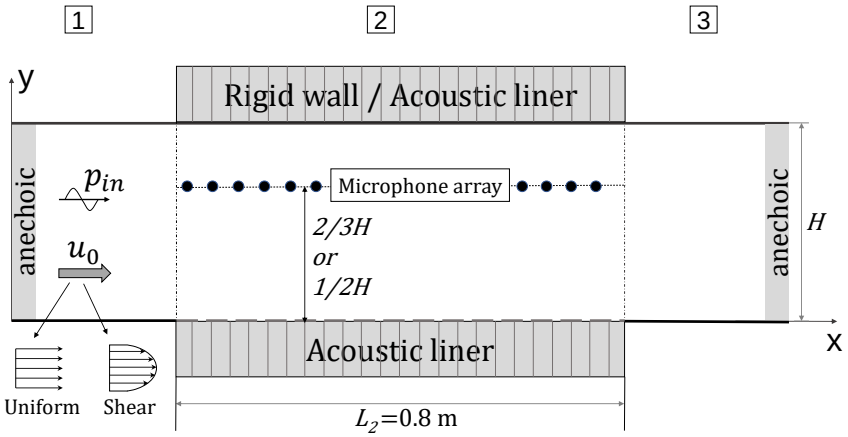

Figure 4.3: Schematic of the 2D MAINE Flow duct composed of three sections. The boundaries of the middle section are either lined-rigid or lined-lined. The incident wave p_{in} is sent from the left.

In the following, the liner is a Single Degree of Freedom (SDOF) liner with a specific impedance given by $Z(\omega) = 1 - \mathrm{i}\cot(k_0 h_{\mathrm{cav}})$. The first term models a perforated facing sheet with a constant resistance while the second term represents the acoustic reactance of a cavity of depth $h_{\mathrm{cav}} = 0.03$ m. Given this boundary condition,

the acoustic field is computed between 300 and 3000 Hz with 30 Hz increments using the numerical multimodal model with shear flow described in Section 2.2.3. The mean velocity profile is obtained in the dimension normal to the liner by fitting the inverse-power law profile in Eq. (3.1) to data measured using a Pitot tube at the mid-width in the cross–section of MAINE Flow [12]. Figure 4.4 shows the corresponding data points and the fitted velocity profile.

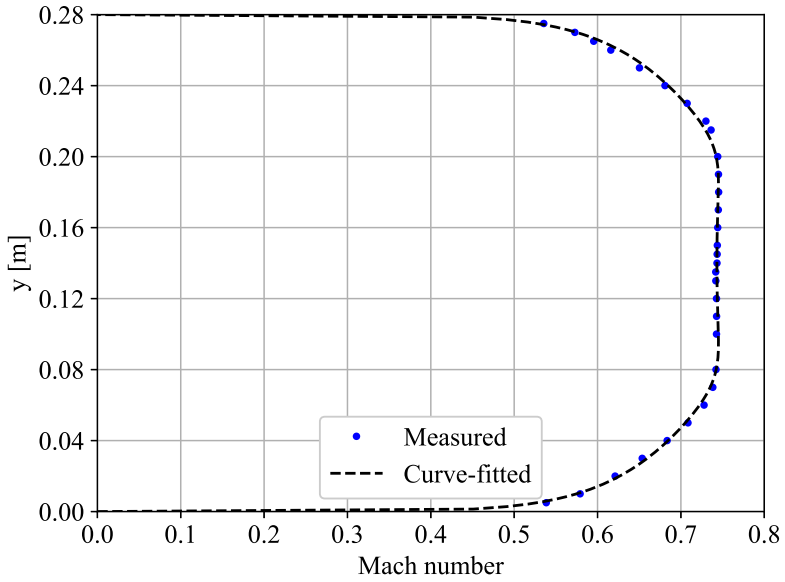

Figure 4.4: Measured and fitted mean velocity profile in the cross-section of the MAINE Flow facility. The fitted profile is obtained using Eq. (3.1).

4.2.1.2 Wavenumber retrieval process

Based on the pressure data obtained at the 40 microphone points, the HTLS method is used to retrieve the axial wavenumbers. The parameter L is set as 22, following the recommendation of $[0.4N, 0.6N]$ in [120]. Not all the wavenumbers identified by the HTLS technique correspond to physical acoustic modes in the duct lined section. It is therefore necessary to filter out the spurious results and select a physical wavenumber that will be adequate for the impedance eduction.

To this end, the approach is similar to what has been done for the mode classification during the mode computation in Section 2.2.3. Firstly, we expect the physical wavenumbers k_x to be located in specific regions of the complex plane. To identify right-running modes, the following heuristic rule is used:

$$\mathrm{Im}(k_x) \leq \mathrm{Re}(k_x) - k_0 \frac{M_{\mathrm{ave}}}{M_{\mathrm{ave}}^2 - 1} \,. \qquad ((2.15))$$

This corresponds to the region of the complex plane below the diagonal intersecting with the real axis at $k_x = k_0 M_{\mathrm{ave}}/(M_{\mathrm{ave}}^2 - 1)$. With a uniform flow with Mach number M_{ave}, this is the wavenumber of modes that are just cut-on. Moreover, only modes on or below the real axis are used, so as to exclude unphysical modes with wavenumbers having a positive imaginary part.

Next, a second criterion is needed to separate acoustic modes from hydrodynamic modes. As described in Section 2.2.3, for acoustic modes, the largest expected value for $\mathrm{Re}(k_x)$ is close to $k_0/(1+M_{\mathrm{ave}})$. For hydrodynamic modes when $M_{\mathrm{ave}} > 0$, the smallest value of $\mathrm{Re}(k_x)$ is expected to be close to k_0/M_{max} with M_{max} being the largest Mach number of the velocity profile. We use the average of these two values as a threshold to discriminate between acoustic and hydrodynamic modes. More specifically, a wavenumber is retained as an acoustic mode if

$$\mathrm{Re}(k_x) < \frac{k_0}{2}\left(\frac{1}{M_{\mathrm{ave}}+1} + \frac{1}{M_{\mathrm{max}}}\right) . \qquad ((2.31))$$

The two conditions are only qualitative, but their robustness has been proven in practice. For example, Figure 4.5 shows the region defined to select the retrieved wavenumbers in the double-liner configuration with an incident plane wave at $f = 2500\,\mathrm{Hz}$ and with $M_{\mathrm{ave}} = 0.5$. The wavenumbers computed numerically are also shown to compare with those retrieved by the HTLS method.

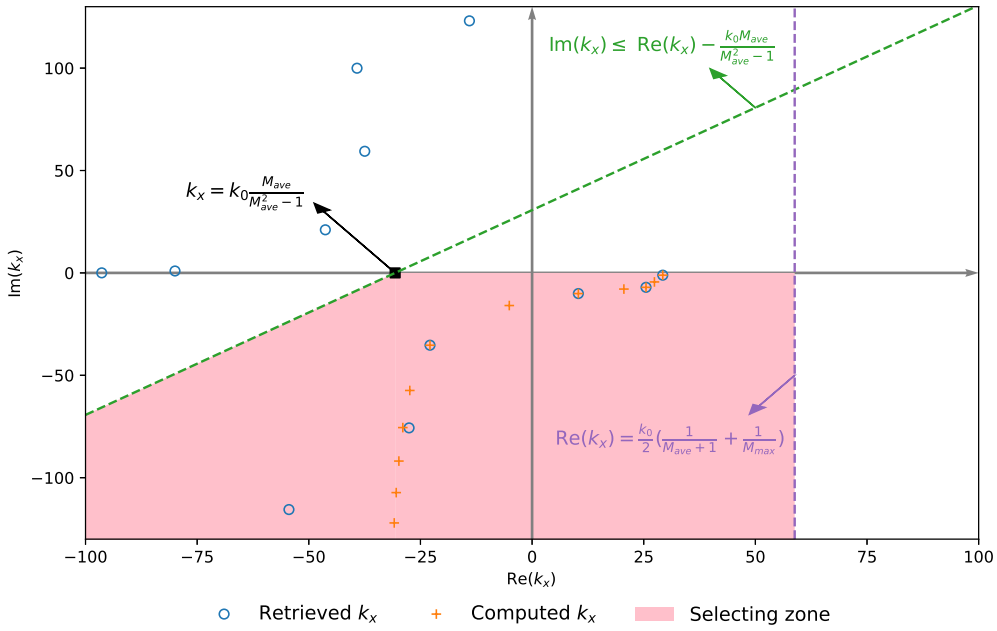

Figure 4.5: Illustration of the computed (orange plus signs) and retrieved wavenumbers (blue circles), and the pink region defined to select the wavenumbers used in the subsequent impedance eduction. The green dashed line stands for Eq. ((2.15)); the purple dashed liner for Eq. ((2.31)). The case is: the double-liner configuration, incident plane wave, $M_{\mathrm{ave}} = 0.5$ and $f = 2500$ Hz.

After enforcing these conditions, several wavenumbers calculated by the HTLS technique remain, and one of them should be selected for the impedance eduction. In the literature [9, 15, 18] it is common to use the least attenuated mode for the impedance eduction, i.e. the wavenumber closest to the real axis. As shown in Section 4.1.2, this choice is well suited for small ducts and at low frequencies (that is, for small Helmholtz numbers) where only the plane wave is propagating, i.e. the sound field is composed of a single mode in each direction. For large ducts or at high frequencies, it is possible to have several modes that are only weakly attenuated and the sound field in the lined section is clearly composed of several modes. In such

cases, and according to the simulations, the least attenuated wavenumber does not always yield the most accurate result for the impedance eduction.

When the least attenuated mode does not perform adequately, an alternative criterion is proposed for selecting the wavenumber. This criterion is based on the number of cut-on modes in the hard-wall section of the duct. The wavenumbers identified in the lined section are selected according to the constraints previously described and ordered by their rate of attenuation, which is determined by the value of $|\mathrm{Im}(k_x)|$. The mode ranked first is indeed the least attenuated. For a given frequency, if there are n propagating modes in the hard-wall duct, the n-th wavenumber calculated by the HTLS technique will be used to calculate the liner impedance. Since the HTLS technique may struggle to identify enough accurate wavenumbers at very high frequencies, we apply this criterion only up to the 5-th cut-off frequency. Beyond this point, if $n \geq 6$, we continue to use the 5-th wavenumber. For instance, with the single-liner configuration, if two modes are cut-on in the hard-wall section, then the second wavenumber will be used to calculate the impedance; if seven modes are cut-on in the hard-wall section, then the fifth wavenumber will be used to calculate the impedance. Note that for the double-liner configuration, only the cut-on modes with the same symmetry as the incident wave should be counted. For example, with the double-liner configuration, if the incident mode is symmetric and there are two symmetric cut-on modes in the hard-wall duct, then the second measured wavenumber will be used. This is because the total sound field retains the symmetry of the incident mode in the double-liner configuration. This property is also visible in the example in Figure 4.5 where only symmetric modes are identified by the HTLS technique.

4.2.2 Results without noise

The eduction process is first simulated without noise perturbation in the absence of flow. Since the uniform and shear flow methods provide indeed the same impedance results in the absence of flow, here are only shown the results obtained using the model with shear flow. The first two modes are studied individually, namely mode 0 (plane wave) and mode 1 (first transverse mode). These are considered representative of the symmetric and antisymmetric modes, respectively. Figure 4.6 displays the educed impedance for both single- and double-liner configuration in the absence of flow. The alternative criteria described in Section 4.2.1.2 is only applied for the former configuration, where it brings improvements. The results for the double-liner configuration show an excellent agreement with the imposed impedance for both incident modes. However, for the single-liner configuration, the educed impedance exhibits oscillations at high frequencies (above 2200 Hz).

Then, to consider the presence of flow, the Mach number is varied from 0.1 to 0.7 by scaling the fitted flow profile already shown in Figure 4.4. The alternative criterion described in Section 4.2.1.2 is applied.

Figure 4.7 compares the educed impedance obtained by assuming a uniform or a sheared mean flow in the impedance calculation, while the pressure was calculated by taking into account shear. The results obtained with the plane wave as the incident mode in the downstream direction and for the single and double-liner configurations are shown. The results in Figure 4.7(a) and (c), obtained with the shear flow model, show an excellent agreement with the imposed impedance for the two liner configurations (except at high frequencies for the single-liner configuration). Increasing the flow velocity makes little difference to the agreement of the eduction results, except at low frequencies for $M_{\mathrm{ave}} = 0.7$. In that specific case, results can be

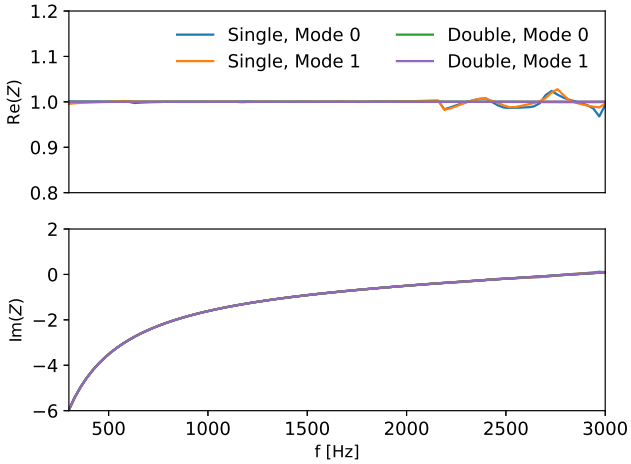

Figure 4.6: Educed impedance without flow nor noise using the shear flow assumption for both single- and double-liner configuration. The incident wave is individually the mode 0 or 1. Black line: imposed value. Coloured lines: educed value.

improved by selecting the second educed wavenumber, as shown in the inset graphs of Figure 4.7. When using the uniform flow assumption, the double-liner configuration tends to improve the accuracy of the educed impedance, as seen by comparing Figure 4.7(b) with (d). However, the impedance educed with the uniform flow assumption shows notable discrepancies from the imposed value that increase with the flow velocity. This is because the formula in Eq. (2.54) based on the uniform flow assumption is not able to represent accurately the relationship between axial wavenumbers and wall impedance in large ducts. This confirms that the validity of the uniform flow assumption with the Ingard-Myers boundary condition is poor for the impedance eduction in the MAINE Flow, which is in line with the conclusions in Chapter 3.

Figure 4.8 presents the eduction results with the plane mode incident in the upstream direction. The results in Figure 4.8(a) and (c), obtained with the shear flow model, show an excellent agreement with the imposed impedance for both liner configurations (except at high frequencies for the single-liner configuration). Using the uniform flow assumption with Ingard–Myers boundary condition as done in Figure 4.8(b) and (d) leads to very poor agreement when the flow velocity is greater than $M_{\text{ave}} = -0.1$.

The eduction results above demonstrate that using the shear flow model combined with the double-liner configuration yields significant benefits compared to the standard approach (that is, the model based on the uniform flow assumption and the single-liner configuration). Similar comparisons have also been performed with single incident higher-order modes (see results for the mode 1 in Figure 4.9 and 4.10), and the conclusions remain the same as above.

4.2.3 Discussion on the configurations

In this section, the mechanisms underlying the performance disparities between single-liner and double-liner configurations are examined in detail. Furthermore, an explanation is provided as to why the double-liner configuration yields more precise eduction results.

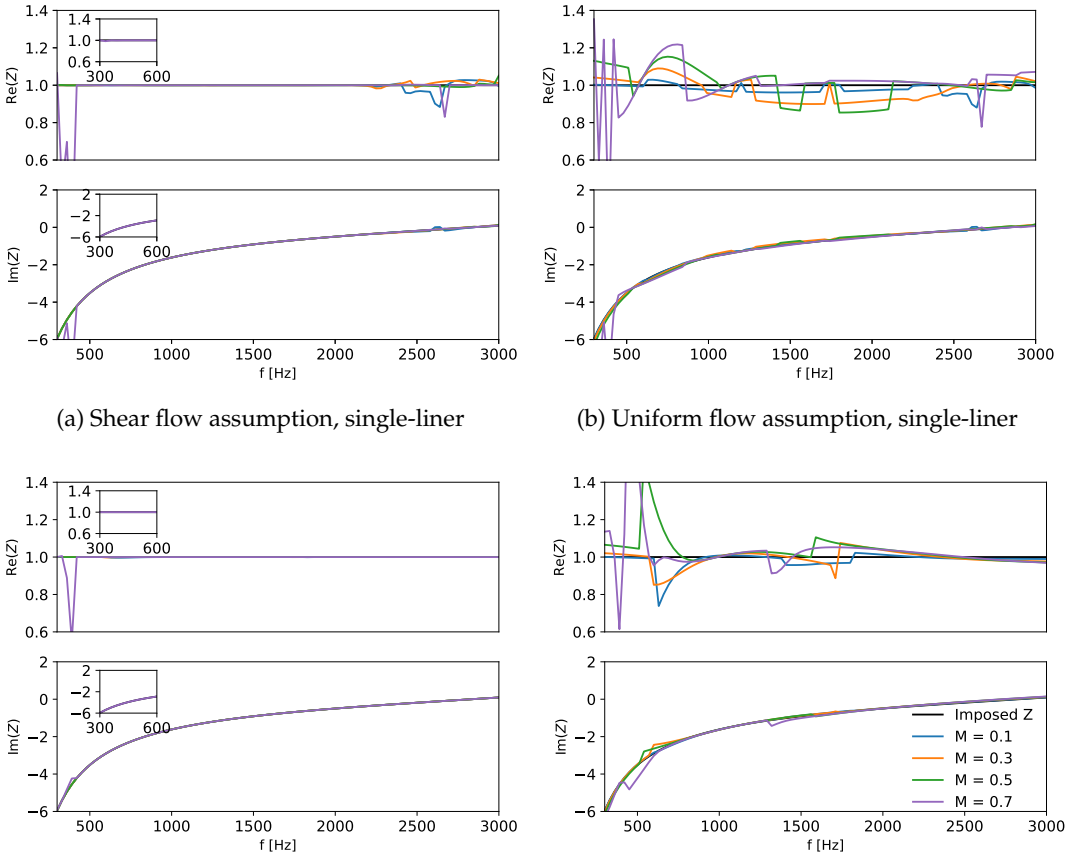

(a) Shear flow assumption, single-liner

(b) Uniform flow assumption, single-liner

(c) Shear flow assumption, double-liner

(d) Uniform flow assumption, double-liner

Figure 4.7: Educed impedance without noise using the uniform (right) and shear (left) flow models, for different flow velocities in the same direction as the incident plane wave. The insets show the impedance calculated using the second educed wavenumber. Top: single-liner configuration. Bottom: double-liner configuration. Black solid line: imposed impedance.

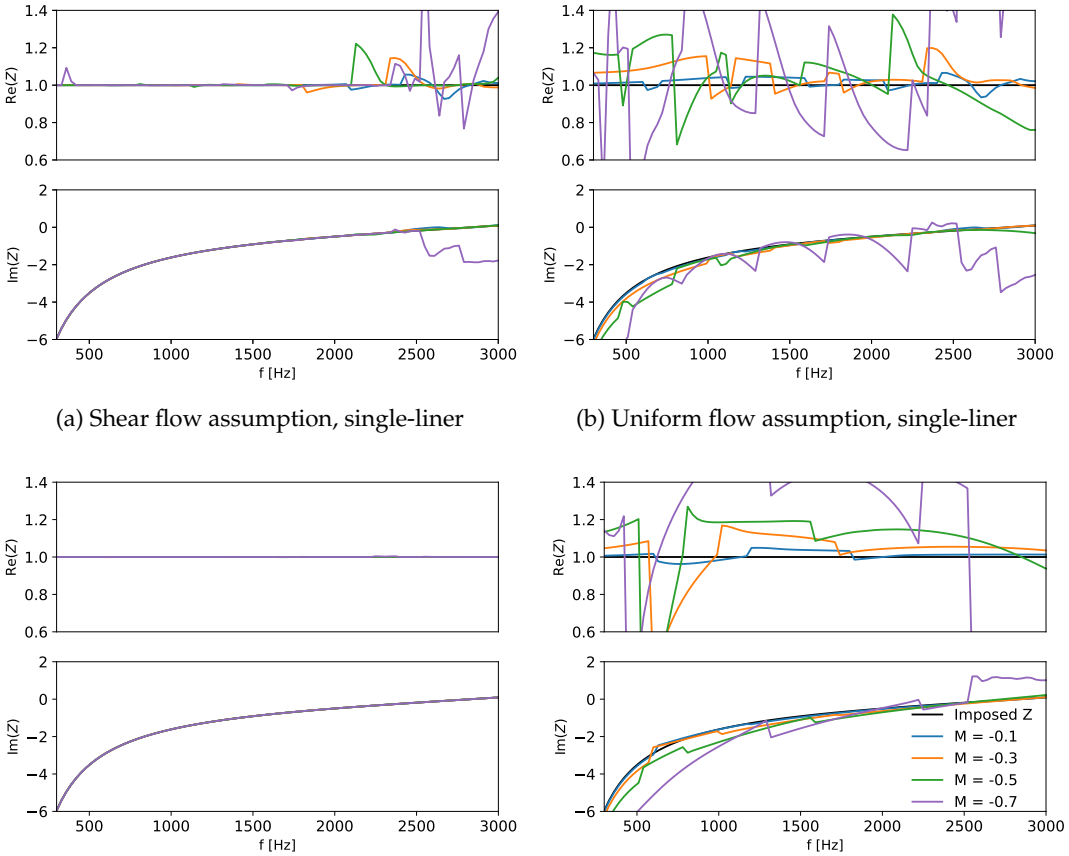

(a) Shear flow assumption, single-liner

(b) Uniform flow assumption, single-liner

(c) Shear flow assumption, double-liner

(d) Uniform flow assumption, double-liner

Figure 4.8: Educed impedance without noise using the uniform (right) and shear (left) flow models, for different flow velocities in the opposite direction as the incident plane wave. Top: single-liner configuration. Bottom: double-liner configuration. Black solid line: imposed impedance.

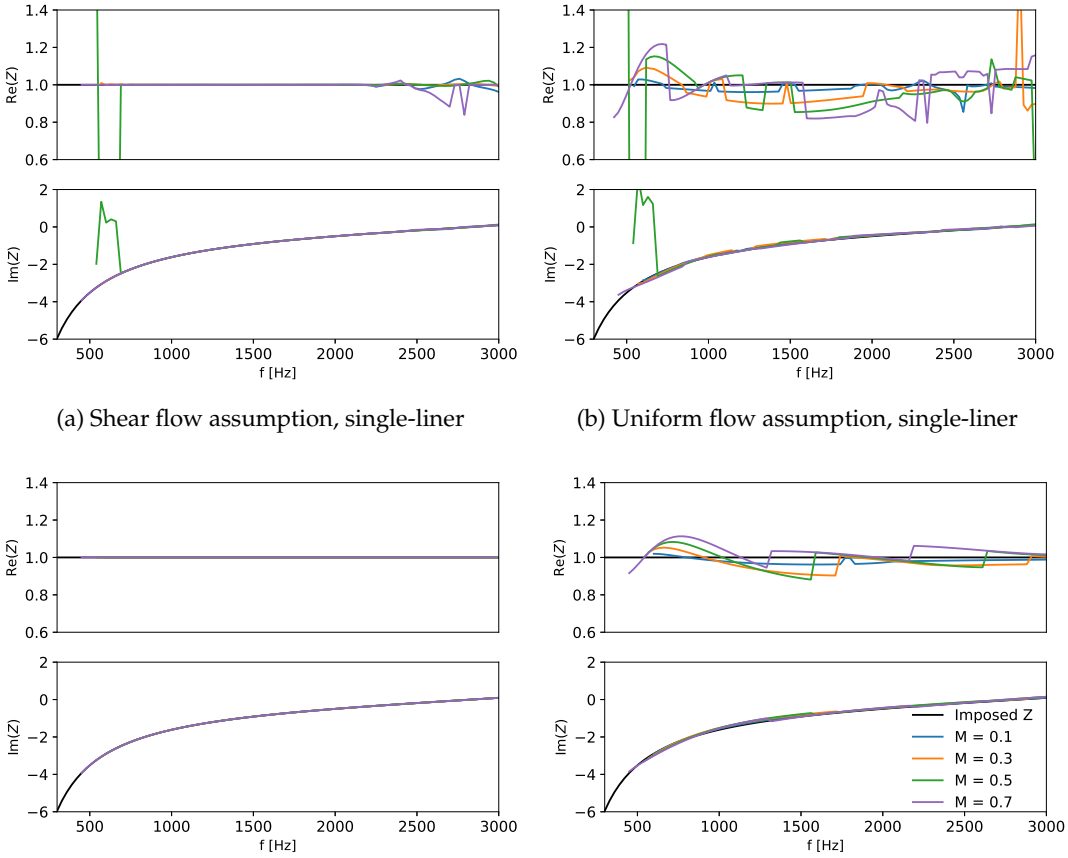

(a) Shear flow assumption, single-liner

(b) Uniform flow assumption, single-liner

(c) Shear flow assumption, double-liner

(d) Uniform flow assumption, double-liner

Figure 4.9: Educed impedance without noise using the uniform (right) and shear (left) flow models, for different flow velocities in the same direction as the incident mode 1. Top: single-liner configuration. Bottom: double-liner configuration. Black solid line: imposed impedance.

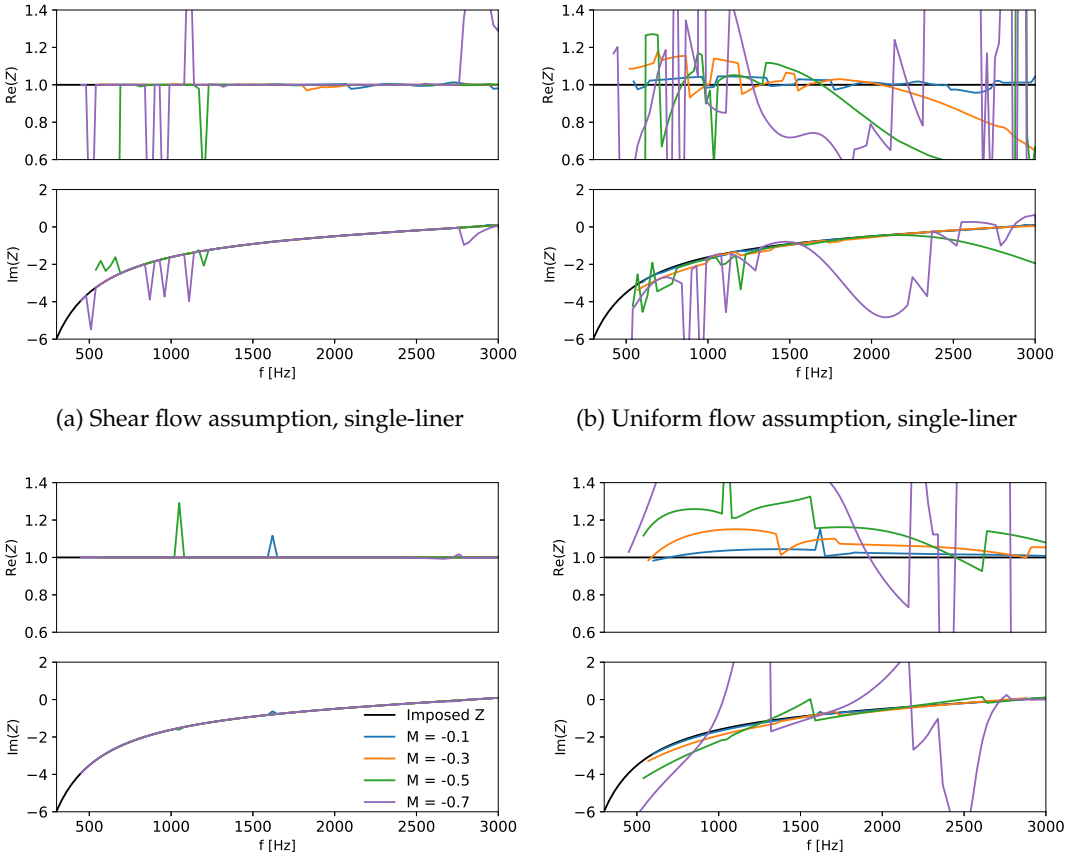

(a) Shear flow assumption, single-liner

(b) Uniform flow assumption, single-liner

(c) Shear flow assumption, double-liner

(d) Uniform flow assumption, double-liner

Figure 4.10: Educed impedance without noise using the uniform (right) and shear (left) flow models, for different flow velocities in the opposite direction as the incident mode 1. Top: single-liner configuration. Bottom: double-liner configuration. Black solid line: imposed impedance.

Figure 4.11 shows the acoustic pressure field in the treated section of the single-liner and of the double-liner configurations at a selected frequency $f = 1500$Hz. The liner impedance remains $Z = 1 - \cot(k_0 h_{cav})$i, with $h_{cav} = 0.03$ m. The flow profile is scaled to $M_{\text{ave}} = +0.3$. Through a rough comparison, the double-liner configuration preserves the symmetry of the acoustic field, so that the scattered acoustic field of symmetric incident modes (such as the plane wave) remains symmetric and the acoustic field of antisymmetric incident modes (such as the mode 1) remains antisymmetric.

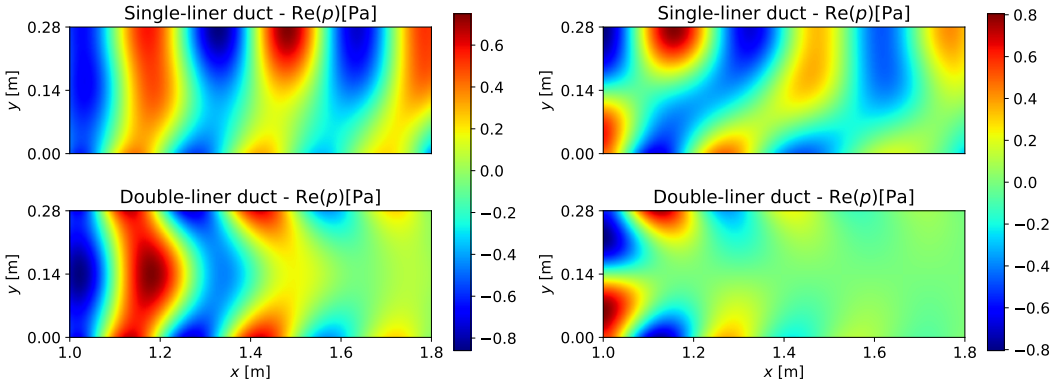

(a) Mode 0. (b) Mode 1.

Figure 4.11: Acoustic pressure field in the lined section of the single-liner and the double-liner case ($f = 1500$Hz) with $M_{\text{ave}} = +0.3$. Incident wave: mode 0 (left) and 1 (right) in the downstream direction.

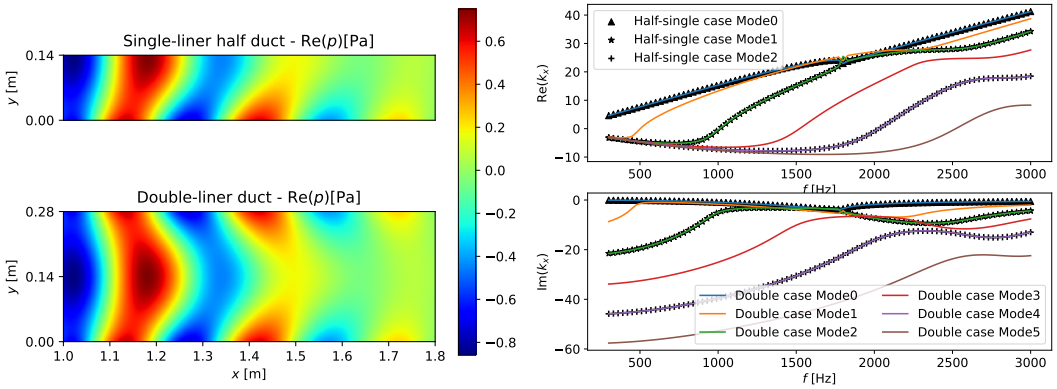

(a) (b)

Figure 4.12: Left: acoustic pressure field in the lined section of a half-height duct with single-liner and of the double-liner case ($f = 1500$Hz): the plane wave in the downstream direction with $M_{\text{ave}} = +0.3$. Right: simulated axial wavenumbers in both cases.

Figure 4.12(a) illustrates the acoustic pressure field in the lined section of a half-height duct with a single liner on the lower wall, as well as in a double-liner duct, by taking the plane wave as the incident mode. The acoustic field in the double-liner duct is symmetric and is equivalent to that of two rigid-lined ducts with half the height, placed symmetrically face to face. As shown in Figure 4.12(b), the axial wavenumbers in the half single-liner duct match those of the symmetric modes in the double-liner duct. Therefore, with symmetric incident modes, the double-liner configuration effectively makes the acoustic field resemble that of a half-height duct

and then permits simplifying the acoustic field components. To some extent, this reduces the difficulty of the impedance eduction for large ducts by virtually reducing the height in front of the liner.

To further investigate the reasons for the good performance of the double-liner configuration, the pressure signals ($f = 1500$Hz) obtained by the microphone array at $2/3H$ are plotted to clarify the evolution of the acoustic field along the axis in the lined section. In addition to this, in the numerical simulation, the acoustic field in the lined section are modal-decomposed and then modes are superposed through several combinations to discover the dominant modes that contribute the most to the total acoustic field.

Figure 4.13 shows the modal decomposition and the recombination of the dominant modes in the lined section in the single-liner case, and Figure 4.14 depicts the double-liner case. The total signal stands for the total acoustic field recorded by the microphone array, and mode $n^{\pm}$ represents the n-th mode with the index of direction $\pm$. The least modes required to accurately reconstruct the acoustic field are revealed. Note that if fewer modes are taken, there will be a poor match between the reconstruction and the original signal.

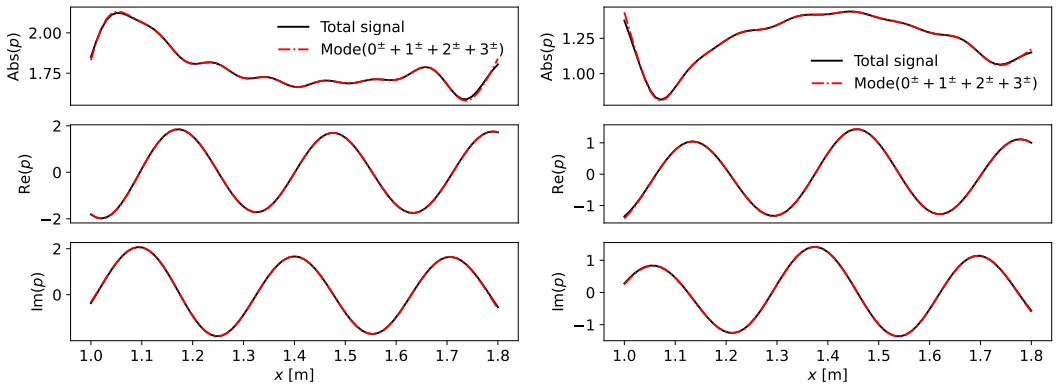

(a) Incident mode 0.

(b) Incident mode 1.

Figure 4.13: Mode decomposition and recombination in the lined section of the single-liner at $f = 1500$Hz: the mode 0 and 1 in the downstream direction with $M_{\text{ave}} = +0.3$.

For the double-liner configuration, it is worth noting that with a symmetric incident mode, the acoustic field in the treated section is only composed of symmetric modes; similarly, with an antisymmetric incident mode, antisymmetric modes are the most dominant in the acoustic field. From the energy point of view, the symmetry of the double-liner configuration preserves the symmetry type of the incident wave, thus allowing the energy to be transferred to higher-order modes of the same symmetry as much as possible. However, in the single-liner case shown in Figure 4.13, the acoustic field always consists of more modal components, 2 times more than in the double-liner case. In addition, the issue in the single-liner case is the inability to reconstruct the complete acoustic field with the same few number and order of dominant modes as in the double-liner case. Therefore, it is more complicated in the single-liner case to retrieve the most dominant axial wavenumber during the process of exponential parameter estimation.

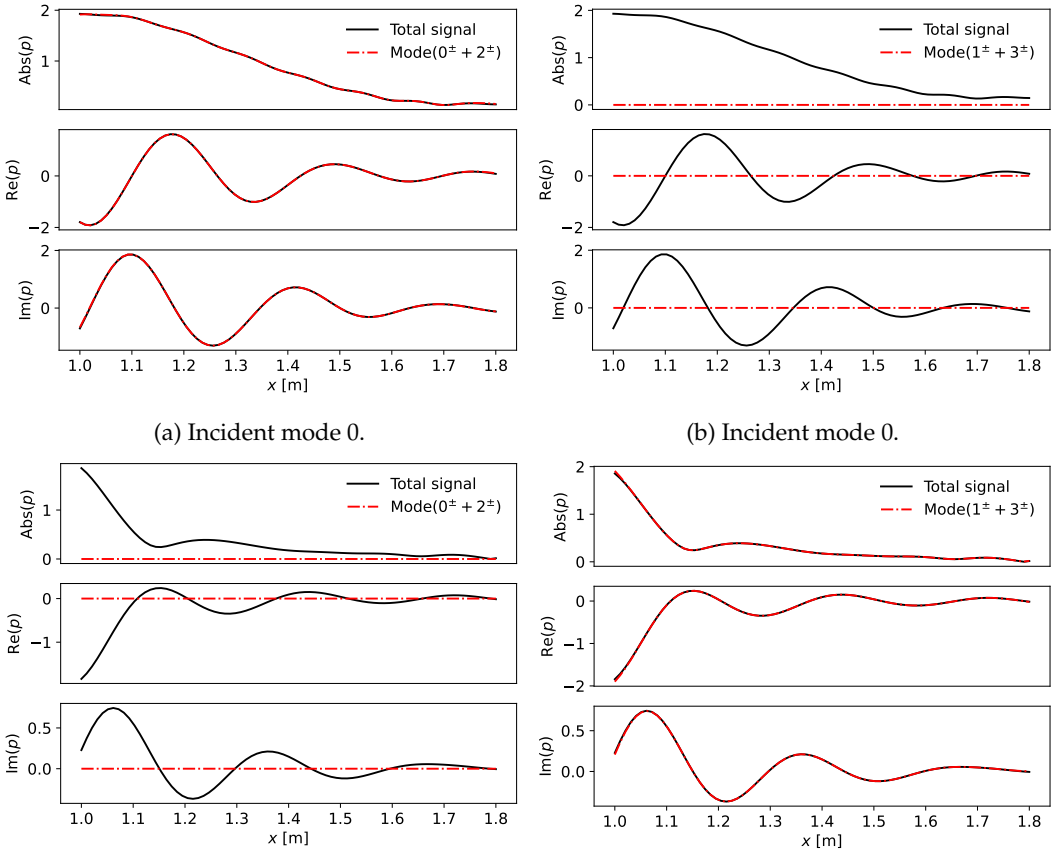

(a) Incident mode 0.

(b) Incident mode 0.

(c) Incident mode 1.

(d) Incident mode 1.

Figure 4.14: Mode decomposition and recombination in the lined section of the double-liner at $f = 1500$Hz: the incident plane wave and the first transverse mode in the downstream direction with $M_{\text{ave}} = +0.3$. Combination: symmetric modes $0^{\pm}$ and $2^{\pm}$; antisymmetric modes $1^{\pm}$ and $3^{\pm}$.

4.2.4 Issues with the single-liner configuration with noise

4.2.4.1 Results for original single-liner configuration

The simulation is now conducted for the eduction process in the presence of noise. Various SNRs are tested, between 20 and 40 dB. Note that, in real experiments, the SNR will vary with frequency, depending on the source strength, the background noise in the test rig and the liner efficiency (e.g. the SNR will decrease when the liner absorption is strong). In this numerical simulation, the amplitude of noise for each signal is defined relative to the incident amplitude, resulting in a decreasing SNR along the propagation direction. To compute the mean value and the standard deviation of the educed impedance, 1000 realizations of the random noise are calculated, and the eduction process is applied to each one, along with the criteria described in Section 4.2.1.2.

Figure 4.15 shows the eduction results in the single-liner configuration for both incident modes. Large discrepancies with the mode 0 appear between the imposed and educed impedances at several frequencies below 1800 Hz. For the mode 1, the eduction results are poor on the whole frequency range. This failure can be explained by the small attenuation of the sound field achieved by a single-liner. The small decay of the acoustic pressure over the liner is more easily swamped by the noise added to the microphone data. Even with a SNR of 40 dB, the deviations of the results from the imposed value is significant. It is also shown that the increase of SNR influences only weakly the mean values and only reduces the standard deviation of results. Figure 4.15 shows results obtained with the shear flow assumption. The results obtained with the uniform flow assumption are even worse, as can be predicted by the results in the absence of noise in the previous section.

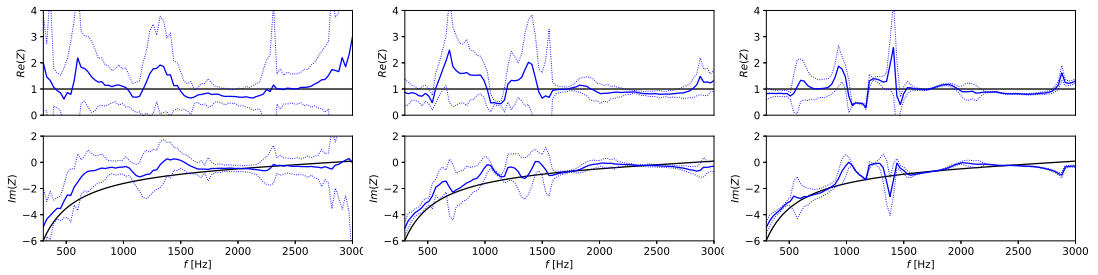

(a) Mode 0, SNR = 20 dB (b) Mode 0, SNR = 30 dB (c) Mode 0, SNR = 40 dB

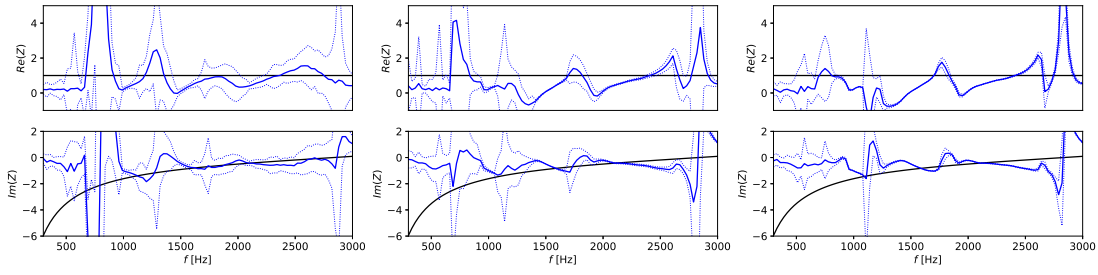

(d) Mode 1, SNR = 20 dB (e) Mode 1, SNR = 30 dB (f) Mode 1, SNR = 40 dB

Figure 4.15: Educed impedance with noise (with SNR being from 20 to 40 dB) using the shear flow assumption, with the 0.8 m liner for the single-liner configuration, with flow of $M_{\text{ave}} = +0.3$ in the same direction as the incident mode (the mode 0 or 1). Black solid line: imposed impedance. Blue solid line: mean value of educed impedances. Blue dashed line: standard deviation of educed impedances.

4.2.4.2 Possible improvements

Given that the results above obtained for the single-liner configuration are not satisfactory in the presence of noise, other configurations based on the MAINE Flow facility are tested to see whether they would provide any improvement. Except the proposition and the application of the double-liner configuration (in the next section), several attempts based on the single-liner configuration are made to improve the impedance eduction results with noise. In the presence of flow (M_{ave} = 0.3) and noise (SNR = 30 dB), tests include:

- to increase the length of the liner,
- to change the number of microphones,
- to change the position of the liner from the narrow side to the wide side in the lined section of MAINE Flow (i.e. the height of the duct is reduced in the numerical simulation).

Effects of liner length and microphone spacing

The first attempt is to change the length of the liner. Besides the original liner length 0.8 m in the MAINE Flow facility, simulations are also conducted for the impedance eduction in lined sections with lengths of 1.2 and 1.6 m. For each length, the effect of the microphone number is also evaluated by modifying the distance between the data points.

For the 1.6 m liner, the chosen spacing Δx are 0.04, 0.06, and 0.08 m, which corresponds to arrays of respectively 40, 27, and 20 microphones. For the 1.2 m liner, the chosen spacing are 0.03, 0.04 and 0.06 m, which correspond to arrays of respectively 40, 30, and 20 microphones. For the 0.8 m liner, the chosen distance are 0.01, 0.02, and 0.04 m, corresponding to arrays of respectively 80, 40, and 20 microphones. For all layouts, the first and last microphones are placed $\Delta x/2$ into the lined section. For each configuration, the column number L is selected in $[0.4N, 0.6N]$. Table 4.2 summarises the setting parameters.

0.8 m			1.2 m			1.6 m		
N	Δx [m]	L	N	Δx [m]	L	N	Δx [m]	L
80	0.01	42	40	0.03	22	40	0.04	22
40	0.02	22	30	0.04	16	27	0.06	14
20	0.04	10	20	0.06	10	20	0.08	10

Table 4.2: Layout, for the liners of various lengths L, of the arrays containing N microphones separated by distances Δx.

For this study, we consider as an incident acoustic field the mode 0 propagating in the downstream direction. Since the higher-order modes lead always to worse results compared to the plane wave, for the sake of brevity, only the results for the latter are shown in this part.

Figures 4.16, 4.17 and 4.18 show the impedance eduction results with noise for a SNR=30 dB and liners of length 0.8, 1.2, and 1.6 m, respectively. Based on these numerous results, it can be observed that increasing the number of microphones, i.e. increasing the resolution, does not significantly improve the accuracy of results. For instance, in Figure 4.16, when the number of microphones increases from 20 to 80, the standard deviation of the educed impedance is reduced. However, the overall

quality of the eduction results remains poor. Moreover, through an analysis of the results for various liner lengths, it is evident that increasing the liner length significantly improves the results between 500 and 1500 Hz, because the sound attenuation is increased. The longest liner with a length of 1.6 m gives the best results in spite of the large discrepancy near 1500 Hz which can be slightly mitigated by a smaller microphone spacing.

To summarise, increasing the liner length indeed improves the accuracy of eduction results, as the sound attenuation increases, thereby reducing the uncertainty in impedance eduction [17, 121]. Conversely, the improvement gained by increasing the number of microphones (i.e., refining the microphone array) is minimal. The influence is only reflected in the reduction of the standard deviation, indicating a decreased sensitivity of educed results to noise. Nevertheless, it does not essentially alter the accuracy of the predictions.

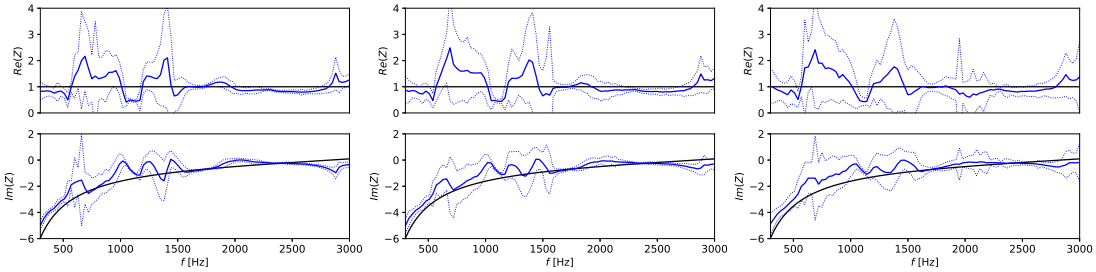

(a) $N = 80$, $\Delta x = 0.01$ m (b) $N = 40$, $\Delta x = 0.02$ m (c) $N = 20$, $\Delta x = 0.04$ m

Figure 4.16: Educed impedance with noise (SNR=30dB) using the shear flow assumption, with the 0.8 m liner for the single-liner configuration, with flow of $M_{\text{ave}} = +0.3$ in the same direction as the incident plane wave. Black solid line: imposed impedance. Blue solid line: mean value of educed impedances. Blue dashed line: standard deviation of educed impedances.

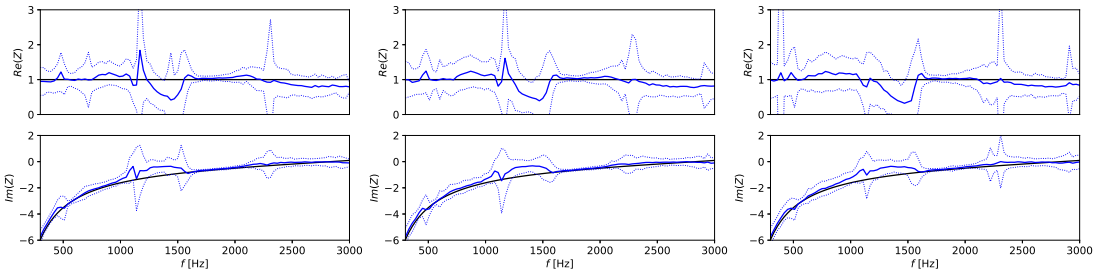

(a) $N = 40$, $\Delta x = 0.03$ m (b) $N = 30$, $\Delta x = 0.04$ m (c) $N = 20$, $\Delta x = 0.06$ m

Figure 4.17: Educed impedance with noise (SNR=30dB) using the shear flow assumption, with the 1.2 m liner for the single-liner configuration, with flow of $M_{\text{ave}} = +0.3$ in the same direction as the incident plane wave. Black solid line: imposed impedance. Blue solid line: mean value of educed impedances. Blue dashed line: standard deviation of educed impedances.

Effect of reducing the duct height

The second test consists in simulating the impedance eduction for the single-liner configuration in a duct with a height of 0.15 m, in order to imitate the installation

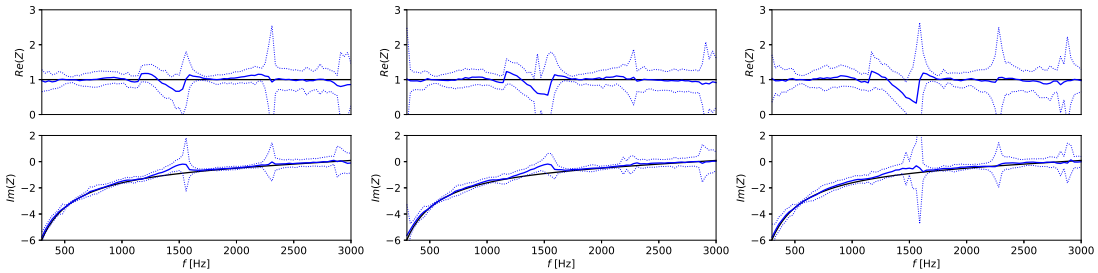

(a) $N = 40$, $\Delta x = 0.04$ m (b) $N = 27$, $\Delta x = 0.06$ m (c) $N = 20$, $\Delta x = 0.08$ m

Figure 4.18: Educed impedance with noise (SNR=30dB) using the shear flow assumption, with the 1.6 m liner for the single-liner configuration, with flow of $M_{\text{ave}} = +0.3$ in the same direction as the incident plane wave. Black solid line: imposed impedance. Blue solid line: mean value of educed impedances. Blue dashed line: standard deviation of educed impedances.

of the liner on one of the wide sides (0.28 m × 0.8 m) in the MAINE Flow facility. The flow velocity remains $M_{\text{ave}} = +0.3$. The modes 0 and 1 are sent separately, and the eduction is performed over the frequency ranges from 300 to 3000 Hz and 1200 to 4000 Hz, respectively, with 30 Hz increments. The latter range begins at a higher frequency than in previous analyses because the cut-off frequency of the mode 1 ($f_c \simeq 1081$ Hz) is higher in a duct of this height.

The eduction results are depicted for the SNRs of $20, 30, 40$ dB and for the first two modes in Figure 4.19. Compared to the results of the original single-liner configuration in Figure 4.15, it can be seen that reducing the duct height improves the eduction results. In fact, when the height of the duct is smaller, the multimodal acoustic field in the duct become less complicated. Therefore, it is easier to educe the impedance. Furthermore, in Figure 4.19, the performance of eduction is better with a higher SNR, which can be expected. But according to the results in Figure 4.15, the improvement in performance associated to the SNR is limited when the results are poor.

To conclude, some of these attempts improve the performance of the single-liner configuration, mainly by increasing the acoustic attenuation of the liner or simplifying the acoustic field composition. However, they involve significant modifications to the existing experimental facilities, which cannot be easily realised and are therefore not adopted. Nevertheless, these tests provide suggestions for accurate impedance eduction, such as prioritising the increase of liner length over the number of microphones. To deal with the noise perturbations, a simpler and more favourable solution is presented in the next section, without the need to change the fundamental parameters of the experimental bench.

4.2.5 Results with noise for the double-liner configuration

As shown in Section 4.2.3, the double-liner configuration can increase the acoustic attenuation and simplify the acoustic field. It requires only one additional liner to be installed, without the need to change the fundamental parameters of MAINE Flow.

In the presence of noise with a SNR of 30 dB, the educed impedances are obtained for the double-liner configuration using the first two modes individually. Figure 4.20 shows the educed impedance for the incident plane wave in both directions. The results are not entirely satisfactory. For downstream propagation, the mean values

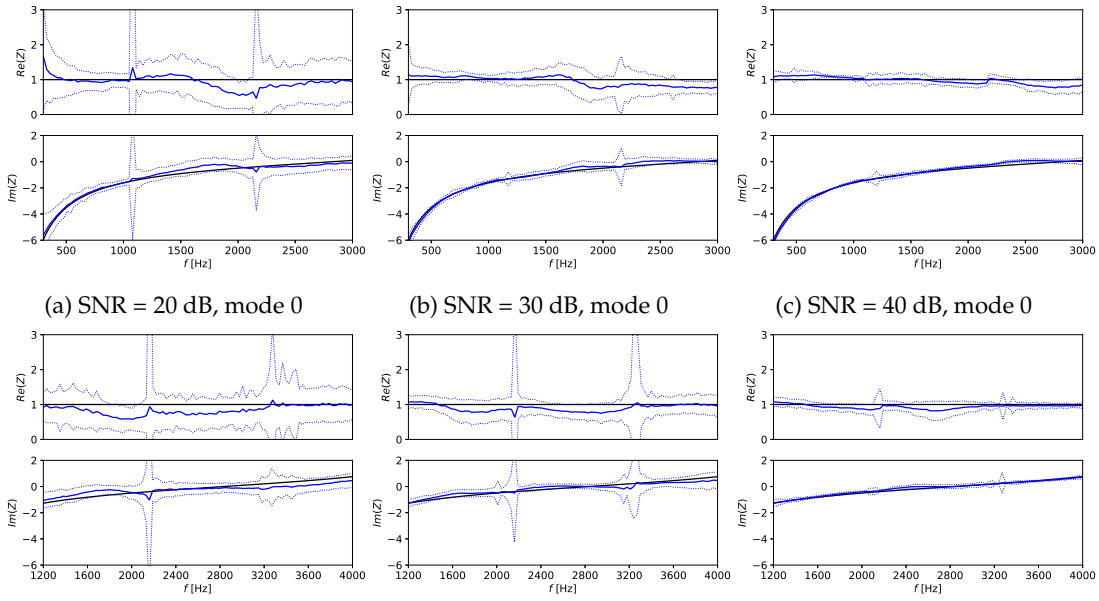

(a) SNR = 20 dB, mode 0 (b) SNR = 30 dB, mode 0 (c) SNR = 40 dB, mode 0

(d) SNR = 20 dB, mode 1 (e) SNR = 30 dB, mode 1 (f) SNR = 40 dB, mode 1

Figure 4.19: Educed impedance with noise (with SNR being from 20 to 40 dB) using the shear flow assumption in the 0.15 m-high duct, with the 0.8 m liner for the single-liner configuration, with flow of $M_{\text{ave}} = +0.3$ in the same direction as the incident plane wave. Black solid line: imposed impedance. Blue solid line: mean value of educed impedances. Blue dashed line: standard deviation of educed impedances.

of the educed resistance deviate from the imposed value, even for a small velocity $M_{\text{ave}} = 0.1$. The upstream results are drastically worse with larger errors and standard deviations. Consequently, strategies are needed to alleviate these issues.

For the double-liner configuration, and in order to increase our chances for a robust eduction by improving the signal amplitudes, the vertical position of the microphone line is now changed depending on the incident acoustic mode. For anti-symmetric modes, the array is still located at 2/3 of the duct height in order to avoid pressure nodes. However, for the case of a symmetric incident mode, the microphone array is placed at the half of the duct height, where the pressure is maximum. Figure 4.21 exhibits the eduction results in the presence of noise, using the positions of the microphone array for both mode 0 and 1. Since the truncation number K must be small enough to avoid noise disturbances, the number of retrieved wavenumbers is consequently reduced, limiting the retrieval of higher-order modes. As a result, the alternative criterion introduced in Section 4.2.1.2 for selecting wavenumbers are not used in this context.

For downstream propagation, in Figure 4.21(a), the results with the mode 0 shows a good agreement with the prescribed impedance, and the standard derivation remains acceptable (except close to 1100 Hz). With $M_{\text{ave}} = 0.7$, there exists a disparity at $f \geq 2500$ Hz between the educed results and the imposed resistance, which might be explained by the appearance of higher-order modes. In addition, the results obtained for $M_{\text{ave}} = 0.1$ show limited standard derivation, but it becomes larger at higher frequencies. A similar trend is observed for larger Mach numbers M_{ave}.

Comparing Figure 4.21(a) and (c) shows that the mean impedance value educed for incident mode 1 is closer to the exact value than for incident mode 0. For $M_{\text{ave}} =$

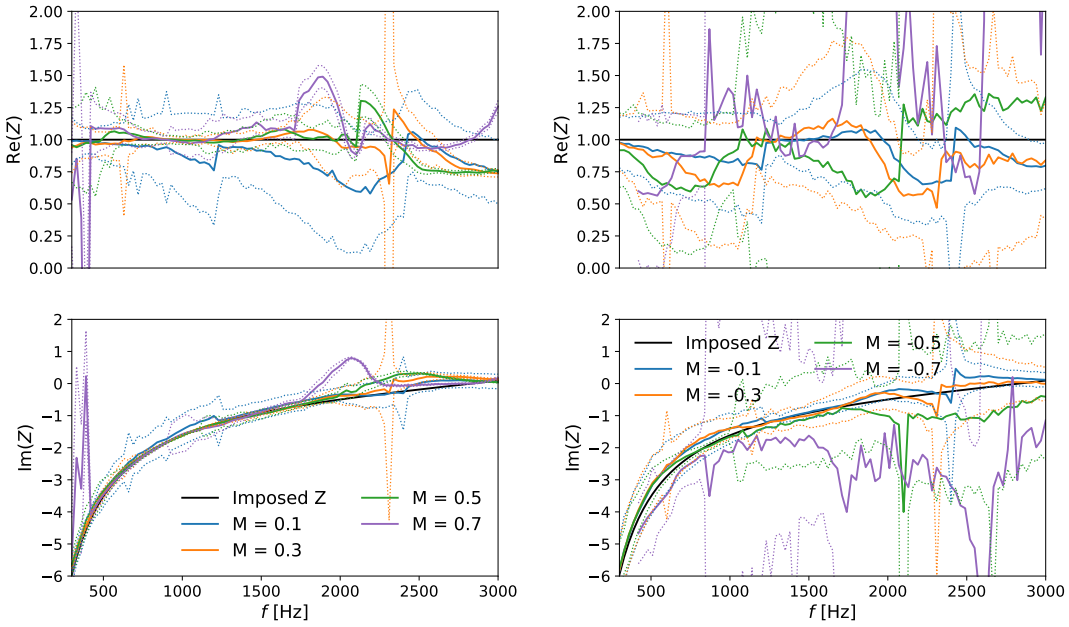

(a) Mode 0, downstream propagation

(b) Mode 0, upstream propagation

Figure 4.20: Educed impedance with noise (SNR $=$ 30 dB) using the model with sheared flow. Incident mode: the plane wave. Black line: imposed impedance. Coloured solid line: mean value of impedance. Coloured dashed line: standard deviation of the educed impedance around its mean value.

0.5 and $M_{\text{ave}} = 0.7$, the standard derivation becomes large in the vicinity of the cut-off frequencies of higher-order modes, indicating that the noise perturbations are significant when one more mode is just cut-on.

In Figure 4.21(b) and (d), incident modes propagating in the upstream direction are considered. It is shown that the mean impedance values remain close to the imposed impedance in most of the cases. For the results obtained for the mode 0, there exists a disparity at high frequencies which might be explained by the reduced accuracy of estimated wavenumbers with the appearance of higher-order modes. Note that there is a trade-off between the number of considered modes and the avoidance of noise perturbations when estimating the wavenumbers. If more wavenumbers are needed, more noise will be involved in the calculation due to the increased truncation number in the algorithm. Therefore, the standard variation becomes notable, and the mean value deviates more from the imposed value at high frequencies ($f > 2400$ Hz). However, high-speed flows in the opposite direction of the incident acoustic wave pose challenging conditions which require more work to be tackled. In particular, for $M_{ave} = -0.7$ the mean impedance value is only close to the imposed one at low frequencies before deviating dramatically.

Except when $M_{\text{ave}} = -0.7$, comparing the results obtained for the two modes shows that the antisymmetric incident mode provides a better performance in the impedance eduction due to a greater attenuation. This suggests an experimental perspective that would use attenuated high-order modes or antisymmetric modes as incident waves to improve the robustness of the method.

To conclude, and according to the results above, using the shear flow method with the double-liner configuration improves the accuracy and the reliability of the eduction process. This is critical for understanding the behaviour of acoustic liner

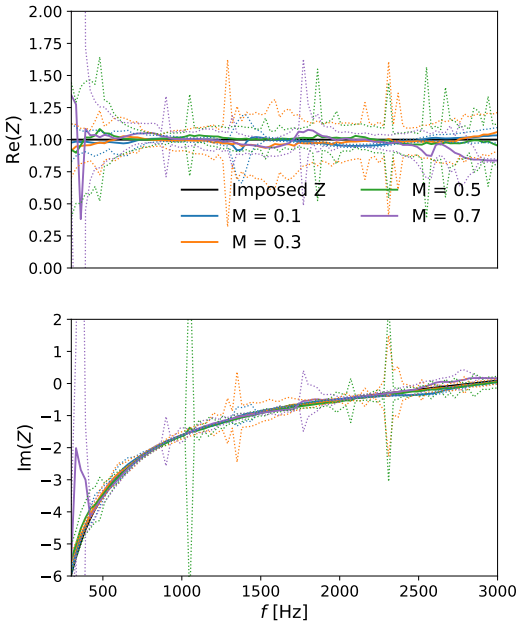

(a) Mode 0, downstream propagation

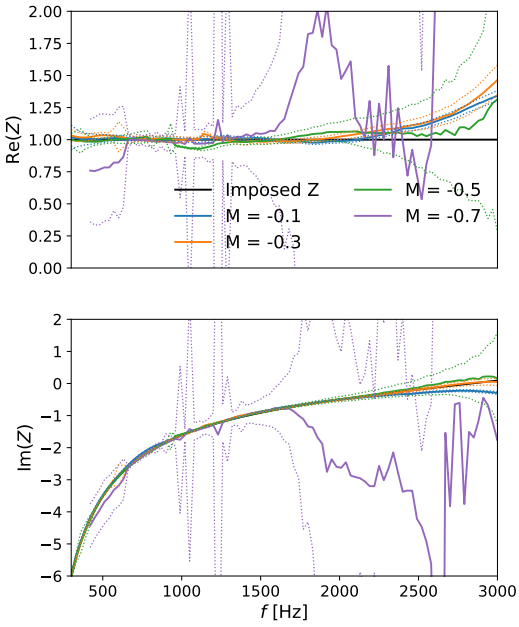

(b) Mode 0, upstream propagation

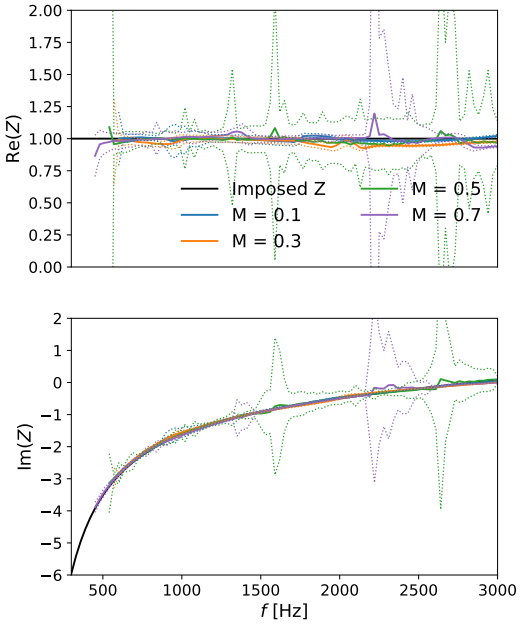

(c) Mode 1, downstream propagation

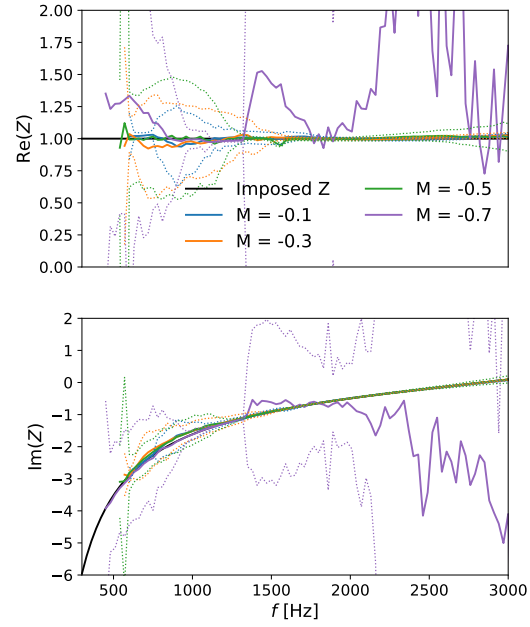

(d) Mode 1, upstream propagation

Figure 4.21: Educed impedance with noise (SNR $=$ 30 dB) using the model with sheared flow. The microphone array is installed at $1/2H$ for the mode 0 and at $2/3H$ for the mode 1. Black line: imposed impedance. Coloured solid line: mean value of impedance. Coloured dashed line: standard deviation of the educed impedance around its mean value.

submitted to high speed flows and multimodal acoustic conditions where the uniform flow assumption is not applicable.

4.3 Development of microphone arrays

The double-liner configuration proposed above aims at increasing the accuracy of impedance eduction by enforcing the acoustic attenuation and simplifying the acoustic field composition. However, in real experiments, when one incident mode is generated, the controlled incident field includes not only the desired one but also additional modes at much lower SPLs. Consequently, the incident acoustic field is indeed multimodal and thus the presence of these additional modes disrupts the separation between symmetric and antisymmetric modes achieved by the double-liner configuration.

This section, therefore, examines the impact of these additional modes on the effectiveness of impedance eduction with the double-liner configuration. Subsequently, to mitigate this influence, a new microphone array is proposed taking advantage of the properties of the mode (anti)symmetry. In this section, the impedance is always calculated using the shear flow model.

4.3.1 Influence of additional modes

First, when generating a single incident mode, other modes are present at a SPL about 30 dB below the main incident mode. To mimic this situation in our numerical simulation, the other modes are set at 30 dB below the main incident mode, and the acoustic field is computed between 300 and 3000 Hz with 30 Hz increments using the propagation model with shear flow. The pressure signal acquisition is performed by the 40-microphone array at $2/3H$ as depicted in Figure 4.3.

The first analysis is conducted in the absence of flow. For both incident modes, the impedance is calculated from the first three wavenumbers retrieved with the HTLS method, as shown in Figure 4.22. The results for the incident mode 1 begin at 600 Hz. According to the impedance calculation method described in Section 2.3.2.2 for the double-liner, each wavenumber can provide two impedances, associated to either a symmetric or an antisymmetric solution. According to the results for the incident mode 0, the symmetric solution provided by the first retrieved wavenumber $k_{x1,ed}$ is in line with the imposed impedance. However, the correct solutions, calculated from the second and third retrieved wavenumbers, correspond to different symmetry types which alter along the frequency. Therefore, with the perturbation of the additional modes, the correct results cannot identified by using the symmetry type of the incident mode. For the results with the mode 1, conclusions are similar.

When only one incident mode is present, the correct solution can be identified based on the symmetry of that mode, because the acoustic field is only composed of modes of the same symmetry (see Figure 4.14). However, when the incident field contains not exactly one mode, the acoustic field is as complicated as with the single-liner configuration where all modes are present. Figure 4.23 shows the wavenumbers $k_{x,simu}$ computed by the multimodal model and the ones retrieved from the pressure signals of the microphone array. It is noted that the retrieved wavenumbers are associated to modes of both symmetry types, indicating that there are modes of both symmetry types constituting the acoustic field. This explains the altering symmetry type of the correct solutions shown in the results in Figure 4.22.

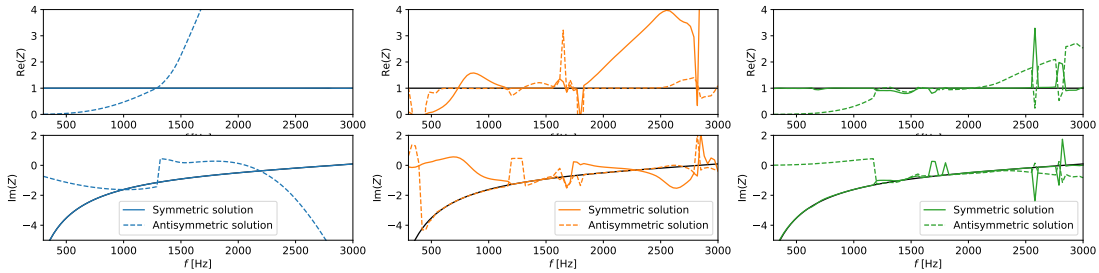

(a) Incident mode 0. From $k_{x1,ed}$. (b) Incident mode 0. From $k_{x2,ed}$. (c) Incident mode 0. From $k_{x3,ed}$.

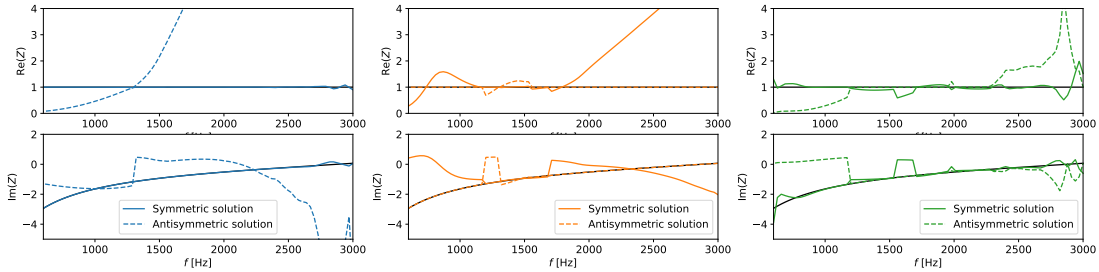

(d) Incident mode 1. From $k_{x1,ed}$. (e) Incident mode 1. From $k_{x2,ed}$. (f) Incident mode 1. From $k_{x3,ed}$.

Figure 4.22: Educed impedance from n-th retrieved wavenumbers, for the incident mode 0 (top) and 1 (bottom) with other modes at 30 dB lower as perturbation. Solid line: symmetric solution of impedance, dashed line: antisymmetric solution of impedance.

The influence of the additional modes is thus revealed. On the one hand, this introduces the difficulty of identifying the correct solution in the calculation of impedances. On the other hand, the acoustic field contains twice as many modes (compared to the case with a single incident mode), thus increasing the complexity of the wavenumber estimation.

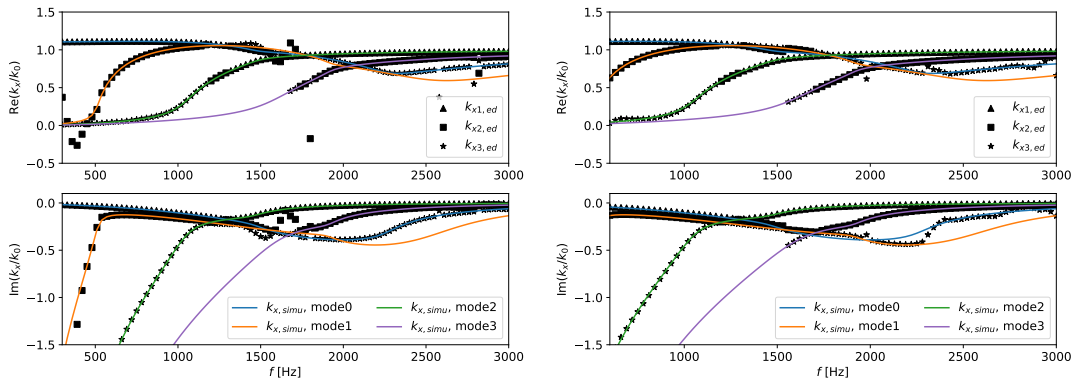

(a) Incident mode 0. (b) Incident mode 1.

Figure 4.23: Comparison between the wavenumbers ($k_{x,simu}$) calculated by the multimodal model and n-th retrieved wavenumber ($k_{xn,ed}$) in the cases with incident mode 0 (left) and 1 (right) in the presence of other modes at 30 dB lower.

Furthermore, it is noteworthy that the presence of noise can surprisingly alleviate the challenges posed by the perturbation of additional modes. Simulations conducted with noise (SNR = 30 dB) are shown in Figure 4.24, which presents the

impedance solutions corresponding to the same symmetry type as that of the incident mode. These impedances are still calculated using the first three retrieved wavenumbers. The figure demonstrates that in the presence of noise, the impedance solutions of the assumed symmetry type (same as that of the incident mode) are correct, in contrast to the situation shown in Figure 4.22. This effect may be due to the noise level masking the amplitudes of the additional modes. Consequently, the experiments in the next chapter can begin with the 1-line array.

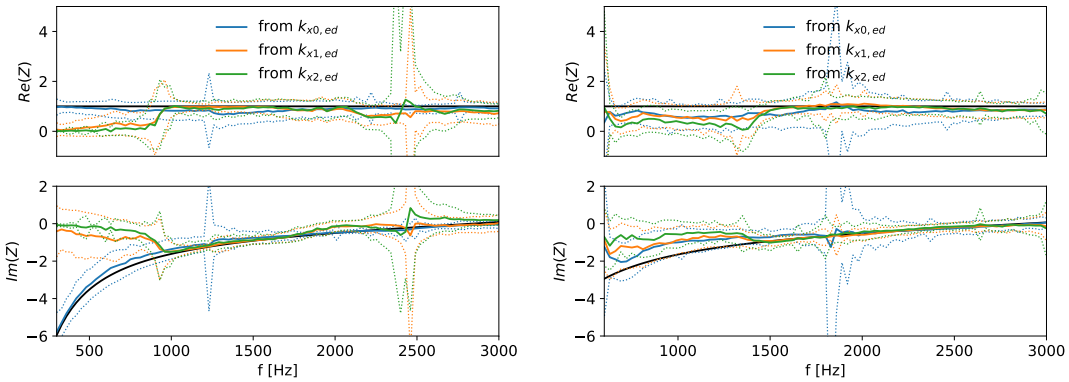

(a) Incident mode 0. Symmetric solution.

(b) Incident mode 1. Antisymmetric solution.

Figure 4.24: Educed impedance calculated by n-th retrieved wavenumber ($k_{xn,ed}$), for the incident mode 0 (left) and 1 (right) in the presence of other modes at 30 dB lower and of white noise at SNR of 30 dB. Solid line: mean value. Dashed lines: standard deviation.

4.3.2 2-line microphone array

The previous section demonstrates that the presence of additional modes undermines the advantages of the double-liner configuration. To address this issue, it is necessary to eliminate modes of undesired symmetry types from the pressure signals. Then, by ensuring that the signals consist solely of a single type of mode, the double-liner configuration can perform as intended.

It has been shown in Section 4.2.5 that positioning the microphone at H/2 can enhance the performance of impedance eduction for symmetric incident modes. This position corresponds to a pressure node of all antisymmetric modes, making it effective for isolating symmetric modes in the pressure signals and thereby eliminating antisymmetric modes. Conversely, the elimination of symmetric modes cannot be achieved merely by altering the position of the microphone array. Moreover, it is impractical to adjust the microphone position for different incident modes in practice.

To realise the elimination of both types of modes without complicated experimental implementation, a 2-line microphone array is developed. Figure 4.25 shows the deployment of the microphones in this new array. Two lines of 40 microphones are located at $1/3$ and $2/3$ of the duct height, recording pressure signals $p(H/3)$ and $p(2H/3)$, respectively. According to the property of the (anti)symmetry, the elimination can be achieved through simple operations on these two line pressure signals. For symmetric incident modes, the pressure signals used to estimate the axial wavenumbers are the sum of $p(H/3)$ and $p(2H/3)$. Conversely, for antisymmetric incident modes, the pressure signals used are the subtraction of $p(H/3)$ and $p(2H/3)$.

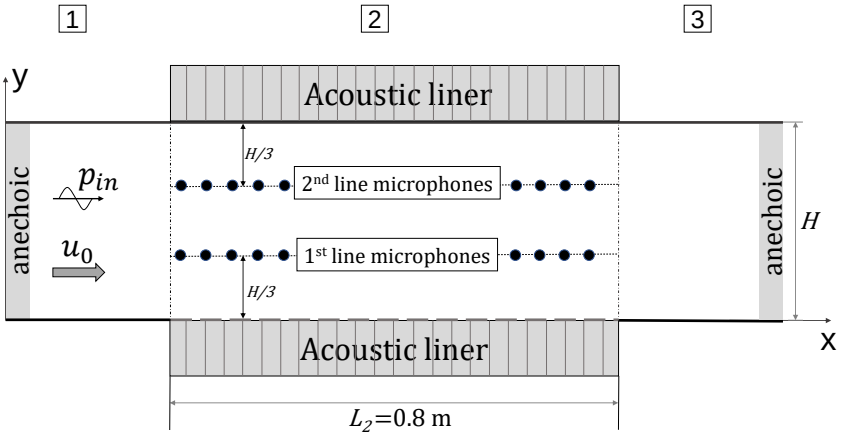

Figure 4.25: Schematic of the 2-line microphone array for the impedance eduction with the double-liner configuration, i.e. lined-lined boundaries in the middle section. The first and second lines are located at 1/3 and 2/3 of the duct height, respectively.

4.3.3 Results with the 2-line array for the double-liner configuration

4.3.3.1 Validation without flow

Using the newly developed array, the impedance eduction is conducted for the first two incident modes, again in the absence of flow. The acoustic field is still computed in the presence of perturbation modes. Figure 4.26 shows the impedance educed from the first three wavenumbers retrieved by HTLS method. It can be observed that the correct impedance is in accordance with the symmetry type of the incident mode.

In addition, Figure 4.27 displays the wavenumbers computed by the multimodal model and the ones retrieved from the operated pressure signals of the 2-line microphone array for both incident modes. The retrieved wavenumbers are associated to the modes that have the same symmetry as the incident one. Therefore, the use of the 2-line microphone array indeed eliminates the undesired modes and recovers the advantages of the double-liner configuration.

4.3.3.2 Validation with flow

Following the validation without flow, this section shows the eduction results using the 2-line microphone array for the double-liner configuration, in the presence of flow, without and with noise. The parameters remain the same as in the simulations for the double-liner configuration with the 1-line array (Section 4.2.2 and 4.2.5).

Figure 4.28 shows the educed impedance without noise for both incident modes propagating in both directions, and for several flow velocities. All results obtained for both directions agree well with the imposed impedance, except for those with $M_{\text{ave}} = \pm 0.5$, which show discrepancies at frequencies below 700 Hz. This is likely due to a numerical issue.

Figure 4.29 displays the eduction results in the presence of noise (SNR=30 dB). Compared with the results obtained by the 1-line array with a pure incident mode (refer to Figure 4.21), the results obtained using the signals from the operations between the 2-line are quite similar, except for results with $M_{\text{ave}} = 0.5$, which is previously observed in the noiseless case.

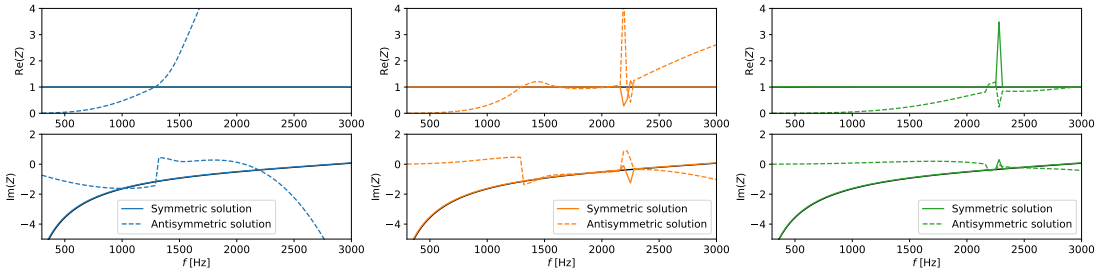

(a) Incident mode 0. From $k_{x1,ed}$. (b) Incident mode 0. From $k_{x2,ed}$. (c) Incident mode 0. From $k_{x3,ed}$.

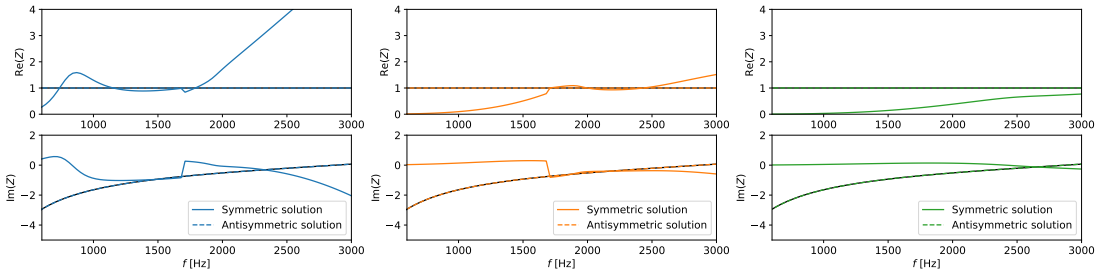

(d) Incident mode 1. From $k_{x1,ed}$. (e) Incident mode 1. From $k_{x2,ed}$. (f) Incident mode 1. $Z(k_{x3,ed})$.

Figure 4.26: Educed impedance from n-th retrieved wavenumbers, using the pressure signals obtained by the 2-line microphone array, for the incident mode 0 (top) or 1 (bottom) in the presence of other modes 30 dB smaller.

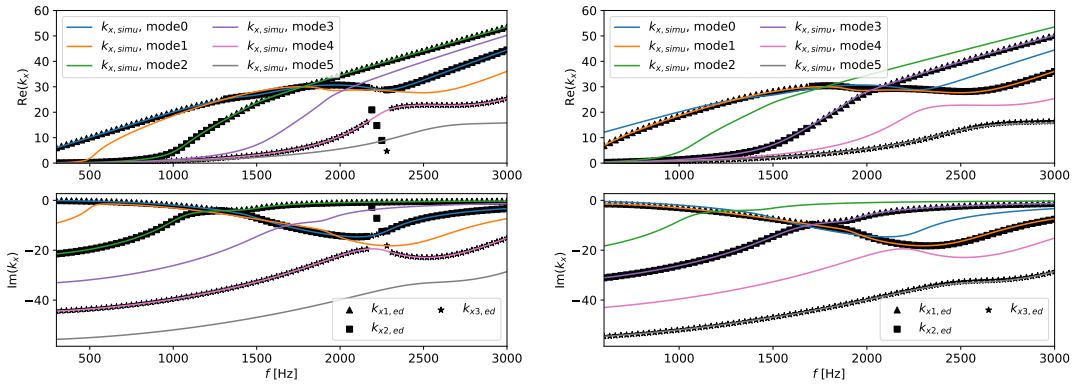

(a) Incident mode 0. (b) Incident mode 1.

Figure 4.27: Comparison between the wavenumbers ($k_{x,simu}$) computed by the multimodal model and the n-th retrieved wavenumber ($k_{xn,ed}$) in the cases with incident mode 0 (left) and 1 (right) in the presence of other modes 30 dB smaller. Retrieved wavenumbers are obtained using the operated signals of 2-line microphone array.

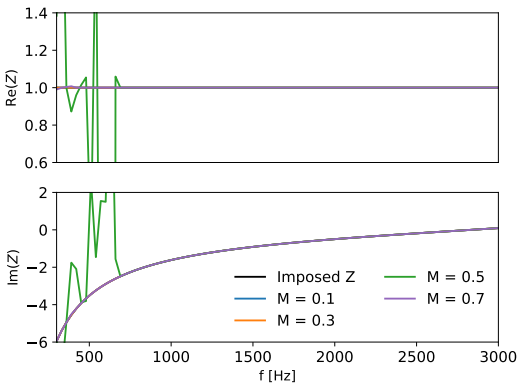

(a) Incident mode 0, downstream propagation

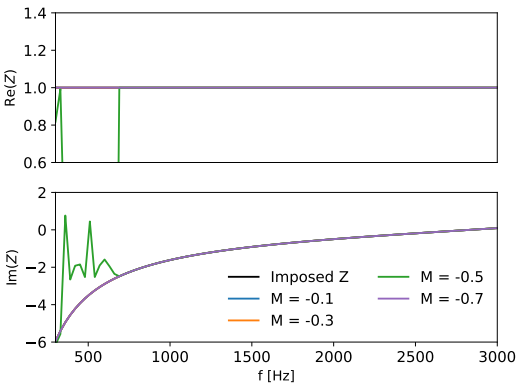

(b) Incident mode 0, upstream propagation

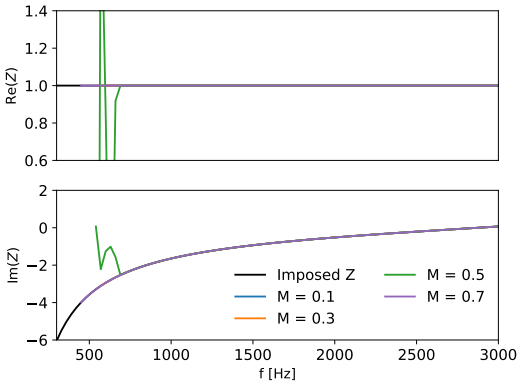

(c) Incident mode 1, downstream propagation

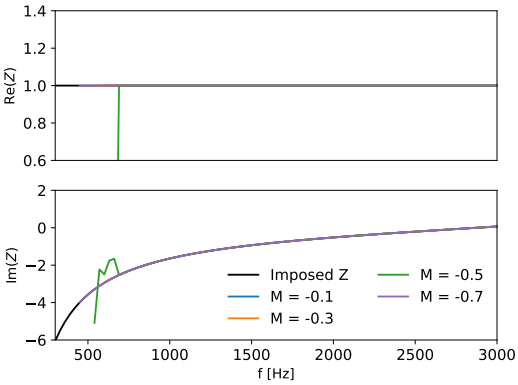

(d) Incident mode 1, upstream propagation

Figure 4.28: Educed impedance without noise using the 2-line microphone array, for different flow velocities in the same or opposite direction relative to the incident mode. Top: main incident mode 0. Bottom: main incident mode 1. Black solid line: imposed impedance.

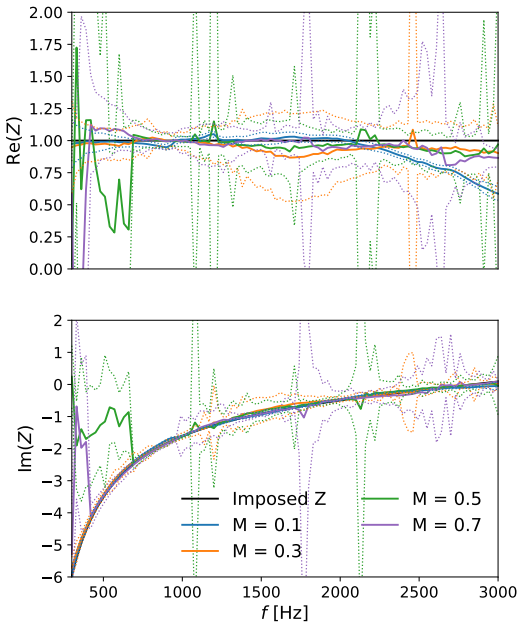

(a) Mode 0, downstream propagation

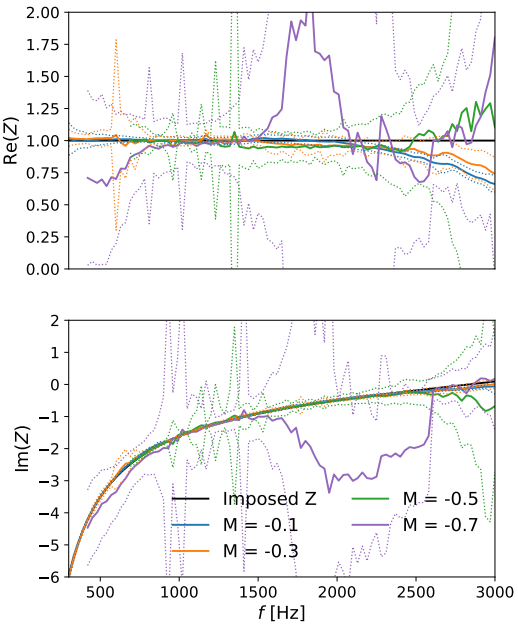

(b) Mode 0, upstream propagation

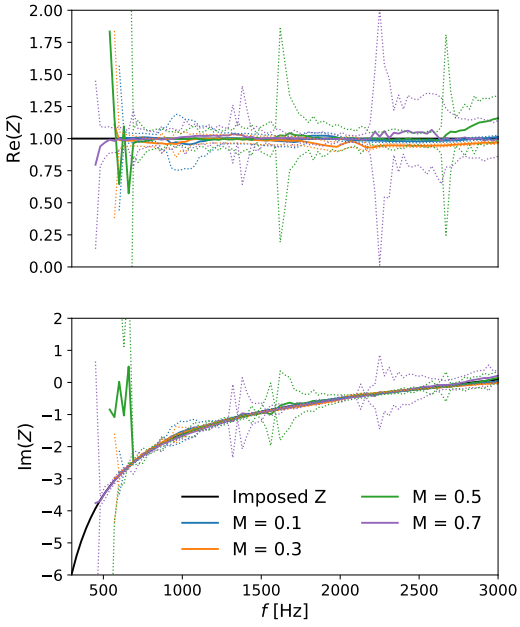

(c) Mode 1, downstream propagation

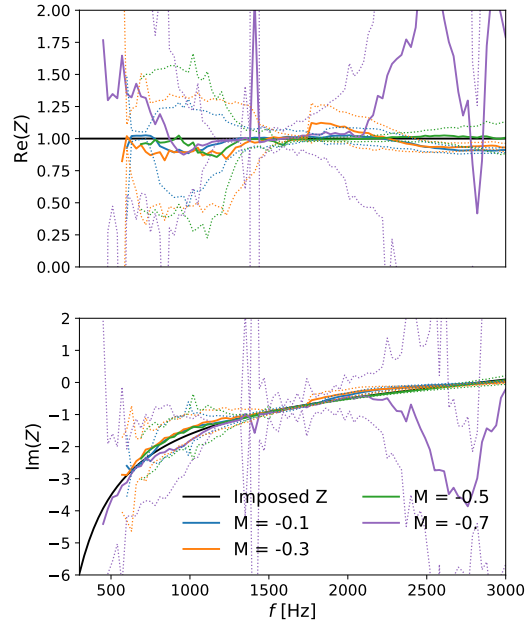

(d) Mode 1, upstream propagation

Figure 4.29: Educed impedance with noise (SNR = 30 dB) using the model with sheared flow. The 2-line microphone array is applied. Black line: imposed impedance. Coloured solid line: mean value of impedance. Coloured dashed line: standard deviation of the educed impedance around its mean value.

However, the standard deviation is larger for the results obtained with the two-line signals. This increase can be attributed to the operations (addition or subtraction) performed on the signals, both of which contain noise with an amplitude following a normal distribution. When two normal distributions are added or subtracted, the resulting distribution has a larger standard deviation σ, thereby reducing the SNR (which is inversely related to the noise standard deviation σ) in the final signal used for impedance eduction. Despite this, the results in real experiments, discussed in the next chapter, are expected to remain unaffected.

4.4 Conclusions

This chapter has explored various aspects of direct impedance eduction using pressure signals from simulations performed by the multimodal models introduced in Chapter 2.

The comparative analysis of the KT and HTLS methods have revealed that both approaches are viable for wavenumber estimation in small ducts (tests only performed in the single-liner configuration). However, the KT method generally offered lower accuracy under certain conditions, while the HTLS method shows greater robustness when the attenuation is weak. In addition, the KT method fails in the presence of noise perturbation. The HTLS method is selected thereafter, accompanied by the recommended setting for the Hankel matrix column number L in $[0.4N, 0.6N]$ [120].

In the context of the large MAINE Flow duct, numerical simulations have replicated the impedance eduction process, showing that the performance of the impedance eduction is significantly influenced by the flow assumption (uniform vs. shear) and the liner configuration (single vs. double-liner). The shear flow model combined with the double-liner configuration yields significant benefits compared to the standard approach (the model based on the uniform flow assumption and the single-liner configuration). The double-liner configuration consistently provides better performance compared to the single-liner configuration. The analysis of the mechanisms underlying this difference shows two main advantages of the double-liner, and offers insights for optimising the accuracy of impedance eduction. First, the symmetry of the double-liner configuration maintains the symmetry of the acoustic field according to the incident mode, and simplifies its modal content. On the other hand, the double-liner enhances the attenuation, thereby reducing the uncertainty of the impedance eduction method.

With these benefits, the double-liner also provides satisfactory impedance results in the presence of noise perturbations. The impact of noise in pressure signals is significant, affecting the accuracy of the impedance eduction with the single-liner configuration. It is confirmed by various tests with noise perturbations that the eduction results can be improved principally by increasing the acoustic attenuation along the lined section or simplifying the acoustic field composition. Therefore, the double-liner configuration is more favourable and promising in experiments.

In real experiments, perturbations in the incident field from modes other than the desired incident one are shown to mislead the impedance eduction, necessitating some changes to clear the signals feeding the wavenumber estimation. The development and implementation of a 2-line microphone array provides a practical solution to tackle this difficulty. Through the operations between the pressure signals at $1/3$ and $2/3$ of the duct height, this array effectively isolates symmetric and antisymmetric modes, leading to more accurate impedance eduction with the double-liner

configuration. This approach offers a significant improvement for real experiments, where mode perturbations are unavailable, and provides a robust method for enhancing the efficiency of the double-liner configuration.

Overall, this chapter demonstrates the effectiveness of various methods and configurations for the direct impedance eduction, preparing for the experiments on MAINE Flow in the next chapter. The studies highlight the benefits of the shear flow method, the double-liner configuration and the new 2-line microphone array.

Chapter 5

Experimental investigation of impedance eduction in multimodal ducts

This chapter contains the experimental part of this thesis, including the investigations within a large multimodal duct. Section 5.1 introduces the new configurations for the direct impedance eduction on MAINE Flow. The two microphone arrays proposed in the previous chapter are deployed on the test rig. The installation of acoustic liners and the procedure for the measurements are detailed. In the post-processing of experimental data, it is vital to select the correct wavenumbers from all the retrieved values in order to correctly calculate the impedance. For this task, two methods are developed and compared. When coming to the tests, a DDOF liner is first measured under various conditions in Section 5.2. The results are analysed, with an emphasis on the effects of different liner configurations (single or double), incident modes, SPLs, flow velocities and propagation directions. For the calculation of impedance from the wavenumbers, the uniform and shear flow method are compared through the experimental results. Section 5.3 discusses then the influence of the microphone spacing and compares the performance of one or two lines of microphones in the impedance eduction. Finally, Section 5.4 presents results with two sets of optimised SDOF liners in order to assess the performance of our impedance eduction methods with larger attenuation at high frequencies in the presence of flow.

5.1 Set-up

The main parameters of the experimental facility have been described in Chapter 2, including the dimensions and the methods for multimodal control of the incident field which were developed before the present thesis [10, 11].

This section focuses on the development and the implementation of the experiments for the direct impedance eduction on the MAINE Flow facility. The installation of liners and the microphones are first described, followed by the experimental procedure. Then, for the wavenumber estimation based on signals obtained by the microphone array, two new techniques are developed to select the right wavenumbers.

5.1.1 Configurations

5.1.1.1 Installation of the liner sample

Firstly, the installation of the acoustic liner, as mentioned in Chapter 2, can be carried out on both narrow sides (150×800 mm^2) of the duct test section. This

allows experiments using both single-liner and double-liner configurations. The inside length of the sample holder is 800 mm, and the width is 190 mm. The surface of the test liner is tightly pressed against the opening of the lined section (150×800 mm^2), and the extra part of the surface of the liner is pressed on the edge next to the opening. This ensures that the surface of the liner is flush with the inner wall of the duct and that the tested surface area of the liner is fixed at 150×800 mm^2. The sample holder is designed as a closed structure, ensuring rigid wall conditions around the liner. To accommodate liners of different thicknesses, the sample holder is equipped with a depth-adjustable rigid back plate. In the preparation of measurement, the position of the rigid slider is adjusted to fit snugly against the backplate of the liner.

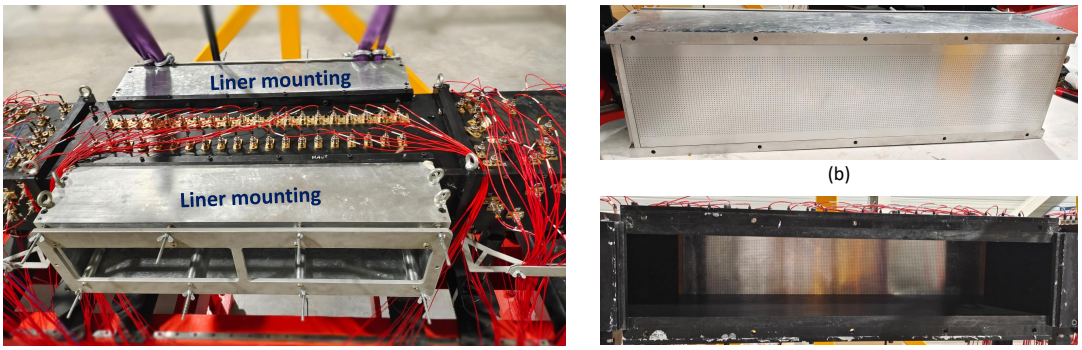

Figure 5.1: Illustration of the liner installation. (a): general view of the test section of the MAINE Flow duct, with liners installed at both sides, referring to the double-liner configuration. The 2-line microphone array is mounted in the test section. (b): sample holder with a liner inside. (c): opening (150×800 mm^2) of the lined section, against which the liner is pressed.

5.1.1.2 Microphone arrays

To acquire pressure signals for direct impedance eduction, and following the numerical simulations in Chapter 4, microphones are flush-mounted on the top wall (which is perpendicular to the liner) in the lined section, either along a single line (1-line) or along two parallel lines (2-line). Figure 5.2 shows the microphone arrays installed on the MAINE Flow rig.

The 1-line array of 40 evenly spaced microphones is positioned along the axis of the lined section and is situated at $2/3$ of the width from one of the lined walls. The distance between adjacent microphones is $\Delta x = 0.02$ m, with the first and last microphones placed 0.01 m into the lined section.

The 2-line microphone array is also composed of 40 microphones, with 20 situated both at $2/3$ and at $1/3$ of the duct width. In each line, the distance between adjacent microphones is $\Delta x = 0.04$ m. When using the 2-line microphone array, the 20 unused positions along the 40 points are sealed flush with the inner wall. Using half of the position in 1-line array, the first pair of microphones (in the flow direction) is placed 0.01 m into the lined section and the last pair is placed 0.03 m into the lined section.

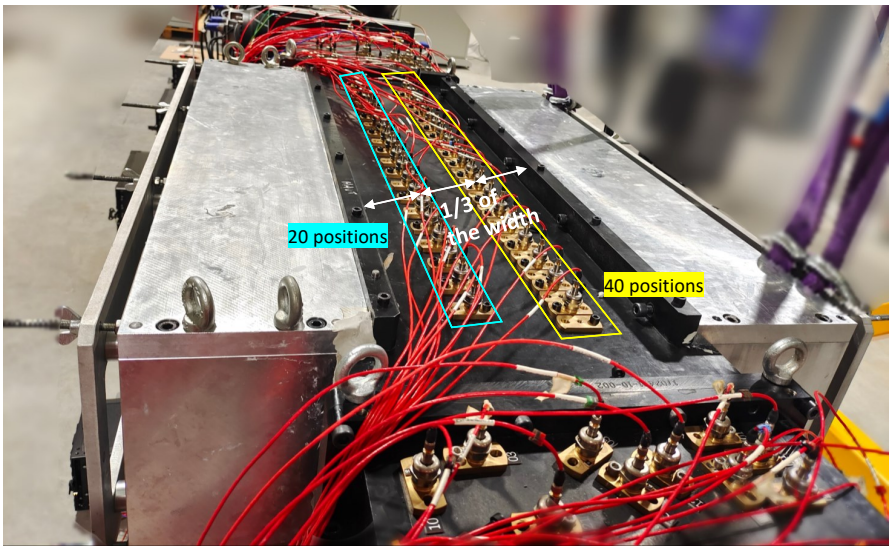

Figure 5.2: General view of the microphone arrays in the lined section for direct impedance eduction. The yellow box marks the 1-line microphone array that contains 40 evenly spaced positions with the distance $\Delta x = 0.02$ m. The blue box marks the second line of the 2-line microphone array, which contains 20 positions with a spacing of $\Delta x = 0.04$ m.

Before recording signals, the calibration of microphones is also essential in acoustic measurements when quantitative results are required. There are two types of calibration: absolute and relative. The absolute calibration is achieved individually for all the microphones (both in rigid and lined sections) using the GRAS 42AG, which concerns only the amplitude of signals. The relative calibration is also done for the microphones in the lined section, which concerns both the amplitude and phase of signals. To that end, a small cavity displaying an uniform acoustic field up to 3000 Hz is used for the two microphones to be compared. The most upstream microphone is taken as a reference, and the transfer functions are computed between the signals recorded by each microphone and the reference one at the frequencies of interest. In the processing of the pressure data, the transfer function is used to correct the signals of the associated microphone. For example, Figure 5.3 shows the signal before and after correction by the relative calibration. Note that, compared to the absolute calibration that is performed at 1000 Hz, the relative method gives an information about the frequency dependency of the calibration. However, it is a more time-consuming process.

5.1.1.3 Measurement procedure

Following the installation of the acoustic liner and microphones, the measurement procedure includes the following steps:

1. Flow speed monitoring: Acoustic measurements only begin once the flow speed is stabilised at the prescribed value. Golliard et al. [10] have detailed the methodology for measuring the Mach number in the MAINE Flow facility. A differential pressure sensor is installed between the settling chamber

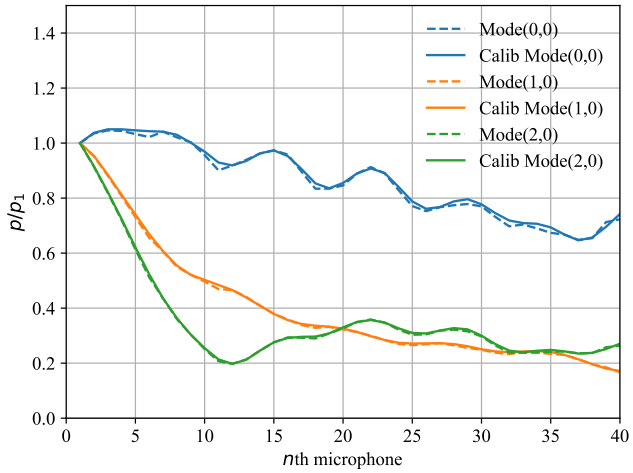

Figure 5.3: Pressure signals obtained by the 40 microphones in the 1-line array, normalised by the most upstream microphone, at $f = 1400$ Hz before (dashed lines) and after (solid lines) the relative calibration process. The various colours correspond to the individual incident modes (0,0), (1,0) and (2,0), at SPL=120 dB.

(where air enters at atmospheric conditions) and the test duct inlet. By measuring also the total temperature in the settling chamber, the Mach number at the upstream end of the duct can be obtained. Additionally, temperature and atmospheric pressure are monitored along the test duct, enabling the Mach number at the liner to be obtained.

2. Temperature control: High flow speeds can induce a severe drop of the temperature in the test section, due to the fact that the facility is working with a fan in suction mode. Therefore, in cases of high flow speeds or cold weather, heating resistances are employed to maintain a chosen and appropriate temperatures within the duct test section, preventing issues such as condensation or freezing. If heating is necessary, the temperature within the test section is controlled and kept constant during the tests.

3. Modal excitation: Through previous measurements, the transfer function between all the sources (upstream or downstream) and the rigid duct modes is known. Thus, we can select a desired incident mode (n, m) and incident amplitude. The control system then adjusts the amplitude and phase of each source as a function of frequency to produce a stepped-sine excitation signal. For an incident mode (n, m), n denotes the direction perpendicular to the liner, while m represents the transverse direction.

4. Data acquisition and analysis: The temperature and pressure conditions recorded are used to calculate the air density and speed of sound. The microphones in the lined section capture the acoustic pressure data, and then the data are post-processed using the methodologies outlined in Chapter 2 to educe the impedance of the tested liner.

Based on this, we can perform the impedance eduction with a controlled multimodal acoustic field in the large MAINE Flow duct. Since the proposed method (using shear flow assumption) considers mean flow shear in 2D case, only the flow profile in the direction perpendicular to the acoustic liner shown in Figure 4.4 is

used for the impedance calculation. The 2D model introduced in Chapter 2 already includes the key features for this study: a parallel shear flow and high-order cut-on modes. The effects of these two features are equally relevant in 2D and 3D. In 3D, the presence of additional modes along the depth of the cross-section is not expected to change the trends identified with the 2D model in Chapter 3 and 4. Hence, the present facility allows for the experimental investigation of the effects of different incident modes, various SPLs, different flow velocities and wave incident directions relative to the flow, and microphone arrays.

5.1.2 Wavenumber selection in signal post-processing

The first task after acquiring the signals from the microphone array is to extract the axial wavenumbers for subsequent calculation of the impedance. In the process of estimating the wavenumber using the HTLS method described in Chapter 2, numerous parameters need adjustment, and there are various choices to consider. This section focuses on how to accurately extract wavenumbers based on the experimental data obtained from the microphone array.

Given N microphones, the minimum failure rate of the HTLS method occurs with the column number L of the Hankel matrix in the interval $[0.4N, 0.6N]$ [120], so L is set to 22, following Chapter 4. In that chapter, criteria for wavenumber selection are applied on simulated data. However, these criteria often prove unsatisfied when processing experimental data due to noise perturbations and incertitudes in measurements. Consequently, the following methods are specifically designed to address the nuances of experimental data, providing more practical and accurate means for impedance eduction. The wavenumber estimation process contains two main choices: the truncation number K in the HTLS method, and selecting the wavenumber from multiple wavenumbers once K is set.

In the first step, K can be interpreted as the expected number of propagating modes within the duct test section. It is understood that a larger K includes more modal information but increases the risk of noise influence, whereas a smaller K limits the number of modes. While the latter is more stable, it may not yield enough accurate results. Several supplementary algorithms exist in the field of exponential parameter estimation, such as SAMOS [122], which aims to select automatically the optimal truncation number that appropriately exclude noise channels, thus providing more accurate exponential parameters. However, these algorithms, effective in numerical simulations, have been found to be difficult to work accurately with the experimental data obtained in the present study.

Therefore, K is here selected based on the physical considerations and the accuracy of the reconstruction of the pressure signal along the liner, compared to the measurement, when the amplitudes and wavenumbers are obtained. To that end, different values of K from 1 to 8 are first tested, and for each K a set of wavenumbers $\{k_{x1,ed}, k_{x2,ed}, ..., k_{xn,ed}\}$ is obtained. For each set of wavenumbers, the amplitudes A_n corresponding to each retrieved wavenumber are calculated using the Least Squares Estimation method based on the measured pressure signals $\mathbf{p}_{\mathrm{me}}$. Then, wavenumbers and amplitudes are used to reconstruct the pressure at all microphone positions $\mathbf{x}$. Each K corresponds to a reconstructed signal $\mathbf{p}_{\mathrm{re}}$, and the K that induces the smallest L2-norm error between the reconstructed and measured signals is optimal. This can be summarised as:

$$\mathbf{p}_{\text{re}} = \sum_n A_n \mathrm{e}^{-\mathrm{i}k_{xn}\mathbf{x}} \quad , \tag{5.1a}$$

$$K = \arg\min_K \frac{\|\mathbf{p}_{\text{re}} - \mathbf{p}_{\text{me}}\|_2}{\|\mathbf{p}_{\text{me}}\|_2} \quad . \tag{5.1b}$$

When K is set to a small value, less noise subspace is contained in the decomposition of signal and the results will be less perturbed; when K is set to a large value, the errors of reconstructed signal decreases due to the consideration of more modes, but with a risk of noise perturbation. Thus, a trade-off between a smaller K and minimal reconstruction error is sought.

Once the truncation number K is determined, and hence a set of wavenumbers is identified in the pressure evolution at a given frequency, the next step is to select one wavenumber ($k_{x,ed}$) from this set for the impedance calculation. To this end, two approaches are developed in this study.

The first method is inspired by, though not entirely equivalent to, the approach used by NASA in [22]. For the obtained set of wavenumbers $\{k_{x1,ed}, k_{x2,ed}, ..., k_{xn,ed}\}$, the impedance corresponding to each wavenumber can be calculated using either the uniform flow method or the shear flow method. Subsequently, each impedance value $Z(k_{xn,ed})$ is used to compute the acoustic field by means of the multimodal model described in Chapter 2, which provides a set of simulated signals $\mathbf{p}_{\text{simu}}$ at the same microphone points as in the experiments. Then, the L2-norm error between each set of simulated signals and the original measured signals is calculated. Finally, the wavenumber corresponding to the simulated signal with the smallest error is selected. This method is computationally intensive, since it requires numerous computations of the acoustic field, and it can be expressed as:

$$k_{x,ed} = \frac{\arg\min_{Z(k_{xn,ed})} \|\mathbf{p}_{\text{simu}}(Z(k_{xn,ed})) - \mathbf{p}_{\text{me}}\|_2}{\|\mathbf{p}_{\text{me}}\|_2}. \tag{5.2}$$

The second method is to select the wavenumber associated with the mode that contributes most to the whole signal. The contribution of each mode is defined as the L2 norm of the decomposed signal, i.e. $\|\mathbf{p}_n\|_2 = \|A_n \mathrm{e}^{-\mathrm{i}k_{xn}\vec{x}}\|_2$ with A_n the n-th mode amplitude. This method can be expressed as

$$k_{x,ed} = \arg\max_{k_{xn,ed}} \|\mathbf{p}_n\|_2. \tag{5.3}$$

This method offers the distinct advantage of computational efficiency.

Comparison of the two methods

The comparison between the two methods (described in Eq. (5.2) and Eq. (5.3)) for the selection of the wavenumber to be used in the impedance eduction is illustrated in Figure 5.4. The figure displays the wavenumbers retrieved by both methods and the resulting educed impedance using the shear flow method. The incident modes considered separately are (1,0) and (3,0), and they propagate downstream with an average Mach number M_{ave}= 0.3. The impedance results are not smoothed for the purpose of comparisons based on their intrinsic quality.

As shown in Figure 5.4(a), the wavenumbers selected by both methods are consistent at low frequencies, with differences becoming more apparent in the high-frequency range, where more modes propagate. Despite the differences in

wavenumber selection, the final impedance results using both methods, displayed in Figure 5.4(b), are mostly consistent.

Given the comparable accuracy of the eduction results, this study prefers the second method due to its significantly shorter computational time. This choice simplifies the analysis process without compromising the quality of the impedance eduction results, making it the preferred approach in the following for handling experimental data efficiently.

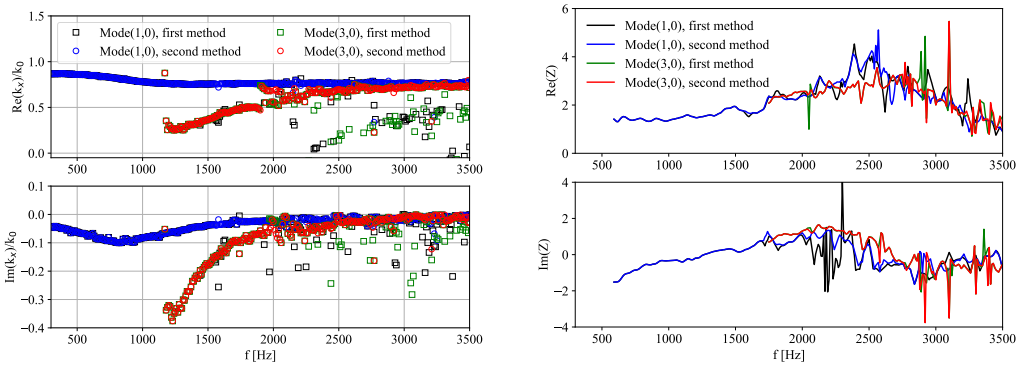

(a) Retrieved wavenumber.

(b) Educed impedance.

Figure 5.4: Left: retrieved wavenumbers used to calculate the impedance, selected using the two methods (in Eq. (5.2) and in Eq. (5.3)). Right: impedance computed using the shear flow model with the wavenumbers in (a). Incident modes are individually (1,0) and (3,0), in the downstream propagation direction, with an average Mach number of 0.3.

5.2 Tests with DDOF liners

The experiments are first conducted with double-degree-of-freedom (DDOF) liners. Figure 5.5 presents the impedance predicted by the liner model of the industrial partner, with incident amplitudes ranging from 120 to 150 dB without flow, and Mach numbers ranging from 0 to 0.6 with incident amplitudes at 150 dB against flow. The 1-line array, containing 40 microphones, is firstly used.

The tests cover different flow velocities and wave/flow directions, various incident modes, and different liner configurations. First, the eduction performance of the single- and double-liner configurations are compared without flow. Also, different incident modes at various SPLs are considered in the double-liner configuration. Then, tests are conducted for several flow velocities and the results obtained considering either uniform or shear flow assumptions are described and compared. Finally, the influence of the flow velocity is discussed, as well as the impact of the chosen incident mode.

5.2.1 Without mean flow

5.2.1.1 Liner configurations

First, experiments are conducted without flow for both configurations (single-liner and double-liner) across a frequency range spanning 300 to 2000 Hz, with increments of 10 Hz. The amplitude of the incident mode is 120 dB. As methods are by definition equivalent without flow, the uniform and shear flow methods introduced

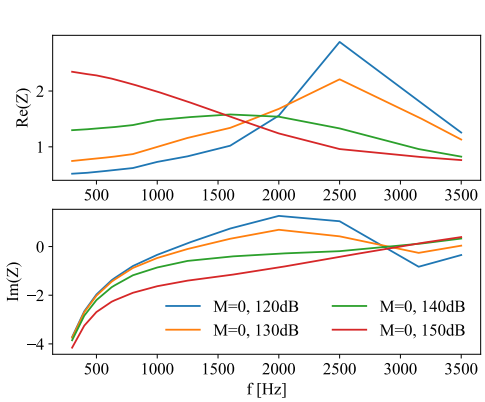

(a) Effect of the incident SPL.

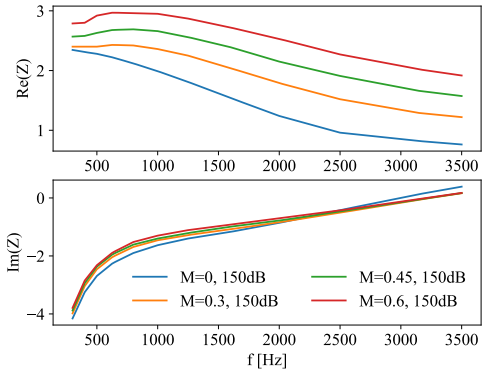

(b) Effect of the Mach number, for upstream propagation at 150 dB

Figure 5.5: Predicted impedances of the tested DDOF liner.

in Section 2.3.2 provide exactly the same educed impedance. Thus, in this section, only the results obtained using the shear flow method are presented.

Figure 5.6 illustrates the educed impedance obtained for the incident modes (0,0) and (1,0) in both directions of propagation. It can be seen that the eduction is more accurate with the double-liner configuration compared to the single-liner one. Indeed, the agreement between results of two directions is improved when there are two liners, and the results are smoother at high frequencies. In the single-liner case, although the mode (1,0) shows similar results between the two directions of propagation, the results follow a trend differing from the model impedance when the frequency increases.

To further understand these discrepancies, Figure 5.7 shows the measured axial wavenumbers for downstream propagation for both configurations, corresponding to the impedance results in blue in Figure 5.6. For the mode (0,0) in the double-liner case, it is apparent from Figure 5.7(b) that the retrieved wavenumbers have a stable trend along the frequency, while for the single-liner in Figure 5.7(a) several wavenumbers after 1200 Hz are far away from the main trend. For the single-liner configuration, the real parts of the two mode wavenumbers overlap perfectly. However, the imaginary part of the mode (1,0) drifts away from 0, despite its clean trend over the frequency range. The main explanation for the results in Figure 5.6(b) is thus that the HTLS method gives inaccurate results in this case.

The attenuation rate also plays a central role in the performance of the impedance eduction [17, 121]. Figure 5.7 shows that the attenuation is larger for the double-liner configuration compared to the single-liner one, for the two incident modes. Both configurations perform well at low frequency, due to the large attenuation rate. For higher frequencies, the single-liner configuration becomes less accurate as the modal attenuation decreases, whereas the double-liner remains accurate. Another reason for the good performance achieved by the double-liner configuration is that it preserves the symmetry of the incident sound field. As described in Chapter 4, a symmetric incident mode will be scattered only onto other symmetric modes (antisymmetric modes will not be excited). As a consequence, the number of modes present in the lined section of the duct is reduced, which makes the identification of their wavenumbers easier. When both symmetric and antisymmetric modes are present (such as in the single-liner case), a greater number of exponentials should be identified by the HTLS method, which can increase the error.

To further clarify the difference in effectiveness between the two configurations,

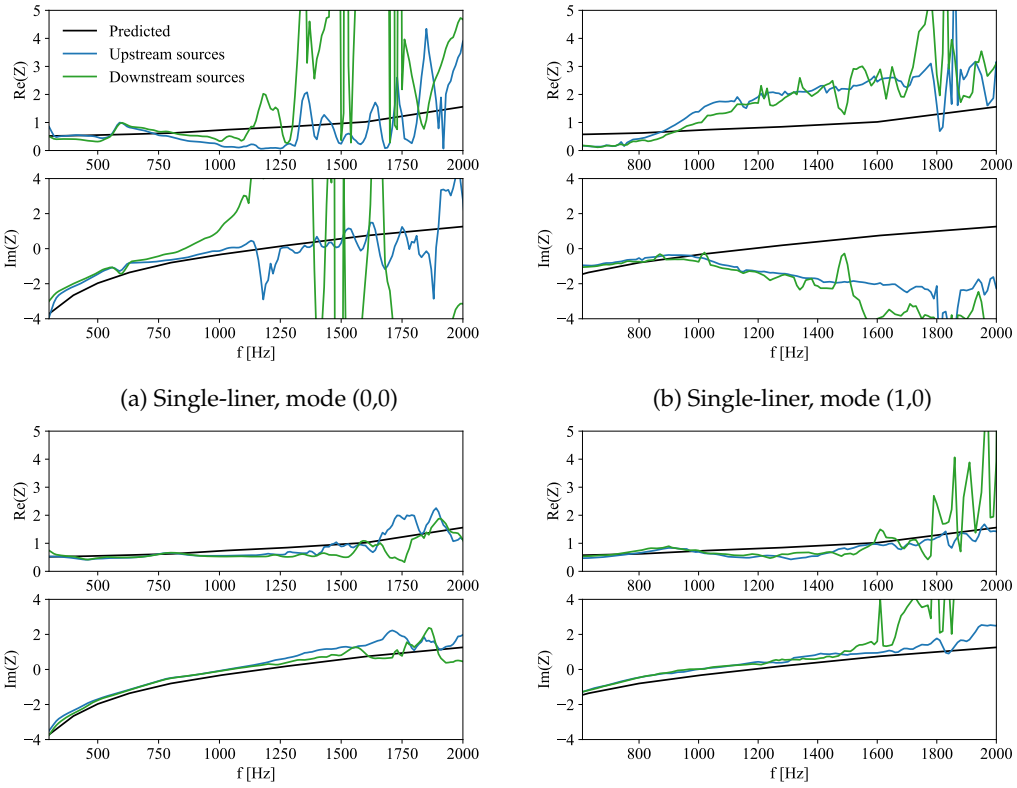

(a) Single-liner, mode (0,0)

(b) Single-liner, mode (1,0)

(c) Double-liner, mode (0,0)

(d) Double-liner, mode (1,0)

Figure 5.6: Educed impedance without flow for both single- (Top) and double-liner (Bottom) configurations. Left column is obtained for an incident plane wave, right column for an incident vertical mode $(1,0)$. The incident modes with an amplitude of 120 dB are propagating either in the same direction as the flow (blue), either against it (green). Black line: predicted impedance.

Figure 5.8 compares the pressure field $\mathbf{p}_{\text{me}}$ measured by the microphone array and the pressure field reconstructed with the wavenumbers and amplitudes identified by the HTLS method. The latter is computed as $p_{\text{re}}(x) = \sum_n A_n \text{e}^{-\text{i}k_{xn,ed}x}$ with a selected set of retrieved axial wavenumber $k_{xn,ed}$. The difference between the two fields is quantified by the relative L_2-norm error between the pressure values. According to this analysis, the relative error for the double-liner configuration is almost always below 20% and lower than that for the single liner, indicating that the acoustic field is more accurately reconstructed in the double-liner case.

5.2.1.2 Influence of sound pressure levels

In view of the greater performance of the double-liner configuration, the single-liner configuration is not used in the remainder of the manuscript. To study the influence of the incident modes and of the SPL, experiments are now carried out without flow for the first 4 incident modes with amplitudes varying between 120 and 150 dB. To consider higher-order modes, the maximal frequency is now 3500 Hz. Note that a moving-average smoothing is now applied to the measured liner impedance along the frequency axis in order to facilitate the readability of the overall trends. Also,

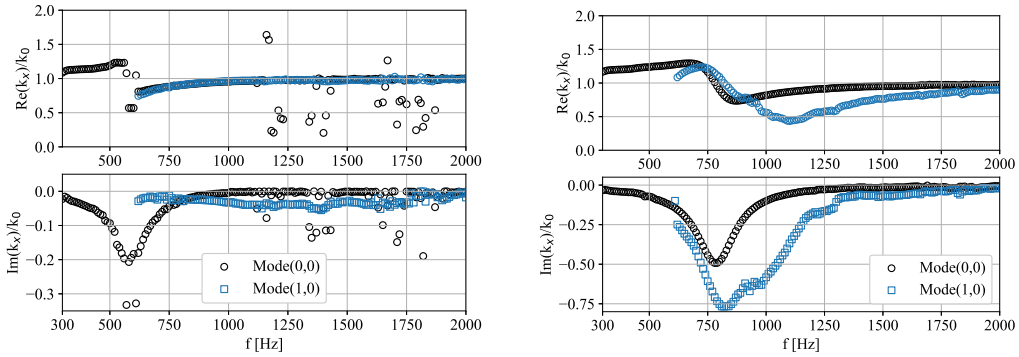

(a) Single-liner (b) Double-liner

Figure 5.7: Retrieved axial wavenumbers, normalised by k_0, as a function of frequency for both single- and double-liner configurations. The sources are located on the upstream side.

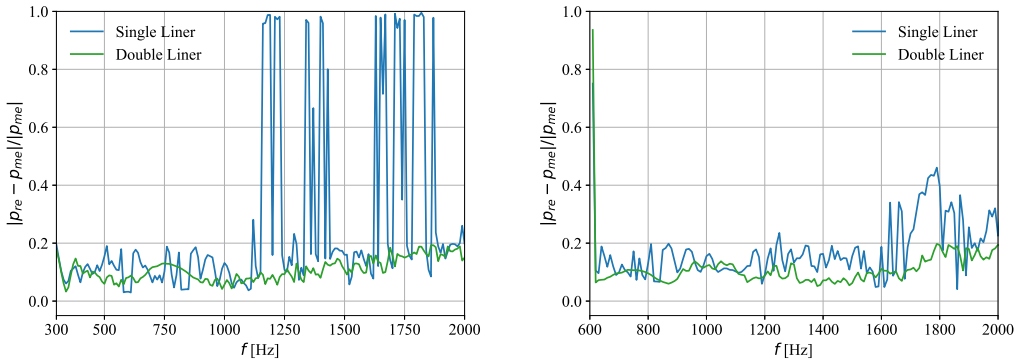

(a) Mode(0,0) (b) Mode(1,0)

Figure 5.8: Relative error $\|\mathbf{p}_{\text{re}} - \mathbf{p}_{\text{me}}\|_2 / \|\mathbf{p}_{\text{me}}\|_2$ of the reconstructed acoustic pressure field at the microphone positions for both single- and double-liner configurations. The sources are located on the upstream side.

for the sake of brevity and given the good agreement between the two directions observed in the previous section, the results are only displayed for downstream propagation.

Figure 5.9 shows the educed impedances using incident modes (0,0) and (3,0) as representatives of the two types of symmetry. First, below 1500 Hz, Figure 5.9(a) shows that the resistance increases and the reactance decreases with increasing SPL. Then, Figure 5.9(b) shows that the first anti-resonance of the liner, located between 2000 and 2750 Hz, fades as the SPL increases. These are clear evidences of a nonlinear behaviour of the tested liner in presence of high SPL. It is also noticeable that the antisymmetric mode used for Figure 5.9(b) provides cleaner results. This is most likely due to its larger attenuation rate, compared to the plane wave. For the latter, as the sound field becomes more complex at high frequencies, the impedance results contain more oscillations. When compared with the predicted impedances of the tested liner, the trends in the measured impedance agree with that of the predicted values.

Figure 5.10 compares the impedance eduction results obtained with the first 4 modes at incident SPLs of 120 and 150 dB. At 120 dB in Figure 5.10(a), it is observed

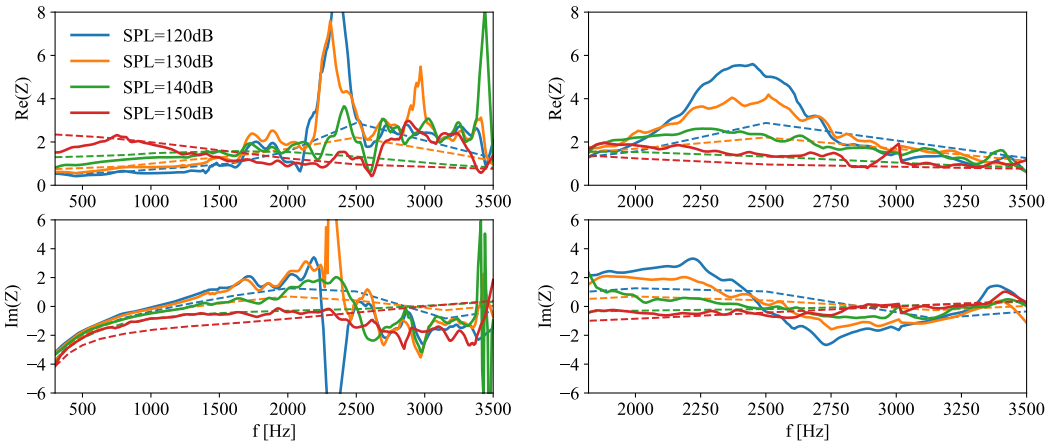

(a) Mode (0,0)

(b) Mode (3,0)

Figure 5.9: Educed impedance without flow for the double-liner configuration using incident modes (0,0) and (3,0), as representative of the two types of symmetry, in the downstream direction. Dashed lines: predicted impedances.

that each incident mode yields similar results before 2000 Hz. After 2000 Hz, depending on the symmetry of the incident mode, the educed impedance exhibits two different behaviours. The impedances measured using the antisymmetric modes (1,0) and (3,0) show a clear anti-resonance, with smaller rise and fall for the higher-order mode (3,0). In comparison, the impedances educed using the symmetric modes (0,0) and (2,0) display large oscillations after 2000 Hz, making it difficult to observe an anti-resonance. Therefore, using antisymmetric incident modes provide more robust results for the direct impedance eduction, most likely due to greater attenuation rates. At 150 dB in Figure 5.10(b), similarly to before, the impedance results show slightly different trends according to the symmetry of the incident mode at high frequencies. However, and in contrast to 120 dB, the results for the symmetric modes are less oscillating and more consistent. The reason might be the disappearance of the anti-resonance due to the non-linear effects at high amplitudes. Indeed, the liner impedance is then closer to the optimal impedance of the duct, inducing more acoustic attenuation, and thus cleaner results.

5.2.2 With mean flow

This section considers the impedance eduction in both directions in the presence of flow. Since the educed impedance can be calculated using a model with a uniform flow, or a model including the mean flow shear, a comparison between these two models is first conducted.

5.2.2.1 Comparison between the two eduction methods

To that end, experiments are carried out with the mode (0,0) at 150 dB for two average Mach numbers: $M_{\text{ave}} = 0.29$ and $M_{\text{ave}} = 0.45$. Since the results in the upstream propagations cases are poor at high frequencies due to the low acoustic attenuation and the large noise perturbations in presence of flow, these comparisons focus on low frequencies.

Figure 5.11 displays the educed impedance using either the uniform or the more accurate one – shear flow model. The predicted impedance is only for the upstream

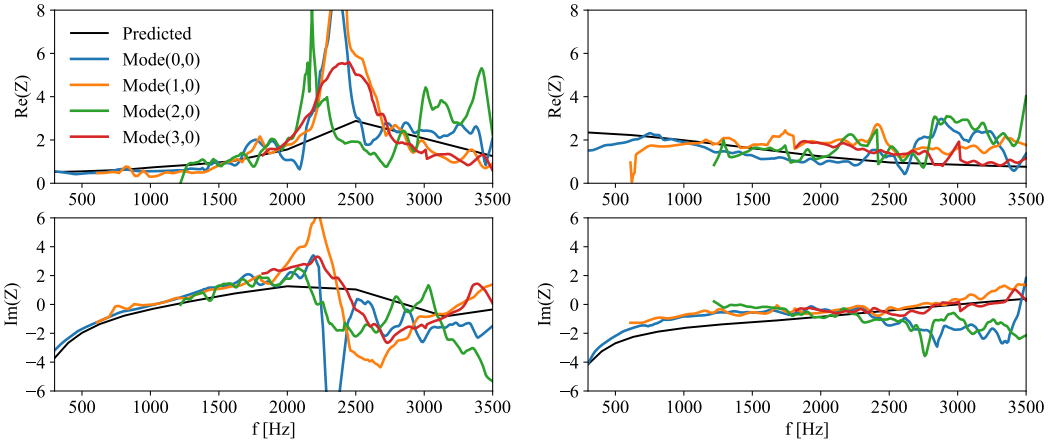

(a) SPL = 120 dB

(b) SPL = 150 dB

Figure 5.10: Educed impedance without flow for the double-liner configuration. The first 4 modes are generated at SPLs of 120 (a) and 150 dB (b) in the downstream direction. Black: predicted impedance.

propagation case. As observed in Figure 5.11(a), the difference between the educed impedance obtained by the two methods is not significant at low frequencies and becomes larger at higher frequencies. Furthermore, the discrepancy is more pronounced when the acoustic propagation is against flow (as seen in Figure 5.11(b) compared to (a)), and when the flow velocity increases (in Figure 5.11(d) compared to (b)). It is therefore important to include the mean flow shear in the impedance eduction process when working with large ducts and for high flow velocities. The present experimental results thus confirm the conclusions of the numerical study in Chapter 3 and Chapter 4. The shear flow method is therefore used for the following experiments.

5.2.2.2 Effects of the flow velocity

This section focuses on the impedance eduction with different average Mach numbers M_{ave}: 0.10, 0.29, 0.45 and 0.575. For each Mach number, the first 2 modes are generated separately with a 130 dB amplitude, either from upstream or downstream. There is no impedance model prediction at 130 dB in presence of flow. Also here the effects of the flow velocity are only assessed for a given incident mode. The discussion regarding the dependence of the educed impedance with respect to the selected incident mode in presence of flow is addressed in Section 5.2.2.3.

Firstly, Figure 5.12(a) shows that when M_{ave} increases from 0.10 to 0.45, the resistance rises and the reactance decreases. However, the curves at $M_{ave} = 0.575$ do not follow this trend, with a resistance between the results obtained at $M_{ave} = 0.29$ and at $M_{ave} = 0.45$ and a reactance significantly lower than the other three. For the upstream propagation (see Figure 5.12(b)), the low-frequency range displays a large increase of the resistance and a decrease of the reactance with increasing flow velocity. These trends are more pronounced than for the downstream propagation case. When comparing Figure 5.12(b) and (a) at low frequency, the resistances appear clearly larger for waves propagating against the flow, especially for high Mach numbers. Unfortunately, the results quality at high frequencies is poor and prevents

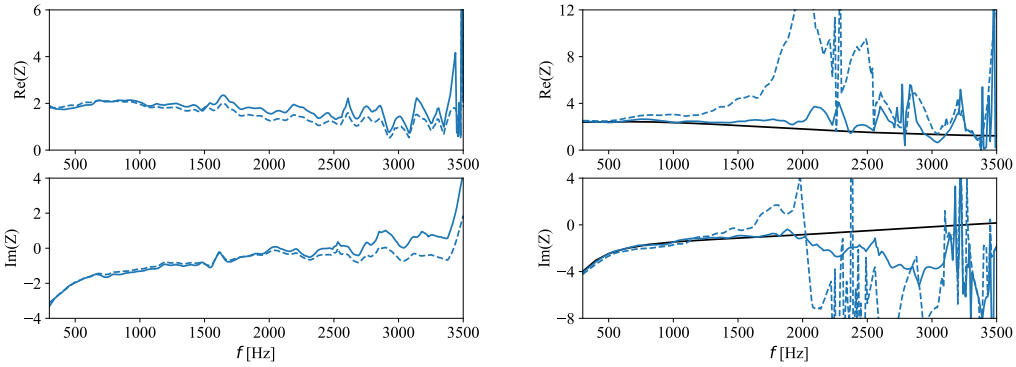

(a) $M_{\text{ave}} = 0.29$, downstream propagation

(b) $M_{\text{ave}} = 0.29$, upstream propagation

(c) $M_{\text{ave}} = 0.45$, downstream propagation

(d) $M_{\text{ave}} = 0.45$, upstream propagation

Figure 5.11: Educed impedance for the double-liner configuration using either shear (blue solid lines) or uniform (blue dashed lines) flow assumptions. Black solid line: predicted impedance of the liner. The mode (0,0) is incident at 150 dB in both directions.

any conclusion for the fast flows. Moreover, the frequency at which large errors appear decreases as a function of flow velocity. This can be explained by the decrease of the signal-to-noise ratio when the flow velocity increases.

When the mode (1,0) is used (see Figure 5.12(c) and (d)), the trends observed as a function of the Mach number in the downstream propagation case are roughly the same as for the plane wave, but they look a bit cleaner. This is probably due to a larger attenuation rate.

The results for the upstream propagation case are only usable at low frequency, and their behaviour is the same as for the plane wave. For the higher-order modes that are not shown here, the results follow trends similar to that of the low-order modes with the same symmetry, but look noisier.

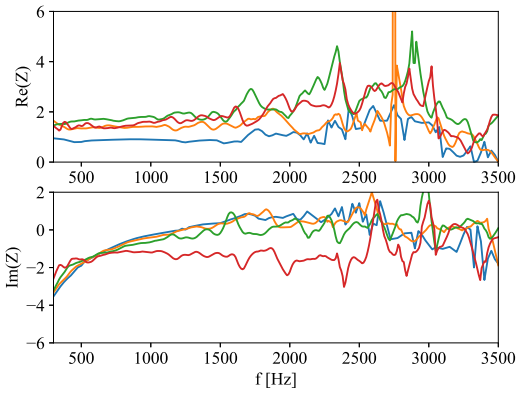

(a) Mode (0,0), downstream propagation

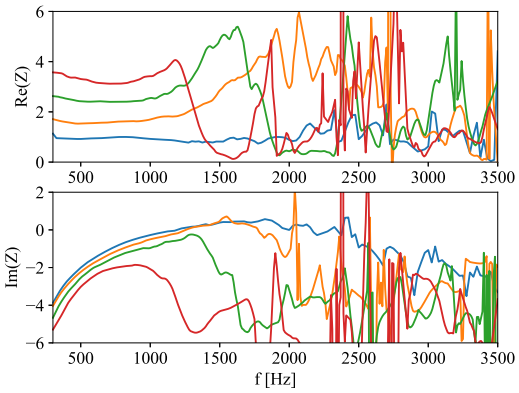

(b) Mode (0,0), upstream propagation

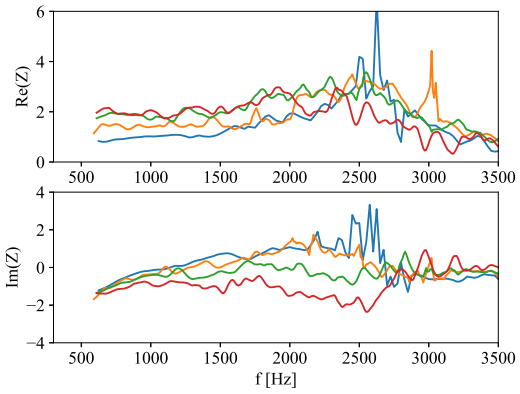

(c) Mode (1,0), downstream propagation

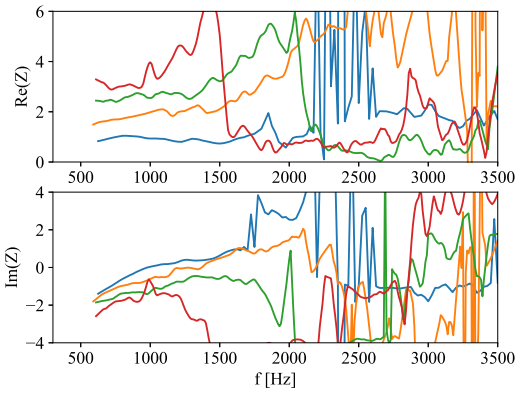

(d) Mode (1,0), upstream propagation

Figure 5.12: Educed impedance as a function of frequency for average Mach numbers 0.10 (blue), 0.29 (orange), 0.45 (green) and 0.575 (red). The incident modes are the modes (0,0) (Top) and (1,0) (Bottom) with an amplitude of 130 dB.

5.2.2.3 Influence of the incident mode

This section discusses the influence of the incident mode on the impedance eduction in the presence of flow.

Figure 5.13 shows the educed impedance with a mean flow Mach number of 0.29. Note that, as for the case without flow, antisymmetric incident modes provide less noisy results, witnessing a more robust direct impedance eduction process. In Figure 5.13(a), it is observed that all incident modes lead to the same impedance below

2000 Hz. For higher frequencies, two trends are followed by the resistance, and this seems to depend on the symmetry of the incident mode. Nevertheless, the reactance obtained with symmetric modes (0,0) and (2,0) show discrepancies. Regarding the upstream propagation case in Figure 5.13(b), the first two cut-on modes provide similar results at low frequency, but then deviate above 1500 Hz. For higher frequencies, each mode seems to provide a different impedance. However, the results are noisy and not conclusive. It is thus difficult to analyse and discuss properly the relation between the incident mode and the educed impedance.

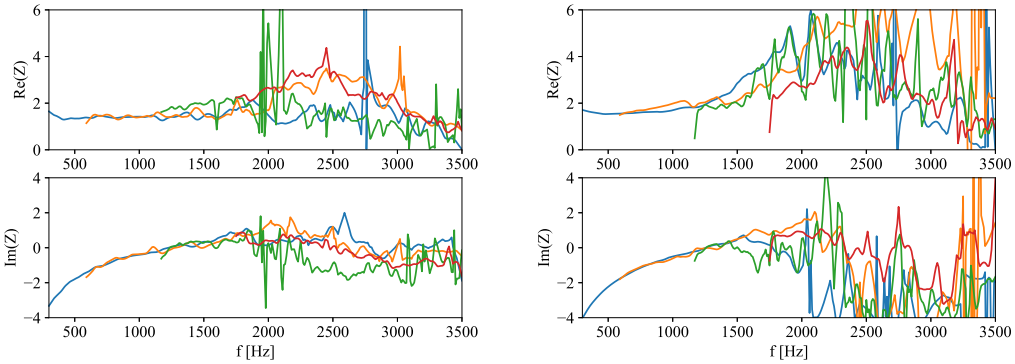

(a) Downstream propagation

(b) Upstream propagation

Figure 5.13: Educed impedance in the presence of flow at M=0.29 with incident modes at 130 dB in both directions. Blue: mode (0,0). Orange: mode (1,0). Green: mode (2,0). Red: mode (3,0).

5.3 Comparison of microphone arrays

According to the previous results, the trend of the educed impedance obtained with various incident modes depends on the mode symmetry. Moreover, while accurate measurements can be obtained in many cases, the performance of the eduction method at high frequencies and for sound propagation against the flow remains to be improved.

This section uses the 2-line microphone array to perform the impedance eduction with the DDOF liners. As proved in Chapter 4, the 2-line array allows separating symmetric and antisymmetric modes in the pressure signals, enhancing the accuracy of impedance eduction with the double-liner configuration.

5.3.1 Comparison between 20 and 40 axial positions

Given that the 2-line array has twice the axial spacing between microphones compared to the 1-line array, the performance of 20 versus 40 microphone positions is first compared to assess the impact of reduced axial resolution (Δx increasing from 2 cm to 4 cm). This analysis uses pressure signals from either all the 40 microphones or only the half of them within the 1-line array setup. To evaluate the quality of the results, the moving-average smoothing is not applied in this comparison. Results are obtained using the incident mode (1,0), because as an antisymmetric mode it performs well while covering a wide frequency range $[600, 3500]$ Hz.

Figure 5.14 presents the educed impedance for incident amplitudes of 120 dB and 150 dB in the absence of flow. The results obtained using microphone arrays with different axial resolutions show consistent results.

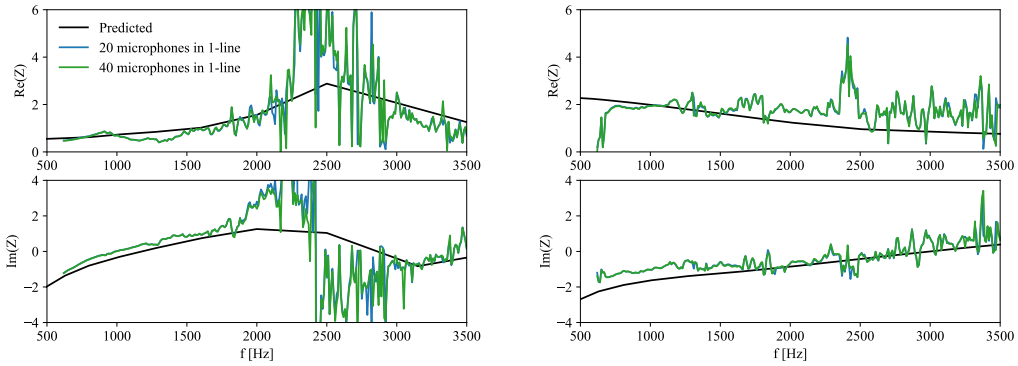

(a) 120 dB.

(b) 150 dB.

Figure 5.14: Comparison of educed impedance using 20 (blue) and 40 (green) microphones in the 1-line array. Incident mode (1,0) is present at amplitude of 120 dB (a) and 150 dB (b), in the absence of flow.

Then, the comparison of the two axial resolutions is done in the presence of flow, with the incident mode (1,0) at 130 dB. Figure 5.15 compares the results for flow velocities $M_{\text{ave}} = \pm 0.29, \pm 0.45, \pm 0.575$. For downstream propagation, the increase in axial spacing between microphones shows negligible impact on the impedance eduction results. However, for upstream propagation, the results diverge notably at higher frequencies, particularly at $f \geq 3000$ Hz for $M_{\text{ave}} = -0.3$, $f \geq 2400$ Hz for $M_{\text{ave}} = -0.45$, and $f \geq 1600$ Hz for $M_{\text{ave}} = -0.575$. At higher frequencies and for upstream propagation with high flow velocities, the wavelengths become comparable to the microphone spacing, resulting in unreliable results. For instance, at $M_{\text{ave}} = -0.575$ and 3000 Hz, the plane wave wavelength is approximately 4.8 cm in the rigid section, whereas the Shannon criteria specifies that at least two points are required by wavelength. This is verified for the complete antenna but not with 20 microphones. Note that the wavelength of the mode (1,0) is supposed to be slightly larger than this value, but this may not influence the validation of the Shannon criteria.

In conclusion, the microphone spacing of $\Delta x = 4$ cm in the 2-line array is adequate for most cases. However, resolution issues may arise in cases of upstream propagation with high-speed flow and at high frequencies.

5.3.2 Comparison between 1-line and 2-line

This section assesses the improvement brought by the use of the 2-line array through a comparison with the results obtained using 20 microphones from only one line. Remember that simple operations introduced in Chapter 4 are conducted on two line pressure signals in order to eliminate the undesired modes. For symmetric incident modes, the signals used to educe the impedance are the sum of the pressures of both lines, while for antisymmetric incident modes, such as the mode (1,0) in this section, the signals are the subtraction of the pressures of both lines. The mode (1,0) is excited at 120 and 150 dB in the downstream direction with Mach numbers at $M_{\text{ave}} = 0, 0.29$ and 0.45. The moving-average smoothing is not applied for a natural comparison between results.

Figure 5.16 illustrates the educed impedances obtained using 1-line of 20 microphones and the complete 2-line array with 2*20 microphones. The overall trends for results obtained using both microphone arrays are consistent, aligning well with

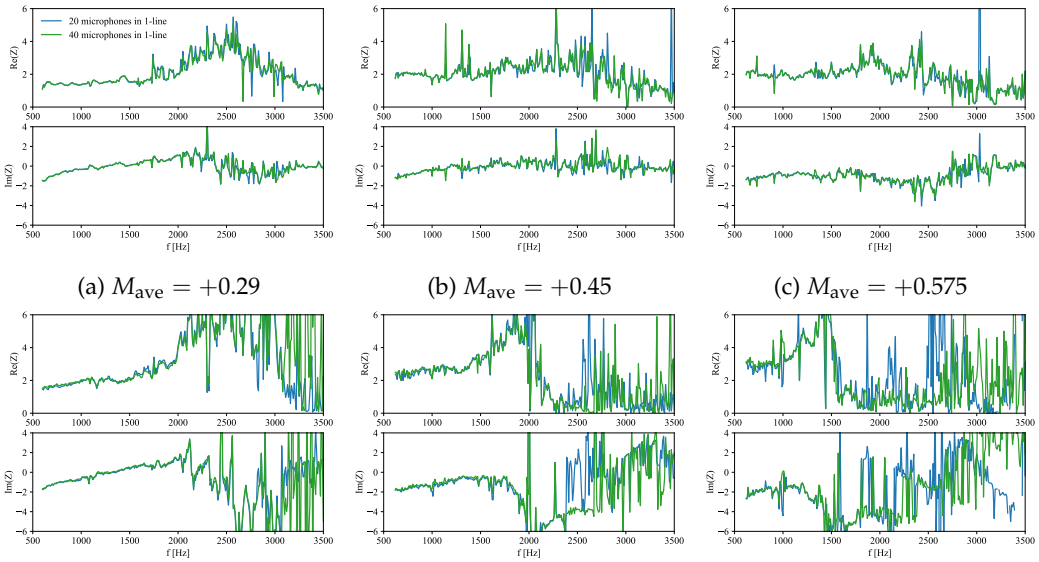

(a) $M_{ave} = +0.29$ (b) $M_{ave} = +0.45$ (c) $M_{ave} = +0.575$

(d) $M_{ave} = -0.29$ (e) $M_{ave} = -0.45$ (f) $M_{ave} = -0.575$

Figure 5.15: Comparison of educed impedance using 20 (blue) and 40 (green) microphones in the 1-line array. Incident mode (1,0) is present at amplitude of 130 dB in both directions, with flows at $M_{ave} = \pm 0.29, \pm 0.45, \pm 0.575$.

the predicted impedance values. The comparison shows that using the complete 2-line array yields smoother results at low frequencies ($f \leq 2000$ Hz) and mitigates oscillations at high frequencies.

5.3.3 Results with the 2-line array

The 2-line microphone array is now used to conduct impedance eduction at various flow velocities with different incident modes.

5.3.3.1 Influence of the incident mode

Figure 5.17 shows the impedances obtained without flow. The first 6 modes are individually excited at 140 dB, including symmetric modes (0,0), (2,0) and (4,0) and antisymmetric modes (1,0), (3,0) and (5,0). Similar to the observation in Section 5.2.1.2, antisymmetric modes provide more consistent results and perform better for the impedance eduction.

5.3.3.2 Influence of the flow velocity

For downstream propagation, Figure 5.18 shows the results for the mode (1,0) at amplitudes of 130 dB and 150 dB. The flow velocities considered are $M_{ave} = 0, 0.29, 0.445$ and 0.575 for both amplitudes, with an additional $M_{ave} = 0.15$ for 130 dB and $M_{ave} = 0.10$ for 150 dB.

For 130 dB, Figure 5.18(a) clearly shows an increase in resistance and a decrease in reactance as the flow velocity increases, particularly below 1500 Hz. These trends are more distinct compared to the results obtained using the 1-line array with 40 microphones, as shown in Figure 5.12(c). With increasing frequency, the overall trends remain consistent for results using both arrays.

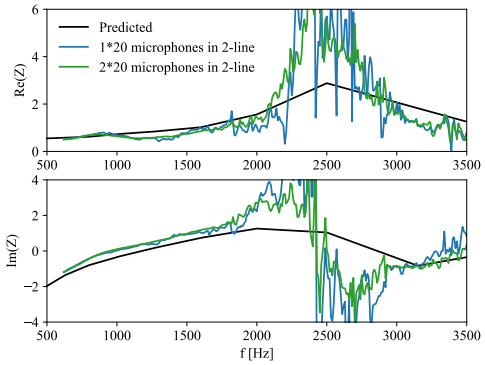

(a) 120 dB, $M_{\text{ave}} = 0$

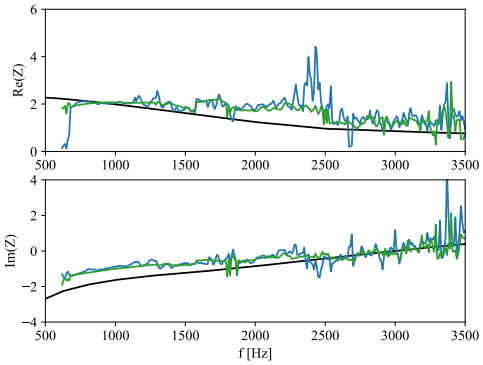

(b) 150 dB, $M_{\text{ave}} = 0$

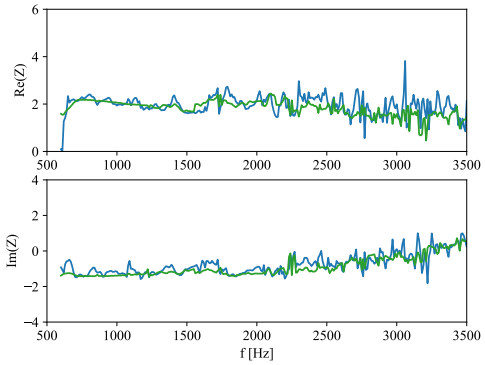

(c) 150 dB, $M_{\text{ave}} = 0.29$

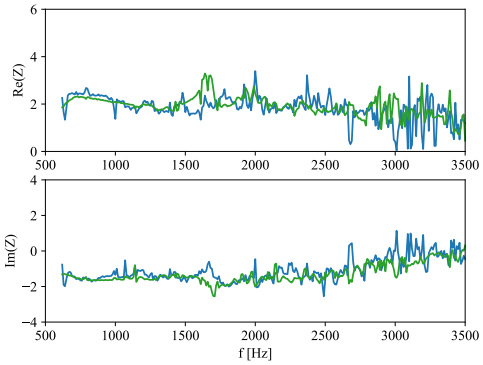

(d) 150 dB, $M_{\text{ave}} = 0.45$

Figure 5.16: Comparison of educed impedance using 20 (blue) and 2*20 (green) microphones in the 2-line array. Incident mode (1,0) is present in the direction of downstream propagation. Black line: predicted impedances.

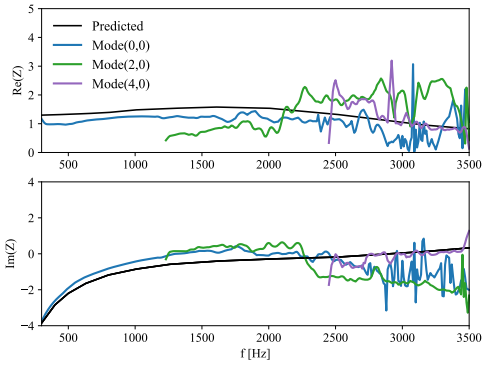

(a) Symmetric incident modes.

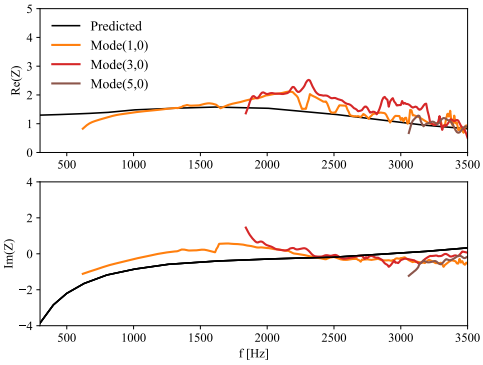

(b) Antisymmetric incident modes.

Figure 5.17: Educed impedance using symmetric (a) and antisymmetric (b) incident modes at 140 dB without flow, using the 2-line array. Black: predicted impedance.

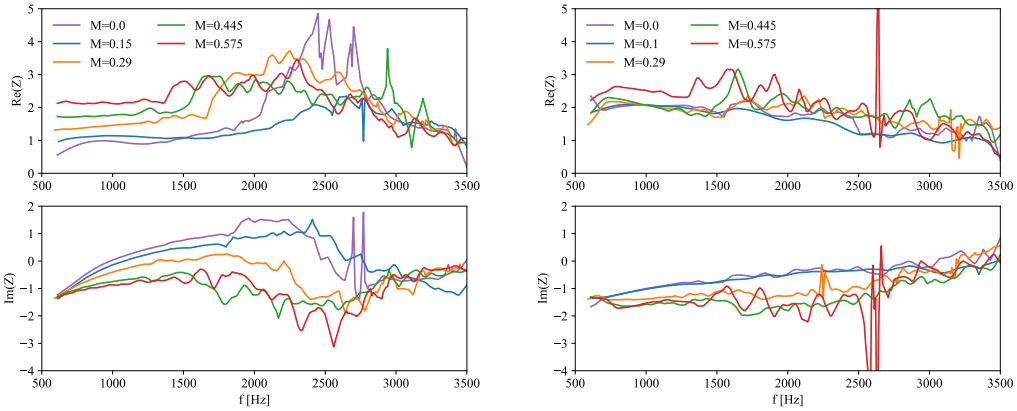

(a) 130 dB.

(b) 150 dB.

Figure 5.18: Educed impedance as a function of frequency for different average Mach numbers using the 2-line microphone array. The incident mode is the mode (1,0) at amplitudes 130 dB and 150 dB, propagating in the downstream direction.

For 150 dB, Figure 5.18(b) indicates that the educed impedances are quite similar for $M_{\text{ave}} = 0$ and $M_{\text{ave}} = 0.1$. Then, as the flow velocity increases further, the reactance decreases. Notably, the resistance for $M_{\text{ave}} = 0.575$ is significantly higher than for the other Mach numbers before 1500 Hz. Overall, the impedance results for 150 dB show less variation with the Mach number compared to the case with 130 dB.

For upstream propagation, to avoid the resolution issues previously discussed, experiments are conducted only at $M_{\text{ave}} = 0, 0.15$, and 0.29. Additionally, to prevent potential damage to the acoustic sources that happen more frequently against flow with modal amplitudes of 150 dB, the incident amplitude is set to 140 dB. Figure 5.19 presents separately the educed impedances using the mode (0,0) as the incident wave up to 1800 Hz, and the mode (3,0) for the remainder of the spectrum. It appears that these upstream results are superior to those obtained using the 1-line array in Figure 5.12. The figure also compares the results between upstream and downstream propagation. At $M_{\text{ave}} = 0.15$, the educed impedances for both directions are similar. At $M_{\text{ave}} = 0.29$, the upstream results exhibit greater resistance and more pronounced oscillations compared to the downstream results, with a significant increase in oscillations particularly after 2500 Hz.

To summarise, the use of the 2-line array for the impedance eduction improves the clarity of results and shows more clearly the trends of impedance with the variation of incident modes, Mach numbers and propagation directions. However, the results for $M_{\text{ave}} = 0.29$ are still noisy for upstream propagation at high frequencies (above 3000 Hz), potentially due to weak signal to noise ratio, insufficient spatial resolution and small attenuation. Therefore, more tests are needed with liners that have greater attenuation in these cases, so as to assess in the high-frequency band with flow the performance of direct impedance eduction.

5.4 Tests with optimised liners

This section begins with designing and optimising acoustic liners with the aim of effective acoustic attenuation in the high-frequency band in presence of flow. Once optimised, the impedance of the liners are measured in the MAINE Flow facility.

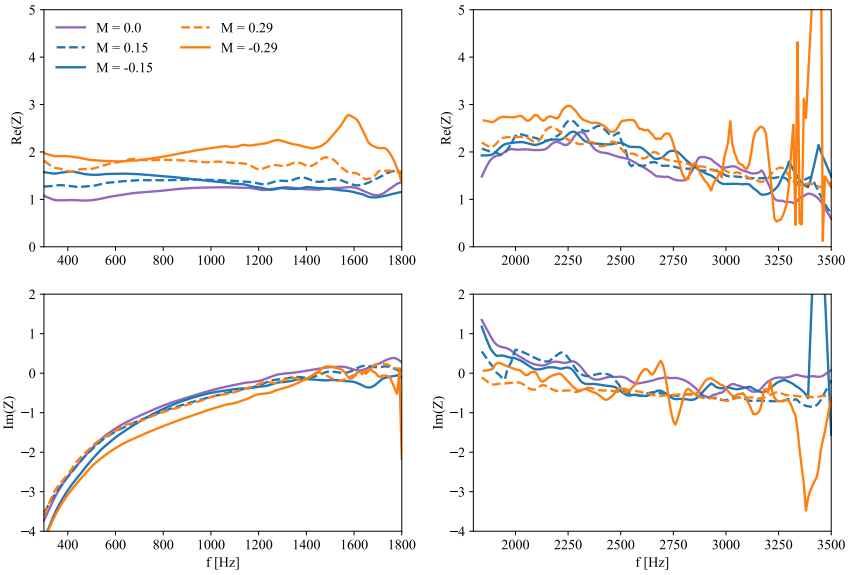

Figure 5.19: Educed impedance using the plane wave (left column) and mode (3,0) (right column) with an incident amplitude of 140 dB in both directions for average Mach numbers: 0 (purple), 0.15 (blue), 0.29 (orange). Dashed lines: downstream propagation; solid lines: upstream propagation.

5.4.1 Optimisation and design of liner

The objective of the optimisation is to maximise the transmission loss (TL) of the first two modes in the frequency range of $[1500, 2500]$ Hz. The calculation of TL employs the 2D multimodal model with shear flow described in Chapter 2, using the flow profile in Figure 4.4 with an average Mach number 0.3. The optimisation considers both downstream and upstream propagation directions separately.

The optimisation focuses on the double-liner configuration and looks for single-degree-of-freedom (SDOF) liners, with the link between the impedance and the geometry stemming from the Guess model [36]. Figure 5.20 shows the optimised liners, while their geometric parameters are detailed in Table 5.1. The predicted impedance for the optimised liners, calculated using the Guess model with both the initially designed and the measured parameters, is presented in Figure 5.21 for flow velocities of $M_{\text{ave}} = 0, 0.15$, and 0.3. It appears that the fabricated liners exhibit lower porosity and higher resistance compared to the initial design. Note that the face-sheets have been realised by conventional mechanical drilling, and they have been glued to honeycomb of the right length.

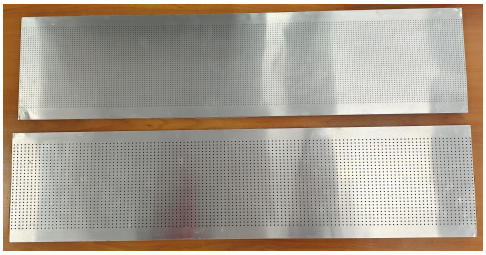

Figure 5.20: Top: the liner optimised for upstream propagation. Bottom: the liner optimised for downstream propagation.

	Perforated plate thickness (mm)	Cavity depth (mm)	Radius of perforations (mm)	POA (%)
Downstream (designed)	0.5	18.63	2.0	8.7
Upstream (designed)	0.5	8.9	1.17	6.8
Downstream (measured)	0.5	18.63	1.945	8.23
Upstream (measured)	0.5	8.9	1.157	6.43

Table 5.1: Geometries of the liners optimised for both propagation directions: initial designed parameters and measured parameters.

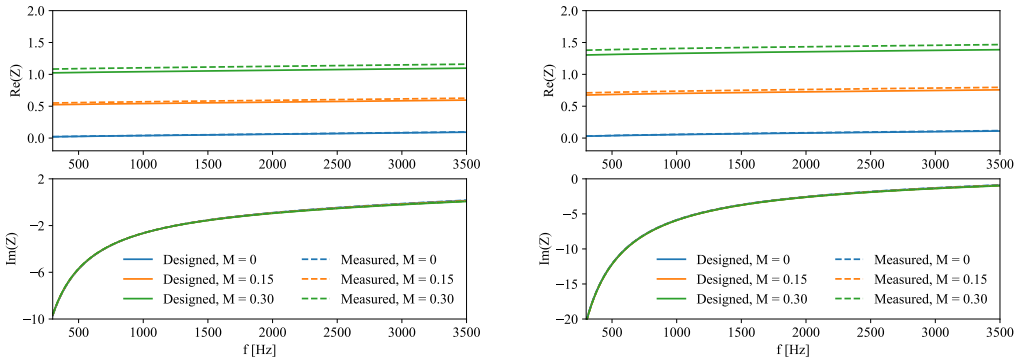

(a) Designed for downstream propagation.

(b) Designed for upstream propagation.

Figure 5.21: Predicted impedance of optimised liners using Guess model with initially designed (solid lines) and measured (dashed lines) parameters, with $M_{\text{ave}} = 0, 0.15$ and 0.30.

Using the impedance values from both the initial design and the fabricated liners, the transmission losses for the first two modes are computed under conditions of equal incident power and uncorrelated modes in the double-liner configuration, with flow at $M_{\text{ave}} = \pm 0.3$. Figure 5.22 compares the resulting TLs, indicating that manufacturing deviations have a minimal impact on the attenuation. Thereafter, the optimised liners are tested in MAINE Flow.

5.4.2 Results for optimised liner - downstream propagation

This section presents the results of the impedance eduction using the liner optimised for downstream propagation at $M_{\text{ave}} = +0.3$. The analysis considers various incident modes and amplitudes, as well as different flow velocities and the two propagation directions. The experiments are performed using the double-liner configuration in conjunction with the 2-line microphone array, over a frequency range from 300 to 3500 Hz.

5.4.2.1 Effects of the incident mode and amplitude

Figure 5.23 shows the educed impedance without flow for the first 6 modes, separately according to the symmetry type of mode. The modes are individually excited at incident amplitudes of 130 and 140 dB.

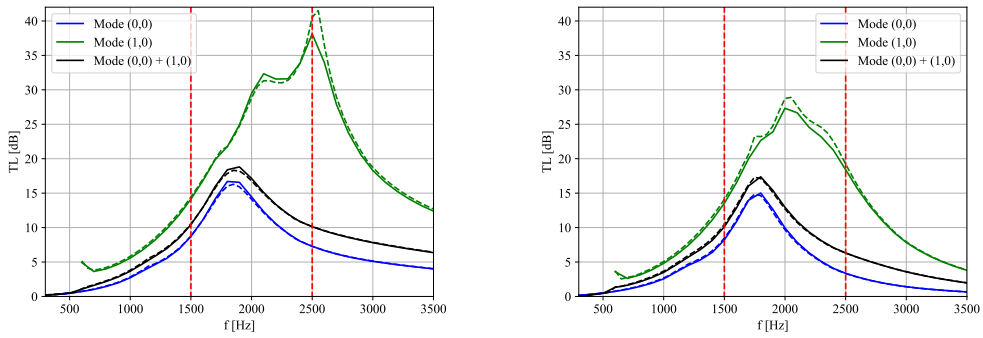

(a) Double-liner, $M_{\text{ave}} = +0.3$.

(b) Double-liner, $M_{\text{ave}} = -0.3$.

Figure 5.22: Transmission loss for the optimised liners within the double-liner configuration, using the impedance predicted by Guess model with initially designed (solid lines) and measured (dashed lines) parameters. Modes (0,0) and (1,0) are uncorrelated with equal powers. Red lines: frequency interval boundaries for the optimisation. (a): the liner designed for downstream propagation; (b): the liner designed for upstream propagation. The flow is sheared with $M_{\text{ave}} = \pm 0.3$.

For symmetric incident modes, in Figure 5.23(a), the results remain consistent up to 2400 Hz and then oscillate. Nevertheless, the results for the mode (4,0) agree satisfactorily with the predicted impedance above 3000 Hz. It is also noticeable that the change in incident amplitude barely affects the results, except for the mode (0,0) below 1000 Hz where there is a significant inconsistency.

For antisymmetric incident modes, in Figure 5.23(b), the results for each mode and both incident amplitudes are consistent. In addition, there is no difference between the results of the two amplitudes before 1000 Hz, which contrasts with the results for mode (0,0), indicating a greater uncertainty due to low attenuation in the measurement for the mode (0,0) in this frequency range.

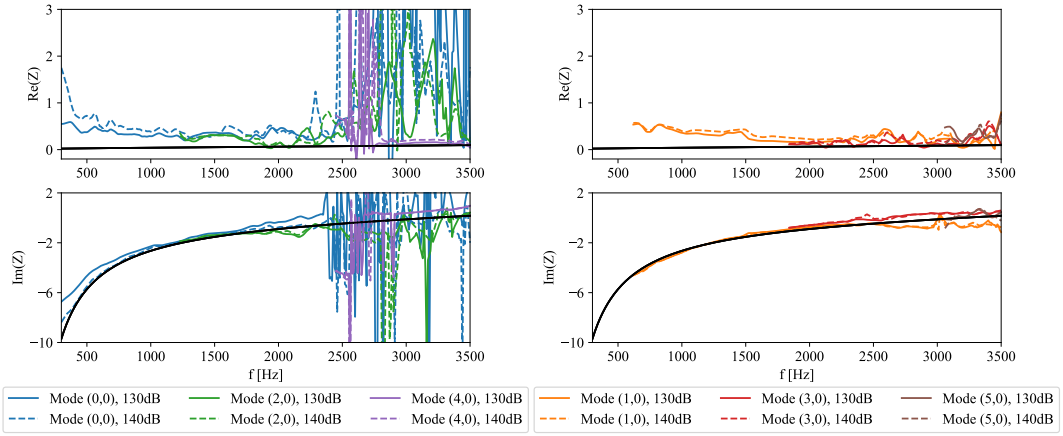

(a) Symmetric incident modes

(b) Antisymmetric incident modes

Figure 5.23: Educed impedance of the liner (optimised for downstream propagation) in the double-liner configuration without flow, using the first 6 modes at amplitudes of 130 and 140 dB. Black line: impedance predicted by Guess model using measured geometric parameters.

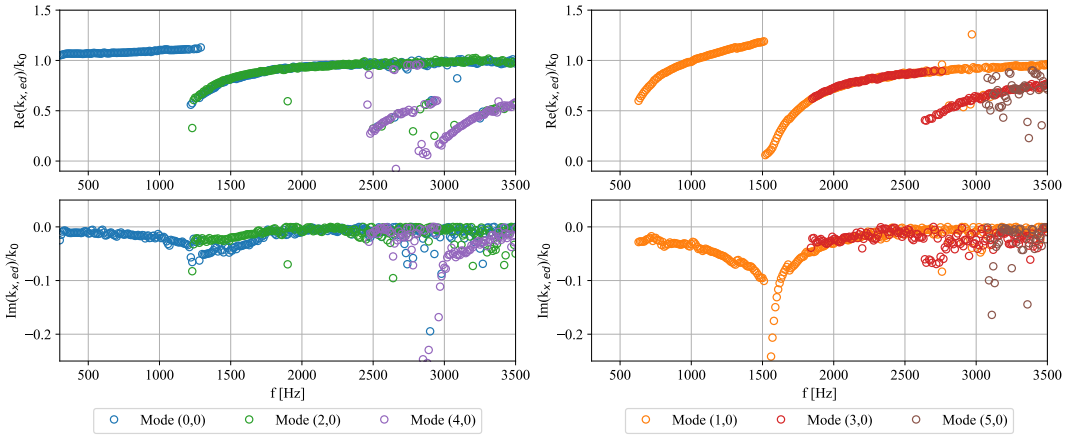

(a) Symmetric incident modes (b) Antisymmetric incident modes

Figure 5.24: Retrieved wavenumbers (normalised by k_0) used for computing the impedance for the liner (optimised for downstream propagation) in the double-liner configuration without flow, using the first 6 modes at 140 dB.

Figure 5.24 presents the retrieved wavenumbers for computing impedances with incident modes at 140 dB (results of Figure 5.23). For the mode (0,0), the low attenuation rate below 1000 Hz explains the variability in impedance results at different amplitudes within this frequency range. For the mode (4,0), the great performance above 3000 Hz benefits from the clean trend of wavenumbers, as shown in Figure 5.24(a). Furthermore, although both symmetry types exhibit similarly imaginary parts of wavenumbers above 2500 Hz, where the attenuation rate is close to zero, the results obtained using antisymmetric modes are more stable.

Overall, in absence of flow, the educed resistance for the optimised liner is greater than the predicted values, while the measured reactance is consistent with the model impedance. Additionally, changes in incident amplitude have a negligible impact on the measurement results for the optimised SDOF liners. Regarding the influence of mode symmetry, similar to the previous results obtained with DDOF liners, antisymmetric modes provide more reliable impedance results.

5.4.2.2 Effects of the flow velocity

Figure 5.25 shows the educed impedance for different flow velocities in both directions, with average Mach numbers set to 0, 0.15, and 0.29. Based on the performance of each mode in different frequency bands, the results are presented using the mode with optimal performance in each band: the mode (0,0) is used for 300-1000 Hz, the mode (1,0) for 1000-2500 Hz, and the mode (3,0) for 2500-3500 Hz. The incident amplitude is set to 140 dB.

In each case, the educed resistance decreases as a function of frequency, differing from the quasi-constant resistance predicted by the Guess model. This trend is similar to the results obtained for SDOF liners by Spillere et al. [18]. In particular, the resistance increases significantly with the Mach number, while the reactance remains similar. Moreover, there is no more oscillations above $f = 2500$ Hz like those observed in the results of DDOF (see Figure 5.19).

Finally, it can be seen that the downstream and upstream results are similar at low frequencies. For $M_{\text{ave}} = 0.15$, noticeable differences appear after 2500 Hz. For

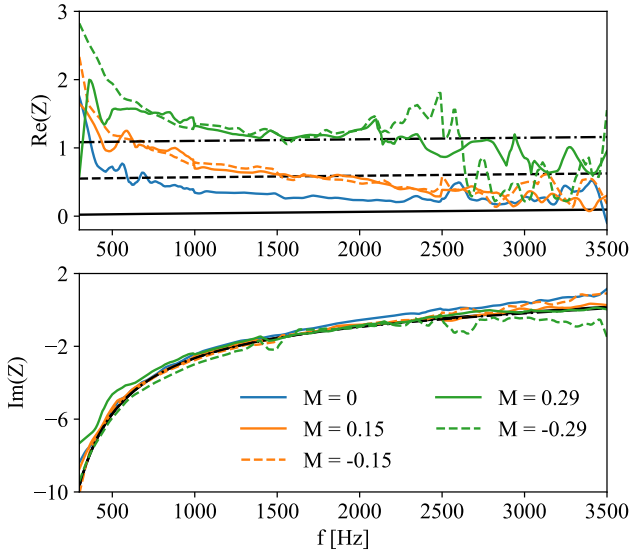

Figure 5.25: Educed impedance of the liner (optimised for downstream propagation) with an incident amplitude of 140 dB, without flow and with flows at $M_{ave} = 0, 0.15$ and 0.29 in both directions. Black lines: impedance predicted by Guess model using measured geometries, for different flow velocities: $M_{ave} = 0$ (solid line), $M_{ave} = 0.15$ (dashed line), and $M_{ave} = 0.29$ (dash-dotted line).

$M_{ave} = 0.29$, the results show significant discrepancies after 2100 Hz, with a reduction in resistance for the upstream results. This may be due to the inability to maintain the set SPL for the selected incident mode at high frequencies for the upstream propagation. Then, the amplitude of the selected mode cannot be distinguished from the other modes, resulting in an incident sound field which is too complex to decompose into wavenumbers, since no mode emerges significantly.

5.4.3 Results for optimised liner - upstream propagation

This section shows the impedance results corresponding to the liner optimised for upstream propagation. Again, the double-liner configuration is applied with the 2-line microphone array. The measurements contain various incident modes, different flow velocities and directions.

5.4.3.1 Influence of the incident mode

Figure 5.26 shows the educed impedance without flow for the liner optimised for upstream propagation. The incident modes are set at 140 dB. The result for the mode (0,0) shows anomalously greater resistance than the other modes between 1800 and 2500 Hz, and the cause needs to be further investigated, such as the liner attenuation. Regarding the symmetry, the same conclusion can be obtained as previous results, namely that the antisymmetric modes provide more consistent results. Also similarly, the measured resistance is larger than the predicted value.

5.4.3.2 Influence of the flow velocity

This part presents the educed impedance of the liner optimised for upstream propagation, for different Mach numbers in both directions. Since the attenuation

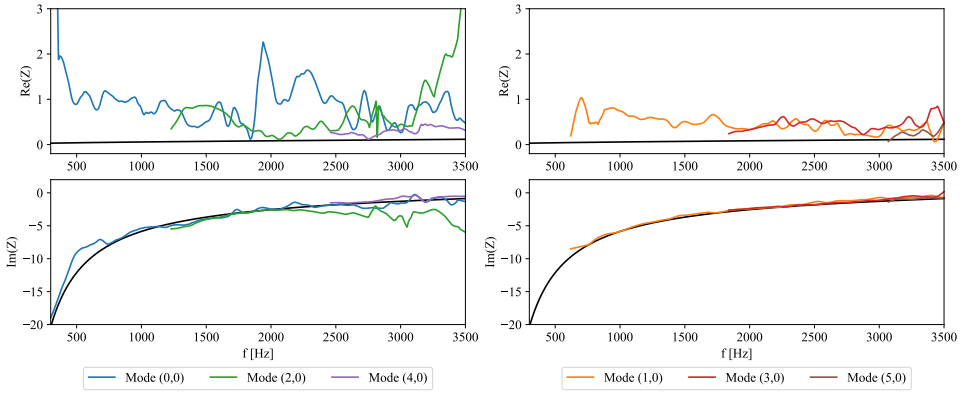

(a) Symmetric incident modes

(b) Antisymmetric incident modes

Figure 5.26: Educed impedance of the liner (optimised for upstream propagation) in the double-liner configuration without flow, using the first 6 modes at 140 dB. Black line: impedance predicted by Guess model using measured geometries.

from 300 Hz to 600 Hz is low (Figure 5.22), the results for the mode (0,0) are not used. The results for antisymmetric modes are similar, so only the results for mode (1,0) are shown to assess the influence of the flow velocity. The incident amplitude is 140 dB.

Figure 5.27 shows the educed impedance without flow and with flow at $M_{\text{ave}} = 0.15$ and 0.29 in both directions. The downstream results indicate that the resistance with flow is higher than without flow, although this increase does not vary with flow velocity. In contrast, the upstream results show that resistance increases with the Mach number. Furthermore, the reactance remains consistent and closely aligns with the model predictions, except for $M_{\text{ave}} = 0.29$ before 1500 Hz. Comparing both directions, the results at $M_{\text{ave}} = 0.15$ are similar. However, at $M_{\text{ave}} = 0.29$, the differences seem significant, with the upstream results exhibiting higher resistance and lower reactance.

Using the optimised liners, which provide significant transmission loss at high frequencies, the results of the impedance eduction are less noisy compared to the DDOF results. These tests highlight the importance of attenuation in impedance eduction. The liner optimised for upstream propagation, characterised by smaller holes and thinner cavity depth, demonstrates larger effects of grazing flow with greater discrepancies between the two propagation directions.

5.5 Conclusions

This chapter presents an experimental implementation of direct impedance eduction including shear flow for a large multimodal duct with high speed flows. It describes the way of mounting acoustic liners, the process of experiments, as well as the deployment of the microphone arrays proposed by the numerical study in Chapter 4. Then, considering the post-processing of the experimental signals, two methods for selecting wavenumbers are developed and compared. Ultimately, given the similarity of the impedance results, the more efficient one is recommended.

Initial measurements are conducted on a DDOF liner. The tests cover various

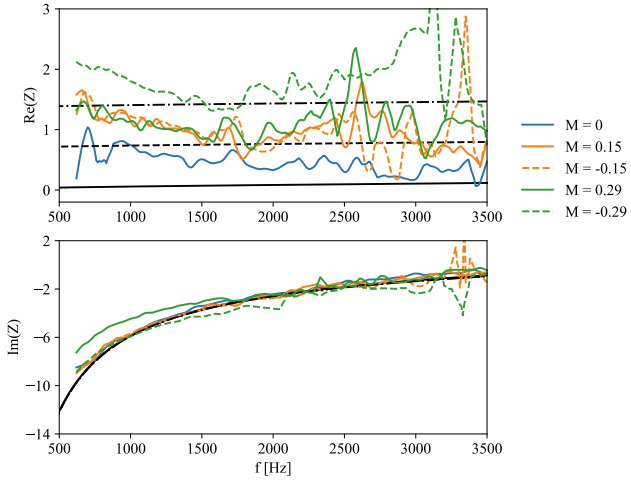

Figure 5.27: Educed impedance of the liner (optimised for upstream propagation) with the incident mode (1,0) at 140 dB, without flow and with flows at $M_{\text{ave}} = 0.15$ and 0.29 in both directions. Black lines: impedance predicted by Guess model using measured geometries. Black solid line: model impedance for $M_{\text{ave}} = 0$. Black dashed line: model impedance for $M_{\text{ave}} = 0.15$. Black dash-dotted line: model impedance for $M_{\text{ave}} = 0.29$.

liner configurations (single or double), different incident modes, varying sound pressure levels, different flow velocities and propagation directions, and different microphone arrays. The double-liner configuration is shown experimentally to be more effective than the single-liner configuration. This is attributed to the enhanced sound attenuation, as shown by the numerical study in Chapter 4. Additionally, for impedance eduction with flow, experimental results confirm that the effects of shear flow are more pronounced at high frequencies, in upstream propagation, and at high flow velocities. The impedance results obtained using the shear flow method are more accurate than those obtained using the uniform flow method.

For impedance eduction with individual incident modes, antisymmetric modes exhibit better performance than symmetric ones. This can be partly attributed to the higher attenuation of antisymmetric modes. While higher-order symmetric modes also demonstrate good attenuation, their overall performance is generally not as satisfactory as that of higher-order antisymmetric modes. Further investigations are needed to understand this discrepancy.

Different microphone arrays, including 1-line and 2-line arrays, are also evaluated. The 2-line array is able to smooth the results, while it does not change the overall trends compared to the results using the 1-line array. The microphone spacing of $\Delta x = 4$ cm in the 2-line array is not always adequate. Resolution issues may arise in cases of upstream propagation at high flow velocities, as the wavelengths in these cases become comparable to the microphone spacing.

To assess the performance of impedance eduction with great attenuation at high frequencies with flow, two sets of SDOF liners are designed for new measurements. These liners are optimised separately for downstream and upstream conditions by maximising the transmission loss at high frequencies. The tests of the optimised liners indicate some improvements in high-frequency impedance results compared to the DDOF liners that induce weaker attenuation in this frequency band. This emphasises the significance of the liner attenuation for the accuracy of impedance eduction method [24, 121].

In the present study, the discrepancies between the results for the two propagation directions notably persist as already observed by Aurégan [105], even though the effects of shear are accounted for in the impedance calculations. Further research should now explore the influence of three-dimensional shear effects [19] or consider additional physical phenomena [101, 123].

Chapter 6

Conclusions and perspectives

In this chapter, the main findings of this PhD thesis are gathered, and perspectives are also provided for future studies.

6.1 Main results

The literature review identifies several gaps in previous research, particularly concerning realistic operating conditions for acoustic liners, such as large section ducts, multimodal sound fields, high flow velocities, and boundary layer effects. Thus, this thesis introduces numerical and experimental techniques aiming at evaluating the effects of shear flow in the context of duct aero-acoustics and studying liners in these realistic conditions.

Using the propagation models and the impedance eduction methods, this study highlights the significant influence of mean flow shear, particularly in large ducts and at high frequencies. The effects are found to be more pronounced for upstream propagation and at larger flow velocities. The analysis also demonstrates that shear flow effects are similar for both single- and double-liner configurations, and that the uniform flow model is not sufficient under high flow velocities and thick boundary layers. In addition, the study reveals that the flow shear has necessarily to be considered for the calculation of impedances from wavenumbers. These findings also emphasise the necessity of incorporating shear flow considerations in the optimisation of acoustic liners to achieve accurate predictions and optimal performance, particularly in practical applications involving complex flow conditions.

Then, a parametric study has been performed to design the direct impedance eduction experiment by comparing several configurations and methods. In particular, significant improvements occur when using a shear flow model combined with a double-liner configuration, compared to the traditional uniform flow and single-liner approach. The double-liner consistently outperforms the single-liner by maintaining the symmetry of the acoustic field and enhancing attenuation, which reduces uncertainty in impedance measurements against noise perturbations or errors in the modal control of the incident field. Finally, using a 2-line microphone array is an effective solution to mitigate mode perturbations in real experiments, which allows separating symmetric and antisymmetric modes.

These features have been observed both in the numerical and experimental studies. It is confirmed that the double-liner configuration is superior to the single-liner configuration, due to the better performance in wavenumber estimation through greater acoustic attenuation. Additionally, the shear flow method provides more accurate experimental impedance results, especially for high frequencies, upstream propagation, and high flow velocities. According to the results, antisymmetric

modes exhibit better performance in impedance eduction compared to symmetric modes, likely due to their higher attenuation, although further investigation is needed to fully understand this behaviour.

The evaluation of different microphone arrays shows that the 2-line array improves result smoothness but does not change overall trends along the frequency. However, the microphone spacing of 4 cm seems inadequate in the MAINE Flow facility, and challenges in resolution are noted in high-velocity, upstream propagation cases. Tests with specially designed SDOF liners highlights again the significance of liner attenuation for the accuracy of impedance eduction method [24, 121].

6.2 Perspectives

Numerical and methodological study

(1) Investigation of higher-order modes: This study has indicated that antisymmetric modes perform generally better than symmetric ones. A deeper analysis of higher-order modes and their interaction with complex flow fields could yield more insights in duct aero-acoustics and improve the accuracy of impedance measurements.

(2) Three-dimensional sheared flows: This study accounts for the effects of shear in the 2D case. Flow features in three-dimensional cases [19] might be interesting to consider for direct impedance eduction. Such extensions to the present models could improve the accuracy and robustness of impedance measurements.

(3) Consideration of other physical effects: The results in this study have shown discrepancies between different propagation directions, despite accounting for effects of shear in 2D. Future work could explore the impact of flow effects in more detail, possibly by developing or refining models that account for other more complex boundary conditions. Beyond 2D shear effects, other physical phenomena such as viscous effects [59, 101, 105] might be interesting to consider and evaluate in the context of the MAINE Flow. Incorporating these factors into existing models could help understand the differences between results with upstream and downstream propagation.

Experimental study

(1) Enhanced microphone array design: While the 2-line microphone array proves effective in experiments, future research could explore the optimisation of microphone spacing and array configurations. For instance, adaptive arrays that adjust spacing based on practical measurements could offer better resolution and accuracy, particularly in high-speed flow conditions.

(2) Flow velocity: The accuracy of flow velocity measurements has been shown important for impedance eduction [17, 124, 125]. The same observation is found in this study. Even though the variations in Mach number are tiny, substantial influence may appear in results, particularly at high flow velocities and in upstream propagation cases. Given this, future experiments should consider minor Mach number fluctuations during measurements and incorporate these variations into impedance calculations at each frequency.

(3) Investigation on flow profiles: This study uses the scaled flow profile that is measured at the maximum Mach number ($M_{ave} = 0.63$) on the upstream side of the tested liner. It is necessary to study the sensitivity of the direct impedance eduction through tests with profiles at lower flow velocities. In addition, it would be interesting to test with the profile measured in the middle and right downstream of the liner.

(4) Consideration of flow shear in inverse impedance eduction: With regard to the quality of impedance results, the inverse method [126] seems to provide more robustness compared to the direct method. Given that the flow shear has significant effects in large ducts, this inverse method could be further developed by including the flow shear.

Appendix A

Description of published flow ducts

The detailed information of main published experimental facility is described as follows:

(1) NASA Grazing Flow Impedance Tube (GFIT)

NASA Langley has developed a series of flow duct benches, with the most recent being the Grazing Flow Impedance Tube (GFIT [57]), launched in 2009. Its predecessors include the Flow Impedance Tube (FIT [127], introduced around 1980) and the Grazing Incidence Tube (GIT [128], introduced around 2000).

The GFIT at NASA Langley has a rectangular cross-section measuring 50.8 mm in width and 63.5 mm in height. The acoustic liner is mounted on the narrow side, enabling the evaluation of liners with lengths ranging from 50.8 mm to 609.6 mm (in 50.8 mm increments). The test liner's surface constitutes a section of the upper wall of the flow duct, as highlighted in blue in Figure A.1). Airflow in the duct is provided by a negative pressure fan, and the velocity profile within the duct is measured using a Pitot tube driven by a 2D stepper motor. Twelve acoustic drivers form an upstream source and six acoustic drivers form a downstream source. Quasi-anechoic terminating diffusers are employed at each end of the duct to control reflections and reduce flow noise.

Some common structural features, including anechoic terminations, flow provider fans, and Pitot tubes, will not be discussed for other ducts. The primary focus will be on the dimensions and the ability to control the acoustic field and the flow velocity.

Tests carried out in the GFIT (and its predecessors) utilize a stepped-sine source, where the acoustic drivers generate tones one frequency at a time over a frequency range from 400 to 3000 Hz, with source SPLs (peak total SPL measured near the leading edge of the liner) up to 155 dB and centreline Mach numbers up to 0.6. Efforts are currently focused on implementing a controlled-amplitude, swept-sine source [129] in the GFIT.

(2) NASA Curved Duct Test Rig (CDTR)

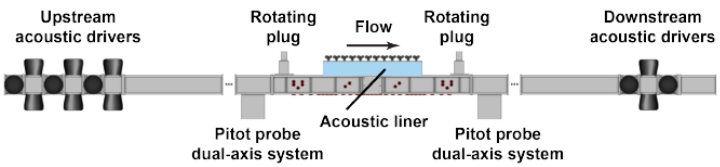

Figure A.1: Schematic of NASA GFIT [22].

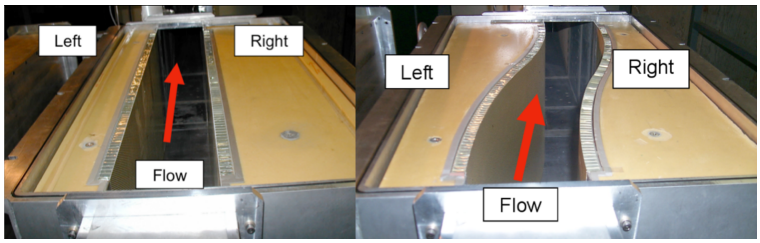

Figure A.2: Two configurations on NASA CDTR.

The NASA Curved Duct Test Rig (CDTR) [23, 130, 131] is also designed to evaluate the acoustic and aerodynamic performance of aircraft engine nacelle liners. The CDTR accommodates testing with a rectangular cross-section of 152.4 mm in width and 381 mm in height. This open-loop wind tunnel employs a fan to draw unconditioned atmospheric air at Mach number up to 0.5 through the test section and offers three test window configurations. The standard configuration is a straight duct (left image in Figure A.2), while the curved configuration has two options of the shift between the outlet and the inlet (76.2 mm or 152.4 mm), shown in Figure A.2 [132]. Acoustic liners can be mounted on one or both sidewalls of the CDTR [130].

To emit acoustic modes in both directions in the CDTR, the acoustic drivers need to be switched from one side to another, which is complicated. The sound generation in the test section is realised by an array of 31 acoustic drivers. Three types of the acoustic excitation are available: controlled-mode stepped sine (with up to 15 modes in each direction), uncontrolled-mode stepped sine, and broadband. Regardless of the source type, tests are typically conducted over the frequency range of 400 to 3000 Hz. The maximum SPL reaches around 140 dB, with the target mode's amplitude typically at least 10 dB higher than other modes. Arrays of 63 microphones, both upstream and downstream of the 381 mm $\times$ 762 mm liners, decompose the acoustic fields into modes. Additionally, for the straight configuration, 32 microphones mounted in the upper wall of the flow path, i.e. lateral to liners, capture the sound field within the treated section, and are used for the direct impedance eduction.

(3) DLR DUct aCoustic Test Rig (DUCT)

The German Aerospace Center (DLR) has built flow duct test facilities to perform acoustic measurements with grazing flow, named DUct aCoustic Test Rig (DUCT) [133]. There are three test rig configurations available with circular (DUCT-C), square (DUCT-S) and rectangular cross-sections (DUCT-R) in order to examine plane as well as circular liner geometries.

The DUCT-C is an aluminium-walled duct with an inner diameter of 140 mm. The cut-on frequency of the first higher-order mode is 1400 Hz. The mean flow Mach number is up to 0.1. Microphones are mounted at 10 positions in axial direction, and there are 8 microphones in the circumference at each position.

When investigating samples of plate liners, the DUCT-S and DUCT-R are used, shown in Figure A.3. The DUCT-S [66, 90, 133–135] has a cross-section of 80 $\times$ 80 mm^2. The duct is set up symmetrically, with loudspeakers at the upstream and downstream ends which can produce discrete tones with peak levels of about 110 $-$ 120dB. Liner samples with a maximum length of 220 mm can be inserted as the bottom wall in the test section at the middle of the duct. The

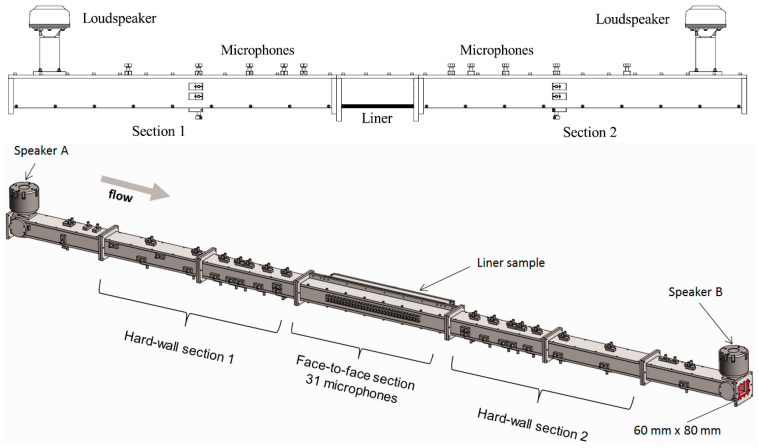

Figure A.3: Schematics of DUCT-S (top) [90] and DUCT-R (bottom) [136].

mean flow Mach number at the centreline can be set up to 0.27. This duct can also be used for investigations with optical measurement techniques thanks to its transparent acrylic glass wall.

Several improvements of the DUCT-S by Busse et al. [134] led to a re-designed version (DUCT-R) with a rectangular cross-section of $60 \times 80\,\mathrm{mm}^2$ (height$\times$width). The DUCT-R facility supports liners with a length of up to 800 mm [85, 101, 136], which can be mounted at the top, at the bottom, or at the side wall. 8 available loudspeakers (4 upstream, 4 downstream) provide SPL up to 130 dB with a multi-tone excitation at a frequency up to 2200 Hz. A microphone array is installed at the narrow side in the lined section, which involves 31 equidistant microphones with a spacing of 16 mm.

(4) NLR Flow Duct Facility (FDF)

The Netherlands Aerospace Centre (NLR) used its Flow Duct Facility (FDF) for in-situ impedance eduction and transmission loss measurements with grazing flow [86], as shown in Figure A.4. The facility consists of two reverberation rooms connected by a variable-section duct with a test section length of 1.05 m. The test section dimensions are constant and the size is $150 \times 300\,\mathrm{mm}^2$. The maximum centreline Mach number in the test section is 0.7. The sound sources include a broadband source, generated in the upstream reverberation room with overall SPLs up to 150 dB, and a pure tone source, produced by a signal generator at frequencies ranging from 1000 to 6000 Hz in 500 Hz increments.

(5) KTH flow acoustic test rigs The KTH test rig [49] has a length of 3.5 m and the inlet duct circular cross-section is reduced gradually and converted to a square measurement section with inner dimensions of $32 \times 32\,\mathrm{mm}^2$. The length of the lined section is 50 mm. The loudspeakers section is placed on the downstream side. The cut-on frequency of the first radial mode in the hard-walled duct is 5300 Hz. The valid operation frequency range is between 550 and 4500 Hz with no flow and between 515 and 4100 Hz at Mach number of 0.3. The impedance measurements are usually performed in the range between 1000 and 4000 Hz.

More recently, tests on another small scale facility in KTH [87] have been published. The rig corresponds to the bottom sketch in Figure A.5. The test section is rectangular, 70 mm wide and 25 mm high. Tested liner is mounted on the

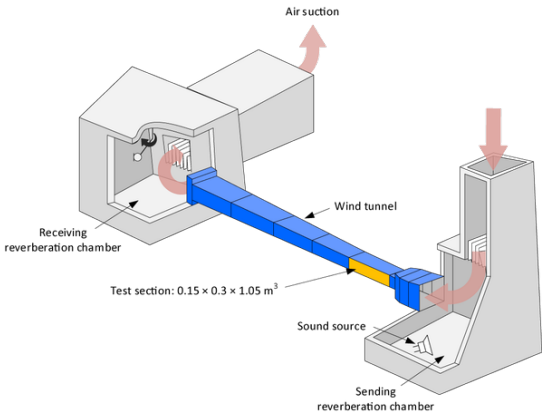

Figure A.4: Schematic of NLR Flow Duct Facility.

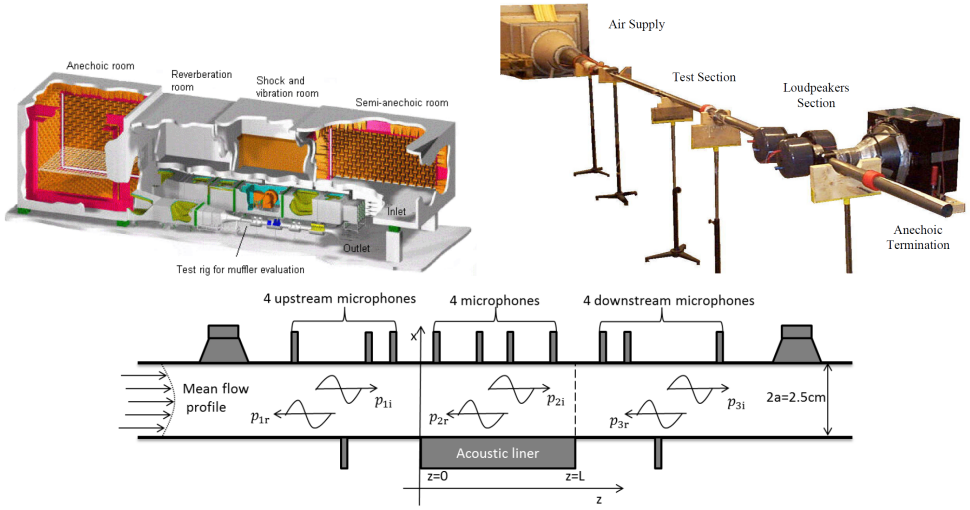

Figure A.5: Liner test setups at KTH [49, 87].

wide side wall. The stepped sine excitation reaches SPL from 100 to 145 dB, with a step of 40 Hz between 200 Hz and 2600 Hz. The mean flow Mach numbers are 0.1 or 0.2. Twelve microphones are installed in the middle of the hard wall opposite to the liner sample, including four microphones mounted on each side of the sample and four microphones mounted in the lined section.

(5) UFSC grazing Flow Liner Impedance eduction test Rig (FLIR)

This test rig (see Figure A.6), situated at the Federal University of Santa Catarina (UFSC) [22, 64, 137], comprises a rectangular duct with a cross-section of $40 \times 100\,\mathrm{mm}^2$. This duct contains a liner test section of length 210 mm in the middle, where the top, the bottom, or both surfaces can be either lined or unlined (hard-walled). Equidistant 8 microphones are spaced by 2 cm and positioned at the half-height of the liner section, on the nodal line of the first transverse mode. Similar to other classical ducts, upstream and downstream of the test section are wall mounted a total of 8 microphones, and beyond these are two or more wall-mounted loudspeakers. Measurements are made using a frequency sweep with a sound pressure level up to 150 dB. The experiments carried out in this test rig are limited between 400 and 3000 Hz [18] or 2500 Hz [22, 64] to avoid the second transverse mode. The cross-section averaged flow

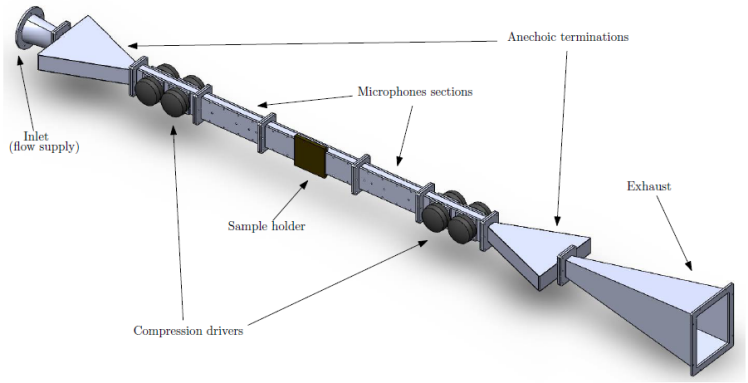

Figure A.6: Representation of UFSC Liner Test Rig [8].

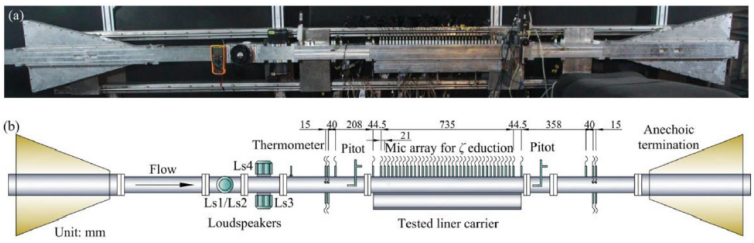

Figure A.7: Schematic of the flow duct test rig at BUAA [78, 88].

achieves a Mach number up to 0.7 (used in tests up to a centreline Mach = 0.5 [22]).

(6) Beijing University of Aeronautics and Astronautics (BUAA) test rig

The test rig in BUAA is constantly evolving with research, so only the most recent is presented here. The aluminium duct setup has a $51 \times 51\,\text{mm}^2$ inner cross-section (see Figure A.7) inside which an air flow can reach up to Mach of 0.25. Four loudspeakers are installed on the four walls upstream the test section and are used to generate incident tones up to an overall SPL of 135 dB in the frequency range $[500, 6000]$ Hz. A nine-microphone array in each of the upstream and downstream rigid wall sections is used for the modal decomposition of the acoustic field. The 800 mm-long tested liner is flush mounted with its faceplate, forming a portion of the duct lower wall. On the upper wall right above the liner, a diagonal microphone array with 21 mm-spacing in length and 1.2 mm-spacing in width is located opposite to the liner in order to acquire synchronously the acoustic pressure field for impedance eduction in [78].

(7) ONERA B2A

The French national aerospace centre, ONERA, established the Aero-Thermo-Acoustic Bench (B2A) for acoustic liner measurements (see Figure A.8) in 2004 [70]. It is a stainless steel 4-m long test duct with a $50 \times 50\,\text{mm}^2$ cross-section. The bulk Mach number of the mean flow inside the duct is capable of reaching up to 0.5, and temperature up to 570 K. The test section is 200 mm long and is equipped with two silica windows for optical impedance measurements via LDV. The surface of the test liner forms a 150-mm-long portion of the lower

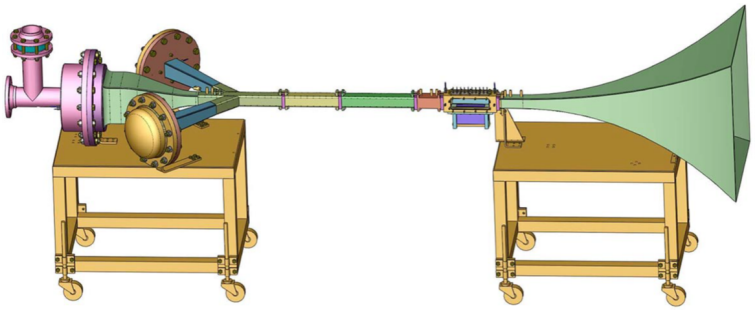

Figure A.8: Sketch of B2A test bench [72].

wall of the flow duct. Two acoustic drivers are mounted upstream of the test section and are used to generate tones (usually a multi-sine signal) at up to 150 dB over a frequency range of $[300, 3500]$ Hz.

(8) Laboratoire d'Acoustique de l'Université du Mans(LAUM)

The acoustic laboratory LAUM, operates a flow duct [116, 138] with $40 \times 50\,\mathrm{mm}^2$ cross-section, where flow speeds up to 80 m/s. The acoustic waves are generated at several levels ranging from 110 dB to 140 dB by two compression chambers either upstream or downstream of the test section. The sine sweep excitation ranges from 200 to 4000 Hz with a step of 5 Hz. Three microphones on each side of the sample can determine the scattering matrix.

Appendix B

Details for the numerical methods

B.1 Uniform flow model

B.1.1 Pseudo-spectral method

This section gives a detailed implementation of the pseudo-spectral method to solve the acoustic field in presence of uniform flow with the single liner configuration, i.e. one liner at the lower wall in the middle section.

Propagation equations and boundary conditions

We recall first that the evolution of the acoustic pressure field inside the duct is described by the convected Helmholtz equation Eq. (2.7), while the boundary conditions Eq. (2.8) and Eq. (2.9) are applied on the walls:

$$\frac{1}{c_0^2}\frac{D_0^2 p}{Dt^2} - \nabla^2 p = 0 \qquad \text{for} \quad 0 < y < H,$$

$$-\frac{\partial p}{\partial y} = -\frac{\rho_0}{\mathrm{i}\omega Z}\frac{D_0^2 p}{Dt^2} \qquad \text{at} \quad y = 0,$$

$$\frac{\partial p}{\partial y} = 0 \qquad \text{at} \quad y = H.$$

Since the solution for the acoustic pressure is sought in the form $p(x,y) = \Psi(y)\mathrm{e}^{-\mathrm{i}k_x x}$, the three previous equations write:

$$\frac{\partial^2 \Psi}{\partial y^2} - [k_x^2 - (k_0 - Mk_x)^2]\Psi = 0 \qquad \text{for} \quad 0 < y < H, \tag{B.1}$$

$$\frac{\partial \Psi(0)}{\partial y} = \mathrm{i}\frac{\rho_0 c_0}{k_0 Z}(k_0 - Mk_x)^2\Psi(0) \qquad \text{at} \quad y = 0, \tag{B.2}$$

$$\frac{\partial \Psi(H)}{\partial y} = 0 \qquad \text{at} \quad y = H. \tag{B.3}$$

Now, we introduce $\Psi(y) = \sum_n^N \alpha_n \phi_n(y)$, which decompose the mode shape function into N functions $\phi_n(y)$ with their associated amplitudes α_n. The system of equations becomes thus:

$$\sum_n^N \alpha_n \{\phi_n''(y) - [k_x^2 - (k_0 - Mk_x)^2]\phi_n(y)\} = 0 \qquad \text{for} \quad 0 < y < H,$$

$$\sum_n^N \alpha_n \{\phi_n'(0) - \mathrm{i}\frac{\rho_0 c_0}{k_0 Z}(k_0^2 - Mk_x)^2 \phi_n(0)\} = 0 \qquad \text{at} \quad y = 0,$$

$$\sum_n^N \alpha_n \{\phi_n'(H)\} = 0 \qquad \text{at} \quad y = H,$$

Collocation method

In this part, the collocation method is applied to complete the pseudo-spectral method. This method transforms the previous problem into an eigenvalue and eigenvector problem. To that end, the three previous equations are rearranged and the eigenfunction is created.

We choose $m = 1, \ldots, M$ points inside the duct. Moreover, as the boundary conditions have to be considered, there are $N = M + 2$ lines in total. After the arrangement, an eigenfunction can be written:

$$B_0\alpha + k_x B_1 \alpha + k_x^2 B_2 \alpha = 0, \tag{B.4}$$

with the details presented as follows:

$$\underbrace{[\phi_n''(y_m) + k_0^2 \phi_n(y_m)]}_{B_0}\alpha_n + k_x \underbrace{[-2k_0 M \phi_n(y_m)]}_{B_1}\alpha_n + k_x^2 \underbrace{[(M^2-1)\phi_n(y_m)]}_{B_2}\alpha_n = 0,$$

$$\underbrace{[\phi_n'(0) - \mathrm{i}\frac{\rho_0 c_0 k_0 \phi_n(0)}{Z}]}_{B_0}\alpha_n + k_x \underbrace{[2\mathrm{i}\frac{\rho_0 c_0 M \phi_n(0)}{Z}]}_{B_1}\alpha_n + k_x^2 \underbrace{[-\mathrm{i}\frac{\rho_0 c_0 M^2 \phi_n(0)}{k_0 Z}]}_{B_2}\alpha_n = 0,$$

$$\underbrace{\phi_n'(H)}_{B_0}\alpha_n = 0.$$

Then, Eq. (B.4) are reformatted in matrix formulation as:

$$\begin{bmatrix} 0 & I \\ B_0 & 0 \end{bmatrix} \begin{bmatrix} \alpha \\ k_x \alpha \end{bmatrix} = k_x \begin{bmatrix} I & 0 \\ -B_1 & -B_2 \end{bmatrix} \begin{bmatrix} \alpha \\ k_x \alpha \end{bmatrix}. \tag{B.5}$$

The basis function ϕ_n are chosen as Chebyshev polynominals of the first kind $T_n(\tau)$ and the collocation points are Chebyshev points y_m.

Chebyshev polynominals of the first kind $T_n(\tau)$ are defined by $T_n(\cos\theta) = \cos(n\theta)$, whose definition domain is $-1 \leq \tau = \cos\theta \leq 1$. $\cos(n\theta)$ can be expressed by $\cos\theta$ using the angle sum formulas, which forms a recurrence relation. Thus, Chebyshev polynominals of the first kind $T_n(\tau)$ can also be written as:

$$T_n(\tau) = \begin{cases} 1 & \text{if } n = 0, \\ \tau & \text{if } n = 1, \\ 2\tau T_{n-1}(\tau) - T_{n-2}(\tau) & \text{if } n \geq 2. \end{cases} \tag{B.6}$$

Note that the Chebyshev polynomials start at $T_0(\tau)$, so the first basis function above corresponds to $T_0(\tau)$.

In the context of the propagation equation, according to the duct height, the range of independent variables is $0 < y < H$. By substituting the variables, the relation between variables are presented as:

$$\tau = 2\frac{y}{H} - 1. \tag{B.7}$$

Chebyshev points are defined as:

$$\tau_m = \cos(\frac{2m-1}{2M}\pi) \qquad \text{for} \quad m = 1, \ldots, M. \tag{B.8}$$

and the m^{th} y-position are chosen as (without the two boundaries):

$$y_m = \frac{\tau_m + 1}{2} H. \tag{B.9}$$

As the calculation in Eq. (B.5) involves the first-order and second-order derivatives, the relationship between the derivations of independent variables is $\mathrm{d}y/\mathrm{d}\tau = H/2$. Then, the relationship between the derived functions can be presented as follows:

$$\phi'(y) = \frac{\mathrm{d}\phi(y)}{\mathrm{d}y} = \frac{2}{H}\frac{\mathrm{d}T(\tau)}{\mathrm{d}\tau}, \tag{B.10}$$

$$\phi''(y) = \frac{\mathrm{d}^2\phi(y)}{\mathrm{d}y^2} = \frac{4}{H^2}\frac{\mathrm{d}^2T(\tau)}{\mathrm{d}\tau^2}. \tag{B.11}$$

Furthermore, by differentiating the polynomials in their trigonometric forms, and we can obtain:

$$T_n'(x) = nU_{n-1} \quad (n \geq 1) \quad ; \quad T_0'(x) = 0. \tag{B.12}$$

$$T_n''(x) = n\frac{nT_n - xU_{n-1}}{x^2 - 1} \quad (n \geq 1) \quad ; \quad T_0''(x) = 0. \tag{B.13}$$

Here, $U_n(x)$ are Chebyshev polynomials of the second kind, given in trigonometric form by :

$$U_n(\cos\theta)\sin\theta = \sin((n+1)\theta), \tag{B.14}$$

or defined by the recurrence relation:

$$U_n(x) = \begin{cases} 1 & \text{if } n = 0, \\ 2x & \text{if } n = 1, \\ 2xU_{n-1}(x) - U_{n-2}(x) & \text{if } n \geq 2. \end{cases} \tag{B.15}$$

Substituting the Chebyshev polynomials into Eq. (B.4) at the positions associated to the Chebyshev points yields

$$\underline{\underline{B_0}}_{N\times N} = \begin{bmatrix} \frac{4}{H^2}T_0''(y_1)+k_0^2T_0(y_1) & \frac{4}{H^2}T_1''(y_1)+k_0^2T_1(y_1) & \dots & \frac{4}{H^2}T_{N-1}''(y_1)+k_0^2T_n(y_1) \\ \vdots & \vdots & \ddots & \vdots \\ \frac{4}{H^2}T_0''(y_M)+k_0^2T_1(y_M) & \frac{4}{H^2}T_1''(y_M)+k_0^2T_1(y_M) & \dots & \frac{4}{H^2}T_{N-1}''(y_M)+k_0^2T_{N-1}(y_M) \\ \frac{2}{H}T_0'(0)-\mathrm{i}\frac{\rho_0c_0k_0}{Z}T_0(0) & \frac{2}{H}T_1'(0)-\mathrm{i}\frac{\rho_0c_0k_0}{Z}T_1(0) & \dots & \frac{2}{H}T_{N-1}'(0)-\mathrm{i}\frac{\rho_0c_0k_0}{Z}T_{N-1}(0) \\ \frac{2}{H}T_0'(H) & \frac{2}{H}T_1'(H) & \dots & \frac{2}{H}T_{N-1}'(H) \end{bmatrix},$$

$$\underline{\underline{B_1}}_{N\times N} = \begin{bmatrix} -2k_0MT_0(y_1) & -2k_0MT_1(y_1) & \dots & -2k_0MT_{N-1}(y_1) \\ \vdots & \vdots & \ddots & \vdots \\ -2k_0MT_0(y_M) & -2k_0MT_1(y_M) & \dots & -2k_0MT_{N-1}(y_M) \\ 2\mathrm{i}\frac{\rho_0c_0M}{Z}T_0(0) & 2\mathrm{i}\frac{\rho_0c_0M}{Z}T_1(0) & \dots & 2\mathrm{i}\frac{\rho_0c_0M}{Z}T_{N-1}(0) \\ 0 & 0 & \dots & 0 \end{bmatrix},$$

and

$$\underline{\underline{B_2}}_{N\times N} = \begin{bmatrix} (M^2-1)T_0(y_1) & (M^2-1)T_1(y_1) & \dots & (M^2-1)T_n(y_1) \\ \vdots & \vdots & \ddots & \vdots \\ (M^2-1)T_0(y_M) & (M^2-1)T_1(y_M) & \dots & (M^2-1)T_{N-1}(y_M) \\ -i\frac{\rho_0c_0M^2}{K_0Z}T_0(0) & -i\frac{\rho_0c_0M^2}{K_0Z}T_1(0) & \dots & -i\frac{\rho_0c_0M^2}{K_0Z}T_{N-1}(0) \\ 0 & 0 & \dots & 0 \end{bmatrix}.$$

Then solving Eq. (B.4) provides the coefficients α_n of polynomials and axial wavenumbers $k_{x,n}$ for each mode.

B.1.2 Mode-matching

Once the axial wavenumbers and the mode shape function obtained in each section, we can use the mode-matching to connect the sections and to solve the amplitudes of modes in each section.

According to the pseudo-spectral method, the acoustic pressure is expressed as $P_{n,a}^{\pm} = \sum_{q=0}^{N}(\alpha_{n,a}^{\pm})_q T_q(2y/H-1)$ with $n = 1,2,3$ for each section, and a stands for the a^{th} mode, while T_q are Chebyshev polynomials.

To solve the matching conditions (2.27) and (2.28), the trial function for the first interface in Eq. (2.27) is $P_{2,b}^{+}$ for $\mathbf{P}_n^{+}$ and $P_{1,b}^{-}$ for $\mathbf{M}_n^{+}$, while the trial function for the second interface in Eq. (2.28) is $P_{3,b}^{+}$ for $\mathbf{P}_n^{+}$ and $P_{2,b}^{-}$ for $\mathbf{M}_n^{+}$. $\mathbf{M}_n^{\pm}$ (including only the first integral term) in Eq. (2.27) writes:

$$(\mathbf{M}_1^{\pm})_{a,b} = (u_0 + c_0^2\frac{k_{x,1,b}^{\pm}}{\omega - u_0k_{x,1,b}^{\pm}})\sum_q\sum_p(\overline{\alpha_{1,a}^{-}})_q(\alpha_{1,b}^{\pm})_p < T_q, T_p >,$$

$$(\mathbf{M}_2^{\pm})_{a,b} = (u_0 + c_0^2\frac{k_{x,2,b}^{\pm}}{\omega - u_0k_{x,2,b}^{\pm}})\sum_q\sum_p(\overline{\alpha_{1,a}^{-}})_q(\alpha_{2,b}^{\pm})_p < T_q, T_p >,$$

$$(\mathbf{M}_3^{\pm})_{a,b} = (u_0 + c_0^2\frac{k_{x,2,b}^{\pm}}{\omega - u_0k_{x,2,b}^{\pm}})\sum_q\sum_p(\overline{\alpha_{2,a}^{-}})_q(\alpha_{2,b}^{\pm})_p < T_q, T_p >,$$

$$(\mathbf{M}_4^{\pm})_{a,b} = (u_0 + c_0^2\frac{k_{x,3,b}^{\pm}}{\omega - u_0k_{x,3,b}^{\pm}})\sum_q\sum_p(\overline{\alpha_{2,a}^{-}})_q(\alpha_{3,b}^{\pm})_p < T_q, T_p > .$$

In the same way, $\mathbf{P}_n^{\pm}$ in Eq. (2.28) can be written as:

$$(\mathbf{P}_1^{\pm})_{a,b} = \frac{\omega}{\rho_0(\omega - u_0 k_{x,1,b}^{\pm})} \sum_q \sum_p (\overline{\alpha_{2,a}^{+}})_q (\alpha_{1,b}^{\pm})_p < T_q, T_p >,$$

$$(\mathbf{P}_2^{\pm})_{a,b} = \frac{\omega}{\rho_0(\omega - u_0 k_{x,2,b}^{\pm})} \sum_q \sum_p (\overline{\alpha_{2,a}^{+}})_q (\alpha_{2,b}^{\pm})_p < T_q, T_p >,$$

$$(\mathbf{P}_3^{\pm})_{a,b} = \frac{\omega}{\rho_0(\omega - u_0 k_{x,2,b}^{\pm})} \sum_q \sum_p (\overline{\alpha_{3,a}^{+}})_q (\alpha_{2,b}^{\pm})_p < T_q, T_p >,$$

$$(\mathbf{P}_4^{\pm})_{a,b} = \frac{\omega}{\rho_0(\omega - u_0 k_{x,3,b}^{\pm})} \sum_q \sum_p (\overline{\alpha_{3,a}^{+}})_q (\alpha_{3,b}^{\pm})_p < T_q, T_p > .$$

Note that the vector α used here has been normalised to avoid the incoherence among the mode solutions in the three sections. The projection of chebyshev polynomials is expressed as $< T_q, T_p >= \int_0^H T_q(2y/H - 1) T_p(2y/H - 1) dy$.

The recurrence relation for the first kind polynomials involves derivatives established by Eq. (B.16), and the Chebyshev polynomials of the first kind satisfy the relation Eq. (B.17).

$$\int_{-1}^{1} T_n(x) \mathrm{d}x = \begin{cases} \dfrac{(-1)^n + 1}{1 - n^2} & \text{if } n \geq 1, \\ 0 & \text{if } n = 0. \end{cases} \tag{B.16}$$

$$T_m(x) T_n(x) = \frac{1}{2} \left[T_{m+n}(x) + T_{|m-n|}(x) \right] \qquad \forall m, n \geq 0. \tag{B.17}$$

By combining the two previous equations, the projection of Chebyshev polynomials can be calculated as:

$$\int_{-1}^{1} T_m(x) T_n(x) \mathrm{d}x = \frac{1}{2} \left[\int_{-1}^{1} T_{m+n}(x) \mathrm{d}x + \int_{-1}^{1} T_{|m-n|}(x) \mathrm{d}x \right]. \tag{B.18}$$

Here, when substituting $x = 2y/H - 1$, it should be considered that the differential relation is $\mathrm{d}x = 2\mathrm{d}y/H$, and then the integral result can be deduced:

$$\int_0^H T_p(\frac{2y}{H} - 1) T_q(\frac{2y}{H} - 1) \mathrm{d}y = \frac{H}{2} < T_q, T_p >$$

$$= \frac{H}{2} \frac{1}{2} \begin{cases} \dfrac{\cos[(p+q)\pi] + 1}{1 - (p+q)^2} + \dfrac{\cos[(p-q)\pi] + 1}{1 - (p-q)^2} & \text{if } p + q \neq 1 \& |p - q| \neq 1 \\ \dfrac{\cos[(p+q)\pi] + 1}{1 - (p+q)^2} & \text{if } p + q \neq 1 \& |p - q| = 1 \\ 0 & \text{if } p + q = 1 (\text{i.e.} |p - q| = 1). \end{cases} \tag{B.19}$$

By using Eq. (B.19), the sub-matrix $\mathbf{M}_n^{\pm}$ and $\mathbf{P}_n^{+}$ can be calculated easily.

Furthermore, when it is necessary to consider the second integration term of sub-matrix $\mathbf{M}_n^{\pm}$ in Eq. (2.27), this term for two interfaces is expressed as:

$$\left[(\mathbf{M}_n^{\pm})_{a,b} \right]_{int2} = -\frac{\mathrm{i} u_0 c_0}{\omega Z} \sum_q \sum_p \overline{(\alpha_{1,a}^{-})}_q (\alpha_{n,b}^{\pm})_p T_q(0) T_p(0),$$

and

$$\left[(\mathbf{M}^{\pm}_{(n+1)})_{a,b}\right]_{int2} = -\frac{\mathrm{i}u_0 c_0}{\omega Z}.$$

Appendix C

Shear flow effects on transmission loss

The transmission loss TL is a measure of the reduction in acoustic energy as the sound travels through the lined section. It is calculated using the axial intensity, defined as $P = (u_0 u + p/\rho_0)(\rho_0 u + \rho u_0)$ [139]. Also, $TL_{m,i}$ represents the ratio in decibels (dB) between the power of the i^{th} incident mode from the left at the first interface and the power of the m^{th} right-running mode at the second interface (see Figure 2.5):

$$TL = 10 \log_{10} \frac{P_i}{P_m}. \tag{C.1}$$

C.1 Validation in no-flow case

First, the two propagation models provide the same transmission loss for the single-liner configuration in the case without flow, using both uniform and shear flow models, as shown in Figure C.1. Each sub-figure contains the transmission loss $TL_{m,i}$ between individual modes as a function of Helmholtz number He.

For the double-liner configuration, Figure C.2 illustrates that the transmission loss TL between modes of the same symmetry type remains consistent when comparing the uniform flow model with the shear flow model. However, discrepancies arise in the TL between modes of different symmetry types. This is attributed to the fact that the acoustic power transmitted to the mode of different symmetry type is nearly zero, but the numerical calculations for the two models yield results of different orders of magnitude. Consequently, while the transmission loss is significantly large in both cases, the values differ. The large values of TL indicate again that there is no acoustic transmission between modes of different symmetry types in this symmetric configuration.

C.2 Boundary layer thickness

Figure C.3 displays the transmission loss in the downstream propagation case with the single-liner configuration, either for the uniform flow model or the shear flow model. The Mach number is $M_{\text{ave}} = \pm 0.3$, and the displacement thickness δ_1 is between 0.01 and 0.1. The curve for $TL_{m,i}$ begins at the cut-off frequency of the mode of index $\min(m, i)$. In each sub-figures, the uniform and shear flow model demonstrate the similar trend of the transmission loss, but the shift between results of two models is more significant for larger boundary layer thickness.

Figure C.4 shows the transmission loss in the upstream propagation case with the single-liner configuration for both models.

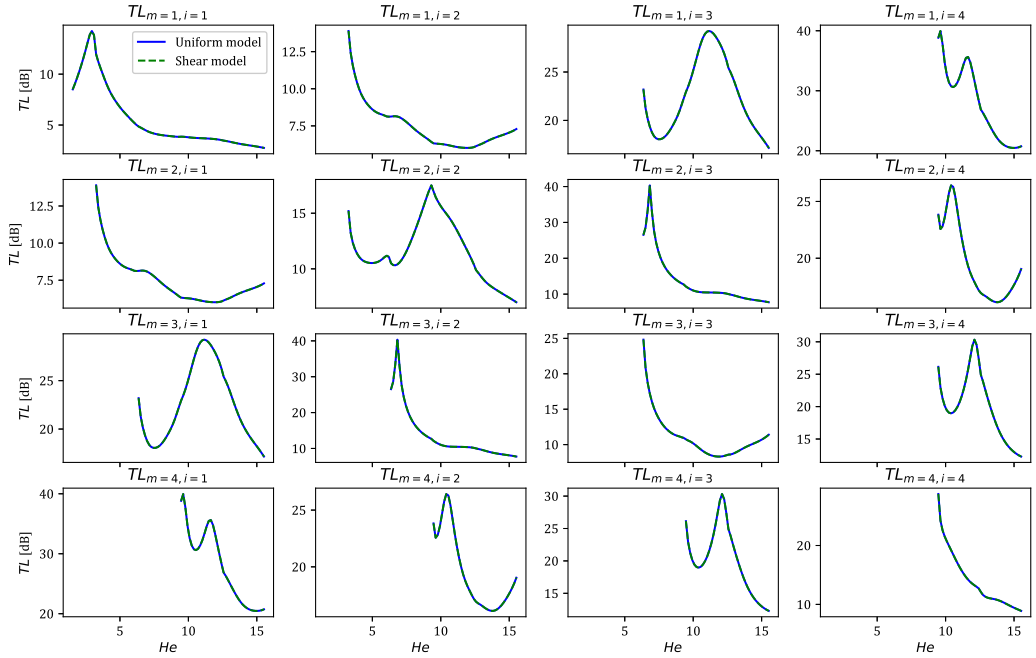

Figure C.1: Transmission loss for each modes in no-flow case using uniform flow model (blue solid lines) and shear flow model (green dashed lines). With i for incident modes and m for transmitted modes.

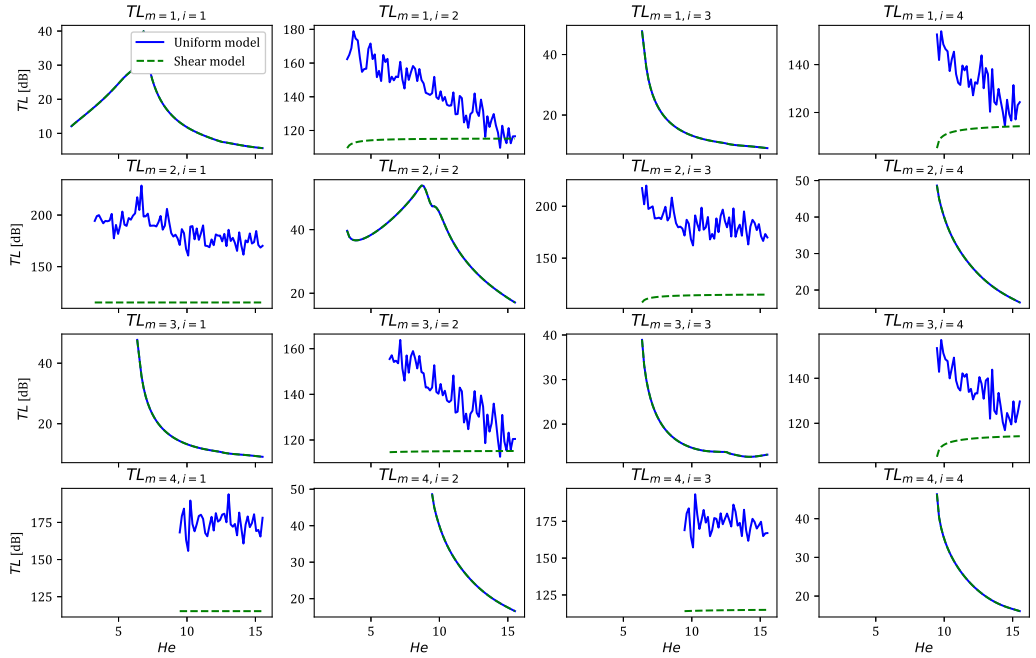

Figure C.2: Transmission loss for each modes in no-flow case using uniform flow model (blue solid lines) and shear flow model (green dashed lines). With i for incident modes and m for transmitted modes.

Figure C.5 displays the transmission loss in the downstream propagation case with the double-liner configuration for both models.

Figure C.6 presents the transmission loss in the upstream propagation case with the double-liner configuration for both models. Due to the dramatic difference in results for $M_{\text{ave}} = -0.7$ and its impact on the visibility of other results, it is omitted from the figures. Nevertheless, it underscores the significance of shear flow effects in the upstream propagation case, particularly at high velocities.

According to these results for the transmission loss, same conclusions can be drawn as in Section 3.4.2. The assumption of uniform flow does not adequately account for flow effects, and the effects of mean flow shear increases with the boundary layer thickness.

C.3 Mean flow velocity

Regarding the influence of flow velocity coupled with the shear flow effects, Figure C.7 displays the $TL_{m,i}$ for the single-liner configuration in the downstream propagation case with $\delta_1 = 0.05$ and various M_{ave}.

Figure C.8 shows the transmission loss in the upstream propagation case with the single-liner configuration for both models.

Figure C.9 displays the transmission loss in the downstream propagation case with the double-liner configuration for both models.

Figure C.10 presents the transmission loss in the upstream propagation case with the double-liner configuration for both models.

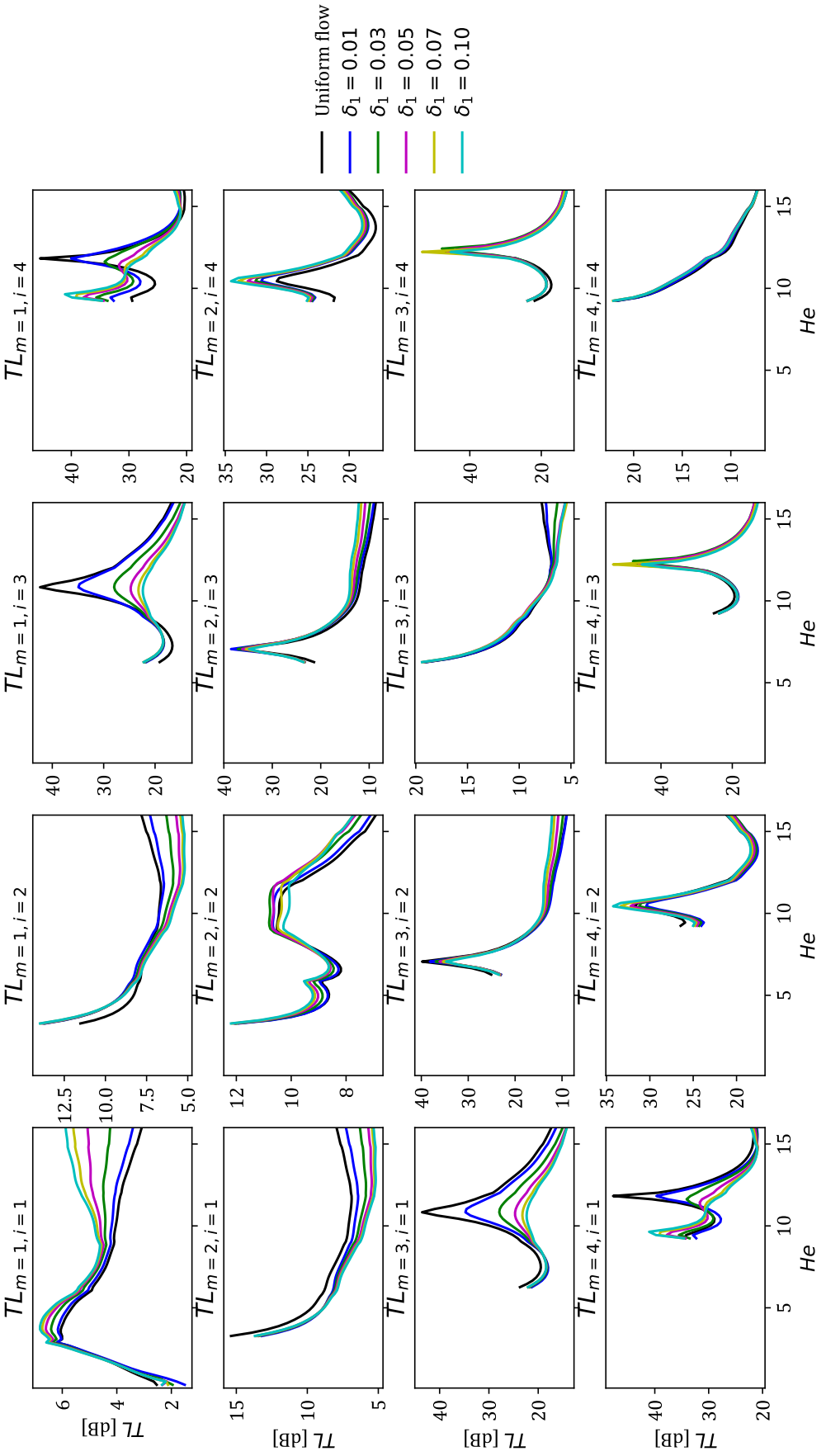

Figure C.3: Transmission loss for the single-liner configuration in the downstream propagation case, with the uniform flow model (black lines) and the shear flow model (coloured lines). With δ_1 varying from 0.01 to 0.1, $M_{\text{ave}} = +0.3$.

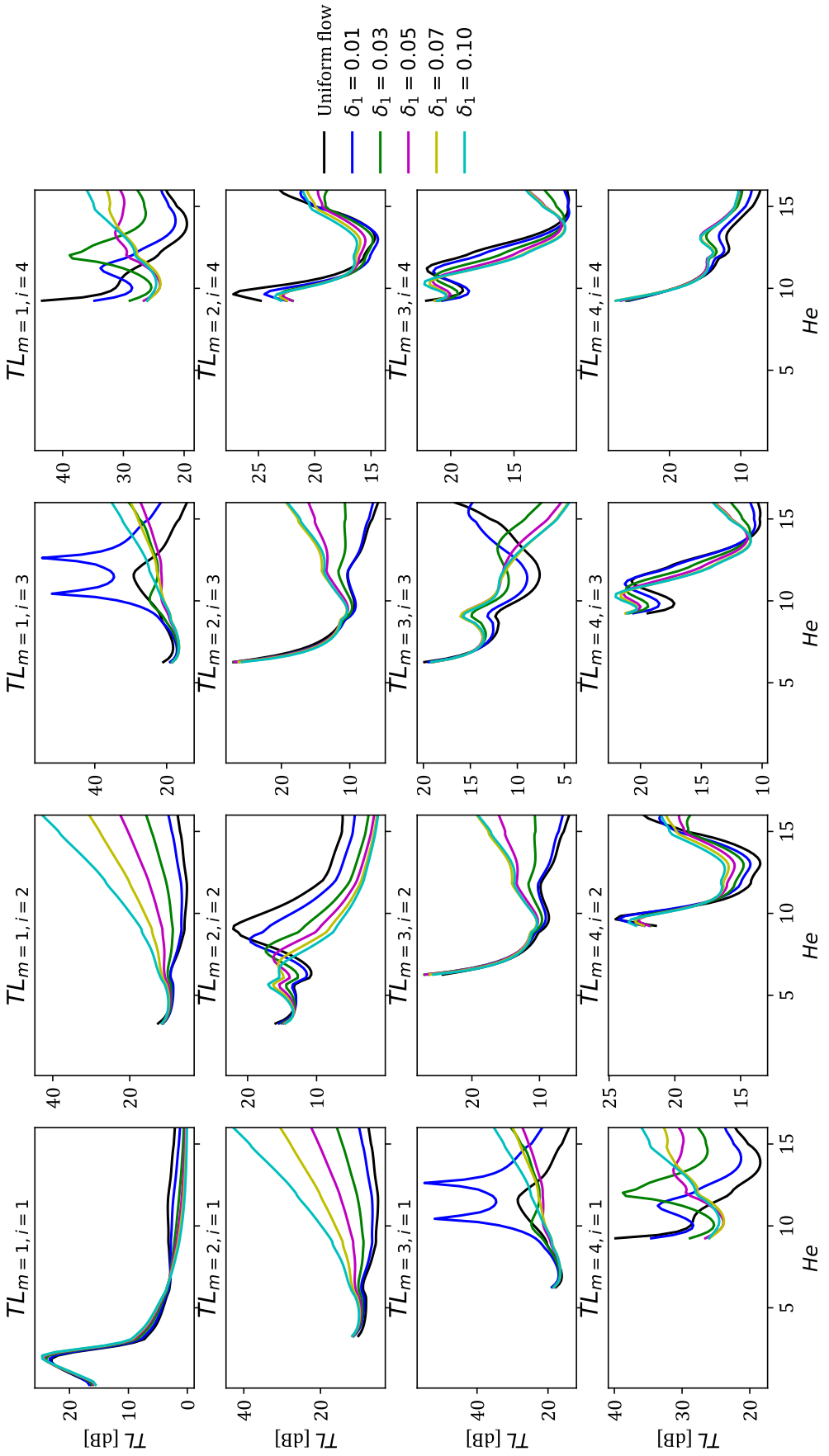

Figure C.4: Transmission loss for the single-liner configuration in the upstream propagation case, with the uniform flow model (black lines) and the shear flow model (coloured lines). With δ_1 varying from 0.01 to 0.1, $M_{\text{ave}} = -0.3$.

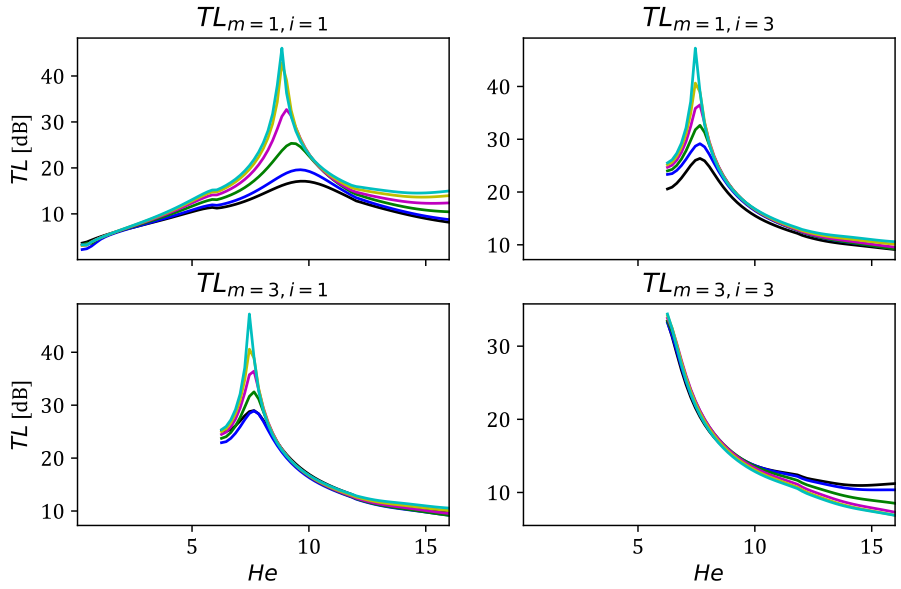

(a) Modes with odd indices.

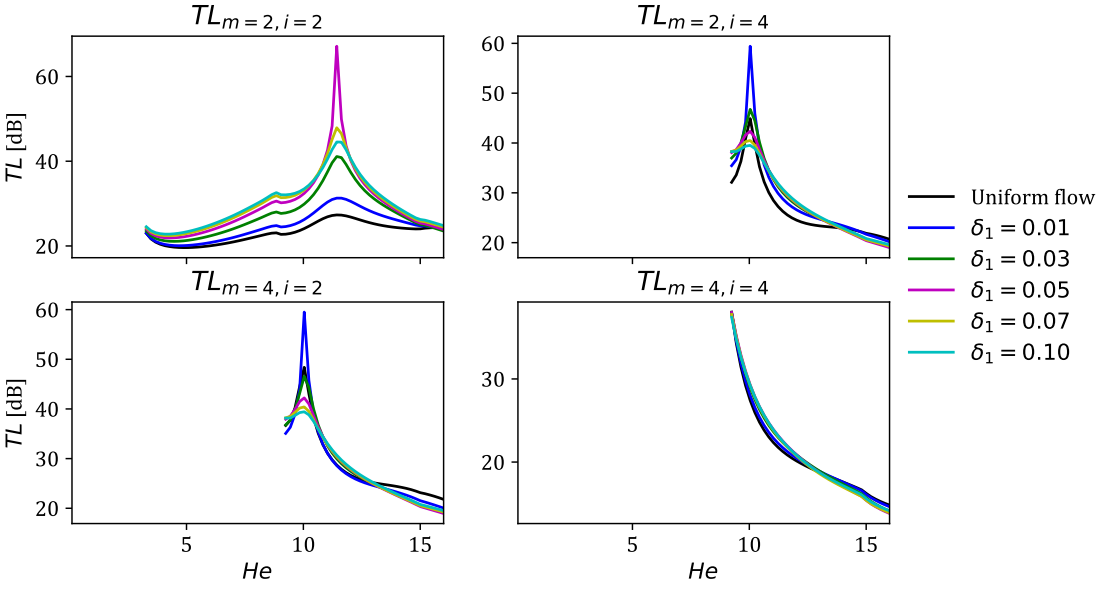

(b) Modes with even indices.

Figure C.5: Transmission loss for the double-liner configuration in the downstream propagation case, with the uniform flow model (black lines) and the shear flow model (coloured lines). With δ_1 varying from 0.01 to 0.1, $M_{\text{ave}} = +0.3$.

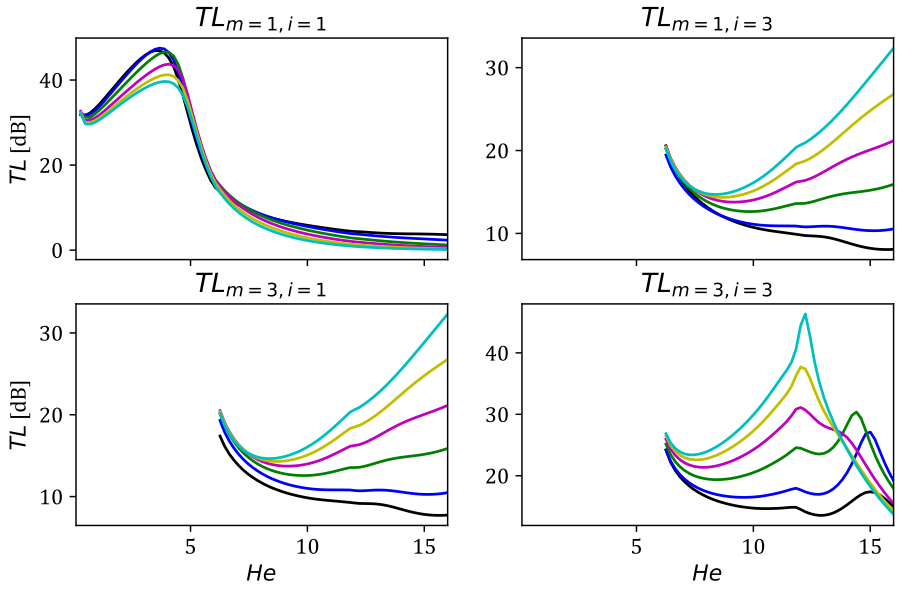

(a) Modes with odd indices.

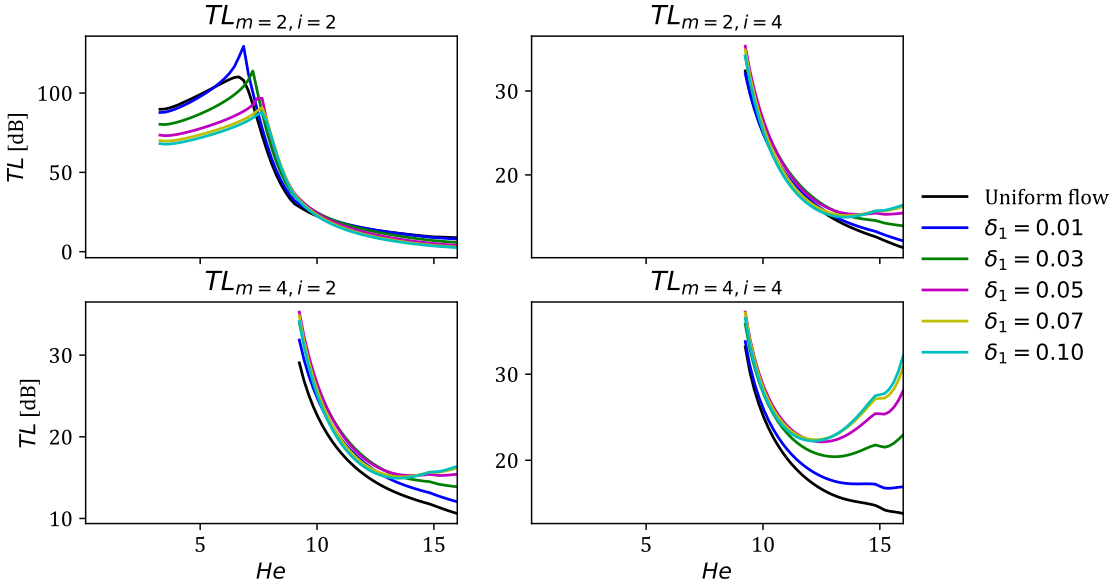

(b) Modes with even indices.

Figure C.6: Transmission loss for the double-liner configuration in the upstream propagation case, with the uniform flow model (black lines) and the shear flow model (coloured lines). With δ_1 varying from 0.01 to 0.1, $M_{\text{ave}} = -0.3$.

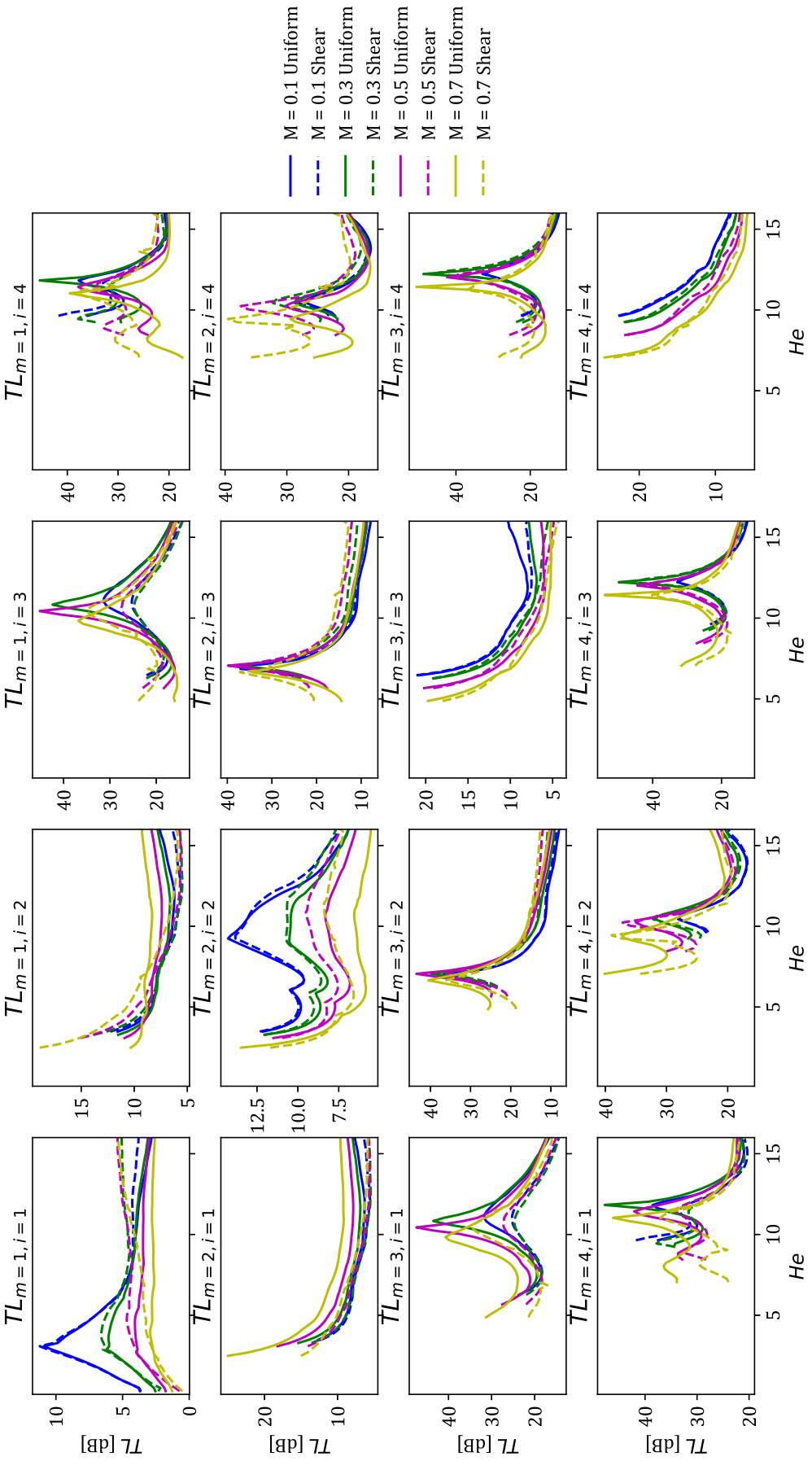

Figure C.7: Transmission loss for the single-liner configuration in the downstream propagation case, with the uniform flow model (solid lines) and the shear flow model (dashed lines). With $\delta_1 = 0.05$ and M_{ave} as $+0.1$ (blue), $+0.3$ (green), $+0.5$ (magenta) and $+0.7$ (yellow).

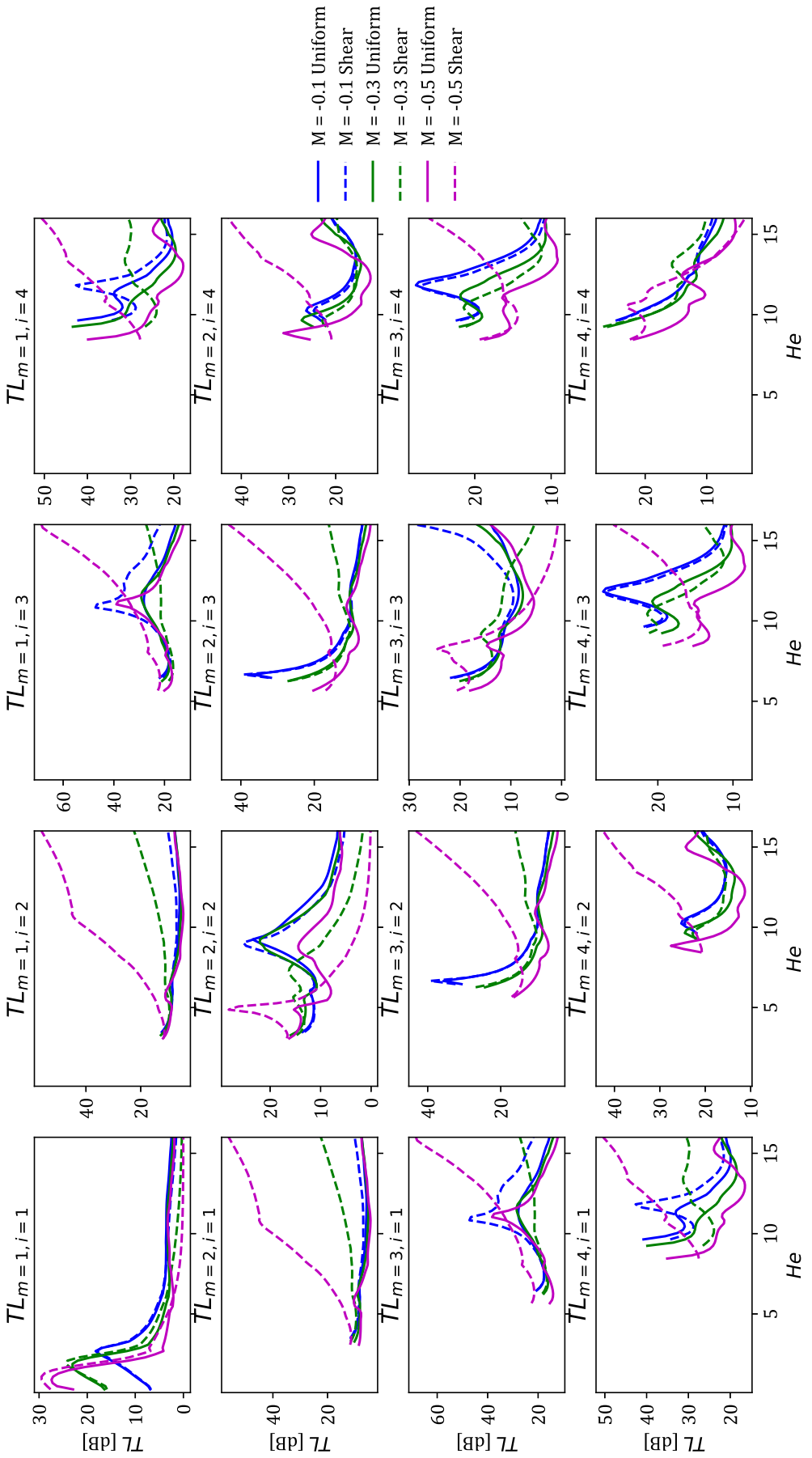

Figure C.8: Transmission loss for the single-liner configuration in the upstream propagation case, with the uniform flow model (solid lines) and the shear flow model (dashed lines). With $\delta_1 = 0.05$ and M_{ave} as -0.1 (blue), -0.3 (green), -0.5 (magenta) and -0.7 (yellow).

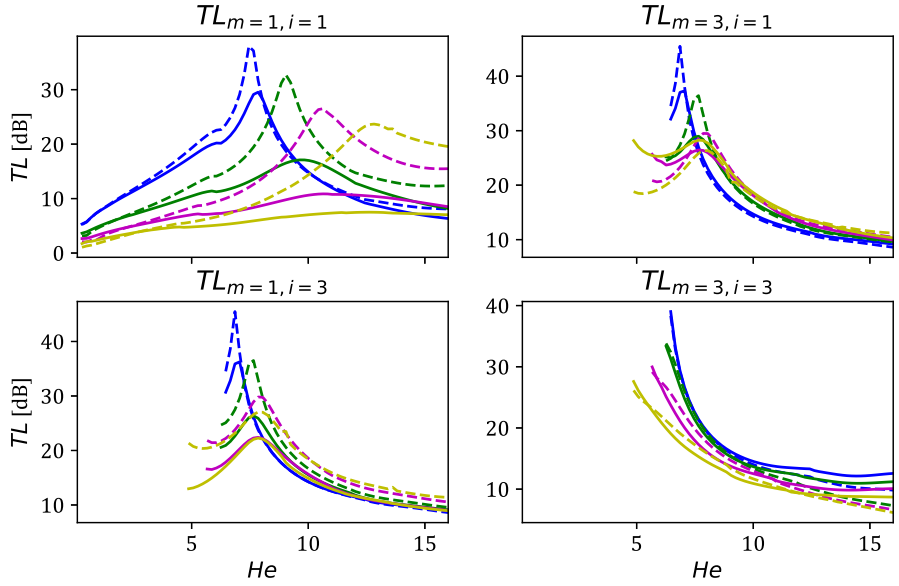

(a) Modes with odd indices.

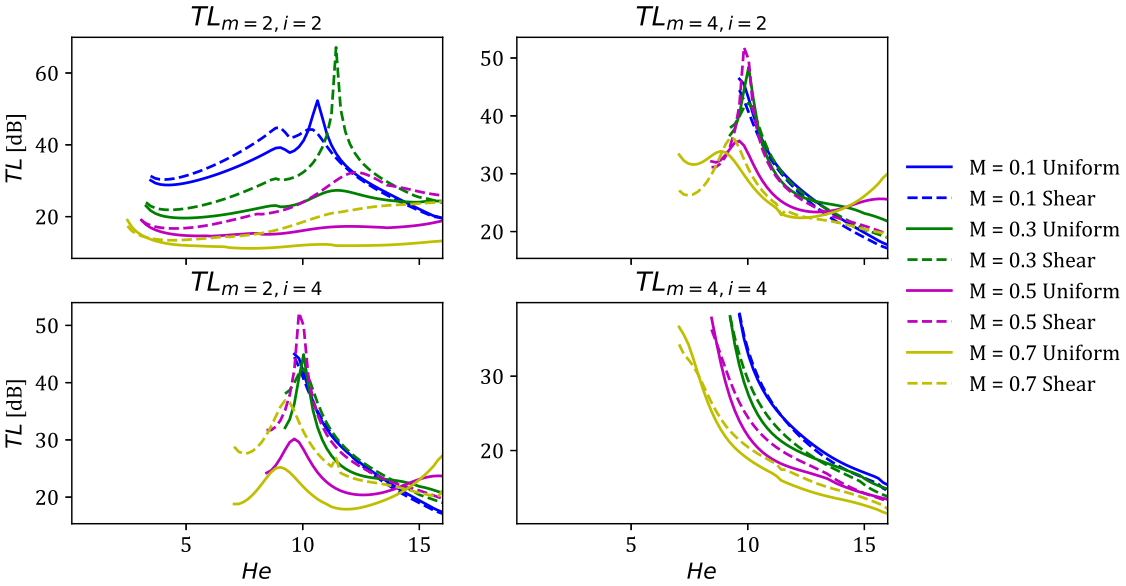

(b) Modes with even indices.

Figure C.9: Transmission loss for the double-liner configuration in the downstream propagation case, with the uniform flow model (solid lines) and the shear flow model (dashed lines). With $\delta_1 = 0.05$ and M_{ave} as $+0.1$ (blue), $+0.3$ (green), $+0.5$ (magenta) and $+0.7$ (yellow).

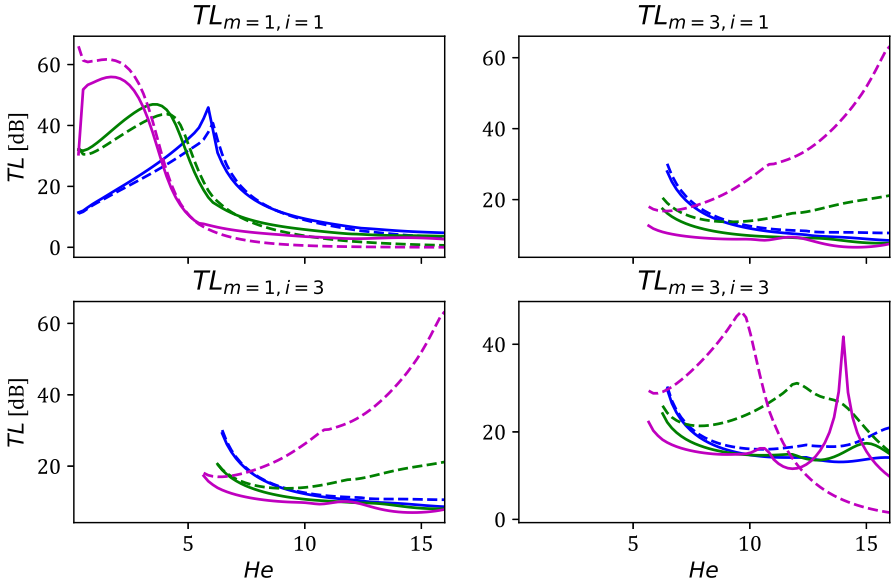

(a) Modes with odd indices.

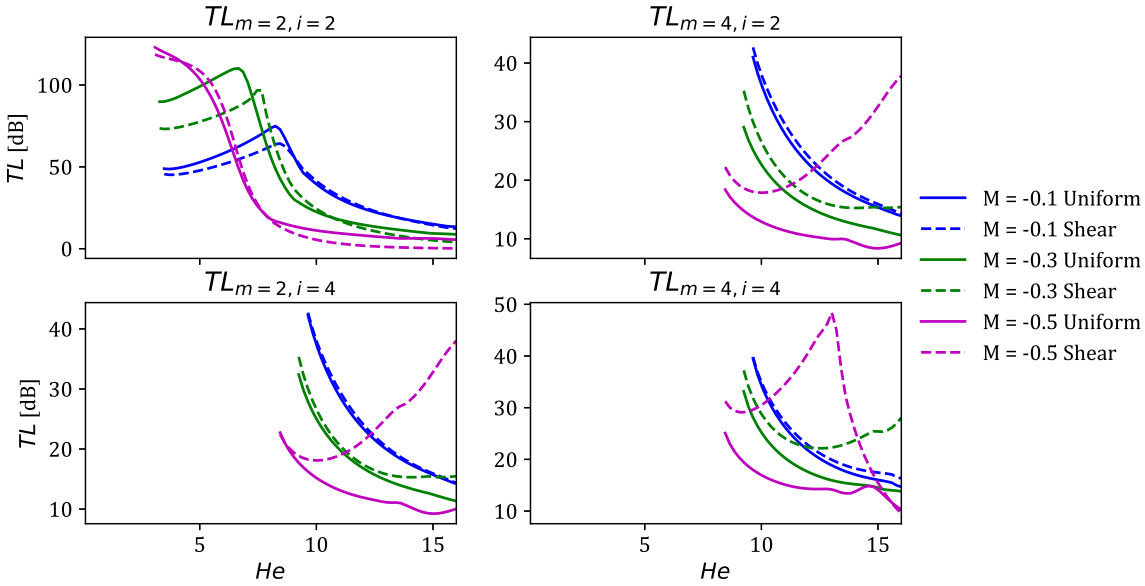

(b) Modes with even indices.

Figure C.10: Transmission loss for the double-liner configuration in the downstream propagation case, with the uniform flow model (solid lines) and the shear flow model (dashed lines). With $\delta_1 = 0.05$ and M_{ave} as -0.1 (blue), -0.3 (green), and -0.5 (magenta).

Bibliography

[1] K. U. Ingard, "Notes on sound absorption technology," *(No Title)*, 1994.

[2] R. Motsinger and R. Kraft, "14 design and performance of duct acoustic treatment," *Aeroacoustics of flight vehicles: theory and practice*, vol. 1, p. 165, 1991.

[3] D. Braga, "Fan noise prediction of aero-engines based on a modal approach in the presence of acoustic treatment and inviscid sheared flows," Ph.D. dissertation, Oct. 2019. DOI: 10.13140/RG.2.2.29395.12320.

[4] R. Billard, "Study of perforated liners for aeronautics," Ph.D. dissertation, Le Mans Université, 2021.

[5] L. Cremer, "Theory regarding the attenuation of sound transmitted by air in a rectangular duct with an absorbing wall, and the maximum attenuation constant produced during this process," *Acustica*, vol. 3, no. 1, pp. 249–263, 1953.

[6] A. M. N. Spillere, "Boundary layer effects on acoustic liners for turbofan engines: From experimental methods to optimization techniques," Ph.D. dissertation, 2022.

[7] U. Ingard and H. Ising, "Acoustic nonlinearity of an orifice," *The journal of the Acoustical Society of America*, vol. 42, no. 1, pp. 6–17, 1967.

[8] L. A. Bonomo, N. T. Quintino, A. Spillere, J. A. Cordioli, and P. B. Murray, "A comparison of in-situ and impedance eduction experimental techniques for acoustic liners with grazing flow and high spl," in *28th AIAA/CEAS Aeroacoustics 2022 Conference*, 2022, p. 2998.

[9] W. R. Watson and M. G. Jones, "A comparative study of four impedance eduction methodologies using several test liners," in *19th AIAA/CEAS Aeroacoustics Conference*, 2013, p. 2274.

[10] J. Golliard, J.-C. Leroux, E. Portier, T. Humbert, and Y. Auregan, "Maine flow: Experimental facility for characterization of liners subjected to representative acoustical excitation and grazing flow," in *25th AIAA/CEAS Aeroacoustics Conference*, 2019, p. 2682.

[11] J. Golliard, E. Portier, J.-C. Le Roux, and T. Humbert, "Maine flow facility for measurement of liner properties in multimodal acoustic field with grazing flow: Qualification and first liner characterization," in *AIAA Aviation 2021 Forum*, 2021, p. 2145.

[12] T. Humbert, J. Golliard, E. Portier, G. Gabard, and Y. Auregan, "Multimodal characterisation of acoustic liners using the maine flow facility," in *28th AIAA/CEAS Aeroacoustics 2022 Conference*, 2022, p. 3082.

[13] P. Dean, "An in situ method of wall acoustic impedance measurement in flow ducts," *Journal of Sound and Vibration*, vol. 34, no. 1, 97–IN6, 1974.

[14] M. Jones, W. Watson, M. Tracy, and T. Parrott, "Comparison of two waveguide methods for educing liner impedance in grazing flow," *AIAA journal*, vol. 42, no. 2, pp. 232–240, 2004.

[15] X. Jing, S. Peng, and X. Sun, "A straightforward method for wall impedance eduction in a flow duct," *The Journal of the Acoustical Society of America*, vol. 124, no. 1, pp. 227–234, 2008.

[16] Y. Aurégan, M. Leroux, and V. Pagneux, "Measurement of liner impedance with flow by an inverse method," in *10th AIAA/CEAS aeroacoustics conference*, 2004, p. 2838.

[17] L. A. Bonomo, A. M. Spillere, and J. A. Cordioli, "Parametric uncertainty analysis for impedance eduction based on prony's method," *AIAA Journal*, vol. 58, no. 8, pp. 3625–3638, 2020.

[18] A. Spillere, J. A. Cordioli, and H. Bodén, "On the effect of boundary conditions on impedance eduction results," in *23rd AIAA/CEAS Aeroacoustics Conference*, 2017, p. 3185.

[19] R. Roncen, E. Piot, F. Méry, F. Simon, M. G. Jones, and D. M. Nark, "Wavenumber-based impedance eduction with a shear grazing flow," *AIAA Journal*, vol. 58, no. 7, pp. 3040–3050, 2020.

[20] X. Jing, S. Peng, L. Wang, and X. Sun, "Investigation of straightforward impedance eduction in the presence of shear flow," *Journal of Sound and Vibration*, vol. 335, pp. 89–104, 2015.

[21] W. Watson and M. Jones, "Validation of a new procedure for impedance eduction in flow," in *16th AIAA/CEAS Aeroacoustics Conference*, 2010, p. 3764.

[22] L. A. Bonomo, N. T. Quintino, J. A. Cordioli, F. Avallone, M. G. Jones, B. M. Howerton, and D. M. Nark, "A comparison of impedance eduction test rigs with different flow profiles," in *AIAA AVIATION 2023 Forum*, 2023, p. 3346.

[23] W. R. Watson, M. G. Jones, and J. C. June, "Single mode theory for impedance eduction in large-scale ducts with grazing flow," in *20th AIAA/CEAS Aeroacoustics Conference*, 2014, p. 3351.

[24] W. R. Watson and M. G. Jones, "Impedance eduction in large ducts containing high-order modes and grazing flow," in *23rd AIAA/CEAS Aeroacoustics Conference*, 2017, p. 3183.

[25] R. Roncen, F. Méry, and E. Piot, "Bayesian inference for modal identification in ducts with a shear flow," *The Journal of the Acoustical Society of America*, vol. 146, no. 4, pp. 2645–2654, 2019.

[26] W. R. Watson, M. H. Carpenter, and M. G. Jones, "Performance of kumaresan and tufts algorithm in liner impedance eduction with flow," *AIAA Journal*, vol. 53, no. 4, pp. 1091–1102, 2015.

[27] B. L. Bertolucci, *An experimental investigation of the grazing flow impedance duct at the University of Florida for acoustic liner applications*. University of Florida, 2012.

[28] P. Joseph and M. Smith, "Aircraft noise," *Advanced Applications in Acoustics, Noise and Vibration*, p. 292, 2004.

[29] D. Casalino, F. Diozzi, R. Sannino, and A. Paonessa, "Aircraft noise reduction technologies: A bibliographic review," *Aerospace Science and Technology*, vol. 12, no. 1, pp. 1–17, 2008.

[30] D. Sutliff, "A 20 year retrospective of the advanced noise control fan – contributions to turbofan noise research," Aug. 2019. DOI: 10.2514/6.2019-3824.

[31] J. M. Tyler and T. G. Sofrin, "Axial flow compressor noise studies," SAE Technical Paper, Tech. Rep., 1962.

[32] D. L. Huff, "Noise reduction technologies for turbofan engines," in *35th International Congress and Exposition on Noise Control Engineering (INTER-NOISE 2006)*, 2007.

[33] T. Zandbergen, "Do locally reacting acoustic liners always behave as they should?" *AIAA Journal*, vol. 18, no. 4, pp. 396–397, 1980.

[34] A. H. Nayfeh, J. E. Kaiser, and D. P. Telionis, "Acoustics of aircraft engine-duct systems," *Aiaa Journal*, vol. 13, no. 2, pp. 130–153, 1975.

[35] Y. Aurégan, R. Starobinski, and V. Pagneux, "Influence of grazing flow and dissipation effects on the acoustic boundary conditions at a lined wall," *The Journal of the Acoustical Society of America*, vol. 109, no. 1, pp. 59–64, 2001.

[36] A. Guess, "Calculation of perforated plate liner parameters from specified acoustic resistance and reactance," *Journal of Sound and Vibration*, vol. 40, no. 1, pp. 119–137, 1975.

[37] C. Zwikker and C. Kosten, *Sound Absorbing Materials*. Elsevier Publishing Company, 1949.

[38] M. R. Stinson, "The propagation of plane sound waves in narrow and wide circular tubes, and generalization to uniform tubes of arbitrary cross-sectional shape," *The Journal of the Acoustical Society of America*, vol. 89, no. 2, pp. 550–558, 1991.

[39] S. W. Rienstra and A. Hirschberg, "An introduction to acoustics," 2004.

[40] U. Ingard, "On the theory and design of acoustic resonators," *The Journal of the acoustical society of America*, vol. 25, no. 6, pp. 1037–1061, 1953.

[41] T. H. Melling, "The acoustic impendance of perforates at medium and high sound pressure levels," *Journal of Sound and Vibration*, vol. 29, no. 1, pp. 1–65, 1973.

[42] C. K. Tam and K. A. Kurbatskii, "Microfluid dynamics and acoustics of resonant liners," *AIAA journal*, vol. 38, no. 8, pp. 1331–1339, 2000.

[43] C. K. Tam, H. Ju, M. G. Jones, W. R. Watson, and T. L. Parrott, "A computational and experimental study of resonators in three dimensions," *Journal of Sound and Vibration*, vol. 329, no. 24, pp. 5164–5193, 2010.

[44] X. Jing and X. Sun, "Sound-excited flow and acoustic nonlinearity at an orifice," *Physics of Fluids*, vol. 14, no. 1, pp. 268–276, 2002.

[45] R. Scott, "An apparatus for accurate measurement of the acoustic impedance of sound-absorbing materials," *Proceedings of the Physical Society*, vol. 58, no. 3, p. 253, 1946.

[46] M. J. Crocker, *Handbook of noise and vibration control*. John Wiley & Sons, 2007.

[47] J. Kooi and S. Sarin, "An experimental study of the acoustic impedance of helmholtz resonator arrays under a turbulent boundary layer," in *7th aeroacoustics conference*, 1981, p. 1998.

[48] J. Simonich, B. Morin, S. Narayanan, and W. Patrick, "Development and qualification of an in-situ grazing flow impedance measurement facility," in *12 th AIAA/CEAS Aeroacoustics Conference(27 th AIAA Aeroacoustics Conference)*, 2006.

[49] T. Elnady and H. Bodén, "An inverse analytical method for extracting liner impedance from pressure measurements," in *10th AIAA/CEAS aeroacoustics conference*, 2004, p. 2836.

[50] A. Alomar and Y. Aurégan, "Liner impedance determination from piv acoustic measurements," *Euronoise. Maastricht, The Netherlands*, vol. 31, 2015.

[51] T. Zandbergen, "On the practical use of a three-microphone technique for in-situ acoustic impedance measurements on double layer flow duct liners," in *7th Aeroacoustics Conference*, 1981, p. 2000.

[52] D. Armstrong, R. Beckemeyer, and R. Olsen, "Impedance measurements of acoustic duct liners with grazing flow," *The Journal of the Acoustical Society of America*, vol. 55, no. S1, S59–S59, 1974.

[53] A. A. Syed, "On the prediction of sound attenuation in acoustically lined circular ducts," Ph.D. dissertation, Loughborough University, 1980.

[54] W. R. Watson, M. G. Jones, and T. L. Parrott, "Validation of an impedance eduction method in flow," *AIAA journal*, vol. 37, no. 7, pp. 818–824, 1999.

[55] M. Jones, W. Watson, and T. Parrott, "Benchmark data for evaluation of aeroacoustic propagation codes with grazing flow," in *11th AIAA/CEAS Aeroacoustics Conference*, 2005, p. 2853.

[56] W. Watson and M. Jones, "Comparison of a convected helmholtz and euler model for impedance eduction in flow," in *12th AIAA/CEAS Aeroacoustics Conference (27th AIAA Aeroacoustics Conference)*, 2006, p. 2643.

[57] M. Jones and W. Watson, "On the use of experimental methods to improve confidence in educed impedance," in *17th AIAA/CEAS Aeroacoustics Conference (32nd AIAA Aeroacoustics Conference)*, 2011, p. 2865.

[58] W. R. Watson and M. G. Jones, "Impedance eduction in a duct using linearized euler equations," in *2018 AIAA/CEAS Aeroacoustics Conference*, 2018, p. 3442.

[59] C. Weng, A. Schulz, D. Ronneberger, L. Enghardt, and F. Bake, "Flow and viscous effects on impedance eduction," *AIAA Journal*, vol. 56, no. 3, pp. 1118–1132, 2018.

[60] A. M. N. Spillere, L. A. Bonomo, J. A. Cordioli, and E. J. Brambley, "Experimentally testing impedance boundary conditions for acoustic liners with flow: Beyond upstream and downstream," *Journal of Sound and Vibration*, vol. 489, p. 115 676, 2020.

[61] J. Yang, H. Rashidi, T. Humbert, G. Gabard, Y. Aurégan, J. Golliard, and E. Portier, "Impedance eduction of acoustic liners using the maine flow facility," 2023.

[62] A. Scofano, P. Murray, and P. Ferrante, "Back-calculation of liner impedance using duct insertion loss measurements and fem predictions," in *13th AIAA/CEAS Aeroacoustics Conference (28th AIAA Aeroacoustics Conference)*, 2007, p. 3534.

[63] R. Troian, D. Dragna, C. Bailly, and M.-A. Galland, "Broadband eduction of liner impedance under multimodal acoustic propagation," in *22nd AIAA/CEAS Aeroacoustics Conference*, 2016, p. 2725.

[64] A. M. Spillere, L. A. Bonomo, J. A. Cordioli, and E. J. Brambley, "Testing impedance eduction boundary conditions with four wavenumbers per frequency," in *25th AIAA/CEAS Aeroacoustics Conference*, 2019, p. 2488.

[65] W. Watson, M. Jones, and T. Parrott, "A quasi-3-d theory for impedance eduction in uniform grazing flow," in *11th AIAA/CEAS Aeroacoustics Conference*, 2005, p. 2848.

[66] W. Watson and M. Jones, "Impedance eduction in ducts with higher order modes and flow," in *15th AIAA/CEAS Aeroacoustics Conference (30th AIAA Aeroacoustics Conference)*, 2009, p. 3236.

[67] W. Watson and M. Jones, "New numerical procedure for impedance eduction in ducts containing mean flow," *AIAA journal*, vol. 49, no. 10, pp. 2109–2122, 2011.

[68] A. M. Spillere, A. A. Medeiros, and J. A. Cordioli, "An improved impedance eduction technique based on impedance models and the mode matching method," *Applied Acoustics*, vol. 129, pp. 322–334, 2018.

[69] P. Zhang, C. Yang, and Y. Huang, "An improved algorithm for liner impedance eduction in low signal-to-noise ratio flow duct," *International Journal of Aeroacoustics*, vol. 21, no. 3-4, pp. 168–189, 2022.

[70] A. Minotti, F. Simon, and F. Gantié, "Characterization of an acoustic liner by means of laser doppler velocimetry in a subsonic flow," *Aerospace Science and Technology*, vol. 12, no. 5, pp. 398–407, 2008.

[71] E. Piot, J. Primus, and F. Simon, "Liner impedance eduction technique based on velocity fields," in *18th AIAA/CEAS Aeroacoustics Conference (33rd AIAA Aeroacoustics Conference)*, 2012, p. 2198.

[72] V. Lafont, F. Méry, R. Roncen, F. Simon, and E. Piot, "Liner impedance eduction under shear grazing flow at a high sound pressure level," *AIAA Journal*, vol. 58, no. 3, pp. 1107–1117, 2020.

[73] G. R. de Prony, "Essai experimental et analytique: Sur les lois de la dilatabilite des fluides elastique et sur celles de la force expansive de la vapeur de l'eau et de la vapeur de l'alkool, a differentes temperatures," *Journal Polytechnique ou Bulletin du Travail fait a l'Ecole Centrale des Travaux Publics*, 1795.

[74] P. Zhang, Y. Huang, Z. Yang, C. Yang, and W. Jiang, "Effect of source direction on liner impedance eduction with consideration of shear flow," *Applied Acoustics*, vol. 183, p. 108 297, 2021.

[75] X. Qiu, B. Bin, L. Lu, Y. Meng, and X. Jing, "Investigation of straightforward impedance eduction method on single-degree-of-freedom acoustic liners," *Chinese Journal of Aeronautics*, vol. 31, no. 12, pp. 2221–2233, 2018.

[76] Y. Renou and Y. Aurégan, "Failure of the ingard–myers boundary condition for a lined duct: An experimental investigation," *The Journal of the Acoustical Society of America*, vol. 130, no. 1, pp. 52–60, 2011.

[77] X. Qiu, B. Xin, and X. Jing, "Straightforward impedance eduction method for non-grazing incidence wave with multiple modes," *Journal of Sound and Vibration*, vol. 432, pp. 1–16, 2018.

[78] X. Jing, Y. Wang, L. Du, X. Qiu, and X. Sun, "Impedance eduction experiments covering higher frequencies based on the multimodal straightforward method," *Applied Acoustics*, vol. 206, p. 109 327, 2023.

[79] L. Chen, L. Du, X. Wang, X. Jing, and X. Sun, "A three-dimensional straightforward method for liner impedance eduction in uniform grazing flow," *Journal of Sound and Vibration*, vol. 468, p. 115 119, 2020.

[80] X. Qiu, J. Yang, X. Jing, L. Du, and X. Sun, "Mirror-based multimodal straightforward method for impedance eduction using a zigzag array," *Journal of Sound and Vibration*, vol. 576, p. 118 237, 2024.

[81] M. E. d'Elia, T. Humbert, and Y. Aurégan, "Direct impedance eduction of liners from laser doppler velocimetry measurements," in *25th AIAA/CEAS Aeroacoustics Conference*, 2019, p. 2516.

[82] R. Kumaresan and D. Tufts, "Estimating the parameters of exponentially damped sinusoids and pole-zero modeling in noise," *IEEE transactions on acoustics, speech, and signal processing*, vol. 30, no. 6, pp. 833–840, 1982.

[83] T. Humbert, R. Delalande, G. Gabard, J. Golliard, and Y. Auregan, "Performance of the matrix pencil algorithm in direct impedance eduction of liners: Some numerical experiments," in *25th AIAA/CEAS Aeroacoustics Conference*, 2019, p. 2676.

[84] C. Weng, L. Enghardt, and F. Bake, "Comparison of non-modal-based and modal-based impedance eduction techniques," in *2018 AIAA/CEAS Aeroacoustics Conference*, 2018, p. 3773.

[85] S. Busse-Gerstengarbe, F. Bake, L. Enghardt, and M. G. Jones, "Comparative study of impedance eduction methods," in *19th AIAA/CEAS Aeroacoustics Conference*, 2013.

[86] P. Murray, P. Ferrante, and A. Scofano, "Manufacturing process and boundary layer influences on perforate liner impedance," in *11th AIAA/CEAS Aeroacoustics Conference*, 2005, p. 2849.

[87] L. Zhou, H. Boden, C. Lahiri, F. Bake, L. Enghardt, S. Busse-Gerstengarbe, and T. Elnady, "Comparison of impedance eduction results using different methods and test rigs," in *20th AIAA/CEAS Aeroacoustics Conference*, 2014, p. 2955.

[88] B. Xin, J. Yang, X. Jing, and X. Sun, "Experimental and numerical investigation of anechoic termination for a duct with mean flow," *Applied Acoustics*, vol. 139, pp. 213–221, 2018.

[89] M. Jones, T. Parrott, and W. Watson, "Comparison of acoustic impedance eduction techniques for locally-reacting liners," in *9th AIAA/CEAS Aeroacoustics Conference and Exhibit*, 2003, p. 3306.

[90] S. Busse-Gerstengarbe, C. Richter, F. H. Thiele, C. Lahiri, L. Enghardt, I. Roehle, P. Ferrante, and A. Scofano, "Impedance eduction based on microphone measurements of liners under grazing flow conditions," *AIAA journal*, vol. 50, no. 4, pp. 867–879, 2012.

[91] J. Primus, E. Piot, F. Simon, M. G. Jones, and W. Watson, "Onera-nasa cooperative effort on liner impedance eduction," in *19th AIAA/CEAS Aeroacoustics Conference*, 2013, p. 2273.

[92] U. Ingard, "Influence of fluid motion past a plane boundary on sound reflection, absorption, and transmission," *The Journal of the Acoustical Society of America*, vol. 31, no. 7, pp. 1035–1036, 1959.

[93] M. Myers, "On the acoustic boundary condition in the presence of flow," *Journal of Sound and vibration*, vol. 71, no. 3, pp. 429–434, 1980.

[94] W. Eversman and R. J. Beckemeyer, "Transmission of sound in ducts with thin shear layers—convergence to the uniform flow case," *The Journal of the Acoustical Society of America*, vol. 52, no. 1B, pp. 216–220, 1972.

[95] B. Tester, "Some aspects of "sound" attenuation in lined ducts containing inviscid mean flows with boundary layers," *Journal of Sound and Vibration*, vol. 28, no. 2, pp. 217–245, 1973.

[96] L. Zhou and H. Bodén, "A systematic uncertainty analysis for liner impedance eduction technology," *Journal of sound and vibration*, vol. 356, pp. 86–99, 2015.

[97] E. Brambley, "Viscous boundary layer effects on the myers impedance boundary condition," in *15th AIAA/CEAS Aeroacoustics Conference (30th AIAA Aeroacoustics Conference)*, 2009, p. 3241.

[98] S. W. Rienstra and M. Darau, "Boundary-layer thickness effects of the hydrodynamic instability along an impedance wall," *Journal of Fluid Mechanics*, vol. 671, pp. 559–573, 2011.

[99] G. Gabard, "A comparison of impedance boundary conditions for flow acoustics," *Journal of Sound and Vibration*, vol. 332, no. 4, pp. 714–724, 2013.

[100] E. J. Brambley, "Well-posed boundary condition for acoustic liners in straight ducts with flow," *AIAA journal*, vol. 49, no. 6, pp. 1272–1282, 2011.

[101] A. Schulz, C. Weng, F. Bake, L. Enghardt, and D. Ronneberger, "Modeling of liner impedance with grazing shear flow using a new momentum transfer boundary condition," in *23rd AIAA/CEAS aeroacoustics conference*, 2017, p. 3377.

[102] D. Khamis and E. J. Brambley, "Acoustic boundary conditions at an impedance lining in inviscid shear flow," *Journal of Fluid Mechanics*, vol. 796, pp. 386–416, 2016.

[103] A. H. Nayfeh, "Effect of the acoustic boundary layer on the wave propagation in ducts," *The Journal of the Acoustical Society of America*, vol. 54, no. 6, pp. 1737–1742, 1973.

[104] R. Starobinski, "Sound propagation in lining duct with essentially non-uniform distribution of velocity and temperature," *Noise of jet engines*, no. 2, pp. 155–181, 1978.

[105] Y. Aurégan, "On the use of a stress–impedance model to describe sound propagation in a lined duct with grazing flow," *The Journal of the Acoustical Society of America*, vol. 143, no. 5, pp. 2975–2979, 2018.

[106] C. Weng, C. Otto, L. Peerlings, L. Enghardt, and F. Bake, "Experimental investigation of sound field decomposition with higher order modes in rectangular ducts," in *22nd AIAA/CEAS Aeroacoustics Conference*, 2016, p. 3035.

[107] A. Prinn, "Efficient finite element methods for aircraft engine noise prediction," Ph.D. dissertation, University of Southampton, 2014.

[108] J. P. Boyd, *Chebyshev and Fourier spectral methods*. Courier Corporation, 2001.

[109] E. J. Brambley, M. Darau, and S. W. Rienstra, "The critical layer in linear-shear boundary layers over acoustic linings," *Journal of Fluid Mechanics*, vol. 710, pp. 545–568, 2012.

[110] G. Gabard and R. Astley, "A computational mode-matching approach for sound propagation in three-dimensional ducts with flow," *Journal of Sound and Vibration*, vol. 315, no. 4-5, pp. 1103–1124, 2008.

[111] D. C. Pridmore-Brown, "Sound propagation in a fluid flowing through an attenuating duct," *Journal of Fluid Mechanics*, vol. 4, no. 4, pp. 393–406, 1958.

[112] J.-M. Papy, L. De Lathauwer, and S. Van Huffel, "Common pole estimation in multi-channel exponential data modeling," *Signal Processing*, vol. 86, no. 4, pp. 846–858, 2006.

[113] S. Braun and Y. Ram, "Determination of structural modes via the prony model: System order and noise induced poles," *The Journal of the Acoustical Society of America*, vol. 81, no. 5, pp. 1447–1459, 1987.

[114] S.-Y. Kung, K. S. Arun, and D. B. Rao, "State-space and singular-value decomposition-based approximation methods for the harmonic retrieval problem," *JOSA*, vol. 73, no. 12, pp. 1799–1811, 1983.

[115] S. Van Huffel, "Enhanced resolution based on minimum variance estimation and exponential data modeling," *Signal processing*, vol. 33, no. 3, pp. 333–355, 1993.

[116] M. D'Elia, T. Humbert, and Y. Aurégan, "Effect of flow on an array of helmholtz resonators: Is kevlar a "magic layer"?" *The Journal of the Acoustical Society of America*, vol. 148, no. 6, pp. 3392–3396, 2020.

[117] G. Gabard, "Boundary layer effects on liners for aircraft engines," *Journal of Sound and Vibration*, vol. 381, pp. 30–47, 2016.

[118] H. Schlichting and J. Kestin, *Boundary layer theory*. Springer, 1961, vol. 121.

[119] J. Yang, T. Humbert, J. Golliard, and G. Gabard, "Shear flow effects in a 2d duct: Influence on wave propagation and direct impedance eduction," *Journal of Sound and Vibration*, vol. 576, p. 118 296, 2024.

[120] H. Chen, S. Van Huffel, and J. Vandewalle, "Improved methods for exponential parameter estimation in the presence of known poles and noise," *IEEE transactions on signal processing*, vol. 45, no. 5, pp. 1390–1393, 1997.

[121] M. G. Jones and W. R. Watson, "Effects of liner length and attenuation on nasa langley impedance eduction," in *22nd AIAA/CEAS Aeroacoustics Conference*, 2016, p. 2782.

[122] J.-M. Papy, L. De Lathauwer, and S. Van Huffel, "A shift invariance-based order-selection technique for exponential data modelling," *IEEE signal processing letters*, vol. 14, no. 7, pp. 473–476, 2007.

[123] C. Weng, A. Schulz, D. Ronneberger, L. Enghardt, and F. Bake, "Impedance eduction in the presence of turbulent shear flow using the linearized navier-stokes equations," in *23rd AIAA/CEAS aeroacoustics conference*, 2017, p. 3182.

[124] D. M. Nark, M. G. Jones, and E. Piot, "Assessment of axial wave number and mean flow uncertainty on acoustic liner impedance eduction," in *2018 AIAA/CEAS Aeroacoustics Conference*, 2018, p. 3444.

[125] M. G. Jones, D. M. Nark, and B. M. Howerton, "Nasa investigation of flow direction effects on impedance eduction for acoustic liners," in *30th AIAA/CEAS Aeroacoustics Conference (2024)*, 2024, p. 3297.

[126] H. Rashidi, J. Golliard, and T. Humbert, "Inverse impedance eduction of liners in the maine flow facility: Flow effects," in *30th AIAA/CEAS Aeroacoustics Conference (2024)*, 2024, p. 3023.

[127] W. R. Watson, M. G. Jones, S. E. Tanner, and T. L. Parrott, "Validation of a numerical method for extracting liner impedance," *AIAA journal*, vol. 34, no. 3, pp. 548–554, 1996.

[128] M. Jones, W. Watson, T. Parrott, and C. Smith, "Design and evaluation of modifications to the nasa langley flow impedance tube," in *10th AIAA/CEAS aeroacoustics conference*, 2004, p. 2837.

[129] B. Howerton, H. Vold, and M. Jones, "Application of sine sweep excitation for acoustic impedance eduction," *AIAA Paper*, vol. 2487, 2019.

[130] C. Gerhold, M. Brown, M. Jones, D. Nark, and B. Howerton, "Configuration effects on acoustic performance of a duct liner," in *14th AIAA/CEAS Aeroacoustics Conference (29th AIAA Aeroacoustics Conference)*, 2009, p. 2977.

[131] C. Gerhold, M. Brown, M. Jones, and B. Howerton, "Configuration effects on liner performance," in *18th AIAA/CEAS Aeroacoustics Conference (33rd AIAA Aeroacoustics Conference)*, 2012, p. 2245.

[132] C. Gerhold, M. Jones, M. Brown, and B. Howerton, "Report on recent upgrades to the curved duct test rig at nasa langley research center," in *17th AIAA/CEAS Aeroacoustics Conference (32nd AIAA Aeroacoustics Conference)*, 2011, p. 2896.

[133] S. Busse, C. Richter, F. Thiele, C. Heuwinkel, L. Enghardt, I. Röhle, U. Michel, P. Ferrante, and A. Scofano, "Impedance deduction based on insertion loss measurements of liners under grazing flow conditions," in *14th AIAA/CEAS Aeroacoustics Conference (29th AIAA Aeroacoustics Conference)*, 2008, p. 3014.

[134] S. Busse, C. Richter, S. Nitsch, F. Bake, L. Enghardt, F. Thiele, C. Kückens, and U. Müller, "Acoustic investigation of a specially manufactured non-locally reacting liner for aircraft application," in *16th AIAA/CEAS Aeroacoustics Conference*, 2010, p. 3830.

[135] L. Enghardt, A. Schulz, A. Fischer, and S. Busse, "Determination of the impedance for lined ducts with grazing flow," in *18th AIAA/CEAS Aeroacoustics Conference (33rd AIAA Aeroacoustics Conference)*, 2012, p. 2243.

[136] F. Bake, R. Burgmayer, A. Schulz, K. Knobloch, L. Enghardt, and M. G. Jones, "Ifar liner benchmark challenge# 1–dlr impedance eduction of uniform and axially segmented liners and comparison with nasa results," *International Journal of Aeroacoustics*, vol. 20, no. 5-7, pp. 478–496, 2021.

[137] A. M. Spillere, A. A. Medeiros, P. G. Serrano, and J. A. Cordioli, "Cross-validation of a new grazing flow liner test rig using multiple impedance eduction techniques," in *The 22nd International Congress on Sound and Vibration*, 2015.

[138] M. E. D'elia, T. Humbert, and Y. Aurégan, "On articulated plates with micro-slits to tackle low-frequency noise," *Acta Acustica*, vol. 5, p. 31, 2021.

[139] C. Morfey, "Acoustic energy in non-uniform flows," *Journal of Sound and Vibration*, vol. 14, no. 2, pp. 159–170, 1971.

Titre : Mesures d'impédance de traitements acoustiques en présence de champs sonores complexes et d'écoulements cisaillés.

Mots clés : traitement acoustique, mesure d'impédance, effet d'écoulement cisaillé, aéro-acoustique des conduits.

Résumé : Les traitements acoustiques sont largement utilisés pour réduire les émissions sonores des moteurs d'avions. Pour leur développement, il est essentiel de pouvoir mesurer l'impédance acoustique de ces traitements et d'étudier leur comportement en présence d'écoulement. Cette thèse vise à évaluer la performance de la méthode directe de mesure dans des conditions réalistes, en particulier lorsque l'on considère de grands conduits, des modes acoustiques d'ordres élevés et des vitesses d'écoulement représentatives des nacelles d'aéronefs. L'étude est d'abord basée sur des simulations numériques avec une méthode multimodale. Ensuite, le banc d'essai, MAINE Flow, permet de valider et de démontrer expérimentalement les méthodes proposées et les conclusions.

Dans les grands conduits, le champ acoustique est plus complexe que dans les petits, pour la même gamme de fréquences. Ainsi, la mesure d'impédance est un défi, qui est également perturbé par le bruit dû à la présence de l'écoulement. Ce travail conçoit d'abord la configuration expérimentale et des antennes de microphones, pour réaliser une mesure d'impédance précise dans de grands conduits.
Ensuite, la validité de l'hypothèse d'écoulement uniforme qui est souvent appliquée est évaluée, et l'effet d'un écoulement cisaillé est étudié, en particulier dans le cas de conduits de grandes tailles.
Finalement, différentes ondes incidentes entraînent des comportements différents de la méthode de mesure. Par conséquent, l'influence du champ acoustique incident est aussi étudiée.

Title : Impedance eduction of acoustic liners with complex sound fields and shear flows.

Keywords : acoustic liner, impedance eduction, shear flow effects, duct aero-acoustics.

Abstract : Acoustic liners are widely used to reduce noise emissions in aircraft engines. The investigation of liners behavior is essential for their development. Impedance eduction is thus commonly implemented to measure its acoustic impedance in presence of flow. The work in this thesis aims to study the performance of the direct eduction method under realistic conditions, especially when considering large ducts, high-order acoustic modes and flow velocities representative of aircraft nacelles. The study is first based on numerical simulations with a multimodal method. Then the MAINE Flow facility is used for experimental validation and demonstration of the proposed methods and conclusions.
In large ducts, the sound field is more complex compared to small ducts in the same frequency range. Therefore, the impedance eduction is challenging, and also because it is also perturbed by the background noise due to the presence of flow. The first task is to design microphone arrays for the experimental facility with the aim of performing accurate impedance eduction in large ducts.
The second objective is to investigate the effects of shear flow. Impedance eduction is commonly implemented under the hypothesis of uniform mean flow. However, it is reasonable to question the validity of the uniform flow hypothesis, especially when considering large ducts.
The third task is to study the influence of the incident sound field. In large ducts, the sound field contains higher-order modes, and different incident waves result in different behavior of the impedance eduction. It is thus necessary to study how the incident acoustic field affects the eduction results in the presence of flow.